

71304

3235

TR 3235

**ANALYTICAL MODELING OF
BOILING WATER REACTOR DYNAMICS**

On the cover - artist's impression of Figure 4-5



The research described in this thesis was performed within the Department of Reactor Physics of the Interfaculty Reactor Institute, Delft University of Technology, Mekelweg 15, 2629 JB Delft, The Netherlands.

This research was performed within the framework of the PINK-2/II project ("Programma ter Instandhouding van Nucleaire Competentie"), and has been financed by the Ministry of Economic Affairs.

ANALYTICAL MODELING OF BOILING WATER REACTOR DYNAMICS

PROEFSCHRIFT

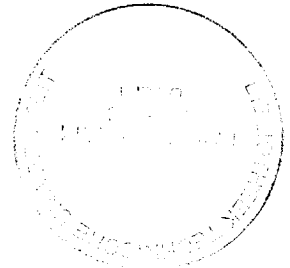
ter verkrijging van de graad van doctor
aan de Technische Universiteit Delft,
op gezag van de Rector Magnificus prof. ir. K.F. Wakker,
in het openbaar te verdedigen ten overstaan van een commissie,
door het College voor Promoties aangewezen,

op dinsdag 24 november 1998 te 10.30 uur
door

David Dominique Bernard VAN BRAGT

natuurkundig ingenieur en doctorandus in de wijsbegeerte

geboren te Roermond



Dit proefschrift is goedgekeurd door de promotor:

Prof. dr. ir. H. van Dam

Toegevoegd promotor:

Dr. ir. T.H.J.J. van der Hagen

Samenstelling promotiecommissie:

Rector Magnificus, voorzitter

Prof. dr. ir. H. van Dam,	Technische Universiteit Delft, promotor
Dr. ir. T.H.J.J. van der Hagen,	Technische Universiteit Delft, toegevoegd promotor
Prof. ir. O.H. Bosgra,	Technische Universiteit Delft
Prof. dr. R.V.A. Oliemans,	Technische Universiteit Delft
Prof. dr. ir. A.H.M. Verkooijen,	Technische Universiteit Delft
Prof. dr. I.T. Young,	Technische Universiteit Delft
Prof. dr. Rizwan-uddin,	Universiteit van Illinois te Urbana-Champaign, V.S.

Published and distributed by:

Delft University Press

Mekelweg 4

2628 CD Delft

The Netherlands

Telephone: +31 15 2783254

Fax: +31 15 2781661

E-mail: DUP@DUP.TUdelft.NL

ISBN 90-407-1719-2 / CIP

Copyright © 1998 by D.D.B. van Bragt

All rights reserved. No part of the material protected by this copyright notice may be reproduced or utilized in any form or by any means, electronic or mechanical, including photocopying, recording or by any information storage and retrieval system, without permission from the publisher: Delft University Press.

Printed in The Netherlands

‘We can forgive a man for making a
useful thing as long as he does not admire
it.

The only excuse for making a useless
thing is that one admires it intensely’

—Oscar Wilde

Table of Contents

Summary	XIII
---------------	------

1. Introduction

1.1 Objective	1
1.2 Principle of BWR Operation	2
1.3 Classification of BWR Instabilities	4
1.4 High Versus Low-Pressure Stability	6
1.5 Coupled Neutronics-Thermohydraulics	7
1.6 Space-Dependent Oscillations	9
1.7 Nonlinear and Chaotic Dynamics	10
1.8 Outline	12
References	13

2. High-Pressure BWR Dynamics: I – Theoretical Model

Abstract	15
2.1 Introduction	15
2.2 Natural Circulation of the Coolant	16
2.3 Model	17
2.3.1 Neutron Kinetics	17
2.3.2 Fuel Dynamics	18
2.3.3 Thermohydraulic Subsystem	18
2.3.4 Boiling Boundary Dynamics	20
2.3.5 Core Void Dynamics	20
2.3.6 Riser Void Dynamics	21
2.3.7 Natural Circulation Loop Dynamics	21
2.3.8 Core	22
2.3.9 Riser	22
2.3.10 Downcomer	22
2.4 Frequency-Domain Analysis	23

2.5 Nondimensional Analysis	26
2.5.1 Thermohydraulic Stability	26
2.5.2 Reactor Stability	29
2.6 Conclusions	30
References	31

3. High-Pressure BWR Dynamics: II – Parametric Study

Abstract	33
3.1. Introduction	33
3.2 Thermohydraulic Stability	35
3.2.1 Influence Riser and Downcomer	35
3.2.2 Influence of Pressure	38
3.3 Reactor Stability	38
3.3.1 Influence of Void Reactivity Feedback	39
3.3.2 Influence of Pressure	41
3.3.3 Influence of Fuel Dynamics	41
3.3.4 Best Estimate Data Set for the Dodewaard BWR	42
3.3.5 In-Phase Versus Out-of-Phase Stability	43
3.3.6 Sensitivity of Reactor Stability to Changes in Operating Conditions	46
3.4 Conclusions	48
References	49

4. High-Pressure BWR Dynamics: III – Nonlinear Analysis

Abstract	51
4.1. Introduction	51
4.2 The Hopf Bifurcation	53
4.3 Thermohydraulic Subsystem	55
4.3.1 Natural Circulation System Without Riser	55
4.3.2 Natural Circulation System With Riser	59
4.4 Reactor System	61
4.4.1 Reactor System Without Riser	62
4.4.1.1 Dynamics in the Vicinity of the Stability Boundary	62
4.4.1.2 ‘Deep’ in the Unstable Region	66
4.4.2 Reactor System With Riser	67

4.5 Conclusions	69
References	70

5. Low-Pressure BWR Dynamics: I – Theoretical Model

Abstract	73
5.1 Introduction	73
5.2 Current Research on Flashing	74
5.3 Model	75
5.4 Conclusions	83
References	84

6. Low-Pressure BWR Dynamics: II – Parametric Study

Abstract	87
6.1 Introduction	87
6.2 Statics	90
6.2.1 Comparison With Other Models	90
6.2.2 Influence of the Operating Conditions	93
6.3 Dynamics	98
6.3.1 Model Assumptions	98
6.3.1.1 Boiling Boundary Model	98
6.3.1.2 Energy Conservation Equation	100
6.3.2 Stability Analysis	102
6.3.3 Influence of the Operating Conditions	106
6.4 Conclusions	109
References	110

7. Validation of the Theoretical Models

Abstract	111
7.1 Introduction	112
7.2 The DESIRE Facility	112
7.3 Thermohydraulic Stability Benchmark	113
7.4 Dodewaard High-Power (Type-II) Experiments	115
7.4.1 Introduction	115
7.4.2 Dodewaard Natural Circulation Flow Predictions	116

7.4.3	Dodewaard Type-II Stability Tests	119
7.4.4	Nonlinear Analysis of the Dodewaard Cycle 26 Instability	121
7.5	Dodewaard Startup (Type-I) Experiments	124
7.5.1	Natural Circulation Flow Predictions	124
7.5.2	Dodewaard Type-I Stability Tests	128
7.6	Conclusions	132
	References	132

8.	Conclusions and Recommendations	135
----	---------------------------------------	-----

Appendices

Appendix A: Out-of-Phase Neutron Kinetics

A.1	Modal Point-Kinetic Equations	139
A.2	λ -Modes in a (Homogeneous) Cylindrical Reactor Core	140
A.3	Importance of the Out-of-Phase Mode	142
	References	144

Appendix B: Equations of the High-Pressure BWR Model

B.1	Neutron Kinetics	145
B.2	Fuel Dynamics	145
B.3	Boiling Boundary Dynamics	146
B.4	Core Void Dynamics	146
B.5	Void Dynamics for the n-th Riser Node	147
B.6	Mass Flux Density Dynamics	147
	References	147

Appendix C: Dimensionless Numbers and Variables

	in the Low-Pressure BWR Model	148
--	-------------------------------------	-----

Appendix D:	Coefficients of Eq. (5-26)	149
-------------	----------------------------------	-----

Nomenclature	151
--------------------	-----

Summary (in Dutch)	157
--------------------------	-----

<u>Table of Contents</u>	<u>XI</u>
Summary (in Japanese)	159
List of Publications	161
Acknowledgments	163
Curriculum Vitae	165

Summary

Dynamics of boiling water reactors (BWRs) is studied using low-dimensional analytical models. We focus on dynamic instabilities induced by the nuclear and thermohydraulic processes inside the vessel of a BWR. Our analytical models strongly increase the physical insight into the complex processes determining BWR stability and enable fast (linear and nonlinear) parametric studies (as opposed to large-scale BWR codes, which are often extremely time-consuming). A broad range of stability issues is explored: coupled neutronics-thermohydraulics, nonlinear dynamics, space-dependent oscillations, natural circulation BWRs and low-pressure dynamics.

First, a theoretical model describing coupled neutronic-thermohydraulic power oscillations in natural circulation BWRs is developed. This model consists of approximating models for the neutron kinetics, fuel dynamics and thermohydraulics. These subsystems are interconnected via void and Doppler reactivity feedback paths. Model equations are transformed to a nondimensional basis, to eliminate all explicit pressure dependence in the model.

Two major types of BWRs instabilities are predicted by the analytical model. BWRs without a riser section (e.g. forced-convection reactors) are susceptible to instabilities of the so-called *Type-II*. This type of instability has a thermohydraulic origin - phase lags between the one- and two-phase friction in the reactor core - and is amplified strongly by the neutronics feedback. It occurs typically at high-power and low-flow conditions, i.e. when the dimensionless Zuber number is large. Natural circulation cooled BWRs are also susceptible to *Type-I* instabilities. *Type-I* instabilities are caused by the significant gravitational pressure drop over the riser section in a natural circulation BWR. They become especially important under low-power and low-pressure (reactor startup) conditions. The influence of spatial out-of-phase oscillations on *Type-I* and *Type-II* stability is investigated in detail.

The analytical model is analyzed in the nonlinear domain with a Hopf-bifurcation code and numerical time-domain simulations. The two main bifurcation types in BWRs, the supercritical and subcritical Hopf bifurcation, are studied for a variety of systems (purely thermohydraulic systems vs. complete nuclear-coupled reactors, forced vs. natural circulation cooled systems). Bifurcation characteristics are shown to be particularly sensitive to the strength of the nuclear feedback, the operating conditions and nodalization approximation in the model. The time-domain model also predicts a sequence of period-doubling pitchfork bifurcations (after the first supercritical Hopf bifurcation), 'deep' in the *Type-II* instability region.

Next, a dynamic model for natural circulation BWRs under low-pressure conditions is developed. This model accounts for the effect of (axial) pressure differences in the flow loop on the saturation enthalpy of the coolant liquid. At a low reactor pressure, the saturation enthalpy becomes strongly dependent on the pressure level. The decreasing hydrostatic pressure along the flow path (when the coolant flows upwards through the core and riser sections) then leads to a rapidly decreasing saturation enthalpy and, possibly, the occurrence of void flashing. A parametric study shows that ex-core boiling, due to void flashing in the unheated riser, is dominant during the startup of a natural circulation BWR. Nuclear void reactivity effects are expected to be small under these circumstances. The Type-I instability region in the operating plane expands dramatically if the pressure is reduced, due to unstable void flashing in the riser at low pressures. This supports the recent concern about the startup stability of natural circulation BWRs.

The developed analytical models are benchmarked successfully against experimental data available from a natural circulation cooled BWR (the Dodewaard reactor, located in the Netherlands) and experimental facilities. Experimentally observed trends in the high power (Type-II) domain are predicted correctly. The nonlinear reactor model is also validated against large-amplitude power oscillations, measured in the Dodewaard BWR. Oscillations encountered in the low power and pressure (Type-I) domain, during the startup of this reactor, are simulated with the low-pressure BWR model. Evaluation of these startup measurements shows that void flashing in the riser indeed becomes important in the low-pressure regime, in agreement with the theoretical predictions.

Chapter 1

Introduction

1.1. OBJECTIVE

The last decade, high-fidelity boiling water reactor (BWR) stability codes have been developed, with state-of-the-art models for the three-dimensional neutron kinetics, heat transfer and thermohydraulics. Significant progress has been made in this numerical field, but an important trade-off between modeling accuracy and computational demands still exists. The most advanced codes are often extremely time-consuming and require the application of sophisticated numerical solution schemes. Therefore, a complementary effort has focused on the development of reduced-order models, often consisting of only a limited set of ordinary differential equations (ODEs).

These 'physical' models include descriptions of the most important processes determining the dynamic characteristics of a BWR, but approximate (or neglect) less important phenomena. Moreover, because most state variables (like for instance the neutron flux density, fuel temperature and coolant density) are spatially distributed, approximating integration schemes of the basic ODEs are used, to keep the dimension of the model (i.e. the total number of ODEs) relatively low.

This analytical approach leads to the development of fast-running codes generating qualitatively correct predictions for a wide range of operating and design parameters. Reduced-order models are therefore suitable candidates to evaluate the consequences of new designs on reactor stability and safety. Because next generation BWRs are probably cooled by natural convection, to enhance the degree of 'passive safety', this thesis focuses on the specific stability problems associated with natural circulation core cooling. This thesis also investigates whether the stability problems encountered in present-day BWRs, which are cooled by forced convection, are important as well for new reactor designs.

Model predictions will be compared with experimental data to assess their accuracy and range of validity. Furthermore, a comparison with detailed BWR stability codes will be presented.

1.2. PRINCIPLE OF BWR OPERATION

The principle of operation of a reference BWR design [a BWR/4 from the General Electric (GE) company] is clarified in Fig. 1-1. Heat is produced by nuclear fission reactions inside more than 700 fuel assemblies, located in the reactor core. A fuel bundle itself consists of a lattice of 8×8 fuel rods. These rods are rather thin – approximately 1 cm in diameter – and very long – about 4 m. Each individual rod has a cladding of zircaloy, which confines the radioactive fission products released by the uranium-dioxide (UO_2) fuel.

Heat produced in the fuel bundles is removed by the coolant (ordinary water, H_2O). Normally, the coolant enters the core several degrees below the saturation temperature. As it flows upwards along the fuel assemblies, the temperature increases, and the coolant starts to boil. At the core outlet, approximately 10% of the coolant mass is converted to steam. This steam-water mixture flows through the steam separators and dryers after exiting the core. The steam leaves the vessel via the main steam line, to drive (a cascade of) turbines. The turbine axis is coupled with an electric generator which produces electricity. The water, which is separated from the steam, flows downwards in the periphery of the vessel and mixes with the recirculated condensate from the turbines.

The electric output of a BWR is approximately 1200 MWe. A typical efficiency of a BWR is 33%, implying that the total thermal power produced is 3600 MWth. This huge amount of energy is generated in a relatively small core volume of only 65 cubic meters, i.e. the average core power density is 56 kW/l. Hence, cooling of the reactor core should be guaranteed under all circumstances, to avoid excessively high fuel temperatures (possibly even leading to fuel damage).

Core cooling is partly sustained by the density differences between the low-density core region (where steam is present) and the downcomer channel (filled with liquid only). These density differences induce a spontaneous or 'natural' convection of the coolant. However, the natural circulation flow is limited by frictional pressure losses in the flow loop, for instance due to wall friction, local flow restrictions, structural

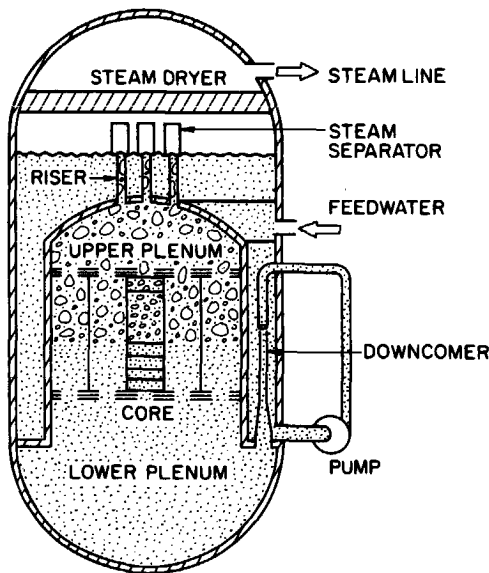


Figure 1-1. The configuration of the BWR recirculating loop.¹

material, etc. In a BWR, this natural circulation limit (~ 4000 kg/s) is reached at a power level of ~ 1800 MWth (50% of full power). Increasing the power level further, the natural circulation flow rate no longer increases. Therefore, pumps are used at higher power levels to force the coolant through the core. These jet pumps, depicted in Fig. 1-1, are driven by coolant flow from pumps in the recirculation loops. Notice that the recirculation pumps are located outside the reactor vessel. In the most recent BWR design of GE, the Advanced BWR (ABWR), the complete recirculation system is installed inside the reactor vessel.

The last decades, passive safety is one of the main concepts in the design of nuclear reactors.² Passively-safe systems are governed by naturally occurring processes, and do not rely on active components (like recirculation pumps or explosion valves) or active controllers (reactor operators, electronic control equipment). Core cooling by natural circulation, instead of active coolant pumps, is an excellent example of a passive process that can be applied in a nuclear reactor.

The prototype of natural circulation BWRs is the Dutch Dodewaard BWR.^{3,4} This small-size reactor (60 MWe) has been operated successfully from 1968 through 1997. A cut-away view of the Dodewaard vessel is shown in Fig. 1-2. Most importantly, the jet pumps in Fig. 1-1 are not present in this design. On top of the Dodewaard core, an unheated riser section (with a length of ~ 3 meters) is installed. This riser section lengthens the region with two-phase flow, and thus enhances the natural circulation flow rate.

Steam separators, shown in Fig. 1-1, are not used in this design. Instead, steam separation takes place at the free water surface. In total, about 10 mass percent of the liquid is converted to steam in the reactor core. Approximately 80% of the produced steam escapes at the surface, and flows upwards in the direction of the steam dryers and main steam line. About 20% of the steam is dragged into the downcomer channel by the down-falling liquid. This complex phenomenon is called carry under. At the feedwater sparger, the voids in the downcomer are condensed by the subcooled feedwater. Carry under reduces the density difference between the riser and the top of the downcomer. It therefore has a negative effect on the natural circulation flow.

In 1982, the General Electric company started the design of a 600 MWe Simplified Boiling Water Reactor (SBWR), which incorporates and refines many passive safety features applied and tested in the Dodewaard BWR. The coolant flow is, again, completely driven by natural convection in this reactor concept. Furthermore, important safety systems like the isolation condensers and the emergence core cooling system mainly depend on passive processes. Steam separators are incorporated in this design to avoid carry under.

Development of the SBWR stopped in 1996, because there was not enough commercial interest in a medium-size BWR. Therefore, a larger SBWR, the European SBWR (ESBWR),⁵ was proposed. This reactor has a design power of 1190 MWe, at the same level as currently operating BWRs, probably making it a more attractive design from economics point of view.

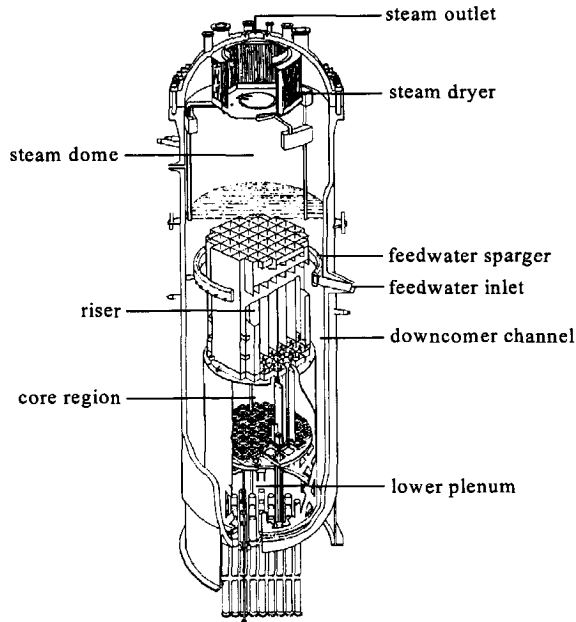


Figure 1-2. Cut-away view of the Dodewaard BWR vessel. Notice that no recirculation pumps are present in this design: the convection of the coolant is driven by the density differences between the core/riser and downcomer.

1.3. CLASSIFICATION OF BWR INSTABILITIES

This section discusses the physical mechanisms that cause instabilities in BWRs. Previous research has shown that the most important instabilities in currently operating BWRs are purely thermohydraulic and coupled neutronic-thermohydraulic instabilities.^{6,7} These instability types are basically induced by the 'density-wave' character of the two-phase flow in the coolant channels. Traditionally, the mechanism causing density-wave oscillations is clarified qualitatively as follows (see Fig. 1-3). Consider a boiling channel with a constant pressure difference between inlet and outlet.^{a)} If the inlet flow rate is reduced at a constant heating power, voids are produced in the channel that travel upwards as a packet, forming a propagating 'density wave'. This traveling density wave causes a change in the local pressure drop at higher axial positions, with a certain delay due to the finite velocity of the propagating wave. The frictional pressure drop becomes particularly large in the region with a high (volumetric) amount of steam (void fraction), i.e. close to the core outlet. The major part of

^{a)}This constant pressure drop boundary condition can be achieved in an experimental setup, by having a large bypass flow parallel with the heated channel.

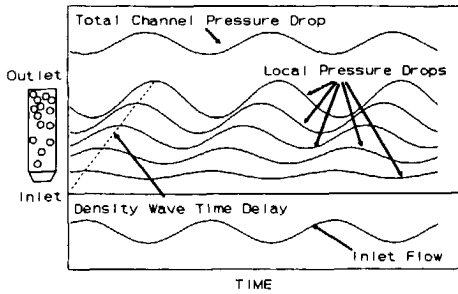


Figure 1-3. Illustration of the local pressure drop delay introduced by the density-wave mechanism.⁸

the total pressure drop will therefore be delayed with respect to the original inlet flow perturbation. Hence, if the inlet flow is perturbed sinusoidally as in Fig. 1-3, the total pressure drop over the channel (which is the sum of the delayed local pressure drops) will be delayed with respect to the inlet flow perturbation. In Fig. 1-3, the total pressure drop is delayed 180 degrees with respect to the inlet flow, i.e. a decrease in inlet flow results in an increase of the total pressure drop (and vice versa).

Perturbations of the inlet flow thus receive a positive feedback, and the oscillations grow at the unstable frequency.

Recently, Rizwan-uddin started a discussion about the dominant feedback mechanism causing density-wave instabilities.⁹ He investigated the physical mechanism causing density-wave oscillations with a sophisticated nonlinear model. Interestingly enough, Rizwan-uddin's results contradict the aforementioned line of reasoning at some points. He found, for instance, that traveling density waves do not play a dominant role during the oscillations. Instead, axial variations in the mixture velocity were identified as the true origin of the dynamic instabilities.

An earlier theoretical study¹⁰ by Fukuda and Kobori focused on the dependence of the density-wave instability on the operating conditions. Basically, these authors used the same differential equations as Rizwan-uddin. However, Fukuda and Kobori linearized the governing equations and performed a frequency-domain stability analysis, whereas Rizwan-uddin solved the nonlinear set of (integro-differential) equations directly in time domain. Fukuda and Kobori demonstrated that at least eight 'types' of density-wave instabilities exist. Three of them are static or 'Ledinegg' flow excursions, and the remaining five of them are all dynamic instabilities. Roughly, however, two main instability types can be distinguished: low-frequency Type-I instabilities due to the gravitational pressure drop term, and high-frequency Type-II instabilities due to frictional pressure losses.

Type-II instabilities have been studied extensively in the past,⁷ because of their importance under low-flow/high-power (reactor accident) conditions. Note, for instance, that the previous discussion focused on Type-II oscillations (only the variations in the frictional pressure drop were considered).

The Type-I instability mechanism becomes dominant in natural circulation reactors operating at low power and pressure conditions, e.g. during the reactor startup. Under these circumstances, the (mass) percentage of steam (the flow quality) at the core outlet becomes

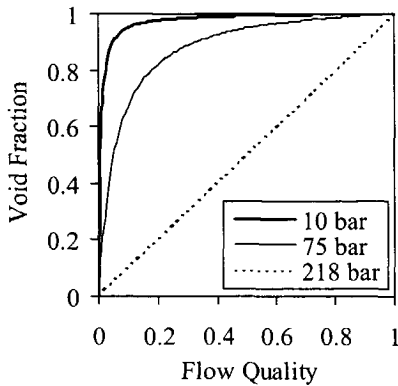


Figure 1-4. Relation between the void fraction and the flow quality for different pressures. The slope of the void fraction vs. flow quality curve becomes steeper when the flow quality and pressure decrease.

very small. Figure 1-4 shows that for small flow qualities and low pressures, the volumetric amount of steam (the void fraction) increases very rapidly as a function of the flow quality. A small decrease in the core inlet flow then leads to a strong increase of the volume of steam produced at the core outlet. In a natural circulation reactor, this causes a low-density wave traveling through the riser section. This enhances the driving head, and the inlet flow will increase. Then the opposite process occurs, and the void fraction in the riser decreases. Consequently, the driving head becomes smaller, and the flow rate will decrease. This completes one cycle of a Type-I oscillation.

The main time constant governing this type of density-wave oscillations is the transit time of the voids through the riser. At low power levels, this transit time becomes rather large (~5-10 s) because the coolant velocity diminishes under these conditions (moreover, the flow velocities in the riser are relatively small due to its large flow area).

1.4. HIGH VERSUS LOW-PRESSURE STABILITY

Until very recently, almost all theoretical density-wave models assumed that the physical properties are constant in the flow loop. This assumption leads to accurate results under nominal operating pressures (~75 bar), when the fluid properties are weakly dependent on the actual pressure level. At high pressures, the saturation temperature (T_{sat}) is, for instance, in good approximation constant in the flow loop. Figure 1-5a illustrates how the liquid temperature (T_l) then increases due to heating in the core region, until T_{sat} is reached and boiling starts.

At lower operating pressures (below 20 bar, for instance during the reactor startup) fluid properties like the saturation temperature become strongly dependent on the pressure level. Figure 1-5b shows the influence of a changing saturation temperature on the steam production in a natural circulation reactor. As the coolant flows upwards, the hydrostatic pressure will decrease. Hence, the saturation temperature will also decrease. This causes a downward shift of the boiling boundary position. The steam production will also continue in the *unheated* riser, whereas the void fraction is constant in this section in Fig. 1-5a. This additional steam production, due to the decreasing saturation temperature along the flow path, is known as

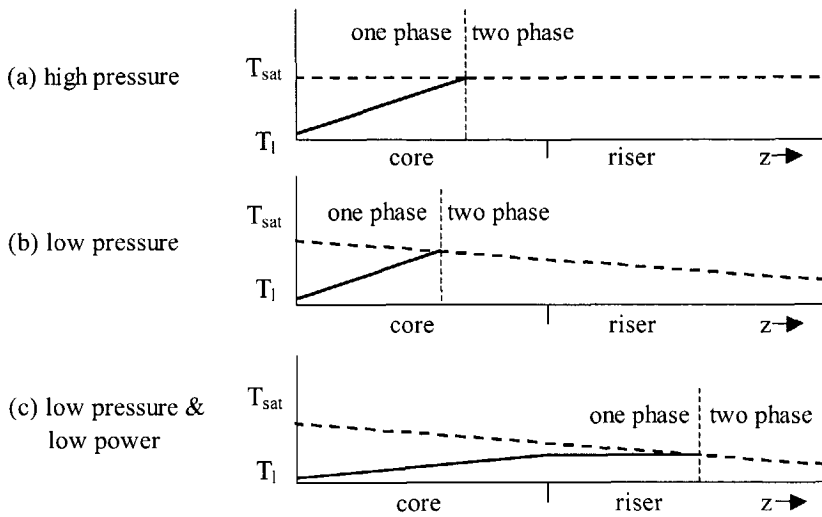


Figure 1-5. Influence of the pressure dependence of the saturation temperature, T_{sat} , on the steam production in a natural circulation BWR. At high pressures, T_{sat} is in good approximation constant in the flow loop, see Fig. 1-5a. The coolant temperature T_1 then increases due to heating, until T_{sat} is reached and boiling starts. At lower pressures, T_{sat} significantly decreases as the coolant flows upwards, see Fig. 1-5b, due to the decreasing hydrostatic pressure along the flow path. At a very low heating power, 'flashing' of the coolant in the riser section is also possible, see Fig. 1-5c.

void 'flashing'.¹¹

This flashing effect becomes very important under low power and pressure conditions. In Fig. 1-5c, the power level is reduced, compared to Fig. 1-5b, and the coolant does not reach the boiling point before the outlet of the heated channels. However, in the riser section the decreasing saturation temperature becomes equal to the (constant) fluid temperature, and boiling out of the heated reactor core starts. Notice that ex-core boiling is not likely to occur at high pressures, because the saturation temperature is in good approximation independent of the axial position under these circumstances (see Fig. 1-5a).

Void production in the riser directly affects the gravitational pressure drop over this section. Hence, it can be expected that the Type-I feedback mechanism is amplified by the occurrence of void flashing, especially in natural circulation BWRs with a tall riser section. This observation has prompted recent experimental and theoretical research on the stability of 'flashing-induced' Type-I oscillations. An overview of this new and rapidly developing field is provided in Section 5.2 of this thesis.

1.5. COUPLED NEUTRONICS-THERMOHYDRAULICS

Up to this point, we have only discussed thermohydraulic instabilities, occurring in boiling channels with a fixed heating power. In BWRs, however, we also need to consider the

important role of the coolant as a neutron moderator.

The fission cross-section of the fissile uranium isotope in the nuclear fuel (^{235}U) is over two orders of magnitude larger for low-energy or 'thermal' neutrons (<1 eV) than for neutrons with energies above 1 keV.¹² After each fission on the average 2.5 high-energy neutrons are released (in the MeV range). These fast neutrons lose their kinetic energy as they collide with the coolant nuclei (the moderator). After several collisions, the neutrons have lost most of their kinetic energy and can cause new fissions with a higher probability.

As neutrons slow down from fission energies in a BWR, there is a certain probability that they leak out of the reactor core or are absorbed in the nuclear fuel. In particular, resonance absorption by ^{238}U nuclei is an extremely important phenomenon. The resonance escape probability increases when the slowing-down process of the neutrons becomes more efficient, e.g. when the density of the coolant material increases. A decreasing moderator density, for instance due to void production inside the coolant channels, has just the opposite effect and will therefore cause an increase of the resonance absorption rate.

The influence of void fraction changes in the coolant channels on the reactor power is depicted schematically in Fig. 1-6. The impact of the void fraction on the reactivity is described with the void reactivity coefficient $\tilde{\rho}_a$ in this block diagram. The (complicated) thermohydraulic subsystem is described by the G_a -transfer function in Fig. 1-6. An extended block diagram, revealing the different feedback paths in the thermohydraulic subsystem, is presented in Fig. 2-2.

Figure 1-6 shows that overall BWR stability is determined by the *interaction* between neutronics (the zero-power reactor transfer function G_R), fuel dynamics (G_F) and thermohydraulics (G_a). For instance, if we increase the external reactivity, the reactor power will increase (via G_R). This causes an increase of the fuel temperature (via G_F) and the void fraction (via G_a). An increase of the void fraction reduces the resonance escape probability, and therefore causes a negative void reactivity effect ($\tilde{\rho}_a$ is negative). Furthermore, an increase of the fuel temperature will broaden the width of the ^{238}U capture resonances, effectively

increasing the resonance absorption. This Doppler effect is accounted for in the (also negative) Doppler reactivity coefficient $\tilde{\rho}_D$. Hence, an increase of the reactor power results in a subsequent decrease of the reactivity via the void- and Doppler feedback paths. This negative feedback mechanism

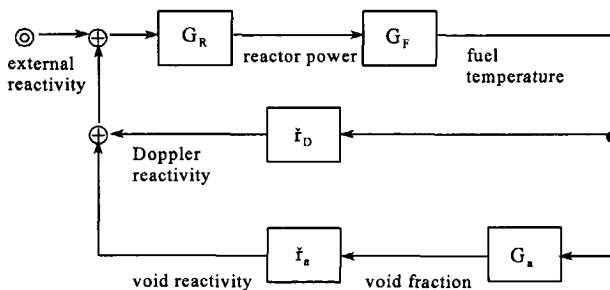


Figure 1-6. Elementary block diagram describing the dynamics of BWRs. A more detailed block diagram is presented in Fig. 2-2.

makes a BWR a very stable system during slow transients.

However, during high-frequency transients (~ 0.5 –1 Hz) the (stabilizing) negative feedback in a BWR can become positive (destabilizing), in particular when the feedback processes occur with a certain time delay. When the feedback gain then exceeds a critical value, coupled neutronic-thermohydraulic instabilities can occur in a BWR.

Theoretical, numerical and experimental research on this topic has been intensified in the last two decades, after instability events in several commercial BWRs were reported.¹³ Unexpectedly large power oscillations were, for instance, measured during the startup of the Italian Caorso plant in 1984. Four years later, in 1988, two recirculation pumps of the LaSalle-2 unit tripped. In the natural circulation mode, this reactor also became unstable. Since the LaSalle unit is located in the United States, the U.S. Nuclear Regulatory Commission (NRC) undertook action, and started a detailed research program to solve the stability problems in BWRs. The proceedings of the 1990 international workshop on BWR stability (in Brookhaven, NY) give a good overview of the research activities following the LaSalle instability event.¹⁴ An excellent review of the current state of the art in this field is provided by a recent OECD/NEA report on BWR stability.¹⁵ However, almost no information about stability problems in natural circulation BWRs is found in Refs. 13 through 15. For instance – to the author's knowledge – the influence of low-frequency Type-I oscillations on coupled neutronic-thermohydraulic stability of natural circulation reactors has not been studied in the past. This is one of the main incentives of the research on nuclear-coupled stability of natural circulation BWRs, presented in this thesis.

1.6. SPACE-DEPENDENT OSCILLATIONS

An excellent example of coupled neutronic-thermohydraulic phenomena are so-called 'out-of-phase' oscillations of the reactor power in a BWR. Typically, in the out-of-phase oscillation mode the power in one half of the reactor core increases, while in the other part the power decreases with the same amount. A schematic picture of the out-of-phase mode is given in Fig. 1-7. The axial component of the neutron flux density is omitted in this picture.

Out-of-phase oscillations have been observed in several European BWR plants, for instance in the Caorso plant (see Section 1.5) and during stability tests in the Swedish Ringhals-1 reactor.¹⁶ These reports have raised considerable concern, because out-of-phase oscillations are very difficult to detect with average power detectors and may therefore not lead to an automatic control rod scram if a reactor instability occurs.

March-Leuba and Blakeman were – to the author's knowledge – the first to point out that out-of-phase oscillations are more unstable from thermohydraulic point of view than global oscillations: because the core pressure drop and total coolant flow rate remain essentially constant, flow oscillations in the core are not damped by friction and inertia in the

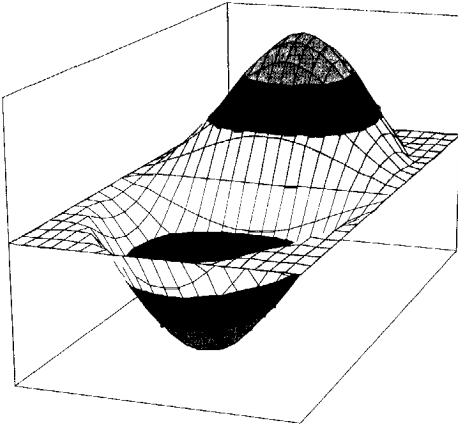


Figure 1-7. Schematic picture of the first-azimuthal or 'out-of-phase' mode. The axial dependence of the neutron flux density is omitted in this figure.

reactivity feedback.

Nowadays, there is a tendency towards designing larger reactor cores, to increase the reactor power while reducing the power density. Good examples are modern BWR designs by GE, like the (E)SBWR and ABWR product lines. The 600 MWe SBWR was, for instance, designed to have a larger core radius (~2.44 m) than currently operating 1200 MWe BWRs (~1.83–2.29 m). Because it is conceivable that especially large (more spatially decoupled) reactor cores are susceptible to out of phase oscillations, the need for an evaluation of these space-dependent phenomena becomes apparent. A detailed comparison between in-phase and out-of-phase reactor stability of natural circulation BWRs will therefore be presented in Chapter 3 of this thesis.

1.7. NONLINEAR AND CHAOTIC DYNAMICS

Nonlinear dynamics of BWRs is one of the main application fields of modern chaos and bifurcation theory. Nuclear engineers started to recognize the importance of these 'new' and 'esoteric' branches of science after the aforementioned instability events in LaSalle and Caorso were reported. The transition from a stable operating point to an oscillatory behavior resulted in rapidly growing power oscillations in these reactors, eventually leading to reactor scrams. This raised questions about the possible consequences of a failing scram system.

Careful experiments in the Forsmark-1 BWR in Norway showed that, due to nonlinear effects, stable limit cycle oscillations can exist in the unstable operating region of a BWR.¹⁹ The transition from a (linearly) stable operating point to a (nonlinearly) stable limit cycle

recirculation loop.¹⁷

On the other hand, the out-of-phase mode is stabilized by the neutronic subsystem due to the fact that all higher harmonic modes have an eigenvalue smaller than unity in the equilibrium state. Hashimoto combined the point-kinetic equation for the out-of-phase mode with an elementary model for the thermohydraulic feedback.¹⁸ He demonstrated that in the low flow/high power domain, out-of-phase oscillations can indeed occur for realistic values of subcriticality and void

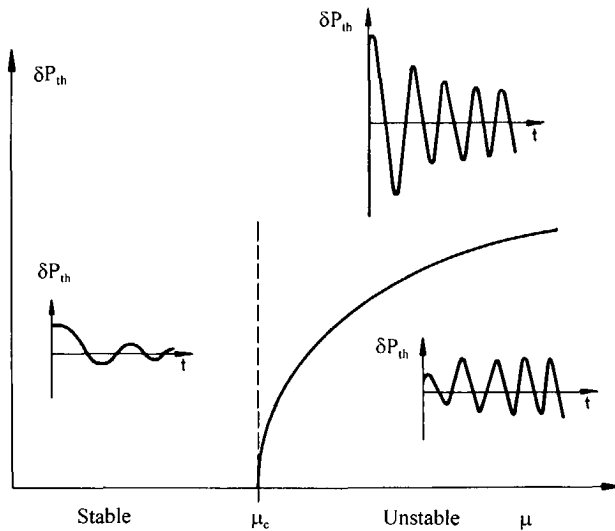


Figure 1-8. Limit cycle oscillations in a BWR (this is an example of a supercritical Hopf bifurcation).²⁰ The reactor becomes (linearly) unstable when the parameter μ is larger than μ_c . In this unstable region, the oscillating reactor power converges to a stable nonlinear oscillation (limit cycle). The oscillation amplitude of the attracting limit cycle depends on μ , as the solid curve in the right half plane (where $\mu > \mu_c$) shows.

oscillation of the thermal reactor power (P_{th}) is clarified schematically in Fig. 1-8. The reactor becomes (linearly) unstable in Fig. 1-8 when the (design or operating) parameter μ is larger than a critical value μ_c . In the stable region ($\mu < \mu_c$), oscillations of the reactor power are damped, and after a perturbation the system returns to the stable operating point. In the unstable region ($\mu > \mu_c$), small-amplitude power oscillations initially diverge. However, when the oscillation amplitude becomes large, stabilizing nonlinear terms prevent a

complete runaway of the system. The resulting limit cycle is a stable ('attractive') solution of the nonlinear equations which govern the dynamics of a BWR. The solid line in the right half plane of Fig. 1-8 shows the increasing limit cycle amplitude as a function of μ . Notice that both small and large-amplitude oscillations finally converge to the same limit cycle.

Figure 1-8 might have a reassuring effect: even if a BWR becomes linearly unstable, the resulting power oscillations are bounded. Recently, however, it has been pointed out that another, more dangerous, scenario might also occur in a BWR.²¹ This scenario is explained in Fig. 1-9. The reactor is now unstable in the linear instability region ($\mu > \mu_c$), and a runaway of the reactor power takes place. More importantly, the reactor also becomes unstable in some region of linear stability ($\mu < \mu_c$) for large enough amplitude excitations. Stated otherwise, the nonlinear periodic solution has become unstable ('repelling') and is now located in the linearly stable region. This is potentially a very dangerous situation, since classical linear stability analysis (for instance in frequency domain) would indicate that the system is stable for $\mu < \mu_c$. In particular, close to the linear stability boundary the 'basin of attraction' of the stable steady-state operating point becomes smaller, and small perturbations (for instance due to control rod movements or noise) could in principle result in diverging and undamped power oscillations. This is the background for performing a detailed nonlinear analysis of our

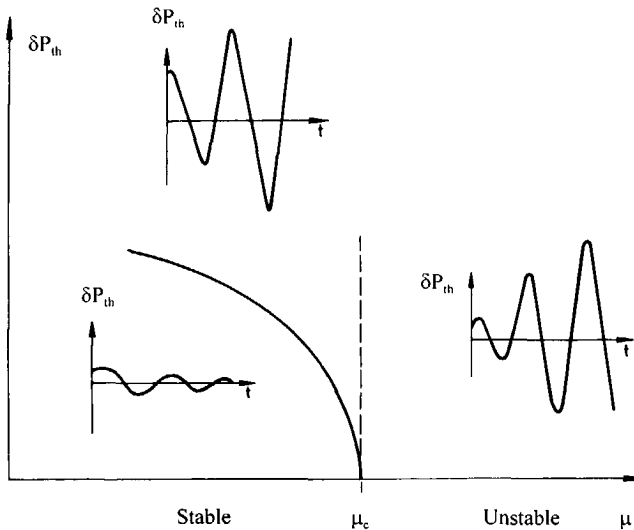


Figure 1-9. Unstable nonlinear oscillations in a BWR (this is an example of a subcritical Hopf bifurcation).²² In the linearly stable region ($\mu < \mu_c$), only small-amplitude power oscillations die out. Large perturbations of the reactor result in rapidly diverging nonlinear oscillations. The amplitude of the repelling nonlinear solution, existing in the stable region, is depicted with a solid curve.

BWR model in this thesis.

The theoretical link between nonlinear BWR dynamics and chaos theory was established by March-Leuba in the early 1980's.²³ Using a highly simplified BWR model, March-Leuba studied the stability of limit cycle oscillations, as depicted in Fig. 1-8, as a function of the μ -coordinate. He showed that, if μ is increased above a certain critical value, the amplitude of the limit cycle can become unstable, yielding a new limit cycle of twice the period. Increasing μ further results in a cascade of instabilities and period

doublings, eventually leading to chaotic oscillations. The practical importance of period-doubling and chaotic phenomena in natural circulation BWRs is discussed further in Chapter 4 of this thesis.

1.8. OUTLINE

This thesis contains eight chapters. Except for the first (Introduction) and the last chapter (Conclusions and Recommendations), this thesis consists of six technical chapters. Each chapter has its own abstract, introduction, conclusions and references, and can be read almost independently from the other chapters.

An analytical model describing coupled-neutronic thermohydraulic power oscillations in natural circulation BWRs is outlined in Chapter 2. This model focuses on the dynamics of BWRs in the high-pressure domain, i.e. the coolant properties are assumed to be constant in the coolant loop (cf. Section 1.4). Model equations are also transformed to a nondimensional basis in Chapter 2, to identify the main dimensionless numbers determining stability.

Chapter 3 consists of a comprehensive parametric study of nuclear-coupled BWR stability, employing the theoretical model proposed in Chapter 2. As an example, the stability

characteristics of the Dodewaard BWR (cf. Section 1.2) are determined. The Dodewaard reactor can be considered as the prototype of next generation natural circulation BWRs. The stability issues that are identified for this prototype reactor are therefore important in the design of new natural circulation BWRs. Special attention is paid to the impact of thermohydraulic Type-I and Type-II oscillations on overall reactor stability. Furthermore, a comparison between in-phase and out-of-phase stability is presented.

Chapter 4 evaluates the complicated nonlinear dynamics of natural circulation BWRs. We analyze the model developed in Chapter 2 with modern bifurcation theory in this chapter. Predictions of a numerical bifurcation code will be compared with direct time-domain simulations.

A dynamic model for natural circulation BWRs under low-pressure conditions is developed in Chapter 5. The pressure dependence of the saturation temperature, neglected in Chapters 2 through 4, is incorporated in this model, to account for the effect of void flashing (cf. Section 1.4).

An extensive parametric study of low-pressure BWR stability is presented in Chapter 6. This chapter focuses on the impact of void flashing on Type-I stability during the startup of a natural circulation BWR. Again, data from the Dodewaard BWR are used to put the parametric results into perspective.

Finally, the theoretical BWR models are benchmarked against experimental data in Chapter 7. In particular, a series of unique experiments on (linear and nonlinear) Type-I and Type-II stability, performed in the Dodewaard BWR, will be evaluated.

REFERENCES

1. Reprinted from *Nucl. Eng. Des.*, **95**, G.-C. Park, M.Z. Podowski, M. Becker, R.T. Lahey, Jr., and S.J. Peng, "The Development of a Closed-Form Analytical Model for the Stability Analysis of Nuclear-Coupled Density-Wave Oscillations in Boiling Water Reactors," p. 261, Fig. 2, 1986, with permission from Elsevier Science.
2. H. van Dam, "Physics of Nuclear Reactor Safety," *Rep. Prog. Phys.*, **11**, 2025 (1992).
3. A.J.C. Stekelenburg, "Statics and Dynamics of a Natural Circulation Cooled Boiling Water Reactor," PhD Thesis, Delft University of Technology, Delft, The Netherlands (1994).
4. T.H.J.J. van der Hagen, "Stability Monitoring of a Natural-Circulation-Cooled Boiling Water Reactor," PhD Thesis, Delft University of Technology, Delft, The Netherlands (1989).
5. S. S. Khorana, B. S. Shiralkar, A. S. Rao, M. Huggenberger, G. Yadigaroglu, and P. M. Stoop, "Technology Basis for the ESBWR - An Overview," *Proc. 5th Int. Conf. Nuclear Engineering (ICONE-5)*, Nice, France, May 26-30, 1997, ICONE5-2060 (on CD-rom), American Society of Mechanical Engineers, New York, NY (1997).
6. J.A. Bouré, A.E. Bergles, and L.S. Tong, "Review of Two-Phase Flow Instability," *Nucl. Eng. Des.*, **25**, 165 (1973).
7. R.T. Lahey, Jr. and F.J. Moody, *The Thermal-Hydraulics of a Boiling Water Nuclear Reactor*, American Nuclear Society, LaGrange Park, Illinois (1979).

8. Reprinted from *Nucl. Eng. Des.*, **145**, J. March-Leuba and J.M. Rey, "Coupled Thermohydraulic-Neutronic Instabilities in Boiling Water Nuclear Reactors: A Review of the State of the Art," p. 99, Fig. 1, 1993, with permission from Elsevier Science.
9. Rizwan-uddin, "Physics of Density-Wave Oscillations," *Proc. Int. Conf. New Trends in Nuclear System Thermohydraulics*, Pisa, Italy, May 30-June 2, 1994, Vol. 1, p. 195 (1994).
10. K. Fukuda and T. Kobori, "Classification of Two-Phase Flow Instability by Density Wave Oscillation Model," *J. Nucl. Sci. Technol.*, **16**, 95 (1979).
11. M. Furuya, F. Inada, and A. Yasuo, "Density Wave Oscillations of a Boiling Natural Circulation Loop Induced by Flashing," *Proc. 7th Int. Mtg. Nuclear Reactor Thermal-Hydraulics (NURETH-7)*, Saratoga Springs, New York, September 10-15, 1995, NUREG/CP-0142, p. 923, U.S. Nuclear Regulatory Commission (1995).
12. J.J. Duderstadt and L.J. Hamilton, *Nuclear Reactor Analysis*, John Wiley & Sons, New York (1976).
13. J. March-Leuba and J.M. Rey, "Coupled Thermohydraulic-Neutronic Instabilities in Boiling Water Nuclear Reactors: A Review of the State of the Art," *Nucl. Eng. Des.*, **145**, 97 (1993).
14. *Proceedings Int. Workshop Boiling Water Reactor Stability*, Brookhaven-Holtville, NY, October 17-19, 1990, OECD-NEA CSNI Report 178 (1990).
15. F. D'Auria, W. Ambrosini, T. Anegawa, J. Blomstrand, J. In de Betou, S. Langenbuch, T. Lefvert, and K. Valtonen, *State of the Art Report on Boiling Water Reactor Stability (SOAR on BWRs)*, OECD/CSNI Report, Paris (France), OECD/GD (97) 13 (1997).
16. T.H.J.J. van der Hagen, I. Pázsit, and O. Thomson, "Methods for the Determination of the In-Phase and Out-of-Phase Stability Characteristics of a BWR," *Nucl. Technol.*, **107**, 193 (1994).
17. J. March-Leuba and E.D. Blakeman, "A Mechanism for Out-of-Phase Power Instabilities in Boiling Water Reactors," *Nucl. Sci. Eng.*, **107**, 173 (1991).
18. K. Hashimoto, "Linear Modal Analysis of Out-of-Phase Instability in Boiling Water Reactor Cores," *Ann. Nucl. Energy*, **20**, 789 (1993).
19. B.G. Bergdahl, F. Reisch, R. Oguma, J. Lorenzen, and F. Åkerhielm, "BWR Stability Investigation at Forsmark I," *Ann. Nucl. Energy*, **16**, 509 (1989).
20. Adapted from *Nucl. Eng. Des.*, **95**, R.T. Lahey, Jr., "Advances in the Analytical Modeling of Linear and Nonlinear Density-Wave Instability Modes," p. 24, Fig. 20, 1986, with permission from Elsevier Science.
21. A.A. Karve, Rizwan-uddin, and J.J. Dorning, "Stability Analysis of BWR Nuclear-Coupled Thermal-Hydraulics Using a Simple Model," *Proc. 7th Int. Mtg. Nuclear Reactor Thermal-Hydraulics (NURETH-7)*, Saratoga Springs, New York, September 10-15, 1995, NUREG/CP-0142, Vol. 4, p. 2677, U.S. Nuclear Regulatory Commission (1995).
22. Adapted from *Nucl. Eng. Des.*, **95**, R.T. Lahey, Jr., "Advances in the Analytical Modeling of Linear and Nonlinear Density-Wave Instability Modes," p. 24, Fig. 19, 1986, with permission from Elsevier Science.
23. J. March-Leuba, "Dynamic Behavior of Boiling Water Reactors," PhD Thesis, University of Tennessee, Knoxville, Tennessee (1984).

Chapter 2

High-Pressure BWR Dynamics: I - Theoretical Model^{a)}

Abstract - A theoretical model describing coupled neutronic-thermohydraulic power oscillations in natural circulation BWRs is developed. The governing equations for the thermohydraulic subsystem are transformed to a dimensionless basis, to eliminate all explicit pressure dependence in the model. It is proved that all necessary information about the operating conditions is incorporated in only two dimensionless numbers: the Zuber and the subcooling number. The density ratio number cancels in the dimensionless equations, because a homogeneous flow model is applied. The Froude number is also shown to be redundant in a natural circulation system, as it can be expressed in the other dimensionless groups. The stability boundary of the complete coupled neutronic-thermohydraulic reactor system in the dimensionless Zuber-subcooling plane is estimated to be rather insensitive to the system pressure as well. Therefore the usage of dimensionless stability maps, instead of the traditional power-flow maps, is strongly recommended as an efficient method to determine the dynamic characteristics of natural circulation BWRs.

2.1. INTRODUCTION

Much research has been performed in recent years in the field of dynamic stability of BWRs, after unexpected large amplitude power oscillations were observed in the Caorso (1984) and the LaSalle (1988) plants: Consequently, several stability tests have been performed under similar low flow and high power conditions.^{1,2} Analytical work on the coupling between the neutronics and the thermohydraulics, the origin of the power

^{a)}This chapter has been published (in a slightly modified form) as:

D.D.B. van Bragt and T.H.J.J. van der Hagen, "Stability of Natural Circulation Boiling Water Reactors: Part I - Description Stability Model and Theoretical Analysis in Terms of Dimensionless Groups," *Nucl. Technol.*, **121**, 40 (1998).

oscillations, was also intensified.^{3,4} Advanced BWR stability codes like TOSDYN-2, STAIF, RAMONA or NUFREQ-N were used to evaluate test data.⁵⁻⁹

Just before BWR dynamics attracted large-scale attention, March-Leuba developed a qualitative reduced-order stability model for BWRs (Ref. 10). This model is very suitable for fast parameter studies in both the linear and the nonlinear domain. However, this reduced-order model, especially the equations describing the thermohydraulic processes, contains several fit-parameters, that need to be estimated via experiments or code calculations. A more elaborate reduced-order model to analyze spatial out-of-phase power oscillations was proposed in Ref. 11. This model reduces to March-Leuba's model when the influence of the dynamic behavior of the boiling boundary between the one-phase and the two-phase region in the core is neglected in the equations for the thermohydraulic subsystem.

This chapter focuses on the topic of natural circulation BWRs. The keyword in modern nuclear reactor designs is so-called passive or inherent safety. Passive safety means that the nuclear reactor always remains within certain safety limits, without active (safety) components. The concept of natural circulation of the coolant in BWRs is a major step towards a passively safe reactor design. The coolant in existing BWRs is circulated by pumps. When these pumps fail or do not work properly, the core can heat-up significantly and the margin to thermal limits decreases. Furthermore, the possibly dangerous low flow and high power region, where dynamic instabilities are to be expected, might be entered.

Natural circulation of the coolant is a gravity-driven process that automatically starts when boiling in the reactor core occurs, see Section 2.2, and therefore it is a very attractive way to cool a nuclear reactor. A time-domain stability model for natural circulation BWRs is developed in Section 2.3. The frequency-domain variant is outlined in Section 2.4. The thermohydraulic model for the natural convection of the coolant can be analyzed in terms of nondimensional groups. The transformation to a nondimensional basis is described in Section 2.5.1, and enables a more general approach and a deeper insight into the primary parameters determining the stability of the natural circulation flow, in case of a constant heat flux density from fuel to coolant. The usefulness of dimensionless numbers in the analysis of coupled neutronic-thermohydraulic reactor stability of natural circulation BWRs is discussed in Section 2.5.2.

2.2. NATURAL CIRCULATION OF THE COOLANT

Figure 2-1 provides a simplified overview of the flow path in a natural circulation BWR. When the coolant enters the core region, coming from the lower plenum, the temperature is normally below the saturation temperature. The fluid is heated in the core region by nuclear fission reactions in the fuel. Bulk boiling occurs at a certain axial position and the quality of the two-phase mixture increases as it travels through the core. An unheated riser (or chimney)

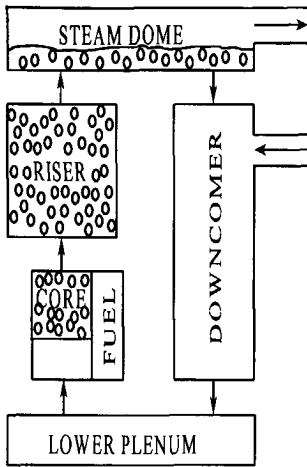


Figure 2-1. Schematic overview of a natural circulation BWR. The arrows indicate the coolant flow direction.

section is placed on top of the core in natural circulation BWRs. The two-phase mixture passes through this region and enters the steam dome. The steam then leaves this dome via the main steam line to drive on the turbine. The liquid, on the other hand, falls into the downcomer section. The condensed steam is carried back to the downcomer at the feedwater inlet. Finally, the down-coming coolant re-enters the lower plenum and the natural circulation loop is completed.

The flow in a natural circulation system is driven by the density differences between the core and the riser sections and the downcomer. The riser lengthens the relatively low-density two-phase region of the core and therefore increases the natural circulation flow rate. The riser flow area is quite large, in order to minimize the negative effect on the flow rate of friction losses in the riser.

2.3. MODEL

The basic equations determining the time-evolution of the main state variables in a natural circulation BWR are listed below. All symbols used are summarized in the Nomenclature. The equilibrium value of a variable is denoted by omitting the explicit time-dependence symbol.

2.3.1. Neutron Kinetics

The ordinary point-kinetic equations, with one effective delayed neutron group, describe the time-evolution of the neutron density and the precursor concentration¹²:

$$\frac{dN(t)}{dt} = \frac{\rho(t) - \beta}{\Lambda} N(t) + \lambda C(t), \quad (2-1)$$

$$\frac{dC(t)}{dt} = \frac{\beta}{\Lambda} N(t) - \lambda C(t). \quad (2-2)$$

The modal point-kinetic equations, governing higher harmonic oscillations of the neutron flux density, are derived in Appendix A. Higher harmonic flux modes are not considered in this chapter. In Chapter 3, however, the dynamics of the out-of-phase mode is discussed in detail. The reactivity term in Eq. (2-1) consists of a constant base reactivity, needed to make

the reactor critical at the initial conditions, an external reactivity, for instance due to a control rod movement, and the void and Doppler feedback reactivity terms:

$$\rho(t) = \rho_0 + \rho_{\text{ext}}(t) + \rho_a(t) + \rho_D(t),$$

where $\rho_a(t) = r_a \langle \alpha(t) \rangle_c$ and $\rho_D(t) = r_D T_f(t)$. (2-3)

2.3.2. Fuel Dynamics

The transfer from linear reactor power to heat flux density from fuel to coolant is described with one effective fuel time constant:

$$\frac{d}{dt} \frac{q''(t)}{q''} = \frac{1}{\tau_f} \left[\frac{q'(t)}{q'} - \frac{q''(t)}{q''} \right]. \quad (2-4)$$

Using Newton's law of cooling the heat flux density term in Eq. (2-4) becomes:

$$q''(t) = k_f [T_f(t) - T_{\text{sat}}]. \quad (2-5)$$

The fuel heat transfer coefficient k_f is assumed to be independent of the void fraction. The coolant saturation temperature T_{sat} has a constant value in Eq. (2-5), supposing that the system pressure is constant. The variation of the saturation temperature as a function of the axial position, a very important effect under low-pressure conditions, is incorporated in the theoretical model outlined in Chapter 5.

2.3.3. Thermohydraulic Subsystem

The thermohydraulic subsystem [Eqs. (2-6) through (2-17) and Table 2-1] influences the reactor power via the void and Doppler reactivity terms in Eq. (2-3). The governing equations for the thermohydraulic subsystem are derived on the basis of the well-known one-dimensional homogeneous equilibrium mixture (HEM) model.¹³ The two phases move with the same velocity in this model, and have the same temperature. The influence of integral slip, originating from the cross-sectional averaging of a nonuniform void profile in the channel, is neglected here. The axial heat flux profile is also assumed to be flat in this chapter. Model equations for nonuniform power and void concentration profiles are presented in Appendix B. The multiple parallel channels in the reactor core are approximated with one average channel, to keep the analysis as transparent as possible. Subcooled boiling and void flashing phenomena are also not taken into account in this chapter. The latter phenomenon is incorporated, however, in the low-pressure BWR model developed in Chapter 5.

Table 2-1. Original and Nondimensional Form of the Dynamic Pressure Drops in the Natural Circulation Loop

	Original Form	Dimensionless Form
Inertia core	$Z_{bb}(t) \frac{dM_{C,i}(t)}{dt} + [L_C - Z_{bb}(t)] \frac{dM_{C,e}(t)}{dt}$ $+ [M_{C,i}(t) - M_{C,e}(t)] \frac{dZ_{bb}(t)}{dt}$	$Z_{bb}^*(t^*) \frac{dM_{C,i}^*(t^*)}{dt^*} + [1 - Z_{bb}^*(t^*)] \frac{dM_{C,e}^*(t^*)}{dt^*}$ $+ [M_{C,i}^*(t^*) - M_{C,e}^*(t^*)] \frac{dZ_{bb}^*(t^*)}{dt^*}$
Inertia riser	$\sum_{n=1}^{N_R} \frac{L_R}{N_R} \frac{d\langle M(t) \rangle_{R,n}}{dt}$	$\sum_{n=1}^{N_R} \frac{L_R^*}{N_R} \frac{d\langle M(t^*) \rangle_{R,n}^*}{dt^*}$
Inertia downcomer	$\left(\frac{L}{A} \right) \frac{d\phi_i(t)}{dt}$	$\left(\frac{L}{A} \right)^* \frac{dM_{C,i}^*(t^*)}{dt^*}$
Acceleration core	$\frac{M_{C,e}^2(t)}{\rho_f} \phi^2[\chi_{C,e}(t)] - \frac{M_{C,i}^2(t)}{\rho_f}$	$M_{C,e}^{*2}(t^*) [1 + J_{2,C}^*(t^*)] - M_{C,i}^{*2}(t^*)$
Acceleration riser	$\frac{M_{R,e}^2(t)}{\rho_f} \phi^2[\chi_{R,e}(t)] - \frac{M_{R,i}^2(t)}{\rho_f} \phi^2[\chi_{R,i}(t)]$	$M_{R,e}^{*2}(t^*) [1 + J_{2,R,e}^*(t^*)] - M_{R,i}^{*2}(t^*) [1 + J_{2,R,i}^*(t^*)]$
Acceleration downcomer	$\frac{\phi_i^2(t)}{2\rho_f} \left(\frac{1}{A_{D,e}^2} - \frac{1}{A_{D,i}^2} \right)$	$\frac{1}{2} \left(\frac{1}{A_{D,e}^{*2}} - \frac{1}{A_{D,i}^{*2}} \right) M_{C,i}^{*2}(t^*)$
Gravity core	$L_C g_c [\rho_f (1 - \langle \alpha(t) \rangle_C) + \rho_g \langle \alpha(t) \rangle_C]$	$\frac{1 - J_{1,C}^*(t^*)}{N_{Fr}}$
Gravity riser	$\sum_{n=1}^{N_R} L_R g_c [\rho_f (1 - \langle \alpha(t) \rangle_{R,n}) + \rho_g \langle \alpha(t) \rangle_{R,n}]$	$\sum_{n=1}^{N_R} \frac{L_R^*}{N_R} \frac{1 - J_{1,R,n}^*(t^*)}{N_{Fr}}$
Gravity downcomer	$-\rho_f g_c (L_C + L_R)$	$-\frac{1 + L_R^*}{N_{Fr}}$
Friction core	$Z_{bb}(t) \frac{f_C}{2D_C} \frac{M_{C,i}^2(t)}{\rho_f} + [L_C - Z_{bb}(t)]$ $\times \frac{f_C}{2D_C} \frac{M_{C,e}^2(t)}{\rho_f} \phi^2 \left[\frac{1}{2} \chi_{C,e}(t) \right]$	$Z_{bb}^*(t^*) \Lambda_C M_{C,i}^{*2}(t^*) + [1 - Z_{bb}^*(t^*)]$ $\times \Lambda_C M_{C,e}^{*2}(t^*) \left[1 + \frac{1}{2} J_{2,C}^*(t^*) \right]$
Friction riser	$\sum_{n=1}^{N_R} \frac{L_R}{N_R} \frac{f_R}{2D_R} \frac{\langle M(t) \rangle_{R,n}^2}{\rho_f} \phi^2 [\langle \chi(t) \rangle_{R,n}]$	$\sum_{n=1}^{N_R} \frac{\Lambda_R}{N_R} \langle M(t^*) \rangle_{R,n}^{*2} \left[1 + J_{2,R,n}^*(t^*) \right]$
Inlet core	$k_{C,i} \frac{M_{C,i}^2(t)}{2\rho_f}$	$\frac{k_{C,i}}{2} M_{C,i}^{*2}(t^*)$

Inlet downcomer	$k_{D,i} \frac{M_{D,i}^2(t)}{2\rho_f}$	$\frac{k_{D,i}}{2} \frac{1}{A_{D,i}^{*2}} M_{C,i}^{*2}(t^*)$
Exit core	$k_{C,e} \frac{M_{C,e}^2(t)}{2\rho_f} \phi^2[\chi_{C,e}(t)]$	$\frac{k_{C,e}}{2} M_{C,e}^{*2}(t^*) [1 + J_{2,C}^*(t^*)]$
Exit riser	$k_{R,e} \frac{M_{R,e}^2(t)}{2\rho_f} \phi^2[\chi_{R,e}(t)]$	$\frac{k_{R,e}}{2} M_{R,e}^{*2}(t^*) [1 + J_{2,R}^*(t^*)]$

2.3.4. Boiling Boundary Dynamics

The equation for the dynamic behavior of the boiling boundary is derived by integrating the differential energy equation from the core inlet to the axial position where the coolant reaches the saturation temperature:

$$\frac{dZ_{bb}(t)}{dt} = 2 \left[\frac{M_{C,i}(t)}{\rho_f} - \frac{Z_{bb}(t) q'(t)}{\rho_f A_C (h_f - h_{l,c,i})} \right] \quad (2-6)$$

Conservation of mass directly implies that the mass flux density in the one-phase region is independent of the axial position (incompressibility of the phases is assumed). The local enthalpy is assumed to change simultaneously at all axial positions. This approximation facilitates the spatial integration over the one-phase region. Because the oscillations in the local single-phase enthalpy are delayed in the upper area of the one-phase region, this approach is appropriate for frequencies smaller than the inverse of the transit time of the one-phase region.

2.3.5. Core Void Dynamics

The equations for the core void dynamics are derived by integrating the differential continuity and energy equations for the two-phase region:

$$\frac{d\langle\alpha(t)\rangle_c}{dt} = \frac{M_{C,e}(t) - M_{C,i}(t)}{(\rho_f - \rho_g) L_C} \quad (2-7)$$

$$M_{C,i}(t) = M_{C,e}(t) \left[1 + \frac{\rho_f - \rho_g}{\rho_g} \chi_{C,e}(t) \right] - \frac{(\rho_f - \rho_g) [L_C - Z_{bb}(t)] q'(t)}{\rho_g A_C (h_g - h_f)} \quad (2-8)$$

Oscillations in the local quality are delayed in the upper area of the cooling channel. This delay effect is neglected and the assumption is made that the local quality changes simultaneously at all axial positions. The HEM void model (no velocity difference between

the phases) is used to relate the void fraction in Eq. (2-7) with the exit quality in Eq. (2-8):

$$\langle \alpha(t) \rangle_c = \frac{H - Z_{bb}(t)}{H} \frac{\rho_f}{\rho_f - \rho_g} \left\{ 1 - \frac{\rho_g}{(\rho_f - \rho_g) \chi_{C,e}(t)} \ln \left[1 + \frac{\rho_f - \rho_g}{\rho_g} \chi_{C,e}(t) \right] \right\}. \quad (2-9)$$

2.3.6. Riser Void Dynamics

The riser is divided in N_R spatial intervals (or “nodes”) of equal length L_R/N_R , to solve the two-phase flow equations for this section. The local quality is assumed to increase or decrease linearly between the node inlet (denoted with the subscript n-1) and the node outlet (referred to with a subscript n) quality. The average void fraction in a riser node then becomes:

$$\langle \alpha(t) \rangle_{R,n} = \frac{\rho_f}{\rho_f - \rho_g} \left\{ 1 - \frac{1}{\frac{\rho_f - \rho_g}{\rho_g} [\chi_{R,n}(t) - \chi_{R,n-1}(t)]} \ln \left[1 + \frac{\rho_f - \rho_g}{\rho_g} \frac{\chi_{R,n}(t) - \chi_{R,n-1}(t)}{1 + \chi_{R,n-1}(t) \frac{\rho_f - \rho_g}{\rho_g}} \right] \right\}. \quad (2-10)$$

The riser quality is constant along the axial coordinate in the equilibrium state. Therefore the result of the expression for the nodal riser void fraction in Eq. (2-10) is a singularity. A Taylor expansion of the logarithmic term in Eq. (2-10) is recommended to remove this singularity. Integrating the differential mass and energy equations over the n-th riser node consequently yields:

$$\frac{d\langle \alpha(t) \rangle_{R,n}}{dt} = \frac{M_{R,n}(t) - M_{R,n-1}(t)}{\rho_f - \rho_g} \frac{N_R}{L_R}, \quad (2-11)$$

$$M_{R,n-1}(t) \left[1 + \frac{\rho_f - \rho_g}{\rho_g} \chi_{R,n-1}(t) \right] = M_{R,n}(t) \left[1 + \frac{\rho_f - \rho_g}{\rho_g} \chi_{R,n}(t) \right]. \quad (2-12)$$

Conservation of mass and energy at the junction of the core and the riser implies that:

$$M_{R,i}(t) = \frac{A_C}{A_R} M_{C,e}(t), \quad \chi_{R,i}(t) = \chi_{C,e}(t). \quad (2-13)$$

2.3.7. Natural Circulation Loop Momentum Dynamics

The dynamic pressure is continuous along the closed natural circulation loop, so the integral momentum equation can be stated directly:

$$\Delta P_C(t) + \Delta P_R(t) + \Delta P_D(t) = 0. \quad (2-14)$$

All pressure drop terms accounted for in the model are summarized systematically in the second column of Table 2-1. The specific section in the natural circulation loop (core, riser,

or downcomer) is denoted in the first column. The first column also gives information about the pressure drop type (inertial, accelerational, gravitational, frictional, inlet, or outlet). Not all pressure drop terms are discussed separately in this chapter, because there already exists a vast literature on this subject.¹³ However, special assumptions or methods used in the derivation of specific pressure drops are explained in more detail.

2.3.8. Core

The dynamic pressure drop over the core results from an integration of the differential momentum equation for the one-phase and the two-phase regions of the core. Because the mass flux density in the one-phase region is constant in space (conservation of mass), integration over this region is straightforward. The mass flux density ranges axially from $M_{C,i}$ to $M_{C,e}$ in the two-phase region. However, in the integration process, the assumption is made that the two-phase mass flux density is equal to $M_{C,e}$. Regarding channel stability, this is a conservative assumption, because of the (destabilizing) delay of $M_{C,e}$ with respect to $M_{C,i}$ [on the other hand, the spatial assumptions in Eqs. (2-6) through (2-8) lead to a nonconservative estimation of channel stability] (Ref. 14). The HEM two-phase friction multiplier is used in the evaluation of the core and the riser frictional pressure drop. This multiplier is dependent on the vapor and the liquid densities and the flow quality only:

$$\phi^2(\chi, P) = 1 + [\rho_f / \rho_g - 1] \chi. \quad (2-15)$$

2.3.9. Riser

Because the riser section is divided in N_R nodes, a nodal riser mass flux density is defined in order to facilitate the integration process:

$$\langle M(t) \rangle_{R,n} = \frac{1}{2} [M_{R,n-1}(t) + M_{R,n}(t)]. \quad (2-16)$$

The two-phase mixture suddenly expands to the steam dome at the riser exit. The local pressure losses associated with this expansion are included in Table 2-1. The node-length needs to be much smaller than the typical "wavelength" of the density-waves propagating through the riser (equal to $L_R / f_{res} \tau_R$), to represent the transient behavior of the riser accurately. This implies that $N_R \gg f_{res} \tau_R$ is required for accurate calculations. However, dividing the riser in many nodes has a practical drawback, because of a rapid increase in calculational labor.

2.3.10. Downcomer

Several simplifying assumptions were made for the downcomer section, to keep the

analysis as transparent as possible. The pressure drops at the lower plenum and the steam dome are not taken into account in the model and momentum exchange between these sections and the downcomer is neglected. The down-coming fluid is assumed to be one phase (i.e. no carry under), incompressible and inviscid, with a fluid temperature uniform in space and time. The downcomer pressure drop terms in Table 2-1 are derived under these assumptions by applying Bernoulli's integral equation for an inviscid and incompressible fluid in a variable geometry.¹³

The total circulation flow is used in Table 2-1 as a state variable. The mass flux density changes in the downcomer due to flow area changes. However, conservation of mass implies that the total circulation flow is independent of the downcomer geometry. The circulation flow is therefore a convenient variable to use. Table 2-1 shows that the gravitational pressure drop over the downcomer is negative. Essentially, this pressure *gain* along the flow path in the downcomer is responsible for the natural circulation of the coolant.

The effect of changing flow areas on the downcomer inertia is accounted for by introducing an equivalent inertia length (L/A):

$$\left(\frac{L}{A} \right) = \int_{D,i}^{D,e} \frac{1}{A_D(z)} dz. \quad (2-17)$$

The model also accounts for the accelerational pressure drop (or gain) due to the different flow areas of the upper respectively the lower sections of the downcomer. The downcomer inlet friction term accounts for pressure losses due to local inlet restrictions.^{b)} Tube friction in the downcomer is neglected, because the downcomer flow area is large compared to the core flow area, and the fluid is assumed to be one phase.

2.4. FREQUENCY-DOMAIN ANALYSIS

Laplace transforming of the linearized equations is a very powerful approach to gain more insight into the physical processes determining natural circulation channel and reactor stability. For instance, using root-locus and Nyquist-diagram techniques, the linear stability boundary can be calculated precisely, without much calculational effort. Direct numerical calculations in the time domain are more time consuming, due to the many nonlinear terms involved.

The most efficient way to present the (multiple regenerative) feedback loops involved is in a block diagram, see Fig. 2-2. The transfer functions in this block diagram are a function of the Laplace variable s . For brevity, this dependence is omitted in the notation of the transfer functions. If a positive step in the reactivity is introduced, the reactor power will increase (via

^{b)}The downcomer inlet is located at the transition steam dome - downcomer.

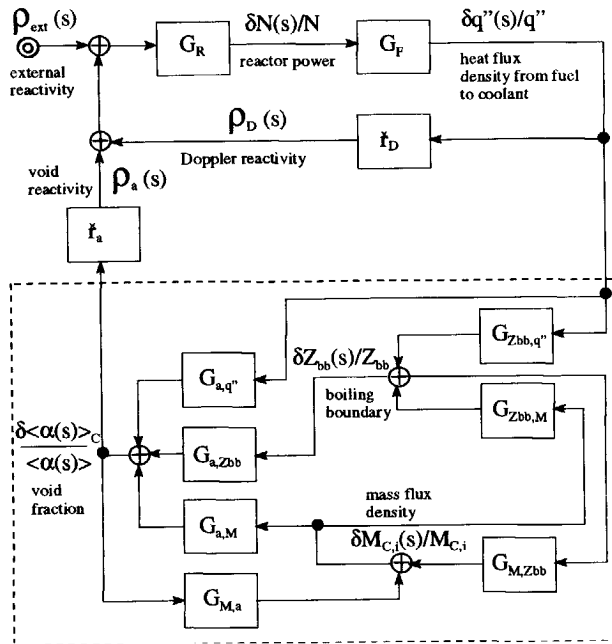


Figure 2-2. Block diagram of natural circulation BWR stability. The thermohydraulic transfer functions are clustered in the dashed rectangle.

functions $G_{a,q''}$, $G_{a,M}$ and $G_{a,Z_{bb}}$ are derived using Eqs. (2-7) through (2-9) and describe the void production and transport in the core.

Oscillations of the void fraction and the boiling boundary position also perturb the dynamic pressure drop in the natural circulation loop sections. The inlet mass flux density responds via the feedback transfer functions $G_{M,a}$ and $G_{M,Z_{bb}}$ to compensate for the impact of these perturbations on the momentum balance. For instance, when the channel void fraction increases, the two-phase frictional pressure drop also increases, and the mass flux density has to decrease to keep the pressure drop over the channel constant. When the inlet mass flux density decreases, the void fraction will increase, and the boiling boundary shifts down ($G_{a,M}$ and $G_{Z_{bb},M}$), etc. Eventually, the resulting void fraction increase will lead to a negative void reactivity ρ_a (via the negative void reactivity coefficient), and the power will decrease. Thus, at low frequencies, this system is stable (negative feedback). However, depending on the phase shifts in the thermohydraulic subsystem, instabilities can occur at higher frequencies. The complicated thermohydraulic transfer functions in Fig. 2-2 are collapsed into one transfer

the zero-power transfer function G_R). This causes (with a certain delay due to the fuel dynamics) a fuel temperature increase (via G_F), and a (negative) Doppler feedback reactivity (via r_D , the Doppler reactivity coefficient).^{c)} When the heat flux density from fuel to coolant increases, several feedback mechanisms in the channel become important. The transfer functions of the thermohydraulic subsystem are clustered in the dashed rectangle. Perturbing and Laplace transforming Eq. (2-6) yields the transfer functions from heat and mass flux density to boiling boundary position ($G_{Z_{bb},q''}$ and $G_{Z_{bb},M}$). The transfer

^{c)}Adjusted void and Doppler coefficients are used in Fig. 2-2, because the state variables are normalized: $\tilde{r}_a \equiv r_a \langle \alpha \rangle_c$ and $\tilde{r}_D \equiv r_D [T_f - T_{sat}]$.

function from heat flux density to void fraction, to investigate these dynamic instabilities:

$$G_a \equiv \frac{\delta \langle \alpha(s) \rangle_c / \langle \alpha \rangle_c}{\delta q''(s) / q''} = \frac{G_1}{1 + G_{M,a} G_1 + G_{M,zbb} G_{zbb,q}''},$$

where $G_1 \equiv G_{a,q}'' + G_{a,zbb} G_{zbb,q}''$.

(2-18)

The thermohydraulic system is on the threshold of instability if the denominator of the transfer function G_a is equal to zero. This means that the operating conditions have to be such that

$$G_{M,a} G_1 + G_{M,zbb} G_{zbb,q}'' = -1$$
(2-19)

for a certain channel resonance frequency. The “closed-loop” reactor transfer function from external reactivity to reactor power is equal to

$$G_T = \frac{\delta N(s) / N}{\rho_{ext}(s)} = \frac{G_R}{1 - G_R G_F [f_D + f_a G_a]}$$
(2-20)

The reactor is on the threshold of instability if the denominator of Eq. (2-20) is equal to zero.

Instead of linearizing and Laplace transforming the nodal equations (2-10) through (2-12) for the two-phase flow in the riser, another approach was made in the frequency-domain analysis. Directly perturbing and linearizing the governing differential mass and energy equations and rearranging yields a convection equation describing the transport of the two-phase mixture through the riser:

$$\frac{\partial \delta \alpha_R(z,t)}{\partial t} + \frac{L_R}{\tau_R} \frac{\partial \delta \alpha_R(z,t)}{\partial z} = 0.$$
(2-21)

Laplace transforming and integrating Eq. (2-21) then yields the local riser void fraction response on perturbations of the heated section outlet void fraction:

$$\delta \alpha_R(z/L_R, s) = \delta \alpha_{R,i}(s) \exp(-s \tau_R z/L_R).$$
(2-22)

The local mass flux density in the riser can be derived in a similar way. Substituting these expressions in the differential momentum equation and integrating over the riser length yields the *exact* dynamic pressure drop $\Delta P_R(s)$ in the frequency domain. As an example the important gravitational riser pressure drop is evaluated. It proves to be convenient to introduce a new state variable: the average void fraction in the riser. This quantity is defined in the linearized model as

$$\delta \langle \alpha(s) \rangle_R \equiv \int_{z=0}^{L_R} \delta \alpha_R(z,s) dz = \delta \alpha_{R,i}(s) \frac{1 - \exp(-s \tau_R)}{s \tau_R},$$
(2-23)

where Eq. (2-22) is used. The gravitational pressure drop over the riser then becomes

$$\delta \Delta P_{R,g}(s) = g_c (\rho_g - \rho_f) \int_{z=0}^{L_R} \delta \alpha_R(z, s) dz = L_R g_c (\rho_g - \rho_f) \delta \langle \alpha(s) \rangle_R, \quad (2-24)$$

where Eq. (2-23) is applied. Explicit expressions for the other riser pressure drops are presented in Ref. 15.

2.5. NONDIMENSIONAL ANALYSIS

2.5.1 Thermohydraulic Stability

It is very instructive to write the governing equations for the thermohydraulic subsystem in a nondimensional form. This approach yields important information for scaling purposes: Many dimensionless numbers are important scaling numbers as well. The transparent form of dimensionless equations also gives more insight into the key numbers determining the state of the dynamical system. This latter point is extremely important in the stability analysis of BWRs. Because of the strong influence of the complicated two-phase flow processes on reactor dynamics, many thermohydraulic parameters, for instance the core flow, the reactor power, the subcooling, and the pressure, affect reactor stability. Instead of investigating the influence of all these variables separately, it is more convenient to combine them in only a few key numbers. Nonuniform power and void concentration profiles are not considered here. However, this assumption is not essential and the same general conclusions remain valid when peaked power profiles and nonuniform void distributions are considered (see Appendix B).

Only the thermohydraulic subsystem is studied in this section, so the heat flux from fuel to coolant is kept constant. The procedure followed is comparable with the approach of Rizwanuddin and Dorning,¹⁶ and Inada et al.¹⁷ First, the dimensionless Zuber number N_{Zu} , the subcooling number N_{sub} , the Froude number N_{Fr} , and the density ratio number N_p are introduced:

$$N_{Zu} \equiv \frac{q' L_C}{\phi_1 (h_g - h_f)} \frac{\rho_f - \rho_g}{\rho_g}, \quad N_{sub} \equiv \frac{h_f - h_{c,i}}{h_g - h_f} \frac{\rho_f - \rho_g}{\rho_g}, \quad N_{Fr} \equiv \frac{(M_{c,i} / \rho_f)^2}{g_c L_C}, \quad N_p \equiv \frac{\rho_g}{\rho_f}. \quad (2-25)$$

The dimensionless numbers defined in Eq. (2-25) determine the thermohydraulic operating conditions. The frictional numbers Λ_C and Λ_R are representative for the tube friction in the core and the riser respectively:

$$\Lambda_C \equiv \frac{f_C L_C}{2 D_C}, \quad \Lambda_R \equiv \frac{f_R L_R}{2 D_R}. \quad (2-26)$$

The local inlet and outlet loss coefficients already have a nondimensional form. The geometrical numbers are:

$$A_R^* \equiv \frac{A_R}{A_C}, A_{D,i}^* \equiv \frac{A_{D,i}}{A_C}, A_{D,e}^* \equiv \frac{A_{D,e}}{A_C}, L_R^* \equiv \frac{L_R}{L_C}, \left(\frac{L}{A}\right)^* \equiv \left(\frac{L}{A}\right) \frac{A_C}{L_C}. \quad (2-27)$$

The variables in Eqs. (2-6) through (2-16) and Table 2-1 are made dimensionless by introducing the following variables:

$$M^*(t) \equiv \frac{M(t)}{M_{C,i}}, P^*(t) \equiv \frac{P(t)}{M_{C,i}^2/\rho_f}, Z_{bb}^*(t) \equiv \frac{Z_{bb}(t)}{L_C}, \chi^*(t) \equiv \frac{\chi(t)}{\chi_{C,e}}, t^* \equiv \frac{tM_{C,i}}{L_C\rho_f}. \quad (2-28)$$

Using the definitions of Eqs. (2-25) through (2-28), the nondimensional form of the basic equations (2-6) through (2-13) is derived. The nondimensional equation for the boiling boundary dynamics becomes

$$\frac{dZ_{bb}^*(t^*)}{dt^*} = 2 \left[M_{C,i}^*(t^*) - Z_{bb}^*(t^*) \frac{N_{Zu}}{N_{sub}} \right]. \quad (2-29)$$

The core void-quality relation in Eq. (2-9) is easily transformed to a nondimensional form using the following auxiliary definitions:

$$J_{1,c}^*(t^*) \equiv (1 - N_p) \langle \alpha(t^*) \rangle_c \text{ and } J_{2,c}^*(t^*) \equiv \chi_{C,e}^*(t^*) (N_{Zu} - N_{sub}). \quad (2-30)$$

Using Eq. (2-9), the $J_{1,c}^*$ -function becomes:

$$J_{1,c}^*(t^*) = \left[1 - Z_{bb}^*(t^*) \right] \left\{ 1 - \frac{\ln \left[J_{2,c}^*(t^*) + 1 \right]}{J_{2,c}^*(t^*)} \right\}. \quad (2-31)$$

Equations (2-7) and (2-8), describing the core void dynamics, are transformed into the following expressions:

$$\frac{dJ_{1,c}^*(t^*)}{dt^*} = M_{C,e}^*(t^*) - M_{C,i}^*(t^*), \quad (2-32)$$

$$M_{C,i}^*(t^*) = M_{C,e}^*(t^*) \left[1 + J_{2,c}^*(t^*) \right] - N_{Zu} \left[1 - Z_{bb}^*(t^*) \right]. \quad (2-33)$$

The average void fraction in a riser node is also expressed in auxiliary dimensionless functions:

$$J_{1,R,n}^*(t^*) \equiv (1 - N_p) \langle \alpha(t^*) \rangle_{R,n}$$

$$= 1 - \frac{1}{J_{2,R,n}^*(t^*) - J_{2,R,n-1}^*(t^*)} \ln \left[\frac{J_{2,R,n}^*(t^*) - J_{2,R,n-1}^*(t^*)}{J_{3,R,n-1}^*(t^*)} + 1 \right], \quad (2-34)$$

where the riser J_2^* function is defined as

$$J_{2,R,n}^*(t^*) \equiv \chi_{R,n}^*(t^*)(N_{Zu} - N_{sub}), \quad (2-35)$$

and the J_3^* function is an abbreviation of

$$J_{3,R,n}^*(t^*) \equiv 1 + \chi_{R,n}^*(t^*)(N_{Zu} - N_{sub}). \quad (2-36)$$

Because Eq. (2-34) is based on Eq. (2-10), a Taylor approximation of the logarithmic term in Eq. (2-34) is again recommended to avoid a singularity in the steady state. The governing nodal Eqs. (2-11) and (2-12) for the riser void dynamics are now easily rewritten:

$$\frac{dJ_{1,R,n}^*(t^*)}{dt^*} = \left[M_{R,n}^*(t^*) - M_{R,n-1}^*(t^*) \right] \frac{N_R}{L_R^*}, \quad (2-37)$$

$$M_{R,n-1}^*(t^*) J_{3,R,n-1}^*(t^*) = M_{R,n}^*(t^*) J_{3,R,n}^*(t^*). \quad (2-38)$$

Equation (2-13), stating the conservation of mass and energy at the junction of the core and the riser, becomes

$$M_{R,i}^*(t^*) = \frac{1}{A_R^*} M_{C,e}^*(t^*), \quad \chi_{R,i}^*(t^*) = \chi_{C,e}^*(t^*). \quad (2-39)$$

The nondimensional expressions of the dynamic pressure drops in the natural circulation loop are listed in Table 2-1. Equations (2-29) through (2-39) together with Table 2-1 demonstrate that all pressure dependent parameters, like phasic densities and enthalpies, are incorporated completely in the dimensionless numbers defined in Eq. (2-25). All explicit pressure dependence is therefore eliminated by transforming to these dimensionless groups. The density ratio number N_p cancels in the dimensionless equations, due to the assumption of homogeneous two-phase flow.

Table 2-1 furthermore demonstrates that one of the remaining three numbers defined in Eq. (2-25) is redundant. The dimensionless pressure drops in the last column can be added easily in the equilibrium state. According to Eq. (2-14) their sum is equal to zero. Therefore, the Froude number can be calculated as a function of the Zuber number, the subcooling number, the geometrical numbers, and the frictional numbers for a natural circulation system.

The Zuber and the subcooling number are also coupled in a natural circulation BWR. For instance, when the subcooling number is small, the void fraction in the core and the riser will be relatively high. This affects the circulation flow and the Zuber number, because the Zuber number is inversely proportional to the circulation flow. When the Zuber number is small, the exit quality diminishes and the steam and feedwater flow become relatively small compared to the total circulation flow. Because the down-coming fluid is then mainly at saturation temperature, the subcooling number will become small as well.

Without carry under and with a stationary feedwater system, there exists a simple relationship between the Zuber and the subcooling number. Stating an energy and mass balance at the feedwater sparger level yields an expression for the inlet subcooling:

$$h_f - h_{l_{c,i}} = (h_f - h_{f_w}) \chi_{c,e}. \quad (2-40)$$

Applying Eqs. (2-7), (2-8) and (2-25) then leads to:

$$N_{sub} = \frac{h_f - h_{f_w}}{h_g - h_{f_w}} N_{Zu}. \quad (2-41)$$

With Eq. (2-25) and the auxiliary relationship in Eq. (2-41), typical trajectories in the dimensionless Zuber-subcooling plane can be calculated as a function of different system parameters like the pressure, the reactor power, and the feedwater temperature. The influence of carry under on the subcooling can be important in natural circulation BWRs without steam separators, for instance the Dutch Dodewaard BWR. Equation (2-41) is not valid in that case, and needs to be replaced by a more complicated expression using an appropriate model for carry under.¹⁸

2.5.2 Reactor Stability

The dimensionless stability map of the thermohydraulic subsystem in a natural circulation BWR is independent of the hydrostatic pressure. However, because of the pressure dependence of the (adjusted) void and Doppler reactivity coefficients \tilde{r}_a and \tilde{r}_D ,^(c) the coupled neutronic-thermohydraulic reactor stability is affected by pressure variations.

The core void fraction depends on the density ratio of the vapor and the liquid phase, according to Eqs. (2-30) and (2-31). This ratio increases slowly as a function of pressure. Hence, the void fraction increases slightly in a certain (N_{Zu}, N_{sub}) -coordinate, causing only a slight change in the gain of the void reactivity feedback. The difference between the fuel temperature and the saturation temperature increases in a fixed (N_{Zu}, N_{sub}) -point as a function of pressure (because the power level should be increased strongly at higher pressures, to keep N_{Zu} at a fixed value). Therefore, the Doppler reactivity coefficient \tilde{r}_D becomes larger for higher pressures. However, the Doppler effect has only a minor impact on BWR stability, so reactor stability is not expected to be very dependent on the strength of the Doppler effect.¹⁹ Numerical results in Chapter 3 further demonstrate that the pressure dependence of reactor stability in the dimensionless plane is only very small.²⁰

The assumption was made in the previous analysis that the void reactivity coefficient r_a is independent of the hydrostatic pressure. However, when the pressure changes, the moderator density changes as well. The principal effect is a change in the resonance escape probability p :

$$p = \exp \left[- \frac{\rho_{fuel} A_m V_{fuel} I_{eff}}{\rho_m A_{fuel} V_m \xi \sigma_{s,m}} \right], \tag{2-42}$$

which is explicitly dependent on the moderator density $\rho_m \equiv (1 - \langle\alpha\rangle_c) \rho_f + \langle\alpha\rangle_c \rho_g$ (Ref. 12). The atomic weights A and the volumes V of the fuel and the moderator, the fuel density ρ_{fuel} , the effective resonance integral I_{eff} , the microscopic scattering cross section $\sigma_{s,m}$ of the moderator and the mean lethargy gain per collision ξ are all independent of the hydrostatic pressure. The void reactivity coefficient r_a can be determined with the six-factor formula¹²:

$$r_a \equiv \frac{\partial \rho}{\partial \langle\alpha\rangle_c} = \frac{1}{k_{eff}^2} \frac{\partial k_{eff}}{\partial \langle\alpha\rangle_c} \approx \frac{1}{k_{eff}} \frac{\partial k_{eff}}{\partial \langle\alpha\rangle_c} \tag{2-43}$$

$$= -\rho_{fuel} \frac{A_m V_{fuel} I_{eff}}{A_{fuel} V_m \xi \sigma_{s,m}} \frac{\rho_f - \rho_g}{[(1 - \langle\alpha\rangle_c) \rho_f + \langle\alpha\rangle_c \rho_g]^2}.$$

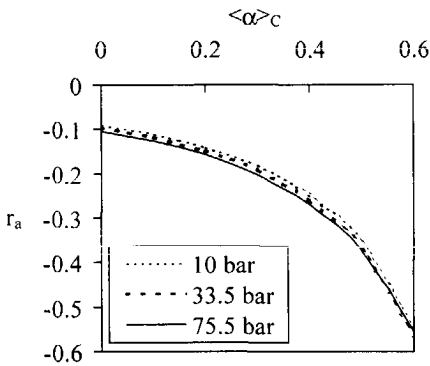


Figure 2-3. Influence of the pressure and the void fraction on the void reactivity coefficient.

The void reactivity coefficient is calculated as a function of the channel void fraction and the pressure in Fig. 2-3. Notice that the pressure dependence is not very large. Up to void fractions of 0.6 the void reactivity coefficient becomes smaller (in an absolute sense) if the pressure is reduced. For void fractions higher than 0.6, the effect of lowering the pressure is just the opposite. The denominator of the pressure-dependent term in Eq. (2-43) then decreases very rapidly as the channel void fraction increases. Thus, for high channel void fractions and low pressures, the void reactivity coefficient is strongly negative. This effect is

not visible on the scale of Fig. 2-3.

Note that only the influence of the resonance escape probability on the reactivity is considered. The thermal utilization factor and the thermal and fast nonleakage probabilities also change as a function of the pressure and need to be taken into account in more detailed calculations of the void reactivity coefficient.²¹

2.6. CONCLUSIONS

A theoretical model for coupled neutronic-thermohydraulic power oscillations in natural

circulation BWRs is developed. The neutron kinetics model consists of the point-kinetic equations with one effective delayed neutron group. The heat transfer from fuel to coolant is modeled as a first-order process. The two-phase flow in the coolant channels is analyzed on the basis of the one-dimensional HEM model for one effective coolant channel. The differential equations of mass, energy, and momentum were integrated over the core region by assuming a time-dependent but spatially linear profile of the one-phase enthalpy and the two-phase quality in the axial direction. The riser section was divided in axial nodes, and a spatially linear quality profile within each node was assumed. The down-coming flow was assumed to be an inviscid and one-phase fluid. The resulting nonlinear time-domain model was linearized and Laplace transformed, to enable an analysis in the frequency-domain. Exact solutions of the HEM equations for the riser section were used in the linearized model.

The nonlinear time-domain equations have been transformed to a dimensionless form, to identify the main parameters determining the dynamic behavior of the thermohydraulic subsystem. After this transformation, all pressure dependent parameters are incorporated implicitly in the dimensionless Zuber, subcooling, and Froude numbers. All explicit pressure dependence in the thermohydraulic equations is eliminated. The density ratio number cancels in the set of dimensionless equations, because a homogeneous flow model is applied. It has been proven that one of the three remaining dimensionless numbers (for instance the Froude number) is redundant in the natural circulation case and can be expressed explicitly in terms of the other dimensionless groups. Furthermore, an elementary model for the steam and feedwater system demonstrates that the Zuber and the subcooling number are related to each other, giving rise to very specific trajectories in the Zuber-subcooling plane as the operating conditions change.

Including nuclear feedback effects, the coupled neutronic-thermohydraulic reactor stability in the dimensionless Zuber-subcooling plane is also rather insensitive to changes of the system pressure. The employment of dimensionless maps, instead of the traditional power-flow maps, in the reactor stability analysis is therefore strongly recommended. A comprehensive parametric study with the proposed theoretical model is performed in a Chapter 3, to identify the main parameters that determine the stability of natural circulation BWRs (Ref. 20).

REFERENCES

1. B.G. Bergdahl, F. Reisch, R. Oguma, J. Lorenzen, and F. Åkerhielm, "BWR Stability Investigation at Forsmark 1," *Ann. Nucl. Energy*, **16**, 509 (1989).
2. E. Pollmann, J. Schulze, and D. Kreuter, "Stability Measurements in the German Nuclear Power Plant Würgassen During Cycle 14," *Nucl. Technol.*, **108**, 350 (1994).
3. M. Tsuji, K. Nishio, M. Narita, Y. Ogawa, and M. Mori, "Stability Analysis of BWRs Using Bifurcation Theory," *J. Nucl. Sci. Technol.*, **30**, 1107 (1993).

4. Y.F. Rao, K. Fukuda, and R. Kaneshima, "Analytical Study of Coupled Neutronic and Thermodynamic Instabilities in a Boiling Channel," *Nucl. Eng. Des.*, **154**, 133 (1995).
5. Y. Takigawa, Y. Takeuchi, S. Tsunoyama, S. Ebata, K.C. Chan, and C. Tricoli, "Caorso Limit Cycle Oscillation Analysis With Three-Dimensional Transient Code TOSDYN-2," *Nucl. Technol.*, **79**, 210 (1987).
6. Y.M. Farawila, D.W. Pruitt, P.E. Smith, L.S. Herrera, and L.P. Fuentes Marquez, "Analysis of the Laguna Verde Instability Event," *Proc. National Heat Transfer Conf.*, Houston, Texas, August 3-6, Vol. 9, p. 198, American Nuclear Society (1996).
7. F.D. Giust and L. Moberg, "RAMONA Stability Analysis on Ringhals-1, Phase 1: Model Qualification," TR1/42.83.06, ScandPower (1991).
8. G.M. Grandi and F.D. Giust, "RAMONA Stability Analysis on Ringhals-1, Phase 2: Predictive Calculations," TR2/42.83.06, ScandPower (1991).
9. G.C. Park, M.Z. Podowski, M. Becker, R.T. Lahey, Jr., and S.J. Peng, "The Development of a Closed-Form Analytical Model for the Stability Analysis of Nuclear-Coupled Density Wave Oscillations in Boiling Water Reactors," *Nucl. Eng. Des.*, **92**, 253 (1986).
10. J. March-Leuba, "Dynamic Behavior of Boiling Water Reactors," PhD Thesis, University of Tennessee, Knoxville, Tennessee (1984).
11. D.D.B. van Bragt and T.H.J.J. van der Hagen, "A Six-Dimensional Model for Coupled Neutronic-Thermohydraulic Out-of-Phase Oscillations in Boiling Water Reactors," *Proc. National Heat Transfer Conf.*, Houston, Texas, August 3-6, Vol. 9, p. 179, American Nuclear Society (1996).
12. J.J. Duderstadt and L.J. Hamilton, *Nuclear Reactor Analysis*, John Wiley & Sons, New York (1976).
13. N.E. Todreas and M.S. Kazimi, *Nuclear Systems I - Thermal Hydraulic Fundamentals*, Hemisphere Publishing Corporation, New York (1990).
14. A.A. Karve, Rizwan-uddin, and J.J. Dorning, "On Spatial Approximations for Liquid Enthalpy and Two-Phase Quality During Density-Wave Oscillations," *Trans. Am. Nucl. Soc.*, **71**, 533 (1994).
15. D.D.B. van Bragt, "A Theoretical and Numerical Study of the Stability of a Natural Circulation Boiling Water Reactor." IRI-131-96-006, Interfaculty Reactor Institute, Delft University of Technology (1996).
16. Rizwan-uddin and J.J. Dorning, "Chaotic Dynamics of a Triply-Forced Two-Phase Flow System," *Nucl. Sci. Eng.*, **105**, 123 (1990).
17. F. Inada, M. Furuya, A. Yasuo, H. Tabata, Y. Yoshioka, and H.T. Kim, "Thermo-Hydraulic Instability of Natural Circulation BWRs at Low Pressure Start-Up: Experimental Estimation of Instability Region with Test Facility Considering Scaling Law," *Proc. 3rd Int. Conf. Nuclear Engineering (ICONE-3)*, Kyoto, Japan, April 23-27, Vol. 1, p. 173 (1995).
18. A.J.C. Stekelenburg, "Statics and Dynamics of a Natural Circulation Cooled Boiling Water Reactor," PhD Thesis, Delft University of Technology, Delft, The Netherlands (1994).
19. J. March-Leuba, D.G. Cacuci, and R.B. Perez, "Nonlinear Dynamics and Stability of Boiling Water Reactors: Part I - Qualitative Analysis," *Nucl. Sci. Eng.*, **93**, 111 (1986).
20. D.D.B. van Bragt and T.H.J.J. van der Hagen, "Stability of Natural Circulation Boiling Water Reactors: Part II - Parametric Study of Coupled Neutronic-Thermohydraulic Stability," *Nucl. Technol.*, **121**, 52 (1998); also published as Chapter 3 of this thesis.
21. M.M. El-Wakil, *Nuclear Energy Conversion*, American Nuclear Society, LaGrange Park, Illinois (1981).

Chapter 3

High-Pressure BWR Dynamics: II – Parametric Study^{a)}

Abstract – A parametric study of coupled neutronic-thermohydraulic stability of natural circulation BWRs is performed. As an example, the stability characteristics of the Dutch Dodewaard reactor, which was cooled by natural circulation, are determined. The Dodewaard reactor can be considered as the prototype of next generation natural circulation BWRs. The stability issues that are identified for this prototype reactor are therefore important in the design of new natural circulation BWRs. Without a riser section installed, only one region of thermohydraulic instability exists in the (dimensionless) stability plane. The significant gravitational pressure drop in a riser section, installed to enhance the natural circulation flow, gives rise to the emergence of an additional region of instability. The oscillations in this zone become especially important during low-power/low-pressure (reactor startup) conditions. Significant damping of these oscillations occurs in a reactor, due to the nuclear void reactivity feedback. A comparison between natural circulation in-phase and out-of-phase reactor stability is made, in particular important for large reactor cores but also yielding unexpected results for small reactors. The impact of downcomer inertia on the stability of the in-phase mode is investigated in detail. Typical trajectories in the dimensionless stability plane are calculated as a function of changing operating conditions, to investigate their influence on reactor dynamics.

3.1. INTRODUCTION

A theoretical stability model for natural circulation BWRs was described and analyzed in

^{a)}This chapter has been published (in a slightly modified form) as:

D.D.B. van Bragt and T.H.J.J. van der Hagen, “Stability of Natural Circulation Boiling Water Reactors: Part II – Parametric Study of Coupled Neutronic-Thermohydraulic Stability,” *Nucl. Technol.*, **121**, 52 (1998).

Chapter 2.¹ Numerical results of the model are discussed in this chapter. Design parameters of the Dutch Dodewaard nuclear power plant, which was cooled by natural circulation, are used as an example in this parameter study. The Dodewaard reactor can be considered as the prototype of next generation natural circulation BWRs. The stability problems that are encountered for this prototype reactor are therefore important in the design of new natural circulation BWRs. A summary of the nominal operating conditions of the Dodewaard reactor is presented in Table 3-1.

Table 3-1. Nominal Conditions of the Dodewaard BWR

Thermal power (MW)	183
Pressure (bar)	75.5
Feedwater temperature (K)	408
Recirculation flow rate (kg/s)	1300 to 1400

Stekelenburg developed a model for the statics and the dynamics of this specific reactor.² He concluded that the reactor is very stable under nominal conditions, in accordance with operational experience and experimental evidence.³ However, computer simulation of startup conditions (low power and low pressure) showed a flow oscillation and decreased stability in the natural-circulation loop. These oscillations were recently measured during startup experiments.⁴

A theoretical explanation of these startup oscillations is given in earlier work of Fukuda and Kobori.⁵ Using an elementary density-wave model, they analyzed the thermohydraulics of a boiling channel, and found two main types of instability: Type-I and Type-II. Type-I instabilities are caused by the gravitational pressure drop in the thermohydraulic system, for instance in the unheated riser sections in natural circulation loops. These instabilities are important under low-power conditions. Type-II instabilities are caused by the interplay of the one-phase and the two-phase frictional pressure drops in the natural circulation loop. Both static (Ledinegg) flow excursions as dynamic density wave oscillations can occur in this case. The thermohydraulic oscillations of the Type-II become important under high-power conditions and have been studied extensively in the past.⁶⁻⁸ Recently, combined stability maps for both types of instabilities were generated.⁹ Lin and Pan used their model to study the transient response of the coolant channel after a step change in power.¹⁰

The main goal of this chapter is to describe and analyze the aforementioned kinds of thermohydraulic instabilities in natural circulation BWRs, and to consider the influence of these thermohydraulic processes on nuclear reactor stability. The influence of both the riser

and the downcomer and the important role of the system pressure on thermohydraulic stability are investigated in Section 3.2. The coupling between neutronics and thermohydraulics in a natural circulation BWR is investigated in Section 3.3. Typical trajectories in the stability plane are calculated, as a function of the operating conditions, in this section as well. Conclusions from the analyses are drawn in Section 3.4.

3.2. THERMOHYDRAULIC STABILITY

The set of dimensionless thermohydraulic, geometrical, and frictional numbers determining the thermohydraulic stability of natural circulation BWRs was identified in Chapter 1.¹ The geometrical numbers for the Dodewaard reactor are calculated using data from Stekelenburg² and listed in Table 3-2. An elementary data set (labelled as data set I) is used in Sections 3.2 through 3.3.3. All friction losses in the natural-circulation loop are lumped and incorporated in the dimensionless friction number Λ_C in data set I. The riser friction number Λ_R and all local inlet and outlet friction coefficients were set equal to zero. With Λ_C equal to 5.1 a recirculation flow rate of 1300 kg/s is predicted by the model (compare with the reference values given in Table 3-1).

Table 3-2. Geometrical Numbers for the Dodewaard BWR

A_R^*	2.25
$A_{D,j}^*$	3.07
$A_{D,e}^*$	2.29
L_R^*	1.71
$(L/A)^*$	1.00

3.2.1. Influence Riser and Downcomer

The stability map for a natural circulation cooled channel, with a constant reactor power, is presented in Fig. 3-1. The fluid is one phase (1ϕ) at the core exit in the half-plane left of the diagonal in Fig. 3-1. When the Zuber number is larger than the subcooling number, a two-phase (2ϕ) mixture leaves the heated section.

The case without the riser has been discussed in detail in Ref. 11. The model predicts both stable and unstable channel behavior in this case, depending on the Zuber and the subcooling number. The stable region in Fig. 3-1 is denoted by the symbol S. The instabilities are caused

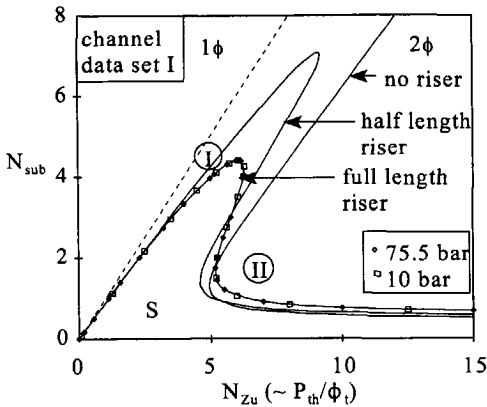


Figure 3-1. Influence of riser length and pressure on natural circulation thermohydraulic stability in the dimensionless Zuber-subcooling plane. The coolant is one phase (1ϕ) at the core exit in the region left of the diagonal. Unstable oscillations of the Type-I occur in a narrow region right of the diagonal. The Type-II unstable region is located at higher values of the Zuber number. The stable zone is denoted by the symbol S. The stability boundaries are independent of the pressure in the dimensionless plane.

by a significant delay of the core outlet flow (and the two-phase frictional pressure drop) with respect to perturbations of the inlet flow, and are the previously mentioned Type-II instabilities. Notice that reducing the Zuber number always has a stabilizing effect. The fluid in the core is almost entirely two phase at very low subcooling numbers. This strongly reduces the destabilizing influence of the boiling boundary dynamics, and the two-phase flow stabilizes. The channel void fraction is relatively small at relatively high subcooling numbers ($N_{Zu} \approx N_{sub}$). This also has a stabilizing influence.

A new region of instability emerges in Fig. 3-1 as the heated channel is coupled with an adiabatic riser section. As opposed to the Type-II instabilities (caused by the frictional pressure drop), these instabilities,

occurring at low exit quality, are caused by the gravitational pressure drop in the riser. These oscillations are of the Type-I, according to the classification scheme of Fukuda and Kobori.⁵

Type-I oscillations are driven by the following feedback mechanism. When the core inlet flow decreases, the core outlet quality will increase. The void fraction increases very rapidly as a function of the quality at low flow qualities, so even a small increase of the core exit quality corresponds to a relatively large increase of the core outlet void fraction, causing a high gain in the feedback loop. Consequently, the void fraction in the riser will increase significantly, and the gravitational pressure drop over the riser decreases. The core inlet flow will increase to compensate for this pressure drop change, causing a core exit quality and riser void fraction decrease. The gravitational pressure drop over the riser then increases and the inlet flow decreases, etc. Because the gravitational pressure drop over the riser is proportional to the riser length, channels with long riser sections are more susceptible to this type of instabilities.

The time scale of Type-I and Type-II oscillations is determined by the transit time of the two-phase mixture through the riser (and the short two-phase region in the core) and the core, respectively. Because the riser length and the riser flow area are both larger than the respective core dimensions (Table 3-2), the riser transit time will be large compared to the transit time of the heated section. Type-I oscillations therefore have a much smaller resonance

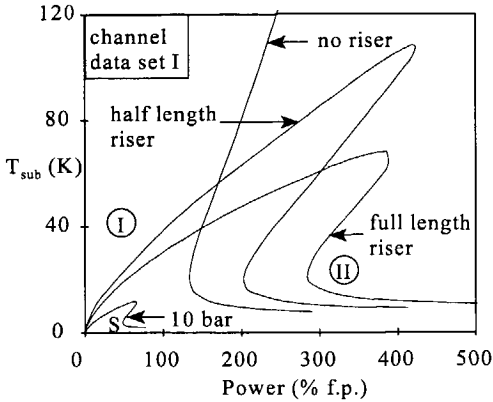


Figure 3-2. Influence of riser length and pressure in the power-subcooling plane. An increase of the riser length results in a larger natural circulation flow and a smaller Zuber number. The region with unstable Type-II oscillations therefore becomes smaller. Type-I oscillations are induced by the unheated riser section and become more important when the riser length increases. Decreasing the pressure has a strong destabilizing effect.

frequency than Type-II oscillations. Furthermore, Type-I oscillations occur under low exit quality conditions, when the natural circulation flow is much smaller (and the riser transit time much larger) than under the high-power Type-II conditions. This results in a more pronounced difference between typical Type-I and Type-II resonance frequencies. Because of the low frequency of Type-I oscillations, the influence of inertia on the Type-I stability boundary is small.

The Zuber number is not only directly but also indirectly dependent on the power level in the natural circulation case, because the flow is not constant but a function of the subcooling and the power. Therefore, it is useful to plot the stability boundaries in the power-subcooling (in units of degrees Kelvin) plane as well, see Fig. 3-2. The borderline between the one-phase and the two-phase regions is not discernible in Fig. 3-2. The coolant flow diminishes when the power is reduced, and therefore the coolant already starts to boil at extremely low power levels. Single-phase convection at low power levels is not taken into account by the model.

The Type-II stability boundary shifts to significantly higher power levels if the riser length increases. This is because a larger riser section enhances the maximum circulation flow rate, and thus reduces the channel void fraction and the two-phase frictional pressure drop. Therefore, the critical power level shifts to higher values, and the size of the Type-II instability region decreases.

The Type-I unstable region in Fig. 3-2, however, becomes larger with increasing riser length. An increase of the riser length causes an increase of the circulation flow, which has a stabilizing effect due to the enhanced one-phase friction, and a destabilizing effect due to the decrease of the exit quality (because the slope of the void fraction-quality curve is steeper for lower qualities, see Fig. 1-4). A longer riser also enlarges the gravitational riser pressure drop, which is the origin of Type-I oscillations. Thus, increasing the riser length has both stabilizing and destabilizing effects. Figure 3-2 shows that the destabilizing effects are dominant. These observations agree with earlier parametric studies.⁹

The Type-II stability boundary shifts to significantly higher power levels if the riser length increases. This is because a larger riser section enhances the maximum circulation flow rate, and thus reduces the channel void fraction and the two-phase frictional pressure drop. Therefore, the critical power level shifts to higher values, and the size of the Type-II instability region decreases.

The Type-I unstable region in Fig. 3-2, however, becomes larger with increasing riser length. An increase of the riser length causes an increase of the circulation flow, which has a stabilizing effect due to the enhanced one-phase friction, and a destabilizing effect due to the decrease of the exit quality (because the slope of the void fraction-quality curve is steeper for lower qualities, see Fig. 1-4). A longer riser also enlarges the gravitational riser pressure drop, which is the origin of Type-I oscillations. Thus, increasing the riser length has both stabilizing and destabilizing effects. Figure 3-2 shows that the destabilizing effects are dominant. These observations agree with earlier parametric studies.⁹

3.2.2. Influence of Pressure

The pressure invariance of thermohydraulic stability in the dimensionless Zuber-subcooling plane was proved in Chapter 2. The conclusions there are supported by the numerical results in Fig. 3-1: The stability boundaries coincide exactly, even if the pressure is reduced from the nominal pressure to 10 bars. This effect has also been observed in Ref. 9. Figure 3-2 demonstrates that the region in the power-subcooling plane where Type-I and Type-II instabilities occur becomes larger at lower pressures because of the larger liquid-to-vapor density ratio.

Oscillations in the Type-I zone become especially important under low-power and low-pressure reactor startup conditions. It has become clear in recent years that a quantitative prediction of low-pressure startup stability is only possible when void flashing in the riser is taken into account.^{12,13} The term "flashing" refers to the occurrence of boiling in the riser section (even when the fluid in the heated section is entirely one phase), due to the decrease of hydrostatic pressure in the axial direction. This effect is accounted for in the theoretical model proposed in Chapter 5, but neglected in the high-pressure model developed in Chapter 2.

The resulting effect of flashing on thermohydraulic stability is very similar to the Type-I feedback mechanism. However, because there is (almost) no void generation in the heated section, the impact of flashing on reactor stability (via the void reactivity feedback path) is very small, as the parametric study in Chapter 6 will demonstrate. The influence of the pressure level on reactor stability, applying the high-pressure model of Chapter 2, is discussed in Section 3.3.2. Further parametric studies of low-pressure dynamics, using the theoretical model of Chapter 5, will be presented in Chapter 6.

3.3. REACTOR STABILITY

The interaction between the neutronic and the thermohydraulic subsystems in natural circulation BWRs is studied in this section. A description of the models for neutron kinetics and fuel dynamics was given in Chapter 2. Table 3-3 summarizes the neutron kinetic data for the Dodewaard BWR in data set I (Ref. 2). The heated perimeter is denoted by the symbol ξ .

Table 3-3. Neutron Kinetic and Fuel Data for the Dodewaard BWR

β	0.0061
λ (s ⁻¹)	0.084

Λ (s)	5×10^{-5}
τ_f (s)	2.11
r_D (K ⁻¹)	-2×10^{-5}
ξk_f (W/m·K)	9.33×10^5

The influence of void reactivity feedback on natural circulation reactor stability is investigated in Section 3.3.1. The effect of system pressure on reactor stability is discussed in Section 3.3.2. Then the influence of fuel dynamics on the coupling between the thermohydraulics and the neutronics is considered (Section 3.3.3). The most accurate data set currently available for our reactor model is summarized in Section 3.3.4. The stability of in-phase and out-of-phase oscillations is compared in Section 3.3.5. The influence of downcomer inertia on stability is considered as well in this section. Finally, in Section 3.3.6, trajectories in the dimensionless stability plane are calculated as a function of the operating conditions, to investigate their impact on reactor stability.

3.3.1. Influence of Void Reactivity Feedback

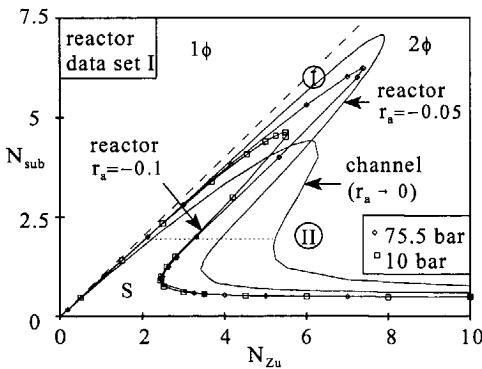


Figure 3-3. Influence of void reactivity feedback on natural circulation reactor stability. The low-frequency Type-I oscillations are stabilized by neutronic feedback effects. The opposite effect is visible for the higher-frequency Type-II oscillations. The effect of pressure changes on the stability boundaries is small in the Type-I and the Type-II regions.

The influence of void reactivity feedback on the coupled neutronic-thermohydraulic reactor system is depicted in Fig. 3-3. Nuclear feedback effects clearly have a strong destabilizing effect on Type-II oscillations. This agrees with results obtained in previous studies.⁸⁻¹¹ Increasing the magnitude of the void reactivity feedback coefficient r_a (in an absolute sense) increases the gain of the void reactivity feedback loop and therefore has a destabilizing effect. However, the interaction between the neutronics and the thermohydraulics has a stabilizing effect on Type-I oscillations.

The phase and the gain of the fuel and the thermohydraulic transfer functions^{b)}

^{b)}The transfer function G_a (see Chapter 2)

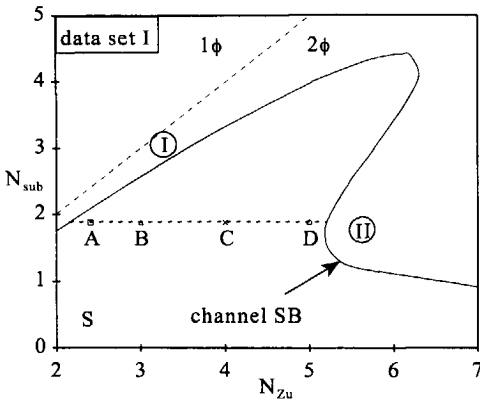


Figure 3-4. Investigated points in the dimensionless Zuber-subcooling plane (SB = stability boundary).

were calculated for four different points on the horizontal dotted line in Fig. 3-3 to explain these two opposite effects. This trajectory is represented in more detail in Fig. 3-4. The channel stability boundary (SB) is also represented in Fig. 3-4. All four points are located in the region where the channel is stable. However, point A is rather close to the Type-I stability boundary and point D is near the Type-II stability threshold.

The gain and the phase of the thermohydraulic transfer function and those of the fuel transfer function (which is independent of the position in the Zuber-subcooling plane) in points A through D are presented in Figs. 3-5 and 3-6, respectively. The rather low-frequency (~ 0.2 Hz) Type-I resonance can be recognized in point A and the higher-frequency (~ 0.6 Hz) Type-II resonance in point D, see Fig. 3-5. Notice that for the intermediate points B and C, a single resonance peak is visible in Fig. 3-5, indicating that oscillations in these points are induced by a combination of Type-I and Type-II oscillations. The transition from Type-I to Type-II oscillations is gradual, and it is not possible to distinguish sharply between those two kinds of oscillations for intermediate points like B or C.

The gain and the phase of the thermohydraulic transfer function and those of the fuel transfer function (which is independent of the position in the Zuber-subcooling plane) in points A through D

are presented in Figs. 3-5 and 3-6, respectively. The rather low-frequency (~ 0.2 Hz) Type-I resonance can be recognized in point A and the higher-frequency (~ 0.6 Hz) Type-II resonance in point D, see Fig. 3-5. Notice that for the intermediate points B and C, a single resonance peak is visible in Fig. 3-5, indicating that oscillations in these points are induced by a combination of Type-I and Type-II oscillations. The transition from Type-I to Type-II oscillations is gradual, and it is not possible to distinguish sharply between those two kinds of oscillations for intermediate points like B or C.

Figure 3-6 shows that the phase lags in the channel and the fuel are relatively small in the

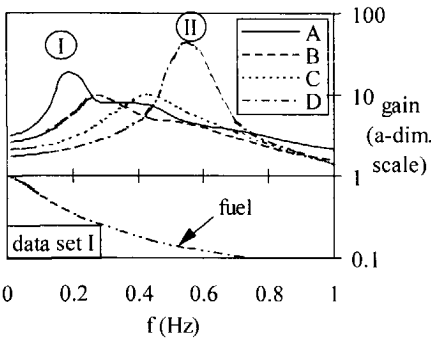


Figure 3-5. Gain diagram of the fuel and channel transfer functions for points A through D in Fig. 3-4. Notice the low-frequency Type-I resonance in point A, close to the Type-I channel stability boundary. The higher-frequency Type-II resonance in point D is also visible.

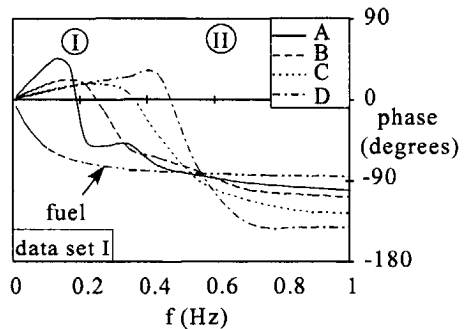


Figure 3-6. Phase diagram for different points in Fig. 3-4. The phase shifts of the fuel and channel transfer functions are small in the Type-I frequency range and much larger for the higher-frequency Type-II oscillations.

Type-I region (point A). Therefore the void reactivity feedback has a stabilizing effect on void fraction oscillations. The stability boundary shifts further away from point A if neutronic feedback is added, see Fig. 3-3. The situation is thus completely opposite to the Type-II region (consider for instance point D). The higher frequency of the Type-II oscillations causes a significant phase lag in the transfer from power to fuel temperature. Together with the phase lag associated with the void production and transport in the channel, the void reactivity feedback can become positive in this region. This can cause coupled neutronic-thermohydraulic reactor instabilities (in point D the channel is stable, but the reactor is unstable).

Finally, Fig. 3-3 demonstrates that the magnitude of the void reactivity feedback coefficient only slightly influences the reactor stability boundary close to the origin of the Zuber-subcooling plane. The previous observation that the void reactivity feedback has a stabilizing influence on Type-I oscillations can be used to explain this insensitivity qualitatively. The reactor becomes more stable if the magnitude of the void reactivity coefficient (in an absolute sense) increases, and the width $\Delta = N_{Zu} - N_{sub}$ of the unstable Type-I region will become smaller (for a certain subcooling number). The exit quality on the new stability boundary decreases, since $\Delta = \chi_{C,e} (\rho_l/\rho_g - 1)$, and the void fraction decreases very rapidly as well. This void fraction decrease reduces the void reactivity feedback, and partly cancels the effect of increasing the magnitude of the void reactivity coefficient.

3.3.2. Influence of Pressure

Figure 3-3 demonstrates that the influence of pressure on the Type-I and the Type-II stability boundaries in the dimensionless plane is very small. The void reactivity coefficient is assumed to be pressure independent and equal to -0.1 in the calculations. The stability boundary shifts significantly in the region of intermediate Type-I/Type-II oscillations if the pressure is reduced to 10 bars (the channel stability boundary is independent of the pressure, see Section 3.2.2). However, this region with a relatively high subcooling number is not reached in practical situations, as will be outlined in Section 3.3.6. The relatively large shift of the stability boundary in this intermediate region will be explained as well in that section.

3.3.3. Influence of Fuel Dynamics

The impact of the fuel time constant on the stability boundaries is depicted in Fig. 3-7. The void reactivity coefficient r_a is equal to -0.05 in the calculations. Large fuel time constants have a stabilizing effect on Type-II oscillations because of a significant filtering of high-frequency oscillations in the void reactivity feedback loop.¹¹ Again, the situation is completely opposite with respect to Type-I oscillations. Small phase lags in the void

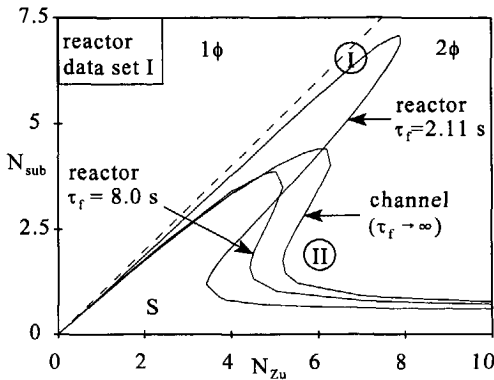


Figure 3-7. Influence of the fuel time constant on natural circulation reactor stability. A larger fuel time constant causes a significant gain reduction of high-frequency oscillations in the fuel and therefore stabilizes Type-II oscillations. The significant phase lag induced by a large fuel time constant has a destabilizing effect on Type-I oscillations.

reactivity feedback loop tend to stabilize the thermohydraulic Type-I oscillations in the reactor. If the fuel time constant increases, the break frequency of the fuel transfer function will shift toward a lower frequency, and the total phase shift in the void reactivity feedback loop will increase at the Type-I resonance frequency. The stabilizing influence of the coupling between the neutronic and the thermohydraulic subsystems therefore diminishes when the fuel time constant is large.

Van der Hagen outlined that the heat transfer for high frequencies is governed by typically small fuel time constants that are associated with heat transfer from the

outer region of the fuel. He proposed a small effective fuel time constant of 2.11 s, to describe Type-II power oscillations of ~1 Hz in the Dodewaard reactor.¹⁴ Larger time constants, associated with variations of the bulk of the fuel, will become more important in the Type-I region, where the oscillation frequency is much lower. Therefore, it is reasonable to use a typically large fuel time constant (of the order of ~5 s) to describe the fuel dynamics in the Type-I region.

3.3.4. Best Estimate Data Set for the Dodewaard BWR

The distribution of friction over the different segments of the natural circulation loop is taken into account in this section (see Table 3-4), to improve the accuracy of the model predictions.¹⁵ The Dodewaard reactor has channel spacers at three different axial positions. The spacer friction losses are included in the core inlet and outlet friction coefficients. A total recirculation flow rate of ~1400 kg/s is calculated by the model at nominal conditions, in good agreement with the characteristic values in Table 3-1.

Table 3-4. Frictional Numbers for the Dodewaard BWR

Λ_C	1.03
Λ_R	0.10

$k_{C,i}$	3.46
$k_{C,e}$	2.19
$k_{R,e}$	1.00
$k_{D,i}$	1.00

The void reactivity $\rho_a(t)$ is related with the core average void fraction $\langle\alpha(t)\rangle_C$, and the core average quadratic void fraction $\langle\alpha^2(t)\rangle_C$, to close the reactor model:

$$\rho_a(t) = r_{a,1} \langle\alpha(t)\rangle_C + r_{a,2} \langle\alpha^2(t)\rangle_C \tag{3-1}$$

Specific values² for the void reactivity coefficients in Eq. (3-1) are provided in Table 3-5.

Table 3-5. Void Reactivity Coefficients Dodewaard BWR

$r_{a,1}$	-0.014
$r_{a,2}$	-0.240

Tables 3-2 through 3-5 constitute data set II. Data set II is used in the remaining sections of this chapter. A fine-tuned friction model, based on flow measurements in the Dodewaard reactor, is proposed in Chapter 7.

3.3.5. In-Phase Versus Out-of-Phase Stability

The total pressure drop over the downcomer section remains essentially constant during out-of-phase oscillations.¹⁶ This boundary condition results in a constant recirculation flow (when the flow in one half of the core increases, it decreases in the other half), causing no extra friction and inertia in the downcomer section. The pressure drop over the recirculation section oscillates during in-phase oscillations, resulting in extra damping in the recirculation loop. Therefore, from thermohydraulic point of view, the out-of-phase oscillation mode is more likely to cause large oscillations in the reactor core.

The thermohydraulic stability of the in-phase and the out-of-phase modes for a natural circulation BWR are compared in Fig. 3-8. The dynamic inertial pressure drop in the downcomer stabilizes thermohydraulic in-phase oscillations. The influence of acceleration and inlet friction on downcomer dynamics is only very small. The oscillation frequency (in hertz) is represented for some points in the dimensionless plane in Fig. 3-8. The underlined number denotes the oscillation frequency of the out-of-phase mode, the other number corresponds to the in-phase oscillation frequency. For instance, the pair of numbers 1.2/2.5 in

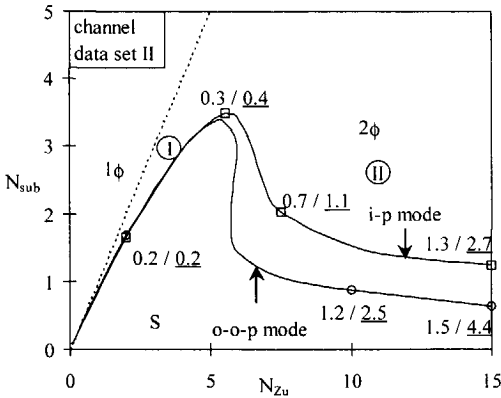


Figure 3-8. In-phase versus out-of-phase thermohydraulic stability. The out-of-phase (o-o-p) mode is less stable than the in-phase (i-p) mode, due to the stabilizing effect of downcomer inertia on in-phase oscillations. The oscillation frequency of the in-phase mode is lower due to the extra inertia. The oscillation frequencies (Hz) for the in-phase and the out-of-phase modes (underlined) are represented for several points.

Fig. 3-8 means that the in-phase oscillation frequency is equal to 1.2 Hz and the out-of-phase frequency is 2.5 Hz. Note that the out-of-phase mode is just on the threshold of stability for this specific point, while the in-phase mode is stable in this Zuber-subcooling coordinate. The frequency of in-phase oscillations is lower because of the extra inertia in the downcomer. Because of the typical low resonance frequency of Type-I oscillations, the difference between the in-phase and the out-of-phase modes is relatively small in the Type-I instability region.

The out-of-phase (or first azimuthal) reactor mode is a higher harmonic solution of the neutron kinetic equations,

see Appendix A. The in-phase (or fundamental) mode has a k_{eff} -eigenvalue equal to one in the equilibrium state. The higher harmonic modes are all subcritical. The subcriticality of these modes will decrease (in an absolute sense) in larger reactor cores [for instance the natural circulation ESBWR concept of GE] and therefore higher harmonic (for instance out-of-phase) oscillations become more likely to occur from neutronic point of view, see Fig. (A-1) in Appendix A.

The active Dodewaard core radius R is only 1.1 m. Applying elementary one-group diffusion theory for a homogenized cylindrical reactor core the subcriticality ρ^S , of the out-of-phase mode is estimated to be -6.5% [applying Eq. (A-20) in Appendix A]. The reactor stability boundaries for the in-phase and the out-of-phase modes are presented in Fig. 3-9. The neutron kinetic model used for the out-of-phase mode is described in detail in Appendix A and Ref. 11. Out-of-phase oscillations are strongly damped in the Type-II unstable region in comparison with in-phase oscillations and are therefore not expected to occur in the small reactor cores. The stabilizing effect of the neutronic feedback is reduced significantly during spatial out-of-phase oscillations in the Type-I unstable region, and the coupling of thermohydraulic out-of-phase oscillations with the out-of-phase reactor mode becomes possible.

It is instructive to investigate the influence of the core radius, and therefore the subcriticality of the out-of-phase mode, on reactor stability. The stability boundaries in case

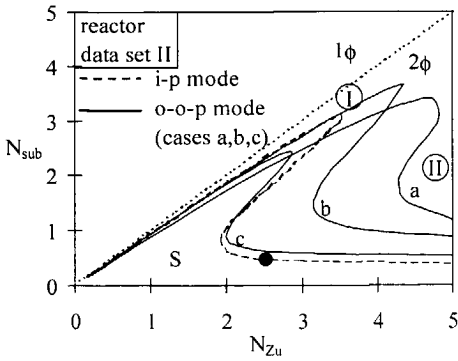


Figure 3-9. In-phase versus out-of-phase reactor stability for (a) the Dodewaard core radius of $R = 1.1 \text{ m}$ ($\rho_1^S = -6.5 \text{ \$}$), (b) $R = 1.9 \text{ m}$ ($\rho_1^S = -2 \text{ \$}$), and (c) $R \rightarrow \infty$ ($\rho_1^S \rightarrow 0$). Type-II out-of-phase oscillations are strongly suppressed if the subcriticality is strongly negative. In-phase oscillations are dominant in the Type-II region, even if the subcriticality of the out-of-phase mode is zero.

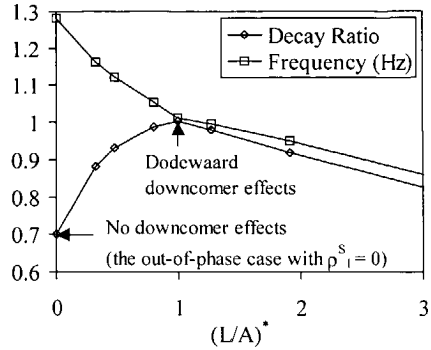


Figure 3-10. Influence downcomer inertia [reflected by $(L/A)^*$] on in-phase Type-II reactor stability. Downcomer inertia has a destabilizing effect on Type-II in-phase oscillations for the Dodewaard BWR.

of a core radius R of 1.9 m ($\rho_1^S = -2 \text{ \$}$) and an infinite core radius $R \rightarrow \infty$ ($\rho_1^S \rightarrow 0$) are depicted in Fig. 3-9 (keeping all other design parameters constant). Notice the rapid decrease of the out-of-phase Type-II stability as the core radius and the neutronic feedback increases. The stronger nuclear feedback stabilizes the Type-I oscillations. If the core radius, of course hypothetically, would be infinitely large, the subcriticality of the out-of-phase mode vanishes, see Eq. (A-20). Neglecting the minor influence of downcomer acceleration and friction, the only difference between the in-phase and the out-of-phase mode (with subcriticality zero) is the effect of the downcomer inertia. Downcomer inertia has a stabilizing influence on the Type-II *thermohydraulic* stability boundary. However, Fig. 3-9 demonstrates that the influence on *reactor* stability is destabilizing in the Type-II region. This apparent paradox can be explained by the resonance frequency lowering effect of downcomer inertia. This frequency lowering causes an increase in the gain of the fuel heat transfer function and the thermohydraulic transfer function from heat flux and inlet mass flux density to void fraction.^{c)}

A time-domain study in the point marked with a dot in Fig. 3-9 was performed to investigate the influence of downcomer inertia in more detail. The minor influence of downcomer friction and acceleration is not considered in this section. The effect of the dimensionless equivalent inertia length $(L/A)^*$ on the reactor decay ratio (DR), the ratio of two successive maxima of the power fluctuations caused by an external perturbation, and the

^{c)}The transfer function G_1 , defined in Eq. (2-18).

oscillation frequency is calculated in Fig. 3-10. The operating point of interest is located on the in-phase Type-II stability boundary, so the influence of the gravitational pressure drop in the riser is relatively small, and therefore only one riser node was used in the calculations. This approximation already yields accurate results: The error in the decay ratio calculated with the time-domain code (compared with the exact value of 1.0 from the frequency-domain code) is only 0.1%. The decay ratio was also calculated with the frequency-domain model, by determining the poles with the largest real part (two complex-conjugate poles in this case) of the closed-loop reactor transfer function. This approach yields results similar to the time-domain analysis.

The destabilizing influence of downcomer inertia [except for large values of $(L/A)^*$] is clear in Fig. 3-10. Note that the value of $(L/A)^*$ for the Dodewaard BWR (1.00, see Table 3-2) is just the least stable situation [as a comparison, the SBWR concept of GE has a much larger $(L/A)^*$ -value of ≈ 4.1] (Ref. 17). So even if the Dodewaard reactor hypothetically had an extremely large core radius, the in-phase mode would still be dominant in the Type-II region compared with the out-of-phase mode, see Fig. 3-9.

3.3.6. Sensitivity of Reactor Stability to Changes in Operating Conditions

The Zuber and the subcooling number are coupled in a natural circulation BWR, as was explained in Chapter 2. Therefore, only specific trajectories in the dimensionless plane as a function of the operating parameters are possible. Typical trajectories in the Zuber-subcooling plane are presented in this section. The model that Stekelenburg developed for the Dodewaard steam and feedwater system² was added to our model, to take into account the relationship between the Zuber and the subcooling number. Stekelenburg's model for carry under is applied as well in this section. It is important to emphasize that the influence of feedwater dynamics and carry under on reactor dynamics is not taken into account: Stekelenburg's model is only used to calculate the steady-state values of the Zuber and the subcooling number.

Applying this extended model, it is possible to calculate trajectories in the Zuber-subcooling plane, as a function of different system parameters. The reactor decay ratio was calculated for many different operating conditions with the developed time-domain code. The calculations were performed with one riser node. The decay ratio is represented in Fig. 3-11 as a function of the Zuber number and the ratio of the subcooling and the Zuber number (which is equal to the boiling boundary position relative to the channel height, because a flat axial power profile is used in the calculations). Using this latter axis removes the one-phase region from the stability plane (the dynamic characteristics of this region are not incorporated in the model of Chapter 2).

Figure 3-11 gives more insight into the dependence of reactor stability on the operating

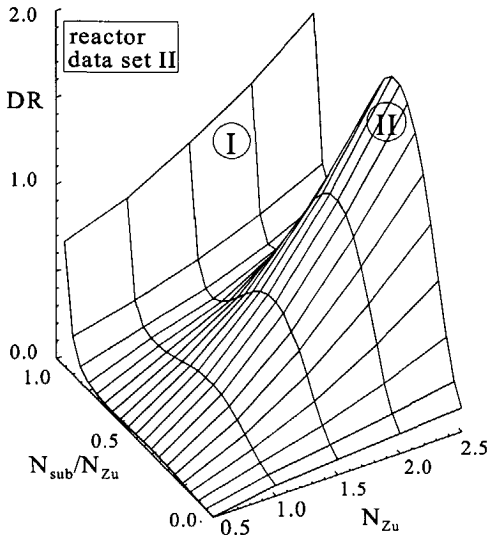


Figure 3-11. Three-dimensional picture of the reactor decay ratio (DR) in the dimensionless stability plane.

conditions in comparison with Fig. 3-9, where only the stability boundaries were plotted. Note for instance that due to the Type-I resonance, the decay ratio increases very rapidly when the boiling boundary position is close to the exit of the heated section ($N_{\text{sub}} / N_{\text{Zu}}$ close to 1). This further explains why the Type-I stability boundary is quite insensitive to important system parameters like the void reactivity coefficient: A change of the decay ratio due to system changes will cause a relatively small shift of the position of the stability boundary.

The decay ratio also increases strongly for large Zuber numbers, especially when the Zuber number is approximately twice the subcooling number. This is the region of Type-II oscillations. Furthermore, Fig. 3-11 reveals that the decay ratio is relatively small and only slowly increasing as a function of the Zuber number for the intermediate region of combined Type-I/Type-II oscillations. This explains why in this region the position of the stability boundary is very sensitive to changing system parameters (for instance, the influence of the system pressure on the stability boundary in Fig. 3-3 is relatively large in this intermediate region): A change of the decay ratio due to an alteration of the system causes a relatively large shift of the stability boundary position.

The impact of changing the operating conditions on reactor stability is visualized in Fig. 3-12. The contour lines of equal decay ratios are extracted from Fig. 3-11. Decreasing the pressure (while keeping the power and the feedwater temperature at their nominal values) has a strong destabilizing effect, completely in line with the earlier conclusions in Section 3.2.2. Type-I and Type-II reactor stability characteristics are only slightly affected by the system pressure in the dimensionless stability plane, as was demonstrated in Section 3.3.2. Therefore, the stability analysis is performed only for the nominal pressure and not repeated for other values of the system pressure. The influence of the thermal power on reactor stability is also shown in Fig. 3-12. Increasing the power level causes an increase of the Zuber number. The subcooling number also increases for higher power levels because in that case, the steam and feedwater flow are relatively large (compared with the total circulation flow). This larger feedwater flow, with a temperature below the saturation temperature, then causes an increase of the subcooling number. Finally, decreasing the feedwater temperature increases the subcooling number and has a destabilizing effect. However, even when the feedwater

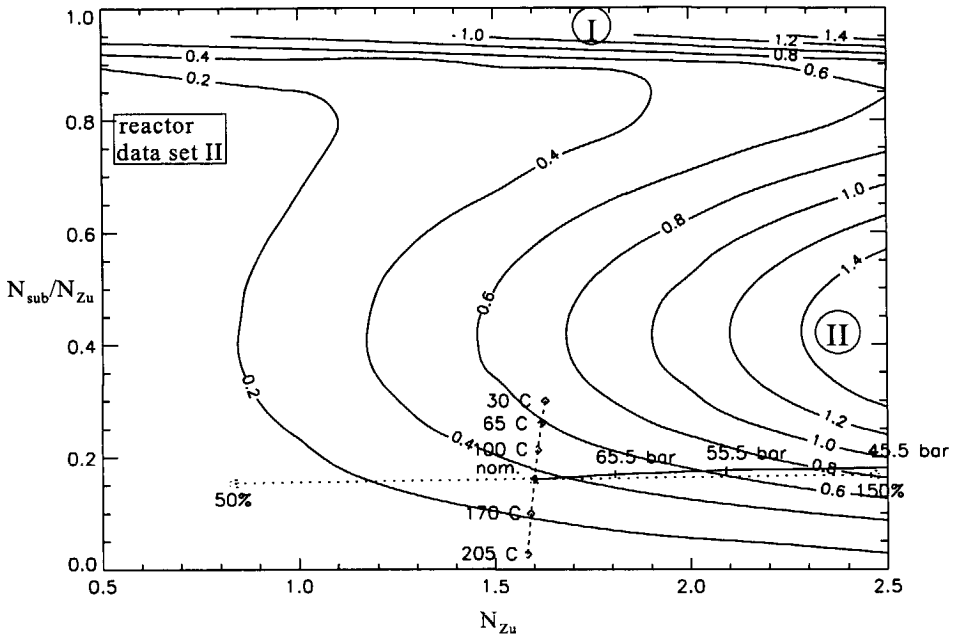


Figure 3-12. Sensitivity of the decay ratio to changes in operating conditions: (a) changing the pressure (solid line), (b) changing the power (dotted line), and (c) changing the feedwater temperature (dashed line).

temperature is as low as 30°C, the region of intermediate Type-I/Type-II or Type-I oscillations is not reached in this high-pressure BWR model. Including the flashing effect in our low-pressure BWR model, we will see in Chapter 6 that the Type-I stability boundary can be crossed at low power and pressure (reactor startup) conditions.

3.4. CONCLUSIONS

A parametric study of coupled neutronic-thermohydraulic stability of natural circulation BWRs is performed. The theoretical model described in Chapter 2 was used to determine the stability characteristics of natural circulation BWRs. Stability was investigated in the nondimensional Zuber-subcooling plane. Without a riser section installed, only one region of thermohydraulic instability exists in this stability plane. This region of instability, caused by the interplay of the one-phase and the two-phase frictional pressure drop in the heated section, is the so-called Type-II instability zone. The significant gravitational pressure drop in a riser section gives rise to the emergence of an additional region of instability in the stability plane. The gravitational or Type-I oscillations in this zone can become especially important during low-power/low-pressure reactor startup conditions, as will be demonstrated further in

Chapter 6.

The coupling between the neutronic and the thermohydraulic subsystems in a natural circulation reactor was found to be strongly dependent on the state of the thermohydraulic subsystem. Because of their typically low resonance frequency, thermohydraulic oscillations of the Type-I are damped by the nuclear void reactivity feedback. However, the higher-frequency Type-II oscillations are amplified in a reactor, because of larger phase shifts in the void reactivity feedback loop.

A comparison between natural circulation in-phase and out-of-phase reactor stability was made. Out-of-phase oscillations in the Type-II region are strongly suppressed in small reactor cores, for instance the Dodewaard core. However, in the Type-I zone, spatial oscillations are possible. The influence of downcomer inertia on in-phase reactor stability was studied in detail, using Dodewaard design parameters. It was found that downcomer inertia has a stabilizing effect of Type-II *thermohydraulic* stability. However, the downcomer inertia has a destabilizing effect on *reactor* stability. This was explained by the decrease of the thermohydraulic resonance frequency as a function of the inertia, and the resulting (destabilizing) increase of the reactor open loop gain. Finally, typical trajectories in the stability plane were calculated as a function of the pressure, the power, and the feedwater temperature, to clarify the impact of changing operating conditions on reactor stability.

REFERENCES

1. D.D.B. van Bragt and T.H.J.J. van der Hagen, "Stability of Natural Circulation Boiling Water Reactors: Part I - Description Stability Model and Theoretical Analysis in Terms of Dimensionless Groups," *Nucl. Technol.*, **121**, 40 (1998); also published as Chapter 2 of this thesis.
2. A.J.C. Stekelenburg, "Statics and Dynamics of a Natural Circulation Cooled Boiling Water Reactor," PhD Thesis, Delft University of Technology, Delft, The Netherlands (1994).
3. T.H.J.J. van der Hagen, "Stability Monitoring of a Natural-Circulation-Cooled Boiling Water Reactor," PhD Thesis, Delft University of Technology, Delft, The Netherlands (1989).
4. T.H.J.J. van der Hagen and A.J.C. Stekelenburg, "The Low-Power Low-Pressure Flow Resonance in a Natural Circulation Cooled Boiling Water Reactor," *Nucl. Eng. Des.*, **177**, 229 (1997).
5. K. Fukuda and T. Kobori, "Classification of Two-Phase Flow Instability by Density Wave Oscillation Model," *J. Nucl. Sci. Technol.*, **16**, 95 (1979).
6. J. March-Leuba and J.M. Rey, "Coupled Thermohydraulic-Neutronic Instabilities in Boiling Water Nuclear Reactors: A Review of the State of the Art," *Nucl. Eng. Des.*, **145**, 97 (1993).
7. R.T. Lahey, Jr. and F.J. Moody, *The Thermal-Hydraulics of a Boiling Water Nuclear Reactor*, American Nuclear Society, LaGrange Park, Illinois (1979).
8. Y.F. Rao, K. Fukuda, and R. Kaneshima, "Analytical Study of Coupled Neutronic and Thermodynamic Instabilities in a Boiling Channel," *Nucl. Eng. Des.*, **154**, 133 (1995).
9. F.-S. Wang, L.-W. Hu, and C. Pan, "Thermal and Stability Analysis of a Two-Phase Natural Circulation Loop," *Nucl. Sci. Eng.*, **117**, 33 (1994).
10. Y.N. Lin and C. Pan, "Non-Linear Analysis for a Natural Circulation Boiling Channel," *Nucl. Eng. Des.*,

- 152, 349 (1994).
11. D.D.B. van Bragt and T.H.J.J. van der Hagen, "A Six-Dimensional Model for Coupled Neutronic-Thermohydraulic Out-of-Phase Oscillations in Boiling Water Reactors," *Proc. National Heat Transfer Conf.*, Houston, Texas, August 3-6, 1996, Vol. 9, p. 179, American Nuclear Society (1996).
 12. M. Furuya, F. Inada, and A. Yasuo, "Density Wave Oscillations of a Boiling Natural Circulation Loop Induced by Flashing," *Proc. 7th Int. Mtg. Nuclear Reactor Thermal-Hydraulics (NURETH-7)*, Saratoga Springs, New York, September 10-15, 1995, NUREG/CP-0142, p. 923, U.S. Nuclear Regulatory Commission (1995).
 13. S.Y. Jiang and D. Emendörfer, "Analysis of Flow Oscillations in a Natural Circulation System Taking Account of Non-Equilibrium Boiling and Void Flashing," *Kerntechnik*, **61**, 23 (1996).
 14. T.H.J.J. van der Hagen, "Experimental and Theoretical Evidence for a Short Effective Fuel Time Constant in a Boiling Water Reactor," *Nucl. Technol.*, **83**, 171 (1988).
 15. J.C. Bruggink, Gemeenschappelijke Kernenergiecentrale Nederland, Personal Communication (Oct. 1995).
 16. J. March-Leuba and E.D. Blakeman, "A Mechanism for Out-of-Phase Power Instabilities in Boiling Water Reactors," *Nucl. Sci. Eng.*, **107**, 173 (1991).
 17. F. Inada, M. Furuya, A. Yasuo, H. Tabata, Y. Yoshioka, and H.T. Kim, "Thermo-Hydraulic Instability of Natural Circulation BWRs at Low Pressure Start-Up: Experimental Estimation of Instability Region with Test Facility Considering Scaling Law," *Proc. 3rd Int. Conf. Nuclear Engineering (ICONE-3)*, Kyoto, Japan, April 23-27, 1995, Vol. 1, p. 173 (1995).

Chapter 4

High-Pressure BWR Dynamics: III - Nonlinear Analysis^{a)}

Abstract - A dynamic model of natural circulation BWRs is analyzed using a bifurcation code and numerical simulations. The two fundamental bifurcation types relevant to BWRs, the supercritical and the subcritical Hopf bifurcations, are first studied in natural circulation systems without nuclear feedback. The effect of nodalization approximation in the riser on stability and bifurcation characteristics of the system is determined. The strong effect of the nuclear-thermohydraulic interaction on the nonlinear characteristics of a natural circulation BWR is then explored in a parametric study. Supercritical bifurcations become dominant in the (high-power) Type-II region for small values of the subcooling number and a strong nuclear-thermohydraulic coupling. A 'cascade' of period-doubling pitchfork bifurcations (deep in the unstable region) is also predicted by the model under these conditions. Subcritical bifurcations in the Type-II instability region were found for larger values of the subcooling number. Both Hopf-bifurcation modes were also encountered in the (low-power, or high-power/high-subcooling) Type-I instability region.

4.1. INTRODUCTION

Prompted by unexpectedly large power oscillations observed in the Caorso (1984) and the LaSalle (1988) plants, significant progress has been made in recent years in better understanding the stability issues in BWRs. Several stability tests have been performed under

^{a)}This chapter is an adapted version of:

D.D.B. van Bragt, Rizwan-uddin[†], and T.H.J.J. van der Hagen, "Nonlinear Analysis of a Natural Circulation Boiling Water Reactor," To appear in Nuclear Science and Engineering (January 1999).

[†]Department of Nuclear Engineering, University of Illinois, 103 S. Goodwin Avenue, Urbana, IL 61801; Also, Computational Science and Engineering Program.

decreased stability conditions.¹⁻³ Detailed time-domain codes like TOSDYN-2,⁴ RAMONA,^{5,6} RETRAN⁷ and TRACG⁸ were used to simulate the experimental data and validate the computer codes for large oscillation incidents.

However, since the complexity of nonlinear calculations increases rapidly as a function of the model order, parametric studies with the aforementioned high-fidelity codes, and others like them, are very expensive and time-consuming. Classical frequency-domain stability analyses of detailed BWR models have been performed to carry out quick parametric studies and to study the impact of various design and operating parameters on system stability.⁹ Important as they are, such frequency-domain analyses nevertheless only identify stability boundaries and shed no information on the system behavior following relatively large perturbations. Therefore a simultaneous, complementary effort has focused on the development of reduced-order models, which are easy to use in fast analytical and numerical studies and still sufficiently accurately describe the main physical phenomena. Just before nonlinear BWR dynamics attracted large-scale attention, March-Leuba et al.^{10,11} developed a qualitative reduced-order stability model for BWRs. This fifth-order nonlinear model is very suitable for fast parametric studies, and predicts the evolution of the reactor power to stable limit cycles in the unstable region close to the stability boundary. 'Deeper' in the unstable region, a cascade of period-doubling bifurcations occurs, eventually resulting in chaotic oscillations. Muñoz-Cobo and Verdú¹² applied Hopf-bifurcation theory to the same model and determined the limit cycle stability, amplitude and oscillation period as a function of model parameters. A more elaborate nonlinear model was analyzed with the bifurcation code BIFOR2¹³ by Tsuji et al.¹⁴ The simple 'damped-spring' equation for the channel two-phase flow dynamics in the model by March-Leuba et al.¹¹ was replaced by a more sophisticated channel model by these authors. Their Hopf-bifurcation analysis showed that the periodic solutions in the vicinity of the stability boundary were orbitally unstable, and they therefore concluded that the experimentally observed stable limit cycles in BWRs should be explained by another nonlinear mechanism. Karve et al.¹⁵ included detailed fuel rod dynamics in their simple model and determined stability boundaries in the inlet-subcooling/external reactivity operating parameter plane. More importantly, they, via mapping, determined the stability of points on the power-flow map. Numerical simulation of the nonlinear ordinary differential equations (ODEs) was also carried out and showed that the Hopf bifurcation is subcritical. Significant progress made in recent years in the stability analyses of single and multiple parallel heated channels with two-phase flow, but without neutronic feedback, will not be reviewed here.

It is quite likely that next generation BWRs will be cooled by natural circulation. Bifurcation studies of natural circulation BWRs - like those reported by Muñoz-Cobo and Verdú,¹² and Tsuji et al.¹⁴ for forced-circulation BWRs - are hence needed. Moreover, most bifurcation analyses have been carried out with the subcooling or the power level as the

bifurcation parameter. Discrepancies between the results obtained by different researchers seem to depend on “other” design or operating parameters, such as the presence of a riser, the riser height, the nuclear feedback strength and even on modeling parameters.

Using the low-dimensional BWR model, developed and successfully used earlier by Van Bragt and Van der Hagen, see Chapters 2 and 3,¹⁶⁻¹⁸ we here report the results of a bifurcation analysis carried out using the Hopf-bifurcation code BifDD,¹⁹ the successor of the aforementioned BIFOR2 code. Comparisons are made between heated channel systems and reactors (with neutronics feedback). The effects of design and operating parameters on the bifurcation characteristics is studied. In addition, the effect of modeling approximation on bifurcation is also analyzed. Specifically, the effect of the number of nodes in the riser on the stability boundary and bifurcation mode is investigated. Numerical simulations were carried out to determine the range of validity of the bifurcation analyses away from the stability boundaries.

A summary of the nonlinear model equations, transformed to a nondimensional basis, is provided in Appendix B. Nonuniform (but symmetrical) axial power profiles and nonuniform void profiles over the channel cross-section are accounted for in this appendix. Furthermore, the algebraic equations in the model of Chapter 2 are eliminated in Appendix B, by substituting them in the model ODEs. This thermo-nuclear model then consists of a set of (normalized) ODEs which describe the time evolution of the neutron and precursor population, the fuel temperature dynamics, the boiling boundary position in the core, the core exit quality and mass flux density, and the nodal exit quality of the axial riser nodes.

In this chapter we will focus on the nonlinear dynamics of only in-phase oscillations. Moreover, all parametric studies are performed with the homogeneous equilibrium model (i.e. both local and integral slip are neglected). Local friction losses are lumped in the global core friction (data set 1 of Chapter 3 is used), and the calculations were performed with an elementary flat profile. A comparison of the model with nonlinear power oscillations, measured in the Dutch Dodewaard reactor,³ is presented in Chapter 7. We there applied a fine-tuned reactor model including distributed friction losses and an axially peaked power profile.

The BifDD code is described in Section 4.2. A bifurcation analysis for the thermohydraulic subsystem of a natural circulation BWR, neglecting nuclear feedback effects, is presented in Section 4.3. The impact of nuclear feedback on the nonlinear dynamics of a natural circulation BWR is investigated in Section 4.4. Conclusions are provided in Section 4.5.

4.2. THE HOPF BIFURCATION

One of the most important bifurcation types in BWR stability problems is the ‘Hopf’ (or dynamic) bifurcation.^{13,20} A Hopf bifurcation occurs when a pair of complex conjugate

eigenvalues of the Jacobian matrix of the dynamical system crosses the imaginary axis with a non-zero speed, as a parameter is varied. The real parts of all other eigenvalues should be negative. When these conditions are satisfied, a family of periodic solutions, with a small amplitude ϵ , exists in a neighborhood of the stability boundary:

$$\bar{\mathbf{x}}(t; \lambda) = \bar{\mathbf{x}}(\lambda_c) + \epsilon \operatorname{Re}(e^{2\pi i t/T(\epsilon)} \bar{\mathbf{v}}_1) + O(\epsilon^2). \quad (4-1)$$

The components of the vector $\bar{\mathbf{x}}(t; \lambda)$ in Eq. (4-1) consist of the different state variables of the system. $\bar{\mathbf{x}}(\lambda_c)$ is the equilibrium value of this state vector at the critical value (on the stability boundary) of the bifurcation parameter λ , and $\bar{\mathbf{v}}_1$ is the eigenvector of the linearized system on the stability boundary. The nonlinear oscillation period $T(\epsilon)$ in Eq. (4-1) is expanded as a function of ϵ :

$$T(\epsilon) = [2\pi/\omega(\lambda_c)] [1 + \tau_2 \epsilon^2 + O(\epsilon^4)], \quad (4-2)$$

and likewise the bifurcation parameter $\lambda(\epsilon)$ is expanded:

$$\lambda(\epsilon) = \lambda_c + \mu_2 \epsilon^2 + O(\epsilon^4). \quad (4-3)$$

State-space trajectories in the direct neighborhood of the periodic solutions in Eq. (4-1) are decaying exponentially to the periodic solutions, if the periodic solution is orbitally stable. Unstable periodic solutions, on the other hand, repel the state-space trajectories in their vicinity. The characteristic exponent characterizing the asymptotic decay to the periodic solutions is denoted as $\beta(\epsilon) = \beta_2 \epsilon^2 + O(\epsilon^4)$.¹³ The periodic solutions are therefore orbitally stable if $\beta(\epsilon) < 0$ and orbitally unstable if $\beta(\epsilon) > 0$.

While it is possible to carry out bifurcation analysis using Lindstedt-Poincaré type analyses,²¹ these quickly become tedious and cumbersome. Several *numerical* bifurcation codes have hence been developed. The Hopf-bifurcation code BifDD (Bifurcation Formulae for Delay-Differential Systems)¹⁹ is here used to analyze the stability characteristics of the outlined BWR model in the design and operating parameter space. The BifDD code can analyze systems of ordinary differential equations with fixed time delays. Our model consists of ordinary differential equations without time delays, so all delays are set equal to zero in the code. Apart from the set of equations, BifDD must be supplied with a subroutine containing explicit expressions for the Jacobian matrix of the system of ODEs. Symbolic expressions for the Jacobian were derived with the Mathematica software package. The BifDD code numerically verifies whether the user-supplied Jacobian is consistent with the set of ODEs.

For given values of all the system parameters except one, the code determines the value of the unspecified parameter and the corresponding frequency at the Hopf stability boundary. By incrementally varying another parameter, the entire stability boundary in a two-dimensional space can be determined. The Hopf-bifurcation equations are also solved numerically. The main result of the bifurcation calculations is the set of expansion coefficients μ_2 , τ_2 and β_2 ,

for each point on the stability boundary.

All numerical calculations were performed with double precision on an IBM-RS6000 workstation at the University of Illinois. Comparative calculations with single precision yielded significantly different quantitative results, indicating that the high-accuracy double precision is required for these nonlinear calculations. We did not check the accuracy of the double-precision calculations by carrying out, for example, quartic-precision calculations. The check was, however, indirectly performed by comparing the predictions of BifDD with the results of numerical integrations, which were carried out using the NDSolve subroutine of the Mathematica package. NDSolve uses an Adams predictor-corrector method for non-stiff differential equations and backward difference formulas (Gear method) for stiff differential equations.

4.3. THERMOHYDRAULIC SUBSYSTEM

An elementary thermohydraulic natural circulation loop, consisting of a heated (core) section and a downcomer channel, is investigated in Section 4.3.1. The natural circulation flow rate in natural circulation BWRs is normally enhanced by installing a tall riser section on top of the core region. The impact of this riser section on the linear and nonlinear characteristics of a natural circulation system is studied in Section 4.3.2.

4.3.1. Natural Circulation System Without Riser

The threshold of (linear) stability for a natural circulation system is most efficiently represented as a function of the dimensionless Zuber number N_{zu} and subcooling number N_{sub} , as we demonstrated in Chapter 3. In Fig. 4-1, we first compare the results of (linear) stability analysis obtained using BifDD with the stability boundary (SB) presented in Fig. 3-1 (the case without riser). Note that the expected good agreement between the stability boundaries only provides a consistency check for the two approaches.

Also shown in Fig. 4-1 are the results of the bifurcation calculations. The Zuber number is used as the bifurcation parameter in these calculations. For each value of the subcooling number and the corresponding critical value of the Zuber number, the expansion coefficients μ_2 , τ_2 and β_2 are calculated. Neglecting terms of order four and higher in Eq. (4-3), the values of the Zuber number for which a periodic solution with amplitude 0.1, 0.3 or 0.5 exists are calculated and plotted in Fig. 4-1. The eigenvector \bar{v}_1 in Eq. (4-1) is normalized with respect to the first component (the normalized core exit flow $M_{c,e}^*$) of the state vector $\bar{x}(t;\lambda)$, meaning that the ϵ in Fig. 4-1 (and all other bifurcation diagrams in this chapter) is the oscillation amplitude (half the peak-to-peak value) of this state variable. Figure 4-1 shows that stable nonlinear ('supercritical') oscillations ($\beta_2 < 0$) are predicted in the region of small

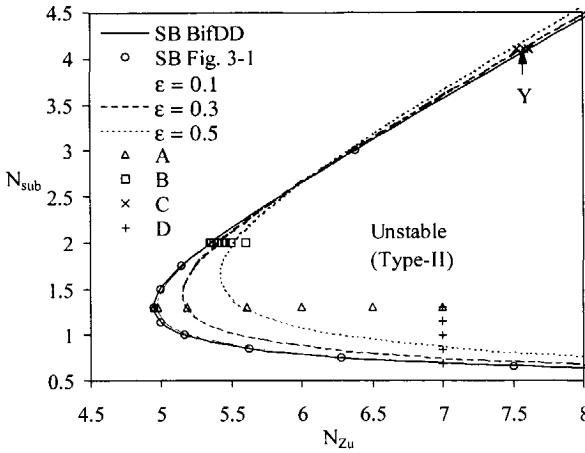


Figure 4-1. Bifurcation diagram for a natural circulation system without riser, and without nuclear feedback. The stability boundary (SB), calculated with the BifDD code, is compared with several points on the SB of Fig. 3-1 (the case without riser). The locations where nonlinear periodic solutions with a relative amplitude of 0.1, 0.3, and 0.5 exist are also depicted in the stability plane. Time-domain simulations were carried out at several points on the trajectories A, B, C and D (see Figs. 4-2 and 4-3).

subcooling numbers ($N_{sub} < 2.7$). However, for large values of the subcooling number unstable ('subcritical') oscillations ($\beta_2 > 0$) are predicted.

Numerical integrations were performed at various points in the stability plane not only as a counter check for the results of the bifurcation code, but also to determine the range of validity of oscillation amplitude and frequency predicted by BifDD in different regions of parameter space. Examples of numerical simulations of both types of Hopf bifurcations are presented in Fig. 4-2. The *supercritical* Hopf bifurcation - predicted for $N_{sub} < 2.7$ - yields a family of orbitally stable ('attracting') periodic solutions in the unstable region. All trajectories in the state space converge to these stable periodic solutions. Time evolutions,

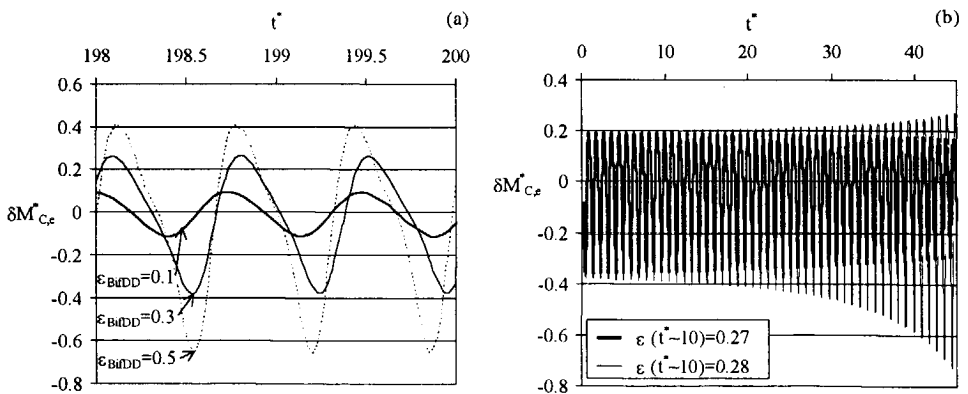


Figure 4-2. (a) Time evolution of the normalized core exit flow M_{Ce}^* for stable oscillations at the supercritical trajectory A in Fig. 4-1. (b) Time evolution for the subcritical point Y in Fig. 4-1. Notice that the long-term time evolution in the subcritical case is strongly dependent on the initial conditions (the two initial conditions are very close to each other).

after initial transients, for three different Zuber numbers (at trajectory A in Fig. 4-1) are shown in Fig. 4-2a. Considering that BifDD calculates only second-order expansion coefficients, implying that the results of this code are strictly speaking only valid for small values of the oscillation amplitude (i.e. close to the stability boundary), the predictions of the BifDD code agree remarkably well with the amplitude of the stable oscillations predicted by numerical simulations. *Subcritical* periodic solutions exist in the stable region where the bifurcation is subcritical, and are unstable: They repel all nearby trajectories in the state space, and are therefore difficult to detect numerically. The growing and decaying oscillations at a point in the stable region with subcritical bifurcation (point Y in Fig. 4-1) are shown in Fig. 4-2b. The influence of initial transients is minimized in Fig. 4-2b by perturbing the system with the calculated eigenvector. Notice that the time evolution for the subcritical case is strongly dependent on the initial conditions: The two initial conditions are almost the same, yet the resulting long-term evolutions are entirely different. Figure 4-2b indicates that the

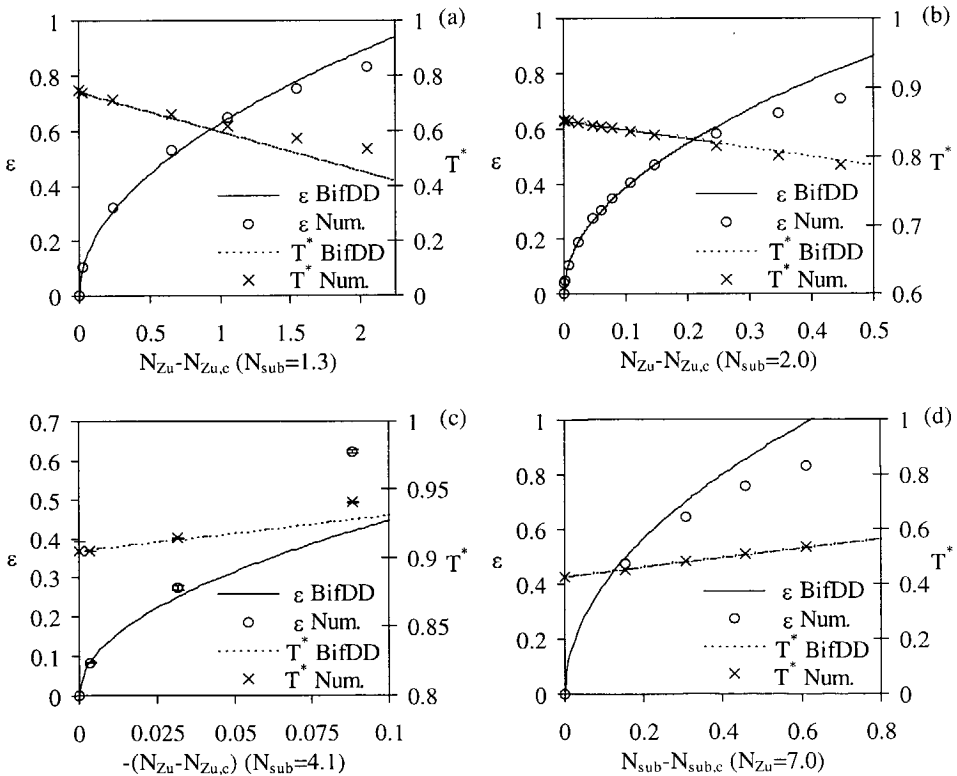


Figure 4-3. Comparison between the Hopf prediction and numerical simulations for four sequences of points (A through D) shown in Fig. 4-1: (a) for trajectory A in Fig. 4-1 ($N_{sub}=1.3$), (b) for trajectory B ($N_{sub}=2.0$), (c) for trajectory C - on the stable side of the SB - with $N_{sub}=4.1$, and (d) for trajectory D ($N_{Zu}=7.0$). Note that the subcooling number (instead of the Zuber number) is the bifurcation parameter in Fig. 4-3d.

unstable periodic solution for parameter values at point Y has an amplitude between 0.27 and 0.28. This time-domain result agrees well with the amplitude of 0.3 predicted by the BifDD code.

Hopf's theorem predicts the amplitude of the stable and the unstable periodic solutions in the *immediate vicinity* of the SB to grow proportional to the square root of the distance from the SB. An estimate for the region that qualifies for "immediate vicinity" is not provided by the theorem, and can only be obtained by comparing the amplitude and frequency of the oscillations predicted by the Hopf theorem with those obtained using the numerical simulation of the full nonlinear set of ODEs. Not surprisingly, the distance over which the Hopf prediction agrees with the amplitude and the frequency of the numerical simulation varies in different regions of the parameter space.

Figure 4-3 shows the comparison between the Hopf prediction and numerical simulations for four sequences of points plotted in Fig. 4-1 - three (A, B and D) in the unstable and one (C) in the stable region. At $N_{sub}=1.3$ and $N_{sub}=2.0$, as N_{Zu} is increased, the Hopf prediction for the oscillation amplitude agrees very well with the numerical simulation results up to $\epsilon=0.6$ (Figs. 4-3a and 4-3b). Note that at $N_{sub}=1.3$, N_{Zu} has to be increased by almost 1 to reach the point in parameter space where $\epsilon \approx 0.6$, whereas for $N_{sub}=2.0$, $\epsilon = 0.6$ is reached with a more modest increase in N_{Zu} (from $N_{Zu,c}$) of about 0.25.

At $N_{sub}=4.1$, the bifurcation is subcritical, and hence the periodic solution is unstable. Numerically, the amplitude of the subcritical oscillations was estimated to be in between the oscillation amplitudes of a decaying and a growing oscillation (after the initial transients have died), obtained by starting from different initial conditions in phase space. These small "error bars" are shown in Fig. 4-3c. The oscillation amplitude of the unstable periodic solution follows the "square-root behavior" up to $\epsilon \approx 0.3$, and then increases more rapidly as the bifurcation parameter N_{Zu} is further decreased. Figure 4-3d shows the results for $N_{Zu}=7.0$, with N_{sub} as the bifurcation parameter.

The effect of the Froude number N_{Fr} [which is proportional to the square of the mass flux density, see Eq. (2-25)] on the SB is known to be small. However, the bifurcation type for large subcooling numbers is strongly dependent on the value of this dimensionless number. The flow rate, and therefore the Froude number, is not an independent variable in a natural circulation system, but is determined by the density differences between the two-phase mixture in the core and the riser and the one-phase fluid in the downcomer. The Froude number is approximately equal to 0.02 (for $N_{sub}>2.7$) for the natural circulation system without riser, being analyzed in this section. As the Froude number is artificially increased (by imposing an external pressure drop over the recirculation section), the stability boundary for large N_{sub} moves slightly to the right, increasing the stable region (see Fig. 4-4a). The nonlinear characteristics of the system change more significantly. The *subcritical* region for high subcooling numbers (Fig. 4-4b) disappears as the Froude number is increased to 0.1

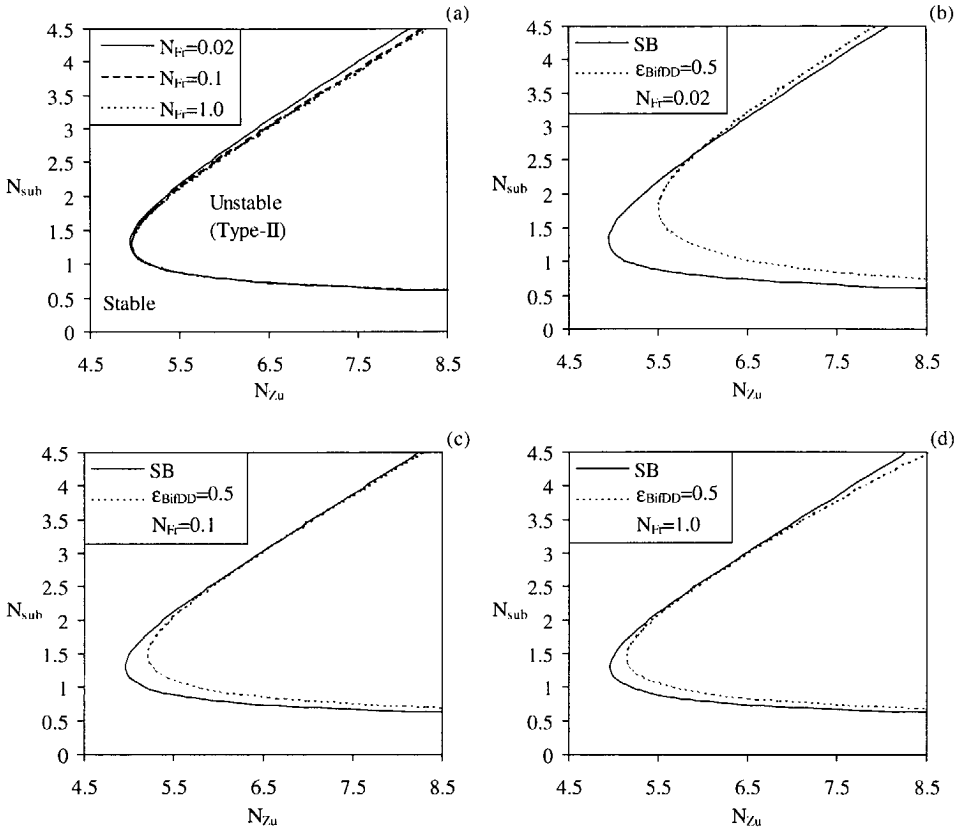


Figure 4-4. Influence of the Froude number on the SB (Fig. 4-4a) and on the bifurcation characteristics (Figs. 4-4b through 4-4d). Figure 4-4a shows that the influence of the Froude number on the SB is rather small. However, the nonlinear characteristics of the system change significantly. Figure 4-4b shows the bifurcation diagram for a Froude number of 0.02, which is close to the natural circulation case investigated in Fig. 4-1. The subcritical bifurcations at larger N_{sub} disappear when the Froude number is increased to 0.1 (Fig. 4-4c) and 1.0 (Fig. 4-4d).

(Fig. 4-4c) or 1.0 (Fig. 4-4d), and the Hopf bifurcation becomes *supercritical* in the entire dimensionless plane. These results agree with observations by Clause et al.,²² who also found that decreasing the Froude number, i.e. increasing the relative importance of the gravitational pressure drop terms, the Hopf bifurcations change from supercritical to subcritical at higher subcooling numbers.

4.3.2. Natural Circulation System With Riser

In this section, the elementary thermohydraulic loop discussed in the previous section is extended with an unheated riser on top of the heated core. Since the riser is not heated, the (linearized) model equations for the riser section can be integrated exactly, see Chapter 2 and

Ref. 23, and hence the SB can be determined without any error due to nodalization in the riser. For the Hopf analysis using BifDD, however, the two-phase quality profile in the riser must be approximated, and hence nodalization is necessary to obtain the set of ODEs given in Appendix B. The impact of such a nodalization in the riser on the SB can be easily studied by comparing the SB obtained using exact integration in the riser (without nodalization error) with those obtained with an approximated quality profile and different number of nodes (N_R) in the riser. The influence of a riser section and the impact of nodalization on the stability boundary of a natural circulation system is shown in Fig. 4-5. Notice that the stability boundaries calculated by the bifurcation code approach the stability boundary obtained with exact treatment of the riser (taken from Fig. 3-1) when the number of riser nodes is increased.

The bifurcation characteristics change significantly in the region of Type-I oscillations when the number of riser nodes is varied, see Fig. 4-6. *Subcritical* nonlinear oscillations are predicted when only one riser node is used (see Fig. 4-6a), whereas calculations with more nodes indicate that the nature of the Hopf bifurcation is *supercritical* in the Type-I region (Figs. 4-6b through 4-6d). Note that the nonlinear solutions depicted in Fig. 4-6 appear to be

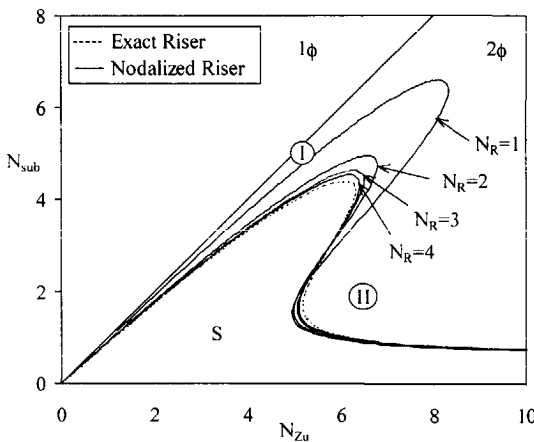


Figure 4-5. Influence of the number of riser nodes (N_R) on the stability boundary for a natural circulation system with riser. The stability boundary approaches the frequency-domain stability boundary with exact treatment for the riser, when the number of riser nodes increases. The circumscribed characters I and II indicate the Type-I and Type-II instability regions. The stable region is denoted with the symbol S.

inconsistent for large values of the subcooling number, indicating a reduced accuracy in the neighborhood of the turning point in the SB. The results in Fig. 4-6 also indicate that a detailed axial nodalization of the riser is necessary, especially in the Type-I region, to account correctly for the nonlinear dynamics of the void transport in this section. Analogously, our model of nonlinear stability in the Type-II region could be improved by applying a more detailed nodalization scheme for the heated section (now only one subcooled and one boiling node are employed in the analysis of the core region). The bifurcation characteristics in Fig. 4-6 have been confirmed by direct nonlinear time-

domain simulations in Ref. 24. Other analytical and numerical studies of nonlinear dynamics in the Type-I instability region^{25,26} also reported supercritical Hopf bifurcations. Three axial riser nodes were used in these references.

Finally, notice that the bifurcations for the Type-II instability at high values of the

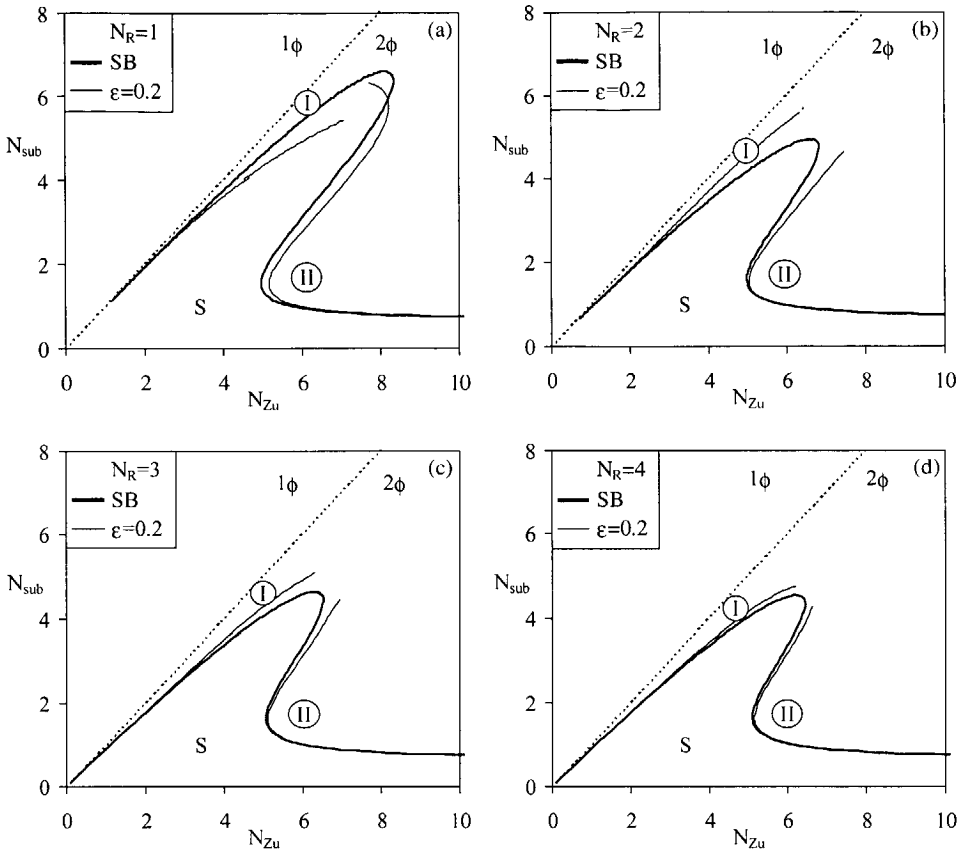


Figure 4-6. Influence of the number of axial riser nodes on the nonlinear stability characteristics. The bifurcation curves change dramatically in the region of Type-I oscillations when the number of riser nodes is increased. *Subcritical* oscillations in the Type-I region are predicted when only one riser node is used (Fig. 4-6a), whereas calculations with more nodes (Figs. 4-6b through 4-6d) indicate that the nature of the Hopf bifurcation is *supercritical* in the Type-I region.

subcooling number are supercritical, instead of subcritical, when the natural circulation system is coupled with a riser (compare Fig. 4-6d with Fig. 4-1). This effect can be explained by the larger natural circulation flow, and therefore the larger Froude number, when a riser section is installed. The influence of the Froude number on the Hopf bifurcation has already been discussed in Section 4.3.1.

4.4. REACTOR SYSTEM

The (nonlinear) interaction between the neutronic and the thermohydraulic subsystems in a natural circulation BWR is investigated in this section. Table 3.3 summarizes the neutron

kinetic and fuel data that were used in the calculations. The influence of nuclear feedback on the stability of an elementary natural circulation reactor without riser is discussed in Section 4.4.1. The dynamics in the vicinity of the stability boundary is first explored in Section 4.4.1.1. The complicated nonlinear oscillations which can occur 'deeper' in the unstable region are then investigated in Section 4.4.1.2. Finally, the influence of an unheated riser on the reactor bifurcation characteristics is considered in Section 4.4.2.

4.4.1. Reactor System Without Riser

4.4.1.1. Dynamics in the Vicinity of the Stability Boundary

The bifurcation diagram for a natural circulation reactor without riser, and a void reactivity coefficient r_a equal to -0.05 , is shown in Fig. 4-7. The channel bifurcation diagram without neutronics coupling (taken from Fig. 4-1) is also shown. Note that nuclear feedback has a negative effect on the Type-II stability, in accordance with the parametric results in Chapter 3. Both the SB and the bifurcation characteristics are affected by the addition of nuclear coupling. The stability boundary for the coupled neutronic-thermohydraulic system moves to the left when compared with the SB for the heated channel, reducing the stable region.

In both cases a supercritical Hopf bifurcation occurs for low values of N_{sub} and a subcritical Hopf bifurcation occurs for larger values of N_{sub} . The transition from a supercritical to a subcritical Hopf bifurcation for the heated channel occurs at approximately $N_{sub} = 2.7$, while for the reactor it occurs at about $N_{sub} = 0.8$.

The influence of the subcooling number on the nonlinear reactor dynamics is neglected in both the qualitative¹¹ as well as the more detailed²⁷ BWR model developed by March-Leuba

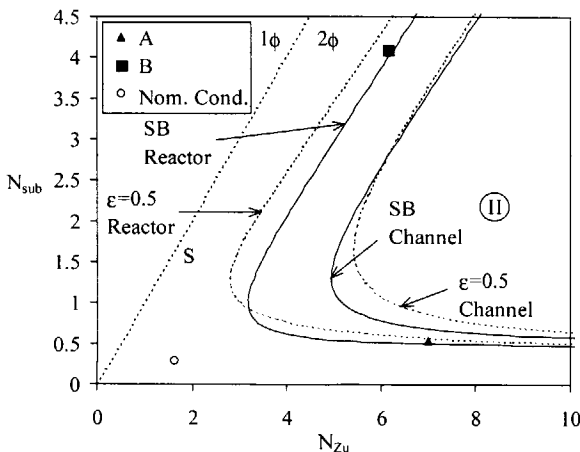


Figure 4-7. Bifurcation characteristics of a natural circulation reactor without riser ($r_a = -0.05$). Nuclear feedback has a strong destabilizing effect on the Type-II stability. The bifurcation characteristics also change: The region in the Zuber-subcooling plane where subcritical bifurcations exist becomes larger for a nuclear-coupled reactor system. Also shown is the normal operating point of the Dodewaard reactor.

et al. For simplicity they assumed in their models that the coolant enters the core as a saturated liquid (i.e. $N_{sub} = 0$). Both models predicted the existence of large-amplitude stable oscillations in the unstable low-flow/high-power domain (i.e. large Zuber numbers). This result is consistent with the supercritical Hopf bifurcations predicted by our model for small subcooling and large Zuber numbers. Similar results were found in other theoretical studies. Karve et al.¹⁵ numerically found the bifurcation in their model of forced circulation BWRs to be subcritical for a large N_{sub} of 1.5. The subcritical bifurcations for higher values of the subcooling number were reported earlier by Tsuji et al.¹⁴ Also shown in Fig. 4-7 is the nominal operating point of the Dodewaard reactor. It is clear that this operating point is in the stable region, far from the SB.

Time-domain illustrations of supercritical and subcritical bifurcations in a reactor system are presented in Fig. 4-8. Figure 4-8a shows the evolution of the normalized reactor power N^* to a stable nonlinear oscillation, in case of a supercritical Hopf bifurcation (point A in Fig. 4-7). The limit cycle amplitude is quite large, although point A is located close to the stability boundary. The bifurcation code predicts oscillations of the reactor power with an amplitude of 100% at point A. Figure 4-8a shows that this estimate is in fact close to the actual time-domain oscillation amplitude (half the peak-to-peak value) of 113%. This relatively small difference in numerical and bifurcation studies should have been surprising, since the BifDD code is strictly speaking only valid for small-amplitude oscillations, but results presented in Fig. 4-3 for the heated channel already showed us that the Hopf-predicted oscillation amplitude in this region of the parameter space can indeed be very accurate, even at points far from the SB. The major differences between the Hopf-predicted stable (and unstable) periodic solutions and those determined using the direct numerical simulations of the set of ODEs is that the Hopf solutions are purely sinusoidal [see Eq. (4-1)], whereas actual oscillations may be quite asymmetric about the fixed point (see Figs. 4-8a and 4-8b).

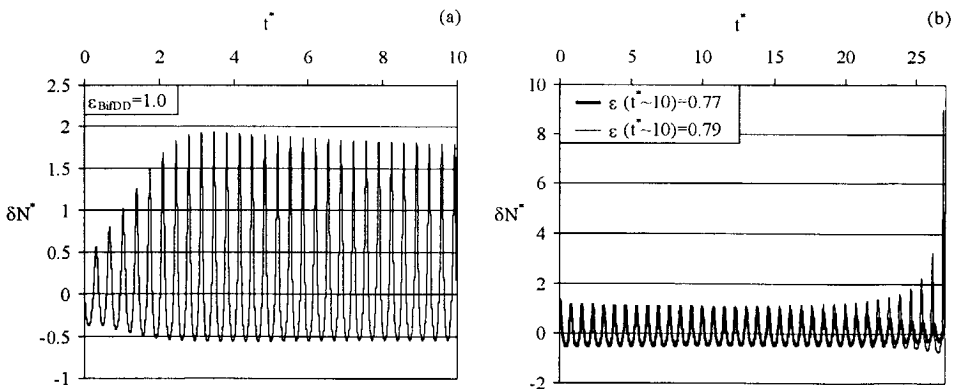


Figure 4-8. (a) Time evolution of the normalized reactor power N^* for stable oscillations at the supercritical point A in Fig. 4-7. (b) Time evolution for the subcritical point B in Fig. 4-7, for two initial perturbations.

Figure 4-8b shows the result of a subcritical Hopf bifurcation, which yields an unstable periodic solution in the stable region. The long-term behavior at point B of Fig. 4-7 is therefore strongly dependent on the initial perturbation of the state variables. The initial conditions for the two cases depicted in Fig. 4-8b are almost the same, yet the slightly larger initial perturbation causes a diverging and large-amplitude power oscillation, whereas the smaller initial perturbation is damped out and the system returns back to the stable fixed point. According to the BifDD code, the unstable and periodic nonlinear oscillation that exists at point B has an amplitude of 0.70. The time-domain simulations in Fig. 4-8b suggest that the amplitude of this periodic oscillation is in fact slightly larger (between 0.77 and 0.79). The agreement between the bifurcation code predictions and the time-domain simulations further improves (as expected) for nonlinear oscillations with smaller amplitudes.

From reactor safety point of view, the existence of subcritical nonlinear oscillations in the stable region has profound consequences, because in case of a subcritical Hopf bifurcation the reactor can become unstable in the *stable* region when the initial perturbation is large enough. Close to the stability boundary the 'basin of attraction' of the stable steady-state operating point becomes smaller, and modest perturbations (for instance due to noise or small control rod movements) could in principle result in diverging and undamped power oscillations, even when linear models still predict a stable system.

The impact of the void reactivity feedback on the Hopf-bifurcation (HB) characteristics is next investigated in more detail. Figure 4-9 shows curves, calculated with the BifDD code, of a constant oscillation amplitude $\epsilon=0.1$, in the $\delta N_{\text{sub}} - r_a$ and $\delta N_{\text{Zu}} - r_a$ planes. The horizontal coordinate $\delta N_{\text{sub}} = (N_{\text{sub}} - N_{\text{sub,c}})/N_{\text{sub,c}}$ in Fig. 4-9a is the relative change in N_{sub} from its value on the stability boundary, $N_{\text{sub,c}}$. Since $\delta N_{\text{sub,c}} = 0$ is the stability boundary (the dotted line in Fig. 4-9a), the periodic solutions that exist for $\delta N_{\text{sub}} > 0$ are stable nonlinear oscillations (caused by a supercritical Hopf bifurcation), and the periodic oscillations are unstable if $\delta N_{\text{sub}} < 0$ (subcritical Hopf bifurcation).

The entire $\epsilon=0.1$ curve in Fig. 4-9a is located on the unstable side of the stability boundary, and the bifurcation type is therefore supercritical in the entire $\delta N_{\text{sub}} - r_a$ space. The parameter study in Fig. 4-9a is performed at $N_{\text{Zu}}=7.0$, close to point A in Fig. 4-7. The heated channel bifurcation characteristics (no nuclear feedback) is obtained by setting $r_a=0$. $r_a=-0.05$ corresponds with the case studied in Fig. 4-7. Notice that the $\epsilon=0.1$ curve in Fig. 4-9a slightly tends toward the stability boundary as r_a is increased (in an absolute sense) from zero, but turns away as r_a is further increased. Hence, the periodic solutions with an amplitude of 0.1 are located deeper in the unstable region when the (absolute) void reactivity coefficient becomes larger.

The Zuber number, instead of the subcooling number, is the bifurcation parameter in Figs. 4-9b through 4-9d. We notice in Fig. 4-9b, for $N_{\text{sub}}=1.3$, that the bifurcation type changes from supercritical to subcritical and then back to supercritical as the strength of the

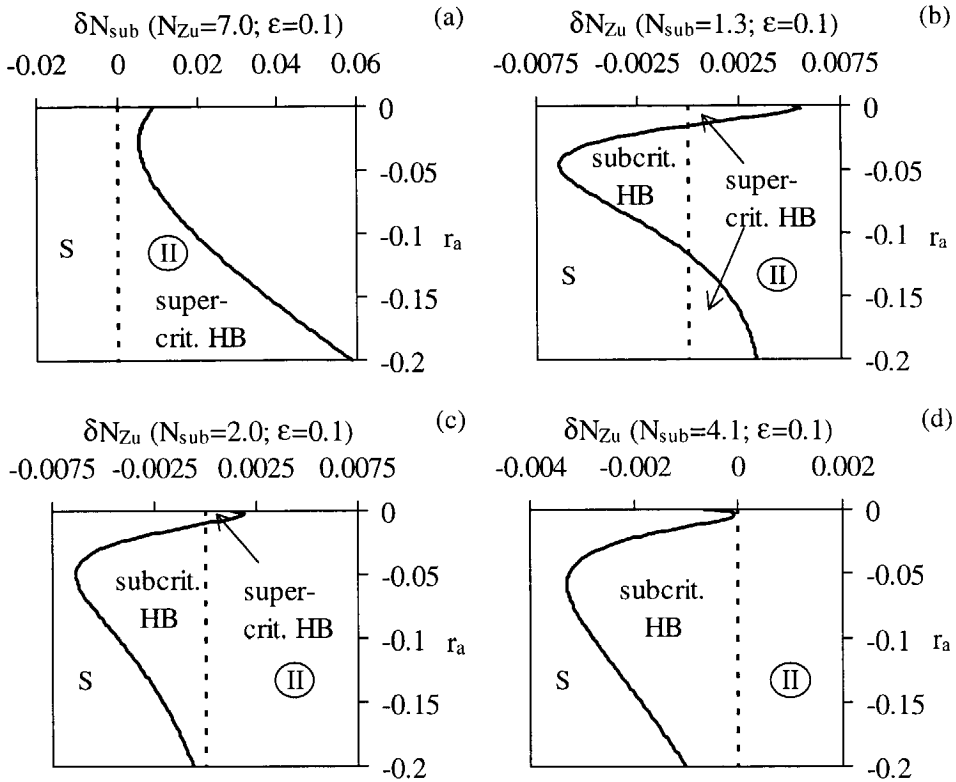


Figure 4-9. Influence of the void reactivity coefficient r_a on the Hopf-bifurcation (HB) curves in the Type-II instability region for a reactor without riser. The horizontal coordinate $\delta N_{sub} = (N_{sub} - N_{sub,c}) / N_{sub,c}$ in Fig. 4-9a is the relative change in N_{sub} from its value on the stability boundary, $N_{sub,c}$. N_{Zu} is the bifurcation parameter in Figs. 4-9b through 4-9d. Shown are constant amplitude periodic solution curves for an oscillation amplitude of 0.1. The vertical dotted line is the stability boundary.

nuclear feedback is varied via the void reactivity coefficient. Neglecting the nuclear feedback by setting $r_a = 0$, Fig. 4-9b shows that the bifurcation type for the thermohydraulic subsystem is supercritical at $N_{sub} = 1.3$, in agreement with Fig. 4-7. The bifurcation remains supercritical for a reactivity coefficient as large as -0.02 . The bifurcation becomes subcritical, however, as the void reactivity coefficient is increased (in an absolute sense) to (for instance) -0.05 (cf. Fig. 4-7). A further increase of the void coefficient once again changes the bifurcation to a supercritical Hopf bifurcation. At larger values of N_{sub} , the “windows” of supercritical bifurcations become smaller (see Fig. 4-9c), and the Hopf bifurcation finally becomes subcritical in the entire $\delta N_{Zu} - r_a$ space (for example for $N_{sub} = 4.1$ in Fig. 4-9d).

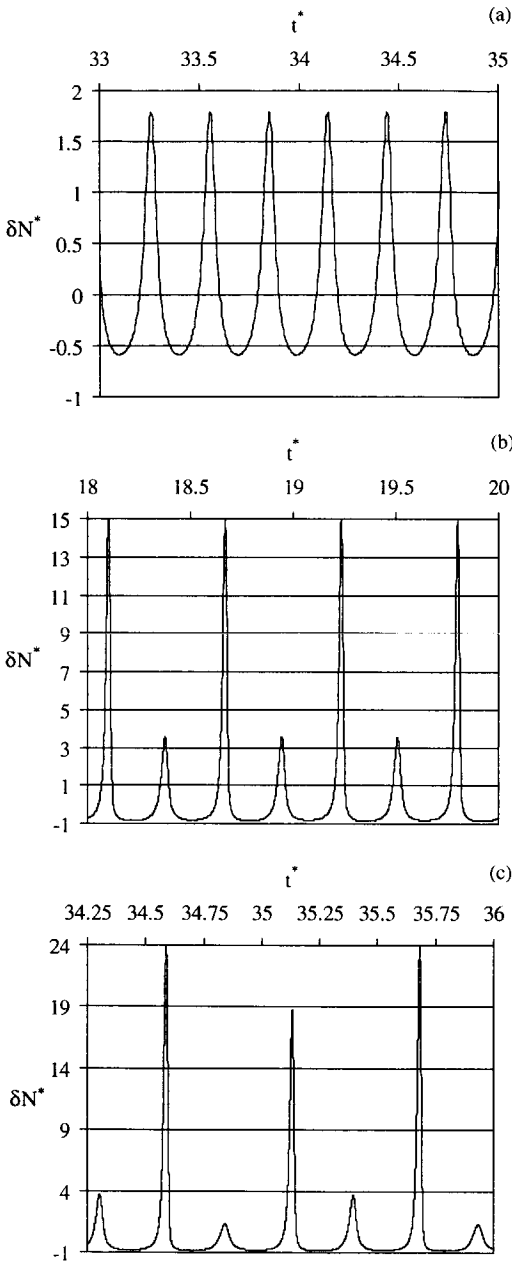


Figure 4-10. Higher-order bifurcations occurring in a natural circulation reactor without riser ($r_a = -0.2$ and $N_{zu} = 7.0$). The evolution of the reactor power after the (a) first (or 'Hopf'), (b) second, and (c) third bifurcation ($N_{sub} - N_{sub,c} = 0.027, 0.176, \text{ and } 0.205$, respectively) is shown.

4.4.1.2. 'Deep' in the Unstable Region

Direct time-domain simulations are necessary to investigate the nonlinear dynamics of a reactor far away from the stability boundary. We performed simulations for $N_{zu} = 7.0$ and $r_a = -0.2$, with the subcooling number as the bifurcation parameter. Figure 4-9a showed that under these circumstances the Hopf bifurcation is supercritical, and therefore stable nonlinear oscillations exist if the subcooling number is increased just above the critical value. Increasing the subcooling further, a cascade of period-doubling pitchfork bifurcations was found, similar to that observed in Refs. 10 and 11. After each higher-order bifurcation, the oscillation period doubles. Figure 4-10 shows as an example the evolution of the reactor power after the first, second, and third bifurcation ($N_{sub} - N_{sub,c} = 0.027, 0.176, \text{ and } 0.205$, respectively). Notice that the oscillation amplitude after the second (see Fig. 4-10b) and the third bifurcation (see Fig. 4-10c) becomes very large. The practical importance of higher-order bifurcations is therefore limited, because a reactor scram system would prevent the development of such extreme oscillations.

The difference in N_{sub} between two successive bifurcations decreases as the bifurcation parameter is increased. This suggests that the cascade of

bifurcations converges to an accumulation point where the oscillations become aperiodic (chaotic), as has been observed earlier in another BWR model¹¹ and is predicted by Feigenbaum’s universal theory.²⁸ The flow rate can become very small (approaching zero) during extremely large-amplitude power oscillations. The time-domain model breaks down, therefore, after the third bifurcation, and the entire ‘path to chaos’ could not be explored with the present model.

4.4.2. Reactor System With Riser

The bifurcation characteristics of a natural circulation reactor system with riser ($r_a = -0.05$) are presented in Fig. 4-11. Also shown in this figure, for comparison, is the SB for the heated channel from Fig. 4-6d. There is a quantitative change in the SB as the neutronics feedback is included. The “nose” or “elbow” of the stable region for the reactor case is narrower, but extends to higher values of the subcooling number compared to the stable region for the heated channel case. For example, the operating point $(N_{Zu}, N_{sub}) = (6,5)$ is stable for the reactor, but unstable for the heated channel. Results of the bifurcation analysis show a more dramatic (qualitative) change in the bifurcation characteristics of the system as the neutronics

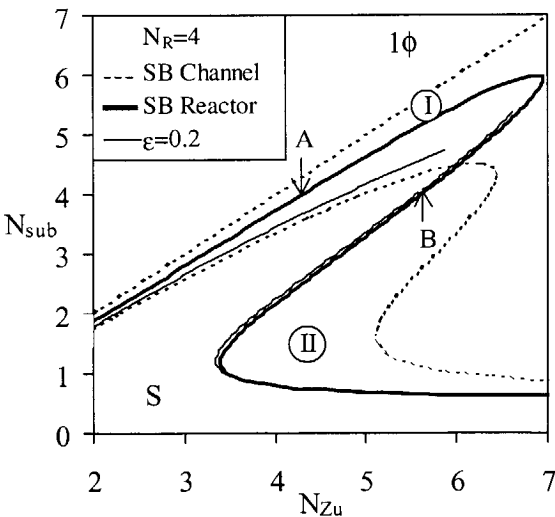


Figure 4-11. Bifurcation characteristics of a natural circulation reactor with riser ($r_a = -0.05$). The bifurcation curves in the Type-I instability region change significantly in a nuclear-coupled reactor system: The supercritical bifurcations in the Type-I instability region for a thermohydraulic system (see Fig. 4-6d) become subcritical in a reactor. For comparison, the SB for the channel is also shown.

feedback is included. Without the nuclear feedback, the bifurcation was always supercritical (see Fig. 4-6d). When neutronics feedback is included, bifurcation for $r_a = -0.05$ is found to be subcritical for the Type-I stability region, and a combination of subcritical (for large $N_{sub} > 0.8$) and supercritical (for low N_{sub}) bifurcation for Type-II instability regions. While the impact of neutronics feedback on the bifurcation in the Type-II instability regions is quite insignificant for small N_{sub} , for large values of N_{sub} the change from super- to subcritical for both the Type-I and the Type-II regions is quite important. Its impact on stability is most important in the

Type-I region where the $\varepsilon=0.2$ bifurcation curve is quite removed from its corresponding SB. This indicates that for systems operating in between the $\varepsilon=0.2$ bifurcation curve and the corresponding SB, a perturbation of 20% magnitude can “kick” the system to “outside” the unstable periodic solution, causing diverging oscillations. The small separation between the Type-II SB (for large N_{sub}) and the corresponding $\varepsilon=0.2$ bifurcation curve indicates that in this case the operating point in the stable region must be much closer to the SB (compared to the Type-I case) in order for a perturbation of 20% magnitude to cause a diverging oscillation.

Because of their importance, the dependence of the bifurcation mode on the strength of the nuclear feedback is investigated next. The impact on the bifurcation characteristics in the Type-I instability region is shown in Fig. 4-12a. The location of the SB depends on the value of the void reactivity coefficient, but is close to point A in Fig. 4-11 (N_{sub} is equal to 4.0).

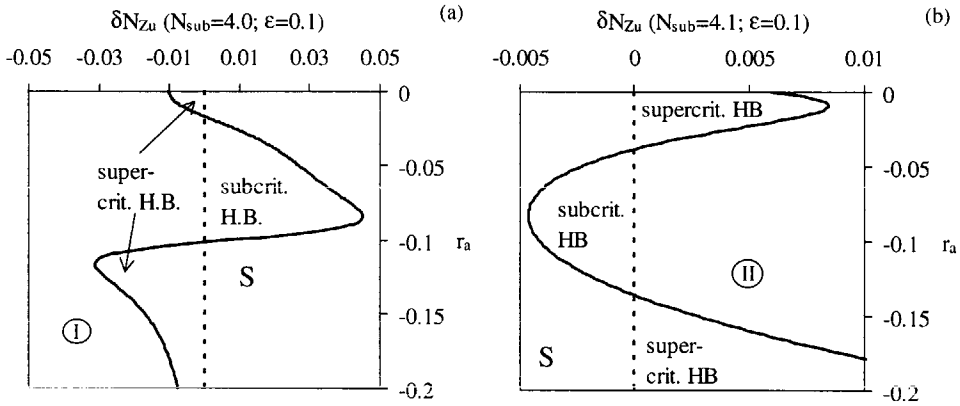


Figure 4-12. (a) Influence of the void reactivity coefficient r_a on the bifurcation characteristics in the Type-I instability region, close to point A in Fig. 4-11 ($N_{sub}=4.0$). Both supercritical and subcritical bifurcations can occur, depending on the value of the void reactivity coefficient. (b) Influence of the void coefficient on the bifurcation characteristics in the Type-II instability region, close to point B in Fig. 4-11 ($N_{sub}=4.1$).

Both sub- and supercritical Hopf bifurcations are possible in this case. As r_a is decreased from 0, the bifurcation is initially supercritical, it changes to subcritical for $-0.102 < r_a < -0.018$, and changes back to supercritical for $r_a < -0.102$.

Results of bifurcation analysis for the Type-II region, as a function of r_a , are shown in Fig. 4-12b. The parameter study in Fig. 4-12b is performed close to point B in Fig. 4-11 ($N_{sub}=4.1$). As remarked in Section 4.3.2, the bifurcation mode in the Type-II instability region for the thermohydraulic system becomes supercritical for higher values of the subcooling number, when the flow rate is enhanced by a riser section. The bifurcation curve in Fig 4-9d, for a system without riser, is hence also expected to change as the riser is added. This is shown in Fig. 4-12b.

4.5. CONCLUSIONS

A low-dimensional stability model of natural circulation BWRs is analyzed successfully. The complicated nonlinear dynamics is investigated with a Hopf-bifurcation code and with time-domain simulations. Good agreement between the results of the two approaches was found, especially in the immediate neighborhood of the stability boundary (where the local analysis of the bifurcation code is the most accurate).

The nonlinear stability of (high-power) Type-II oscillations was studied in an elementary natural circulation loop without a riser section, and without nuclear feedback. Both *supercritical* and *subcritical* Hopf bifurcations were encountered. The *unstable* subcritical oscillations become dominant for large values of the subcooling number and small values of the Froude number, whereas the *stable* supercritical oscillations occur at low values of the subcooling number. The elementary natural circulation loop was extended with a riser, to study the nonlinear Type-I oscillations induced by the gravitational pressure drop over this section. A parametric study demonstrated the importance of using multiple riser nodes in the model: The Hopf bifurcation mode changes dramatically for the Type-I instability from subcritical (one node in the riser) to supercritical (multiple nodes) as the number of axial nodes is increased.

Nuclear feedback has a profound impact on the stability of a natural circulation reactor. For the Type-II instability, parametric studies indicate that supercritical bifurcations become dominant for small values of the subcooling number and a strong nuclear-thermohydraulic coupling. A cascade of period-doubling pitchfork bifurcations, 'deep' in the unstable region, was also encountered under these conditions. The bifurcations for larger values of the subcooling number and small values of the Froude number, were of subcritical nature. Both subcritical and supercritical bifurcations are possible in the Type-I instability region for a natural circulation reactor with riser, again depending on the strength of the nuclear feedback.

Numerical simulations were also carried out to determine the range of validity of the bifurcation analyses away from the stability boundaries. Results for the channel case show that in certain regions of the parameter space, the bifurcation results are accurate for an oscillation amplitude as high as 70% of the nominal value.

The long standing concern over the impact of various design and operating parameters on the nature of bifurcation (subcritical vs. supercritical; stable periodic oscillations vs. growing amplitude oscillations) has been at least partly answered in this study. More work is needed using more elaborate models (such as the drift-flux model for the two-phase flow, and quadratic enthalpy and quadratic quality profiles in the single and two-phase regions), and using continuation codes that allow the continuation of periodic solution paths when asymptotic analyses such as those employed in the bifurcation code BifDD are not applicable.

REFERENCES

1. B.G. Bergdahl, F. Reisch, R. Oguma, J. Lorenzen, and F. Åkerhielm, "BWR Stability Investigation at Forsmark 1," *Ann. Nucl. Energy*, **16**, 509 (1989).
2. E. Pollmann, J. Schulze and D. Kreuter, "Stability Measurements in the German Nuclear Power Plant Wuergrassan During Cycle 14," *Nucl. Technol.*, **108**, 350 (1994).
3. T.H.J.J. van der Hagen, D.D.B. van Bragt, F.J. van der Kaa, D. Killian, W.H.M. Nissen, A.J.C. Stekelenburg, and J.A.A. Wouters, "Exploring the Dodewaard Type-I and Type-II Stability; From Start-Up to Shut-Down, From Stable to Unstable," *Ann. Nucl. Energy*, **24**, 659 (1997).
4. Y. Takigawa, Y. Takeuchi, S. Tsunoyama, S. Ebata, K.C. Chan, and C. Tricoli, "Caorso Limit Cycle Oscillation Analysis With Three-Dimensional Transient Code TOSDYN-2," *Nucl. Technol.*, **79**, 210 (1987).
5. F.D. Giust and L. Moberg, "RAMONA Stability Analysis on Ringhals-1, Phase 1: Model Qualification," TR1/42.83.06, ScandPower (1991).
6. G.M. Grandi and F.D. Giust, "RAMONA Stability Analysis on Ringhals-1, Phase 2: Predictive Calculations," TR2/42.83.06, ScandPower (1991).
7. F. Araya, M. Hirano, K. Yoshida, K. Matsumoto, M. Yokobayashi, and A. Kohsaka, "Summary of RETRAN Calculations on LaSalle 2 Neutron Flux Oscillation Event Performed at JAERI," *Proc. Int. Workshop BWR Stability*, OECD-NEA CSNI Report 178, p. 370 (1990).
8. J. C. Shaug, J.G.M. Andersen, and J.K. Garrett, "TRACG Analysis of BWR Plant Stability Data," *Proc. Int. Workshop BWR Stability*, OECD-NEA CSNI Report 178, p. 354 (1990).
9. S.J. Peng, M.Z. Podowski, R.T. Lahey, Jr., and M. Becker, "NUFREQ-NP: A Computer Code for the Stability Analysis of Boiling Water Nuclear Reactors," *Nucl. Sci. Eng.*, **88**, 404 (1984).
10. J. March-Leuba, "Dynamic Behavior of Boiling Water Reactors," PhD Thesis, University of Tennessee, Knoxville, Tennessee (1984).
11. J. March-Leuba, D.G. Cacuci, and R.B. Perez, "Nonlinear Dynamics and Stability of Boiling Water Reactors: Part I - Qualitative Analysis," *Nucl. Sci. Eng.*, **93**, 111 (1986).
12. J.L. Muñoz-Cobo and G. Verdú, "Application of Hopf Bifurcation Theory and Variational Methods to the Study of Limit Cycles in Boiling Water Reactors," *Ann. Nucl. Energy*, **18**, 269 (1991).
13. B.D. Hassard, N.D. Kazarinoff, and Y.-H. Wan, *Theory and Applications of Hopf Bifurcation*, London Mathematical Society Lecture Note Series 41, Cambridge University Press, Cambridge (1981).
14. M. Tsuji, K. Nishio, M. Narita, Y. Ogawa and M. Mori, "Stability Analysis of BWRs Using Bifurcation Theory," *J. Nucl. Sci. Technol.*, **30**, 1107 (1993).
15. A.A. Karve, Rizwan-uddin, and J.J. Dorning, "Stability Analysis of BWR Nuclear-Coupled Thermal-Hydraulics Using a Simple Model," *Proc. 7th Int. Mtg. Nuclear Reactor Thermal-Hydraulics (NURETH-7)*, Saratoga Springs, New York, September 10-15, 1995, Vol. 4, p. 2677, NUREG/CP-0142 (1995).
16. D.D.B. van Bragt and T.H.J.J. van der Hagen, "A Six-Dimensional Model for Coupled Neutronic-Thermohydraulic Out-of-Phase Oscillations in Boiling Water Reactors," *Proc. National Heat Transfer Conf.*, Houston, Texas, August 3-6, Vol. 9, p. 179, American Nuclear Society (1996).
17. D.D.B. van Bragt and T.H.J.J. van der Hagen, "Stability of Natural Circulation Boiling Water Reactors: Part I - Description Stability Model and Theoretical Analysis in Terms of Dimensionless Groups," *Nucl. Technol.*, **121**, 40 (1998); also published as Chapter 2 of this thesis.
18. D.D.B. van Bragt and T.H.J.J. van der Hagen, "Stability of Natural Circulation Boiling Water Reactors: Part II - Parametric Study of Coupled Neutronic-Thermohydraulic Stability," *Nucl. Technol.*, **121**, 52 (1998); also published as Chapter 3 of this thesis.

19. B.D. Hassard, "A Code for Hopf Bifurcation Analysis of Autonomous Delay-Differential Equations," *Proc. of Oscillation, Bifurcation and Chaos*, Canadian Mathematical Society, p. 441 (1987).
20. J. Hale and H. Koçak, *Dynamics and Bifurcations*, Springer-Verlag, New York (1991).
21. J. Hale, *Theory of Functional Differential Equations*, Appl. Math. Sci., Vol. 3, Springer-Verlag, Heidelberg, Berlin (1977).
22. A. Clause, D.F. Delmastro, and L.E. Juanicó, "A Simple Delay Model for Two-Phase Flow Dynamics," *Proc. 7th Int. Mtg. Nuclear Reactor Thermal-Hydraulics (NURETH-7)*, Saratoga Springs, New York, September 10-15, 1995, pp. 3232, NUREG/CP-0142 (1995).
23. D.D.B. van Bragt, "A Theoretical and Numerical Study of the Stability of a Natural Circulation Boiling Water Reactor," IRI-131-96-006, Interfaculty Reactor Institute, Delft University of Technology (1996).
24. D.D.B. van Bragt, "Hopf-Bifurcation Analysis of a Natural Circulation Boiling Water Reactor Model - Results for the Thermohydraulic Subsystem," IRI-131-97-010, Interfaculty Reactor Institute, Delft University of Technology (1997).
25. Y.N. Lin and C. Pan, "Non-Linear Analysis for a Natural Circulation Boiling Channel," *Nucl. Eng. Des.*, **152**, 349 (1994).
26. A. Clause and R.T. Lahey, Jr., "The Analysis of Periodic and Strange Attractors During Density-Wave Oscillations in Boiling Flows," *Chaos, Solitons & Fractals*, **1**, 167 (1991).
27. J. March-Leuba, D.G. Cacuci, and R.B. Perez, "Nonlinear Dynamics and Stability of Boiling Water Reactors: Part II-Quantitative Analysis," *Nucl. Sci. Eng.*, **93**, 124 (1986).
28. M.J. Feigenbaum, "The Transition to Aperiodic Behavior in Turbulent Systems," *Commun. Math. Phys.*, **77**, 65 (1980).

Chapter 5

Low-Pressure BWR Dynamics: I – Theoretical Model

Abstract – A dynamic model for natural circulation BWRs under low-pressure conditions is developed. The motivation for this theoretical research is the recent concern about the stability of natural circulation BWRs during the low-pressure reactor startup phase. There is experimental and theoretical evidence for the occurrence of void flashing in the unheated riser under these conditions. This flashing effect is included in the differential (homogeneous equilibrium) equations for two-phase flow. The differential equations were integrated over axial two-phase nodes, to derive a nodal time-domain model. The dynamic behavior of the interface between the one and two-phase regions is approximated with a linearized model. All model equations are presented in a dimensionless form.

5.1. INTRODUCTION

The stability of natural BWRs under startup conditions has been recognized in recent years as an important issue that needs to be considered in the design of new reactor types. The key issue under low pressure startup conditions is the phenomenon of void ‘flashing’ in the riser. The term ‘flashing’ refers to the occurrence of boiling in a natural circulation BWR, due to the decrease of hydrostatic pressure and saturation enthalpy along the flow path, when the coolant flows upwards through the core and riser sections. Because the saturation enthalpy is strongly dependent on the pressure at pressures lower

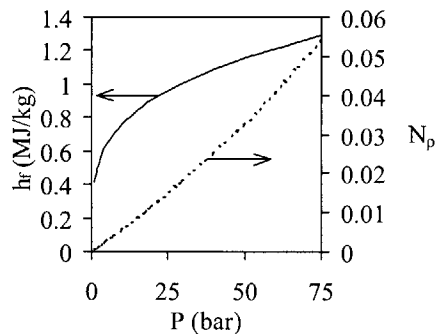


Figure 5-1. Influence of the pressure level on the saturated liquid enthalpy h_f and the vapor to liquid density ratio N_p .

than 20 bar, see Fig. 5-1, the influence of flashing becomes especially important under low-pressure conditions.

Dynamic instabilities can be induced by flashing under these circumstances, since the slope of the void fraction - flow quality curve in Fig. 1-4 is very steep under low power and pressure conditions, i.e. a small increase of the flow quality already induces a large increase of the riser void fraction. As a result, the driving force of the convection and the natural circulation flow increase. The flow quality in the core and the riser will consequently decrease, this way providing a thermohydraulic feedback mechanism that can cause self-sustained oscillations. Because void flashing in the riser directly affects the gravitational pressure drop over this section, it can be classified as a 'Type-I' density-wave stability phenomenon.¹

5.2. CURRENT RESEARCH ON FLASHING

The impact of void flashing on reactor stability is the incentive to recent studies of the stability of natural circulation BWRs under low-pressure startup conditions. A short summary of the main research activities in this new and quickly developing field is provided in this section.

The Central Research Institute of Electric Power Industry (CRIEPI) in Japan has constructed a low-pressure thermohydraulic test facility, which can be used to simulate the startup of the SBWR concept of GE. The design parameters for this facility were estimated by transforming the basic equations of the drift-flux flow model to a nondimensional basis.² Experimental stability maps as a function of the heat flux, subcooling and system pressure (ranging from atmospheric pressure to 5 bar) were presented by Furuya et al.³ Two stability boundaries were found in the heat flux-subcooling plane between which the natural circulation flow becomes unstable due to void flashing in the riser. Intermittent 'pulsed' oscillations with a long oscillation period were measured close to the high subcooling stability boundary. At a smaller subcooling sinusoidal oscillations with a shorter oscillation period were measured. These oscillations stabilize when the subcooling decreases further. Furuya et al. moreover measured an increase of the range of the unstable region (in the heat flux-subcooling plane) when the heat flux is increased. An increase of the pressure has just the opposite, stabilizing, effect on flashing induced stability. A comparison with typical SBWR operating points (calculated with the detailed BWR stability code TRACG) demonstrated² that these operating points were on the stable (highly subcooled) side of the unstable region. A TRACG model of the CRIEPI facility was developed by Andersen and Klebanov.⁴ Good agreement with the CRIEPI measurements was shown, thereby qualifying TRACG as a suitable code for the startup of a natural circulation BWR.

The Chinese Institute of Nuclear Energy and Technology (INET) has developed a 5 MW

nuclear test reactor for district heating, which is in operation since 1989.⁵ This natural circulation reactor operates at a low pressure (15 bar), low steam quality (less than 1% at the core exit), and is cooled by natural circulation. A test loop (HRTL-5), simulating the design and geometry of this reactor, was built at INET to simulate the thermohydraulic stability of the nuclear test reactor. It was observed that subcooled boiling and void flashing have a significant influence on two-phase flow stability, especially at low system pressures.^{6,7} Several kinds of flow instabilities were observed as a function of the inlet subcooling. The HRTL-5 test loop was analyzed numerically with a one-dimensional two-phase flow drift-flux model with four governing equations.⁸ The measured and calculated stability maps in the heat flux-subcooling plane showed a good quantitative agreement.

The first in-core measurements of the startup stability of a natural circulation BWR were performed in the Dutch Dodewaard BWR. A team of specialists from several Dutch institutes has performed measurements during the startup phase of this reactor at the beginning of cycles 23-26.⁹ The Dodewaard startup of cycle 23 was successfully simulated with the TRACG code by Wouters et al.¹⁰ However, during this particular measurement session only minor oscillations were measured (and predicted by TRACG). The first significant decrease of stability was observed during the startup of cycle 25, but these experimental data have not yet been analyzed quantitatively with a BWR stability code that includes a flashing model.

Therefore, the previously developed stability model for natural circulation BWRs, see Chapter 2,^{11,12} is extended in Section 5.3 of this chapter with a description of the flashing effect. This extended model can be used as a powerful analytical tool to gain more physical insight into the complicated flashing phenomenon. A parametric study of low-pressure BWR stability is presented in Chapter 6. A validation of the model on the basis of startup stability data from the Dodewaard BWR is presented in Chapter 7.

5.3. MODEL

Our theoretical flashing model is developed using the one-dimensional homogeneous equilibrium mixture (HEM) equations for two-phase flow. We also employed these equations in Chapter 2. The decrease of the liquid saturation enthalpy along the flow path in the core and riser was, however, neglected in that chapter. Inada and Ohkawa¹³ included flashing effects in the HEM model for two-phase flow by assuming that the liquid saturation enthalpy is proportional to the local pressure. All other fluid properties were assumed to be independent of the pressure. The nondimensional differential equations which Inada and Ohkawa used, based on these assumptions, are the starting point of our flashing model. Precise definitions of all pressure-dependent dimensionless numbers and variables, like the Zuber number and the subcooling number, are provided in Appendix C. The axial power profile is assumed to be flat, to simplify the analysis.

The dimensionless continuity equation for the two-phase region is:¹³

$$\frac{\partial}{\partial t^*} [1 - \alpha(z^*, t^*) + N_p \alpha(z^*, t^*)] + \frac{\partial M^*(z^*, t^*)}{\partial z^*} = 0. \quad (5-1)$$

The dimensionless energy equation for homogeneous two-phase flow can be written as:

$$\begin{aligned} & \frac{\partial}{\partial t^*} \left\{ (1 - N_p) \alpha(z^*, t^*) - N_{\text{flash}} h_f^*(z^*, t^*) [1 - \alpha(z^*, t^*)] \right\} + \\ & \frac{\partial}{\partial z^*} \left\{ \frac{1 - N_p}{N_p} \chi(z^*, t^*) M^*(z^*, t^*) - N_{\text{flash}} h_f^*(z^*, t^*) [1 - \chi(z^*, t^*)] M^*(z^*, t^*) \right\} = N_{\text{Zuq}}^*(t^*). \end{aligned} \quad (5-2)$$

The void production due to flashing is incorporated in the dimensionless flashing number N_{flash} . This number is equal to the difference between the dimensionless subcooling of the fluid at the *core inlet* and the *riser exit*, see Eq. (C-1) in Appendix C. When flashing is neglected, i.e. when the saturated liquid enthalpy is constant over the assembly height, these two dimensionless numbers are equal and the flashing number becomes equal to zero. The differential momentum equation for the boiling region becomes:

$$\begin{aligned} & \frac{\partial M^*(z^*, t^*)}{\partial t^*} + \frac{\partial}{\partial z^*} \left\{ [1 + (1/N_p - 1) \chi(z^*, t^*)] M^{*2}(z^*, t^*) \right\} \\ & + \frac{1}{N_{\text{Fr}}} [1 - \alpha(z^*, t^*) + N_p \alpha(z^*, t^*)] + \Lambda [1 + (1/N_p - 1) \chi(z^*, t^*)] M^{*2}(z^*, t^*) \\ & + \frac{\partial}{\partial z^*} \sum_j \left\{ \frac{1}{2} k_j [1 + (1/N_p - 1) \chi(z^*, t^*)] M^{*2}(z^*, t^*) \delta(z^* - z_j^*) \right\} = \frac{-\partial P^*(z^*, t^*)}{\partial z^*}. \end{aligned} \quad (5-3)$$

The left hand side of Eq. (5-3) consists respectively of the differential inertial, accelerational, gravitational, frictional and local pressure losses. The differential momentum equation (5-3) is identical to the equation previously used in the model without flashing. The pressure drop terms summarized in Table 2-1 are therefore equally valid in this flashing model.^{a)}

The following axial nodalization scheme is used in this low-pressure model. If the coolant reaches the boiling point before the core exit, the two-phase region in the core is treated as a single node with a dimensionless length $1 - Z_{\text{bb,c}}^*(t^*)$. The riser section is divided in N_R axial nodes of equal length L_R^*/N_R if $Z_{\text{bb,c}}^*(t^*) \leq 1$. Neglecting the flashing effect, this condition is always satisfied, and the same nodalization scheme as used in the model without flashing is applied. If $Z_{\text{bb,c}}^*(t^*) > 1$, only out-of-core boiling occurs. The nodalization scheme shown in

^{a)}The (small) accelerational and frictional pressure drops over the downcomer are added to the pressure losses at the core inlet, to simplify the analysis. Therefore a factor $\frac{1}{2} k_{D,i}^*/A_{D,i}^{*2} + \frac{1}{2} (1/A_{D,e}^{*2} - 1/A_{D,i}^{*2})$ is added to the core inlet friction coefficient $k_{C,i}$.

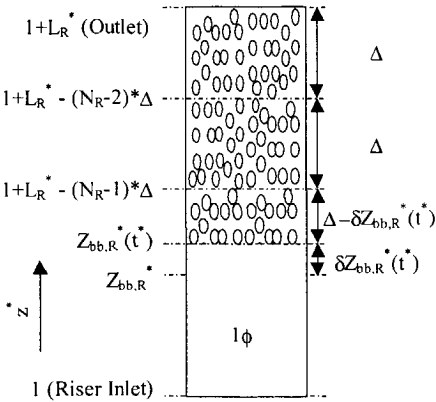


Figure 5-2. Nodalization scheme for the riser section, if out-of-core boiling occurs. A three-node scheme ($N_R=3$) is shown. The height Δ of the upper two nodes is fixed and equal to $(1 + L_R^* - Z_{bb,R}^*)/N_R$. Notice that the height of the lowest riser node changes as the boiling boundary fluctuates.

other riser nodes in Fig. 5-2 have a fixed height Δ . The advantage of this nodalization scheme becomes clear when we integrate Eq. (5-1) over an arbitrary boiling node with a dimensionless length $L_n^*(t^*)$:

$$\frac{d\langle\alpha(t^*)\rangle_n}{dt^*} = \frac{M_n^*(t^*) - M_{n-1}^*(t^*)}{L_n^*(t^*)(1-N_p)} - \frac{\langle\alpha(t^*)\rangle_n}{L_n^*(t^*)} \frac{dL_n^*(t^*)}{dt^*}. \quad (5-5)$$

The quantities with a subscript $n-1$ are evaluated at the node 'inlet', while a subscript n denotes the node 'outlet'. Because their node heights are fixed, the second term on the right hand side of Eq. (5-5) is zero for all riser nodes except the first one, assuming that $Z_{bb}^*(t^*) > 1$. If $Z_{bb}^*(t^*) < 1$, all riser nodes have a fixed height, and this time-derivative term becomes zero for all riser nodes.

Integrating the differential energy equation (5-2) over a two-phase node, and simplifying the result by substituting Eq. (5-5) leads to:

Fig. 5-2 is adopted in this case.

As an example, a three-node scheme is considered here. Applying another number of nodes is straightforward. The height of the first riser node in Fig. 5-2 is dependent on the transient position of the boiling boundary:

$$L_{R,1}^*(t^*) = \Delta - [Z_{bb,R}^*(t^*) - Z_{bb,R}^*], \quad (5-4)$$

with $\Delta = \frac{1 + L_R^* - Z_{bb,R}^*}{N_R}$.

A large increase of the boiling boundary position causes a significant reduction of the height of this node. It is important, therefore, to check whether $L_{R,1}^*(t^*)$ remains positive at all times during the transient calculations.^{b)} All

^{b)}If this restriction causes problems, an alternative nodalization scheme, for instance using N_R time-dependent riser nodes with equal length $[1 + L_R^* - Z_{bb,R}^*(t^*)]/N_R$, might be used.

$$M_n^*(t^*) = \frac{\left\{ 1 + \frac{N_{flash}}{1-N_p} [\langle h_f^*(t^*) \rangle_n - (1-N_p)h_{f_{n-1}}^*(t^*)] + \left[\frac{1-N_p}{N_p} + N_{flash} h_{f_{n-1}}^*(t^*) \right] \chi_{n-1}(t^*) \right\} M_{n-1}^*(t^*) + \Gamma_n^*(t^*)}{1 + \frac{N_{flash}}{1-N_p} [\langle h_f^*(t^*) \rangle_n - (1-N_p)h_{f_n}^*(t^*)] + \left[\frac{1-N_p}{N_p} + N_{flash} h_{f_n}^*(t^*) \right] \chi_n(t^*)}$$

with $\Gamma_n^*(t^*) = q^*/(t^*)L_n^*(t^*)N_{Zu} + N_{flash}L_n^*(t^*)[1 - \langle \alpha(t^*) \rangle_n] \frac{d\langle h_f^*(t^*) \rangle_n}{dt^*} + N_{flash} \langle h_f^*(t^*) \rangle_n \frac{dL_n^*(t^*)}{dt^*}$. (5-6)

The saturation enthalpy $h_f^*(t^*)$ in Eq. (5-6), defined in Eq. (C-1), is assumed to be linearly dependent on the local pressure.¹³

$$h_f^*(t^*) = \frac{P^*(t^*) - P_{C,i}^*(t^*)}{P_{R,e}^*(t^*) - P_{C,i}^*(t^*)} \tag{5-7}$$

This approximation is used because the pressure difference between the core inlet and the riser exit is smaller than 0.5 bar. A linear approximation of the saturation-enthalpy function over such a small pressure range is quite accurate, even in the low-pressure regime, see Fig. 5-3.

The influence of the inertial pressure losses on the saturation enthalpy is neglected in this model. The pressure difference $P_{R,e}^*(t^*) - P_{C,i}^*(t^*)$ between the riser exit and core inlet is then equal to the gravitational pressure drop over the downcomer, when the minor frictional, local and accelerational pressure losses over the downcomer are also neglected. Assuming that the down-coming fluid is subcooled, as has been done in the model without flashing, see Chapter 2, this pressure difference becomes:

$$P_{R,e}^*(t^*) - P_{C,i}^*(t^*) = -\frac{1 + L_R^*}{N_{Fr}} \tag{5-8}$$

As a boundary condition, the pressure at the riser exit is assumed to be kept constant by the reactor pressure controller, so using Eq. (5-8) $P_{C,i}^*(t^*)$ can be calculated.

The local pressure at the boiling boundary (the ‘inlet’ of the first boiling node) is then determined by integrating Eq. (5-3) over the one-phase regions in the core and the riser. Since the pressure drop over each two-phase node is a function of two-phase variables as the flow quality, the saturation enthalpy at the node ‘exit’ becomes a function of these variables, whereas according to Eq. (5-6) these variables

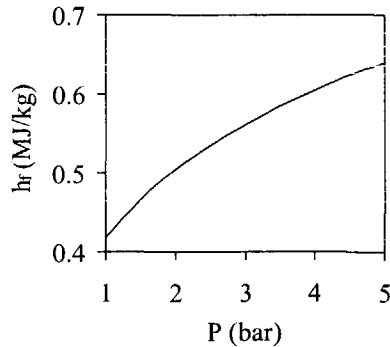


Figure 5-3. The saturated liquid enthalpy h_f as a function of the pressure level, for pressures below 5 bar (cf. Fig. 5-1). A linear approximation of the h_f -function (over a pressure range of ~0.4 bar) is used in the model.

are in their turn dependent on the saturation enthalpy. This leads to recursive equations, which are rather cumbersome in the numerical analysis. Therefore, it is assumed that the saturation enthalpy is a linear function of the axial position between the boiling boundary and the riser exit.

The local quality in Eq. (5-6) is assumed to increase or decrease linearly between the node inlet and outlet (this approximation has been applied as well in the model without flashing). The nodal void fraction then becomes:

$$\langle \alpha(t^*) \rangle_n = \frac{1}{1 - N_p} \left\{ 1 - \frac{1}{(1/N_p - 1)[\chi_n(t^*) - \chi_{n-1}(t^*)]} \times \ln \left[\frac{(1/N_p - 1)[\chi_n(t^*) - \chi_{n-1}(t^*)]}{1 + (1/N_p - 1)\chi_{n-1}(t^*)} + 1 \right] \right\}. \quad (5-9)$$

A Taylor approximation of the logarithmic term in Eq. (5-9) is recommended to avoid a singularity in the steady state.^{11,12}

Finally, the complexity of Eq. (5-6) is reduced further by neglecting the term containing the time derivative of the nodal saturation enthalpy $h_f^*(t^*)$. The magnitude of this term is proportional to the flashing number, and its importance therefore increases at lower pressures. The impact of this neglect is investigated numerically in Chapter 6.

The dimensionless length of the lowest two-phase node is determined by the instantaneous position of the boiling boundary. An evaluation of the one-phase region is therefore necessary, to determine the dynamic behavior of this quantity. In fact, we can employ Eqs. (5-1)-(5-3) for the one-phase region as well, if we set the void fraction and flow quality equal to zero in these equations. Equation (5-1) then shows that $M^*(Z_{bb,c}^*, t^*) = M_{c,i}^*(t^*)$, if $Z_{bb}^* < 1$. Due to conservation of mass at the junction of the core and the riser we also find that $M^*(Z_{bb,r}^*, t^*) = M_{c,i}^*(t^*)/A_R$ if $Z_{bb}^* > 1$. Applying Eq. (5-2), the differential energy equation for the one-phase region becomes:

$$\frac{\partial h_1^*(z^*, t^*)}{\partial t^*} + M^*(z^*, t^*) \frac{\partial h_1^*(z^*, t^*)}{\partial z^*} = - \frac{N_{zu}}{N_{flash}} q^*/(t^*). \quad (5-10)$$

Equation (5-10) is used to determine whether the equilibrium position of the boiling boundary is located in the core or in the riser section. *Assuming* that the saturation temperature is reached in the *core* section ($Z_{bb}^* < 1$), and neglecting the time-dependent term in Eq. (5-10), we integrate this equation from the core inlet to the boiling boundary:

$$h_1^*(Z_{bb}^*) = h_{c,i}^* - \frac{N_{zu}}{N_{flash}} Z_{bb}^*. \quad (5-11)$$

Integrating Eq. (5-3) over the one-phase region in the core, and substituting the pressure differential between the core inlet and the boiling boundary in Eq. (5-7), then yields the saturation enthalpy at the boiling boundary:

$$h_f^*(Z_{bb}^*) = \frac{N_{Fr}}{1+L_R^*} [P_{C,i}^* - P^*(Z_{bb}^*)] = \frac{N_{Fr}}{1+L_R^*} \left(\frac{k_{C,i}}{2} + Z_{bb}^* \Lambda_C + \frac{Z_{bb}^*}{N_{Fr}} \right). \quad (5-12)$$

If the boiling boundary is indeed located in the core section (as has been assumed!), the fluid reaches the saturation enthalpy before the core outlet:

$$h_l^*[Z_{bb}^*(t^*)] = h_f^*[Z_{bb}^*(t^*)]. \quad (5-13)$$

Substituting Eqs. (5-11) and (5-12) in Eq. (5-13) then implies that:

$$0 \leq \frac{N_{subC,i} - \frac{k_{C,i}}{2} \frac{N_{Fr}}{1+L_R^*} N_{flash}}{N_{Zu} + \left(\Lambda_C + \frac{1}{N_{Fr}} \right) \frac{N_{Fr}}{1+L_R^*} N_{flash}} \leq 1, \quad (5-14)$$

when the coolant starts to boil in the core. We now introduce the parameter b_R , which is equal to zero when Eq. (5-14) is satisfied, and equal to one if the condition in Eq. (5-14) is violated. The equilibrium position of the boiling boundary is thus located in the core section if $b_R=0$, while $b_R=1$ if only boiling in the riser occurs. We assume here that two-phase flow is present in at least part of the system. The occurrence of single-phase convection, when $h_{l,r,c} < h_{f,r,c}$, can be predicted with a simple criterion, which will be derived below.

With the new parameter b_R , Eqs. (5-11) and (5-12) can be generalized for an arbitrary position of the boiling boundary:

$$h_l^*(Z_{bb}^*) = h_{l,c,i}^* - \frac{N_{Zu}}{N_{flash}} \left[b_R + Z_{bb}^* (1 - b_R) \right], \quad (5-15)$$

$$\text{and } h_f^*(Z_{bb}^*) = \frac{N_{Fr}}{1+L_R^*} \left\{ \frac{k_{C,i}}{2} + b_R \frac{k_{C,e}}{2} + \Lambda_C \left[b_R + (1 - b_R) Z_{bb}^* \right] + b_R \left(\frac{Z_{bb}^* - 1}{L_R^* A_R^{*2}} + \frac{Z_{bb}^*}{N_{Fr}} \right) \right\}.$$

Equating the liquid enthalpy with the saturation enthalpy in Eq. (5-15), and solving for the boiling boundary position, we arrive at:

$$Z_{bb}^* = \frac{N_{subC,i} - b_R N_{Zu} - \frac{N_{Fr}}{1+L_R^*} N_{flash} \left[\frac{k_{C,i}}{2} + b_R \left(\frac{k_{C,e}}{2} + \Lambda_C - \frac{\Lambda_R}{L_R^* A_R^{*2}} \right) \right]}{(1 - b_R) N_{Zu} + \frac{N_{Fr}}{1+L_R^*} N_{flash} \left[\Lambda_C (1 - b_R) + b_R \frac{\Lambda_R}{L_R^* A_R^{*2}} + \frac{1}{N_{Fr}} \right]}. \quad (5-16)$$

Note that even when $b_R=1$, the outcome of Eq. (5-16) can be smaller than unity! This apparent paradox occurs when the coolant temperature is slightly below the saturation temperature just before the core outlet, and starts to boil at the core exit, due to local core outlet pressure

losses. The boiling boundary position Z_{bb}^* is equal to unity in this particular case.

The boundary between the one- and two-phase regions in the operational N_{Zu} - N_{sub} space can be determined easily using Eq. (5-16). At the onset of boiling, the boiling boundary position will be located at the very end of the riser. Furthermore, the coolant flow rate (and therefore the Froude number) will diminish if the length of the two-phase region decreases. Setting $Z_{bb}^* = 1 + L_R^*$ and letting N_{Fr} approach zero in Eq. (5-16), we find that the boundary between the one- and two-phase regions is located at $N_{Zu} = N_{sub,c,i} - N_{flash}$. Two-phase flow will thus exist if $N_{Zu} > N_{sub,c,i} - N_{flash}$. This criterion suggests that two-phase flow can exist if the power level, and therefore the Zuber number, is equal to zero, provided that $N_{sub,c,i} < N_{flash}$. This apparent paradox is avoided, however, because the latter condition is never satisfied. Assume, for instance, that the coolant enthalpy at the *core inlet* is equal to the saturated liquid enthalpy at the *riser exit*. The core-inlet subcooling is then equal to $(h_{f,c,i} - h_{f,r,e})(\rho_{f,c,i} - \rho_{g,c,i}) / (h_{fg,c,i} \rho_{g,c,i}) = N_{flash}$. Taking the effect of the added feedwater into account, it is clear that $N_{sub,c,i} \geq N_{flash}$. The influence of the system pressure and the feedwater flow on the core inlet subcooling is taken into account in the parametric study in Chapter 6.

The dynamic behavior of the boiling boundary is approximated with a linearized model. Perturbing and Laplace transforming Eq. (5-10) yields:

$$s^* \delta h_1^*(z^*, s^*) + M^*(z^*, s^*) \frac{\partial \delta h_1^*(z^*, s^*)}{\partial z^*} = \frac{N_{Zu}}{N_{flash}} [\delta M^*(z^*, s^*) - \delta q^*(z^*, s^*)]. \quad (5-17)$$

Integrating Eq. (5-17) from $z^* = 0$ to Z_{bb}^* , and assuming that $\delta h_1^*(z^* = 0, s^*) = 0$, results in:

$$\delta h_1^*(Z_{bb}^*, s^*) = \frac{N_{Zu}}{N_{flash}} \frac{1 - \exp(-s^* \tau_{1\phi,C}^*)}{s^*} \exp(-s^* \tau_{1\phi,R}^*) [\delta M_{c,i}^*(s^*) - \delta q^*(s^*)]. \quad (5-18)$$

The dimensionless transit time $\tau_{1\phi}^*$ of the one-phase fluid, introduced in Eq. (5-18), is equal to:

$$\tau_{1\phi,C}^* = Z_{bb,C}^*, \text{ and } \tau_{1\phi,R}^* = (Z_{bb,R}^* - 1) A_R^*. \quad (5-19)$$

Perturbing the pressure difference between the core inlet and the boiling boundary, and applying Eq. (5-7) leads to:

$$\delta h_f^*(Z_{bb}^*, s^*) = \frac{\partial \delta h_f^*(Z_{bb}^*, s^*)}{\partial \delta Z_{bb}^*(s^*)} \delta Z_{bb}^*(s^*) + \frac{\partial \delta h_f^*(Z_{bb}^*, s^*)}{\partial \delta M_{C,i}^*(s^*)} \delta M_{C,i}^*(s^*),$$

$$\text{with } \frac{\partial \delta h_f^*(Z_{bb}^*, s^*)}{\partial \delta Z_{bb}^*(s^*)} = \frac{N_{Fr}}{1 + L_R^*} \left[(1 - b_R) \Lambda_C + \frac{1}{N_{Fr}} + b_R \frac{\Lambda_R}{A_R^* L_R^*} \right], \quad (5-20)$$

$$\text{and } \frac{\partial \delta h_f^*(Z_{bb}^*, s^*)}{\partial \delta M_{C,i}^*(s^*)} = 2 \frac{N_{Fr}}{1 + L_R^*} \left\{ \Lambda_C \left[(1 - b_R) Z_{bb}^* + b_R \right] + \frac{k_{C,i}}{2} + b_R \frac{k_{C,e}}{2} + b_R \frac{(Z_{bb}^* - 1) \Lambda_R}{L_R^* A_R^*} \right\}.$$

Perturbing Eq. (5-13) relates the fluctuations of the liquid and saturation enthalpy at the boiling boundary:

$$\frac{\partial h_l^*(Z_{bb}^*, 0)}{\partial Z_{bb}^*} \delta Z_{bb}^*(s^*) + \delta h_l^*(Z_{bb}^*, s^*) = \delta h_f^*(Z_{bb}^*, s^*), \quad (5-21)$$

$$\text{where } \frac{\partial h_l^*(Z_{bb}^*, 0)}{\partial Z_{bb}^*} = -(1 - b_R) \frac{N_{Zu}}{N_{flash}},$$

according to Eq. (5-10). Substituting Eqs. (5-18) and (5-20) in Eq. (5-21), and solving for the boiling boundary perturbation, leads to:

$$\delta Z_{bb}^*(s^*) = \frac{N_{Zu} \frac{1 - \exp(-s^* \tau_{1\phi,C}^*)}{s^*} \exp(-s^* \tau_{1\phi,R}^*) \left[\delta M_{C,i}^*(s^*) - \delta q^*(s^*) \right] - N_{flash} \frac{\partial \delta h_f^*(Z_{bb}^*, s^*)}{\partial \delta M_{C,i}^*(s^*)} \delta M_{C,i}^*(s^*)}{(1 - b_R) N_{Zu} + N_{flash} \frac{\partial \delta h_f^*(Z_{bb}^*, s^*)}{\partial \delta Z_{bb}^*(s^*)}} \quad (5-22)$$

A first-order Padé approximation¹⁴ for the exponential function is useful, to reduce the order of Eq. (5-22):

$$\exp(-s^* \tau^*) \approx \frac{1 - \frac{1}{2} \tau^* s^*}{1 + \frac{1}{2} \tau^* s^*}. \quad (5-23)$$

The exponential terms in Eq. (5-22) are now rewritten, applying Eq. (5-23):

$$\frac{1 - \exp(-s^* \tau_{1\phi,C}^*)}{s^*} \exp(-s^* \tau_{1\phi,R}^*) \approx \frac{\tau_{1\phi,C}^* - \frac{1}{2} \tau_{1\phi,C}^* \tau_{1\phi,R}^* s^*}{1 + \frac{1}{2} (\tau_{1\phi,C}^* + \tau_{1\phi,R}^*) s^* + \frac{1}{4} \tau_{1\phi,C}^* \tau_{1\phi,R}^* s^{*2}} \quad (5-24)$$

Equation (5-24), in combination with Eq. (5-22), shows that the boiling boundary transfer function is a first-order system, when boiling occurs in the core ($\tau_{1\phi,R}^* = 0$ in this case). The same first-order transfer function that was used in the model without flashing¹⁵ is derived when we set N_{flash} equal to zero in Eq. (5-22) and apply Eq. (5-23):

$$\frac{\delta Z_{bb}^*(s^*)}{\delta M_{C,i}^*(s^*)} = -\frac{\delta Z_{bb}^*(s^*)}{\delta q'^*(s^*)} = \frac{\tau_{1\phi,C}^*}{1 + \frac{1}{2}\tau_{1\phi,C}^*s^*} \tag{5-25}$$

The boiling boundary transfer function becomes of order two, when the coolant is subcooled in the entire core region and starts boiling in the riser. Substituting Eq. (5-24) into Eq. (5-22) and transforming back to the time domain results in a second-order ordinary differential equation for the boiling boundary position:

$$C_{Z,2} \frac{d^2 Z_{bb}^*(t^*)}{dt^{*2}} + C_{Z,1} \frac{dZ_{bb}^*(t^*)}{dt^*} + C_{Z,0} (Z_{bb}^*(t^*) - Z_{bb}^*) = C_{M,2} \frac{d^2 M_{C,i}^*(t^*)}{dt^{*2}} + C_{M,1} \frac{dM_{C,i}^*(t^*)}{dt^*} + C_{M,0} (M_{C,i}^*(t^*) - 1) + C_{Q,1} \frac{dq'^*(t^*)}{dt^*} + C_{Q,0} (q'^*(t^*) - 1). \tag{5-26}$$

The coefficients of this equation are provided in Appendix D.

5.4. CONCLUSIONS

The developed theoretical model for flashing-induced oscillations in natural circulation BWRs can be summarized at this point. The two-phase flow dynamics is governed by Eqs. (5-5) and (5-6), stating the conservation of mass and energy in the two-phase nodes. Conservation of momentum in a natural circulation system implies that the total pressure drop over the core, the riser, and the downcomer sections is equal to zero. The nodal pressure drops over the different sections are listed in Table 2-1.

A time-domain expression for the (linearized) boiling boundary dynamics is provided by Eq. (5-26). Note that this equation contains a term proportional to the *second-order* derivative of the core inlet mass flux density. The governing equation for this quantity is however only a *first-order* differential equation [the momentum equation (5-3), integrated along the entire natural circulation flow path]. The term $C_{M,2}$ in Eq. (5-26) is therefore neglected in the model calculations. The effect of this assumption on the boiling boundary dynamics is evaluated in the parametric study in Chapter 6.

The models for neutron kinetics and fuel dynamics that have been used previously in the natural circulation BWR model without flashing, see Chapter 2, can be coupled directly with this thermohydraulic model. However, nuclear feedback effects are important only when the

coolant reaches the boiling point before the core outlet, and can be neglected if ex-core boiling occurs due to flashing in the riser.

REFERENCES

1. K. Fukuda and T. Kobori, "Classification of Two-Phase Flow Instability by Density Wave Oscillation Model," *J. Nucl. Sci. Technol.*, **16**, 95 (1979).
2. F. Inada, M. Furuya, A. Yasuo, H. Tabata, Y. Yoshioka, and H.T. Kim, "Thermo-Hydraulic Instability of Natural Circulation BWRs at Low Pressure Start-Up: Experimental Estimation of Instability Region with Test Facility Considering Scaling Law," *Proc. 3rd Int. Conf. Nuclear Engineering (ICONE-3)*, Kyoto, Japan, April 23-27, 1995, Vol. 1, p. 173 (1995).
3. M. Furuya, F. Inada, and A. Yasuo, "Density Wave Oscillations of a Boiling Natural Circulation Loop Induced by Flashing," *Proc. 7th Int. Mtg. Nuclear Reactor Thermal-Hydraulics (NURETH-7)*, Saratoga Springs, New York, September 10-15, 1995, NUREG/CP-0142, p. 923, U.S. Nuclear Regulatory Commission (1995).
4. J.G.M. Andersen and L.A. Klebanov, "TRACG Analyses of Flashing Instability During Start-Up," *Proc. 3rd Int. Conf. Nuclear Engineering (ICONE-3)*, Kyoto, Japan, April 23-27, 1995 (1995).
5. D.Z. Wang, C.W. Ma, D. Dong, and J.G. Ling, "A 5-MW Nuclear Heating Reactor," *Trans. Am. Nucl. Soc.*, **61**, 468 (1990).
6. S.Y. Jiang and D. Emendörfer, "Subcooled Boiling and Void Flashing in a Natural Circulation System at Heating Reactor Conditions," *Kerntechnik*, **58**, 273 (1993).
7. S.Y. Jiang, X.X. Wu, S.R. Wu, J.H. Bo, Y.J. Zhang, and P. Han, "Experimental Study on Flashing Concerned Instability in a Natural Circulation System at Nuclear Heating Conditions," *Kerntechnik*, **62**, 148 (1997).
8. S.Y. Jiang and D. Emendörfer, "Analysis of Flow Oscillations in a Natural Circulation System Taking Account of Non-Equilibrium Boiling and Void Flashing," *Kerntechnik*, **61**, 23 (1996).
9. T.H.J.J. van der Hagen, A.J.C. Stekelenburg, S. Kaart, and J.C. Schouten, "Investigations on Start-Up Flow Oscillations in Natural Circulation BWRs," *Proc. National Heat Transfer Conf.*, Houston, Texas, August 3-6, 1996, Vol. 9, p. 188, American Nuclear Society (1996).
10. J.A.A. Wouters, J.B. Morales, and H.T. Kim, "TRACG Simulation of the February 1992 Startup of the Dodewaard Natural Circulation BWR," *Proc. 4th Int. Conf. Nuclear Engineering (ICONE-4)*, New Orleans, Louisiana, March 10-14, 1996, Vol. 3, p. 149, American Nuclear Society (1996).
11. D.D.B. van Bragt, "A Theoretical and Numerical Study of the Stability of a Natural Circulation Boiling Water Reactor," IRI-131-96-006, Interfaculty Reactor Institute, Delft University of Technology (1996).
12. D.D.B. van Bragt and T.H.J.J. van der Hagen, "Stability of Natural Circulation Boiling Water Reactors. Part I - Description Stability Model and Theoretical Analysis in Terms of Dimensionless Groups," *Nucl. Technol.*, **121**, 40 (1998); also published as Chapter 2 of this thesis.
13. F. Inada and T. Ohkawa, "Thermo-Hydraulic Instability of Natural Circulation BWRs (Explanation on Instability Mechanisms at Start-Up by Homogeneous and Thermo-Dynamic Equilibrium Model Considering Flashing Effect)," *Proc. Int. Conference on New Trends in Nuclear System Thermohydraulics*, May 30 - June 2, 1994, Pisa, Italy, p. 187 (1994).
14. C. Brezinski, "Extrapolation Algorithms and Padé Approximations: A Historical Survey," *Appl. Numer. Math.*, **20**, 299 (1996).
15. D.D.B. van Bragt, "A Theoretical Model for Coupled Neutronic-Thermohydraulic Out-of-Phase

Oscillations in Boiling Water Reactors," IRI-131-95-015, Interfaculty Reactor Institute, Delft University of Technology (1995).

Chapter 6

Low-Pressure BWR Dynamics: II – Parametric Study

Abstract – The statics and dynamics of natural circulation BWRs are investigated in a parametric study. We focus on the behavior under low power and pressure (reactor startup) conditions. Ex-core boiling, due to void flashing in the unheated riser, is demonstrated to be dominant during the reactor startup phase. This implies that nuclear feedback effects are of minor importance under these conditions. Stability is investigated in the dimensionless Zuber-subcooling plane. The Type-I instability region in this plane expands strongly if the reactor pressure is reduced, due to the occurrence of unstable void flashing in the riser. Typical trajectories in the stability plane are calculated as a function of changing operating conditions, to determine their influence on reactor stability. Stable reactor operation is not guaranteed during the startup phase, because under low power and pressure conditions the (safe) margin to the Type-I instability region is small. This confirms the recent concern about the stability of natural circulation BWRs in the low power and pressure domain.

6.1. INTRODUCTION

The statics and dynamics of natural circulation BWRs are explored in a parametric study in this chapter. We focus on the behavior of natural circulation BWRs under *low-pressure* conditions, using the theoretical model that has been developed in Chapter 5. The prototype of natural circulation BWRs, the Dodewaard reactor, is analyzed in this chapter. We use data set II from Chapter 3 as the model input data for the calculations.¹

The elementary axial nodalization scheme that was used in Chapter 3 is applied again in this chapter, i.e. only one two-phase node in the riser section is used in the calculations (i.e. $N_R=1$). The boiling region in the heated core section is also treated as a single node ($N_C=1$). We restrict the present analysis to small-amplitude perturbations. Large-amplitude oscillations have been studied in Chapter 4, employing the BWR model without the flashing effect.² We demonstrated there that the usage of multiple nodes in the riser is necessary to

obtain qualitatively correct results in the nonlinear domain. Investigating nonlinearities in the low-pressure regime is thus not recommended with the simple nodalization scheme we use in this chapter. In the linear domain, the trends are predicted correctly, however, with a single-node model for the riser. Section 4.2 provides details about the Mathematica subroutine we used to integrate the model equations numerically.

A comprehensive validation of our model on the basis of several startup experiments in the Dodewaard reactor is provided in Chapter 7 of this thesis. However, to relate the present parametric study to actual operating data, a set of operating conditions, measured during the cycle 23 startup of the Dodewaard BWR, is listed in Table 6-1. The experiments in Table 6-1 cover a broad range of pressure and power levels: From an initial pressure of only 3.1 bar and a power level of 1 MW (case 1), to a final pressure of almost 70 bar and a thermal power of 43 MW (case 9). As a comparison, the nominal operating conditions are also listed in Table 6-1.

Table 6-1. Typical Operating Conditions During the Startup of a Natural Circulation BWR (Cycle 23, Feb. 1992, Dodewaard BWR)

Case	$P_{R,e}$ (bar)	P_{th} (MW)	ϕ (kg/s)	$h_{f,w}$ (J/kg)	T_{sub} (K)	N_{Zu}	$N_{sub,c,i}$	N_{flash}	$N_{Zu} - N_{sub,c,i} + N_{flash}$
1	3.1	1	3.09E2	4.15E5	8.9	0.7	8.5	4.4	-3.3
2	6.3	2	4.13E2	3.86E5	3.5	0.6	1.9	1.4	0.1
3	10.7	2.5	7.32E2	N.A.	1.8	0.3	0.6	0.6	0.2
4	20.3	5.5	8.89E2	N.A.	1.5	0.3	0.3	0.2	0.3
5	30.3	10	9.71E2	N.A.	2	0.3	0.3	0.1	0.1
6	40.2	18	9.64E2	3.26E5	2.4	0.4	0.3	0.06	0.2
7	50	28	9.41E2	3.18E5	2.9	0.5	0.3	0.04	0.3
8	59	40	9.20E2	3.04E5	3.5	0.7	0.3	0.03	0.4
9	69.7	43	8.82E2	3.07E5	3.9	0.6	0.3	0.02	0.4
Nom.	75.5	183	1.30E3	5.72E5	4.7	1.7	0.3	0.02	1.3

Table 6-1 not only contains the main dimensional operating data (riser exit pressure $P_{R,e}$, thermal power P_{th} , flow rate ϕ , feedwater enthalpy $h_{f,w}$, and subcooling T_{sub}), but also the primary dimensionless numbers: The Zuber number N_{Zu} , the (core-inlet) subcooling number

$N_{sub_{c,i}}$ and the flashing number N_{flash} . The definitions of these dimensionless numbers are provided in Appendix C. The transformation to a dimensionless basis requires the evaluation of several pressure-dependent properties (e.g. densities and enthalpies) at the *core inlet*, whereas in Table 6-1 only the *riser exit* pressure is given. The pressure level at the core inlet is calculated by adding the pressure difference over the Dodewaard downcomer (with a height of 4.85 m) to the riser exit pressure level, see Eq. (5-8).

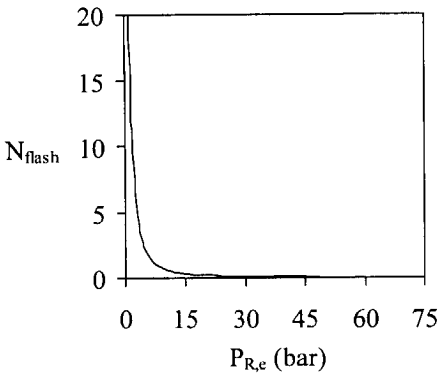


Figure 6-1. Influence of the system pressure on the dimensionless flashing number N_{flash} . Notice the rapid increase of N_{flash} if the pressure is reduced below 20 bar.

The strong dependence of the flashing number on the system pressure is shown in Fig. 6-1. At pressures lower than 20 bar, this number increases very rapidly, indicating that the flashing phenomenon becomes very important in the low-pressure regime. The trend in Fig. 6-1 is also visible in Table 6-1: N_{flash} increases from 0.6 to 4.4, when the pressure is reduced from 10.7 bar (case 3) to 3.1 bar (case 1). The last column of Table 6-1 indicates whether or not two-phase flow (due to flashing and/or heating) exists according to the theoretical model we developed in Chapter 5. We there derived a simple criterion for the occurrence of two-phase flow:

$N_{Zu} > N_{sub_{c,i}} - N_{flash}$. Hence, if the number in the last column of Table 6-1 is positive, boiling occurs in the core or in the riser section. Clearly, in all cases, except case 1, two-phase flow is predicted by the model. Without flashing ($N_{flash}=0$), the coolant would be one phase for cases 1 through 4 ($N_{Zu} < N_{sub_{c,i}}$). The small (but still significant) flow rate in case 1 is possibly due to single-phase density differences. The convection can be driven as well by boiling in only a few (hot) channels, for instance when the power distribution is strongly peaked. Notice the relatively large flow rate for case 2 (the power is only 1% of the nominal power, yet the flow rate has already reached 30% of its nominal value). The flow rate predictions of our model for the Dodewaard cycles 23-26 will be discussed in detail in Section 7.5.1.

A qualitative explanation of the experimentally observed phenomena is provided in the parametric study in Sections 6.2 and 6.3 of this chapter. Section 6.2 focuses on the influence of void flashing on the static behavior of a natural circulation BWR, using the cases in Table 6-1 as examples. First, our model is compared in Section 6.2.1 with an alternative flashing model³ and the previously developed model without flashing (see Chapter 2).⁴ Then the influence of the operating conditions, i.e. the power, subcooling and system pressure, on the void production is studied in Section 6.2.2. After this introductory parametric study, the strong effect of the pressure level on the subcooling of the coolant is considered. Applying

this model for the fluid subcooling, the flow rate is then calculated for a wide range of operating pressures and heating powers.

The strong influence of void flashing on the dynamics of BWRs under low-pressure conditions is investigated in Section 6.3. The impact of the approximations in the model, made in Chapter 5, on the accuracy of the transient calculations is assessed first in Section 6.3.1. The effect of void flashing on the stability boundaries in the dimensionless Zuber-subcooling stability plane is then explained in Section 6.3.2. Applying our elementary model for the fluid subcooling again, we demonstrate that the subcooling number should be defined with respect to the *riser exit* (instead of the core inlet) in the Zuber-subcooling stability plane. This results in a convenient stability map, in which the influence of the operating conditions on stability is studied in Section 6.3.3. Conclusions from the analyses are provided in Section 6.4.

6.2. STATICS

6.2.1. Comparison With Other Models

Model results are compared with the previously developed BWR stability code (see Chapter 2) and the flashing model of Inada and Ohkawa³ in this section. Several cases in Table 6-1 are used as examples here, to illustrate the importance of the flashing phenomenon under experimental conditions. Figure 6-2a shows the calculated void fraction profile along the core and riser sections for case 4 in Table 6-1. The fluid is subcooled at the core inlet ($z^*=0$), and starts to boil at the boiling boundary Z_{bb}^* (for $z^*\approx 0.9$), just before the core exit.

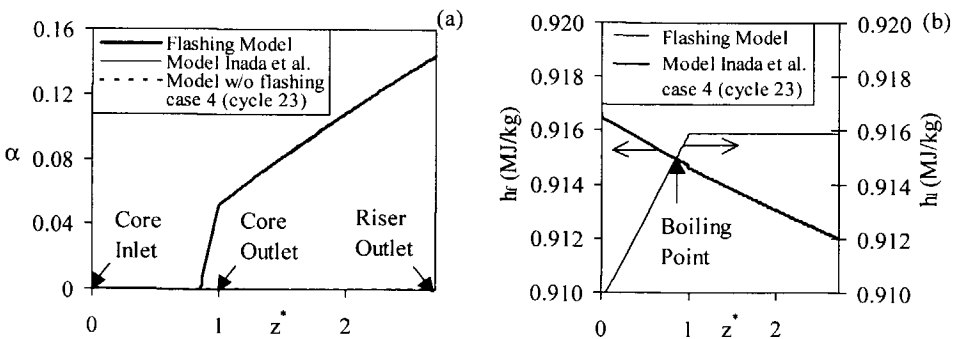


Figure 6-2. Influence of void flashing at a pressure of 20.3 bar (case 4 in Table 6-1). Figure 6-2a shows the calculated void fraction profile in the axial direction. The void fraction increases rapidly in the diatomic core region ($0 < z^* < 1$) where the coolant is heated and starts to boil. The void production in the adiabatic riser ($z^* > 1$) is caused by flashing only. Figure 6-2b shows the axial profile of the saturation enthalpy h_r and the liquid enthalpy h_l . Comparisons with the flashing model of Inada and Ohkawa³ and a model without flashing (see Chapter 2) are provided as well.

The model without flashing predicts that the coolant does not reach the saturation temperature in the core region under these conditions, see Fig. 6-2a. This implies that without the influence of flashing the coolant would not boil in the core region. The void production in the riser ($1 < z^* < 2.71$) should be attributed to the flashing effect only, because this section is unheated.

The decrease of the saturated liquid enthalpy h_f along the core and the riser is shown in Fig. 6-2b. The coolant enters the core region subcooled, i.e. the liquid enthalpy h_l is smaller than the saturation enthalpy at $z^*=0$. In the core region, heat is transferred to the coolant, and h_l increases until the saturation enthalpy is reached (at the boiling boundary position indicated in Fig. 6-2b).

Notice that the slope of the $h_f(z^*)$ -curve is slightly steeper in the core region than in the riser section. This can be explained by considering the different pressure drop contributions. Figure 6-2a shows that the fluid is mainly one phase in the core, but two phase in the riser. The differential gravitational pressure drop $dP(z^*)/dz^*$ will therefore be smaller in the riser region than in the core. Furthermore, the frictional and accelerational pressure losses are relatively small as well in the riser region, because the (hydraulic) flow diameter of the riser is rather large and the void fraction is low. These two effects slightly diminish the decrease of the pressure along the riser, and the void production due to flashing in this section will be somewhat attenuated.

We used the measured flow rate for case 4 (889 kg/s) as a fixed input parameter in the calculations. This procedure was chosen to simulate the operational conditions for case 4 as closely as possible. Iterative model calculations show that the momentum balance is restored completely when the recirculation flow is reduced (slightly) to 850 kg/s.

We compare our flashing model with the alternative model proposed by Inada and Ohkawa.³ Their analytical model is derived from the same basic equations [Eqs. (5-1) through (5-3) and Eq. (5-7)] as our flashing model. The differential two-phase flow conservation equations are simplified in Ref. 3 by assuming that the flow quality χ and the vapor to liquid density ratio N_p are much smaller than unity. The steady-state equations are then integrated numerically, applying a finite-difference method, along the two-phase region. Stability analysis was performed in the frequency domain, by Laplace transforming the perturbed basic equations.

We did not neglect χ and N_p with respect to unity in the theoretical model proposed in Chapter 5. We, furthermore, developed a *reduced-order* time-domain model by integrating the basic partial-differential equations in Chapter 5 over a limited number of two-phase nodes. In spite of the different integration schemes, the calculated axial profiles agree very well for case 4. The differences are in fact indistinguishable on the scales of Figs. 6-2a and 6-2b. This implies that the elementary axial nodalization scheme applied in the static calculations (with N_C and N_R both equal to one) is sufficiently accurate here, since the fine-

mesh nodalization in the model of Ref. 3 leads to very similar results. The assumption of Ref. 3 that χ and N_p are much smaller than unity is justified as well under these low power and pressure conditions.

Figure 6-3 illustrates the occurrence of boiling out of the heated reactor core, due to void flashing in the riser. Case 2 in Table 6-1 is simulated in these calculations. The fluid enters the core inlet highly subcooled ($T_{\text{sub}}=3.5$ K, instead of 1.5 K in Fig. 6-2) and remains one phase in the entire core region. At the end of the unheated riser section, the continuously decreasing saturation enthalpy becomes equal to the fluid enthalpy, and the coolant starts to boil. Notice that the agreement with the flashing model of Inada and Ohkawa is again excellent.

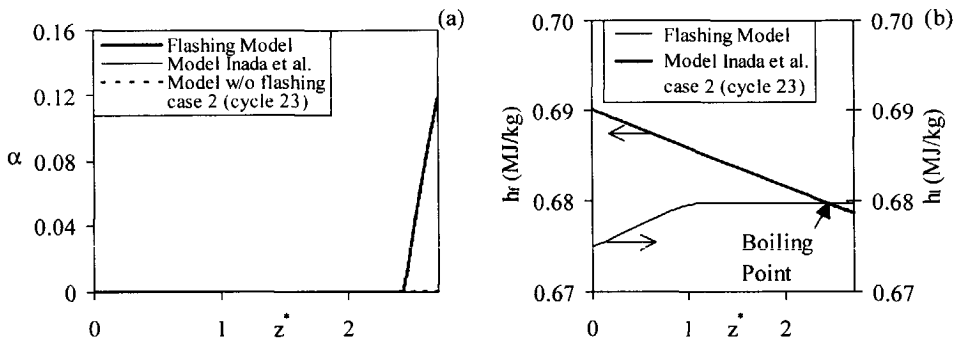


Figure 6-3. Ex-core boiling induced by flashing, at a pressure of 6.3 bar (case 2). The fluid is subcooled in the entire core region and reaches the boiling point at the end of the adiabatic riser section.

The effect of flashing at higher system pressures is investigated in Fig. 6-4. At a pressure of 30.3 bar (case 5 in Table 6-1) the model without flashing predicts the occurrence of boiling in the core and the riser, see Fig. 6-4a. However, the effect of flashing is still significant. Accounting for flashing, the boiling boundary is located at a lower axial position in the core. Close to the core exit, the two-phase mixture flashes quickly, because of the relatively large core-outlet pressure drop. Figure 6-4c shows the axial void profile at a pressure of 40.2 bar (case 6 in Table 6-1). Void flashing is less intense in this case due to the relatively small pressure dependence of the saturation temperature at higher pressures (see Fig. 5-1). Increasing the power and pressure level to the nominal conditions, the heating process almost completely governs the void production, and the predictions of the models with and without the flashing effect become almost identical. Apparently, the flashing phenomenon is only of minor importance under high power and pressure conditions. Note that the model of Inada and Ohkawa underestimates the void fraction in Fig. 6-4d. This discrepancy is caused by the neglect of χ with respect to unity in their model. This assumption is not very accurate in the high power domain (the flow quality is equal to 0.08 at the core exit in Fig. 6-4d, compared to only 0.001 in Fig. 6-4a).

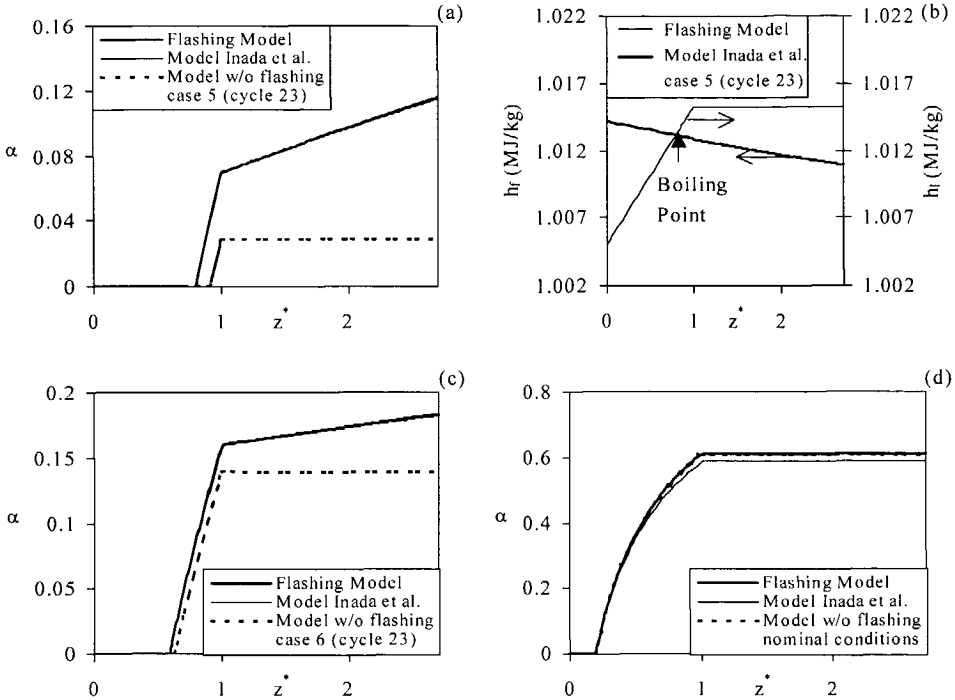


Figure 6-4. Influence of flashing at higher pressures. Figures 6-4a and 6-4b show the void fraction and saturated liquid enthalpy profiles for a pressure of 30.3 bar (case 5). Figures 6-4c and 6-4d show the void fraction profiles for 40.2 bar (case 6) and 75.5 bar (nominal conditions), respectively. The effect of flashing diminishes at a high system pressure, and the predictions of the models with and without flashing become identical (see Fig. 6-4d). The flashing model of Inada et al. however slightly underestimates the void fraction in this case.

6.2.2 Influence of the Operating Conditions

The influence of the operating conditions on the model predictions is investigated systematically in this section. Case no. 4 in Table 6-1 ($T_{sub}=1.5$ K, $P_{th}=5.5$ MW, $P_{R,c}=20.3$ bar) is the reference case (indicated with a thick line in the figures). Starting from this operating point, the subcooling, power and pressure are varied in Figs. 6-5 through 6-7, respectively. The natural circulation flow rate is not an input parameter, like in Section 6.2.1, but is calculated as a function of the operating conditions.

The impact of the degree of subcooling on the void production is shown in Fig. 6-5. The pressure and power level are kept constant at 20.3 bar and 5.5 MW, respectively. Figure 6-5 suggests that the degree of subcooling can be adjusted freely in a natural circulation BWR. This is not the case, however. The impact of the pressure level, the reactor power and the feedwater temperature on the core-inlet subcooling is discussed in detail at the end of this

section, but neglected at this point.

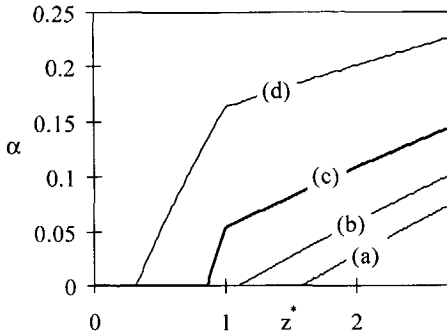


Figure 6-5. Influence of the degree of subcooling on the void production at a pressure of 20.3 bar ($P_{in}=5.5$ MW, cf. case 4 in Table 6-1). The subcooling is decreased from 3.5 K (case a), to 2.5 K (case b), 1.5 K (case c) and 0.5 K (case d). The reference case (case no. 4 in Table 6.1) is indicated with a thick line in Figs. 6-5 through 6-7.

The subcooling is reduced from 3.5 K (case a), to 2.5 K (case b), 1.5 K (case c) and 0.5 K (case d). Void profile (c) in Fig. 6-5 is the base case (see Fig. 6-2a). Figure 6-5 clearly illustrates the major impact of the degree of subcooling on the void production in the core and the riser. Comparing case a with case d, the subcooling differs only 3.0 K, yet the coolant starts to boil already close to the core inlet for case d, whereas the fluid is one phase in the core and only boils in the riser section for case a. The sensitivity of the model predictions to the actual degree of subcooling is investigated further in Chapter 7, where the effect of the experimental uncertainty in the subcooling

(≈ 0.5 K) on the calculated flow rate is taken into account.

The slope of the void fraction curve becomes less steep in the adiabatic riser section if we compare case a with case d in Fig. 6-5. One explanation for this effect is the decreasing slope of the void fraction vs. flow quality curve for higher void fractions, see Fig. 1-4. Because of this nonlinearity, the same increase in flow quality corresponds to a smaller void fraction increase in case d compared to case a. The nonlinearity of the void fraction vs. flow quality curve becomes more pronounced under low-pressure conditions, due to a smaller vapor to liquid density ratio. We also observed in Section 6.2.1 that the flashing effect limits itself at higher void fractions, because the local pressure and saturation temperature decrease relatively slow in the two-phase region.

Figure 6-6 shows the impact of the heating power on the axial void fraction profiles. The pressure is equal to 20.3 bar and the subcooling is equal to 1.5 K in these calculations (cf. case 4 in Table 6-1). The thermal power level is increased, going from case a to case d, from 1.5 MW (case a) to 3.0 MW (case b), 5.5 MW (case c) and 12.0 MW (case d). An increase of the thermal reactor power causes a rapid increase of the liquid enthalpy in the single-phase region, and the boiling process will therefore start at a lower axial position. Comparing case d in Fig. 6-5 with case d in Fig. 6-6 also illustrates that a higher heating power results in a steeper void profile in the boiling region. Figure 6-6 shows (cf. Fig. 6-3) that boiling starting out of the heated reactor core is possible at low heating powers (cases a and b).

The major impact of the pressure level on the void production is illustrated in Fig. 6-7

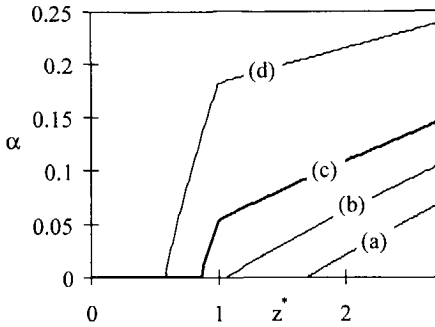


Figure 6-6. Influence of the thermal reactor power on the axial void fraction profiles. The pressure is equal to 20.3 bar and the subcooling is 1.5 K in these calculations (cf. case 4 in Table 6-1). The thermal power level is increased from 1.5 MW (case a), to 3.0 MW (case b), 5.5 MW (case c) and 12 MW (case d). The impact of the heating process in the core on the void production increases at higher power levels (cases c and d), whereas the void production due to flashing in the riser becomes dominant at lower power levels (cases a and b).

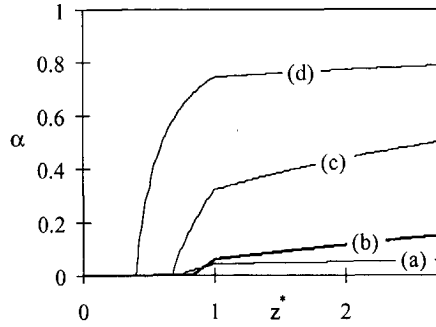


Figure 6-7. Influence of the system pressure on the void production ($P_{th}=5.5$ MW and $T_{sub}=1.5$ K, cf. case 4 in Table 6-1). The pressure is equal to 68.7 bar in case a, 20.3 bar in case b, 6.3 bar in case c and 3.1 bar in case d. The void fraction increases strongly for lower pressures, due to a smaller vapor to liquid density ratio and more intense void flashing.

($P_{th}=5.5$ MW and $T_{sub}=1.5$ K, cf. case 4 in Table 6-1). The pressure is equal to 68.7 bar in case a, 20.3 bar in case b, 6.3 bar in case c and 3.1 bar in case d. Notice that the void fraction increases strongly under reduced-pressure conditions, due to a smaller vapor to liquid density ratio (see Fig. 5-1) and more intense void flashing. However, the boiling boundary position is not continuously decreasing as the pressure is reduced. For instance, the boiling boundary position shifts upwards, in the transition from case a to case b, and then shifts downwards for cases c and d. This behavior of the boiling boundary is caused by the increase of the average void fraction as the pressure is reduced. This results in an increasing natural circulation flow rate and a decreasing specific energy of the coolant. The boiling boundary therefore shifts upwards if the pressure is reduced from case a to case b. At lower pressures, the coolant flashes quickly (the core-inlet subcooling is constant in the calculations), and the boiling boundary position decreases (cases c and d). Notice that the slope of the axial void fraction profile in the riser initially increases when the pressure is reduced (cases a, b and c), and then decreases (compare case c with case d). This clearly illustrates the strong nonlinearity of the void fraction vs. flow quality curve: If the void fraction is high an increase of the flow quality only results in a small additional void fraction increase.

So far, the core-inlet subcooling has been treated as an independent operating condition in the analysis. However, the measurement series in Table 6-1 shows that the subcooling is in fact changing strongly as a function of the pressure, power level and feedwater enthalpy. At a low pressure, the subcooling is relatively high (cases 1 and 2). At a higher pressure, the

subcooling is initially small (cases 3 and 4), but then increases slowly as the power level increases (cases 3 through 9).

The large subcooling at low pressures is mainly caused by the axial variation of the pressure (and therefore the saturation temperature) in the natural circulation loop. The liquid that turns around at the riser exit and falls into the downcomer, will re-enter the core subcooled because the saturation temperature is higher at the core inlet than at the riser exit. Neglecting the influence of the recirculated feedwater and phenomena like carry under (the presence of voids in the downcomer section), we showed in Chapter 5 that the dimensionless core-inlet subcooling $N_{\text{sub},c,i}$ is at least equal to N_{flash} . This rule indeed holds for all cases in Table 6-1,^{a)} and explains the rapid increase of the subcooling at low-pressure (i.e. large flashing number) conditions.

The influence of the feedwater flow on the subcooling becomes important at higher power levels (cases 5 through 9 in Table 6-1), i.e. when the steam and feedwater flow rates increase. Assuming a stationary feedwater system and again neglecting carry under, stating a mass and energy balance at the feedwater sparger yields an expression for the subcooling number:

$$N_{\text{sub},c,i} = N_{\text{flash}} + \chi_{R,c} \frac{h_{f,R,e} - h_{f,w}}{h_{fB,C,i}} (N_p^{-1} - 1). \quad (6-1)$$

A simplified version of Eq. (6-1) has already been given in Eq. (2-41). The N_{flash} -term on the right hand side of Eq. (6-1) has been neglected in Eq. (2-41), which is a good assumption only under high-pressure conditions (i.e. when N_{flash} is small).

The influence of the operating conditions on the subcooling, and the impact of the subcooling on the static behavior of a natural circulation BWR, are shown in Fig. 6-8. Note that the riser exit quality $\chi_{R,c}$ in Eq. (6-1) not only determines, but also depends on the core-inlet subcooling. The core-inlet subcooling is therefore determined iteratively in the model calculations. The feedwater enthalpy $h_{f,w}$ is equal to 4.15×10^5 J/kg for $N_{\text{flash}}=4.44$, $h_{f,w}=3.86 \times 10^5$ J/kg for $N_{\text{flash}}=1.41$, and $h_{f,w}=3.26 \times 10^5$ J/kg for $N_{\text{flash}}=0.06$ (cf. cases 1, 2 and 6 in Table 6-1). Figure 6-8a shows that the subcooling number increases proportional to the flashing number [because $N_{\text{sub},c,i}(N_{\text{Zu}}=0) = N_{\text{flash}}$], and (approximately) proportional to the Zuber number (which is in turn proportional to the heating power). When the influence of flashing on the subcooling diminishes, the role of the feedwater supply becomes more important. Neglecting the flashing effect, i.e. only considering the influence of heating, the

^{a)}Several measurements during the cycle 25 startup of the Dodewaard BWR violate this criterion, however. This apparent paradox is discussed in Section 7.5.

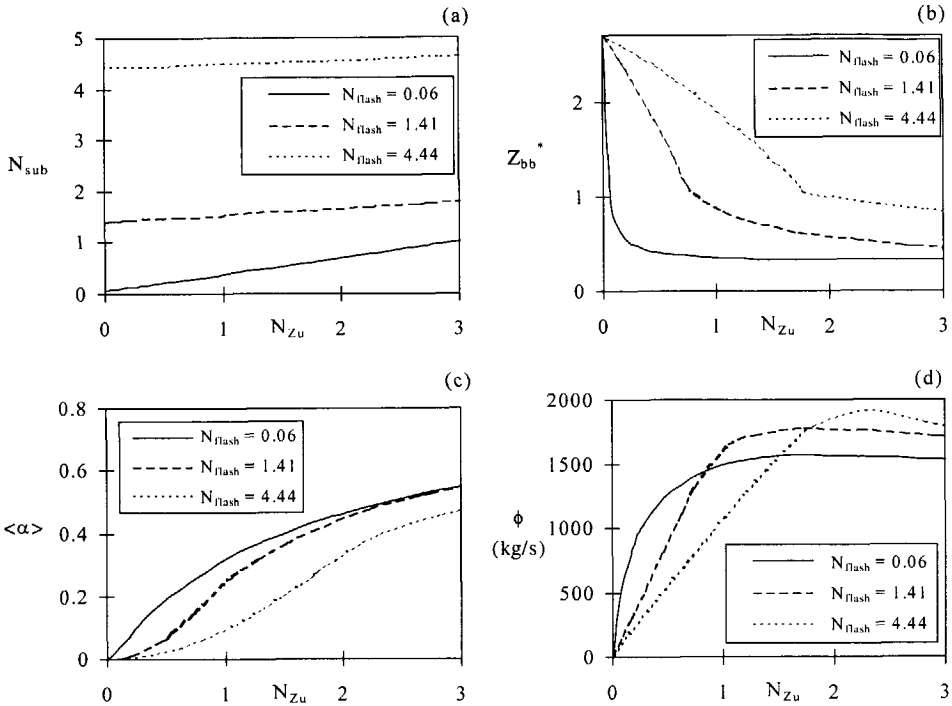


Figure 6-8. (a) Relationship between the dimensionless Zuber and subcooling numbers for different values of the flashing number. The (core-inlet) subcooling number increases proportional to the flashing number and (approximately) proportional to the Zuber number. The feedwater enthalpy h_{fw} is equal to $4.15 \cdot 10^5$ J/kg for $N_{flash}=4.44$, $h_{fw}=3.86 \cdot 10^5$ J/kg for $N_{flash}=1.41$, and $h_{fw}=3.26 \cdot 10^5$ J/kg for $N_{flash}=0.06$ (cf. cases 1, 2 and 6 in Table 6-1). (b) Influence of the Zuber number on the boiling boundary position. (c) Influence on the void fraction (averaged over the core and riser length). (d) Influence on the natural circulation flow rate. The effect of the Zuber number on the subcooling number (see Fig. 6-8a) is taken into account in Figs. 6-8b through 6-8d.

(almost linear) relationship between the subcooling and the Zuber number can be understood easily. In that case, the riser exit quality can be calculated directly:⁴

$$\chi_{R,e} = \chi_{C,i} = (N_{Zu} - N_{sub,c,i}) / (N_p^{-1} - 1). \tag{6-2}$$

Substituting this expression in Eq. (6-1), with $N_{flash}=0$, we arrive at a linear relationship between the subcooling and the Zuber number, Eq. (2-41), which is valid for high-pressure conditions. Examining Eq. (2-41) reveals that the slope of the N_{sub} vs. N_{Zu} curve is proportional to the subcooling of the feedwater Δh_{fw} ($= h_{f_{R,e}} - h_{fw}$), and inversely proportional to the evaporation enthalpy h_{fg} . The subcooling of the feedwater increases with more than 200%, when we compare the cases for which $N_{flash}=4.44$ and $N_{flash}=0.06$ in Fig. 6-8a. This explains the increase of the slope of the N_{sub} vs. N_{Zu} curve when N_{flash} decreases. The

decreasing evaporation enthalpy at a higher pressure (smaller N_{flash}), causes an additional increase of N_{sub} (at a fixed N_{zu}).

The large subcooling of the fluid at low pressures strongly suppresses the occurrence of boiling at low heating powers (i.e. small N_{zu}). The position of the boiling boundary Z_{bb}^* is plotted as a function of N_{zu} in Fig. 6-8b. Boiling out of the heated reactor core ($Z_{\text{bb}}^* > 1$) is dominant at low pressures (large N_{flash}). Only at relatively high heating powers (large N_{zu}) two-phase flow exists in the core under these conditions. This observation implies that under low power and pressure (i.e. reactor startup) conditions nuclear feedback effects, chiefly induced by void production in the core, are of minor importance. At a high system pressure, for instance at 40.2 bar ($N_{\text{flash}}=0.06$ in Fig. 6-8b), the impact of flashing on the subcooling becomes relatively small (especially at large N_{zu}), and in-core boiling dominates. The boiling boundary position becomes independent of N_{zu} under these circumstances, because $Z_{\text{bb}}^* = N_{\text{sub}}/N_{\text{zu}}$ [see Eq. (2-29)] and N_{sub} is proportional to N_{zu} [Eq. (2-41)].

Due to the relatively short two-phase region at a low pressure, the void fraction (averaged over the core and the riser sections) is small under these conditions, see Fig. 6-8c. Hence, the natural circulation flow rate is relatively small for low N_{zu} and large N_{flash} , see Fig. 6-8d. The maximum flow rate is larger at low pressures, however, because two-phase flow then mainly exists in the riser section, where the frictional pressure losses are relatively small.

6.3. DYNAMICS

6.3.1. Model Assumptions

Various model simplifications have been proposed in the development of the theoretical model in Chapter 5, to reduce the model order and to avoid numerical problems. The influence of these assumptions is investigated in detail in this section. Section 6.3.1.1 discusses several models for the boiling boundary dynamics, ranging from exact, but very complicated, frequency-domain solutions to approximate time-domain expressions. Different variants of the nodal energy equation, Eq. (5-6), are then considered in Section 6.3.1.2 The steady-state model, used in the previous section, is not affected by the approximations in the dynamics model, evaluated here.

6.3.1.1. Boiling Boundary Model

The impact of several successive assumptions in the boiling boundary model is shown in Fig. 6-9. The operating conditions for case 3 in Table 6-1 are used in the calculations. The boiling boundary is located in the riser section in this case ($Z_{\text{bb}}^* = 1.58$). First, the influence of the single-phase inertial pressure losses on the gain and phase diagrams of the boiling

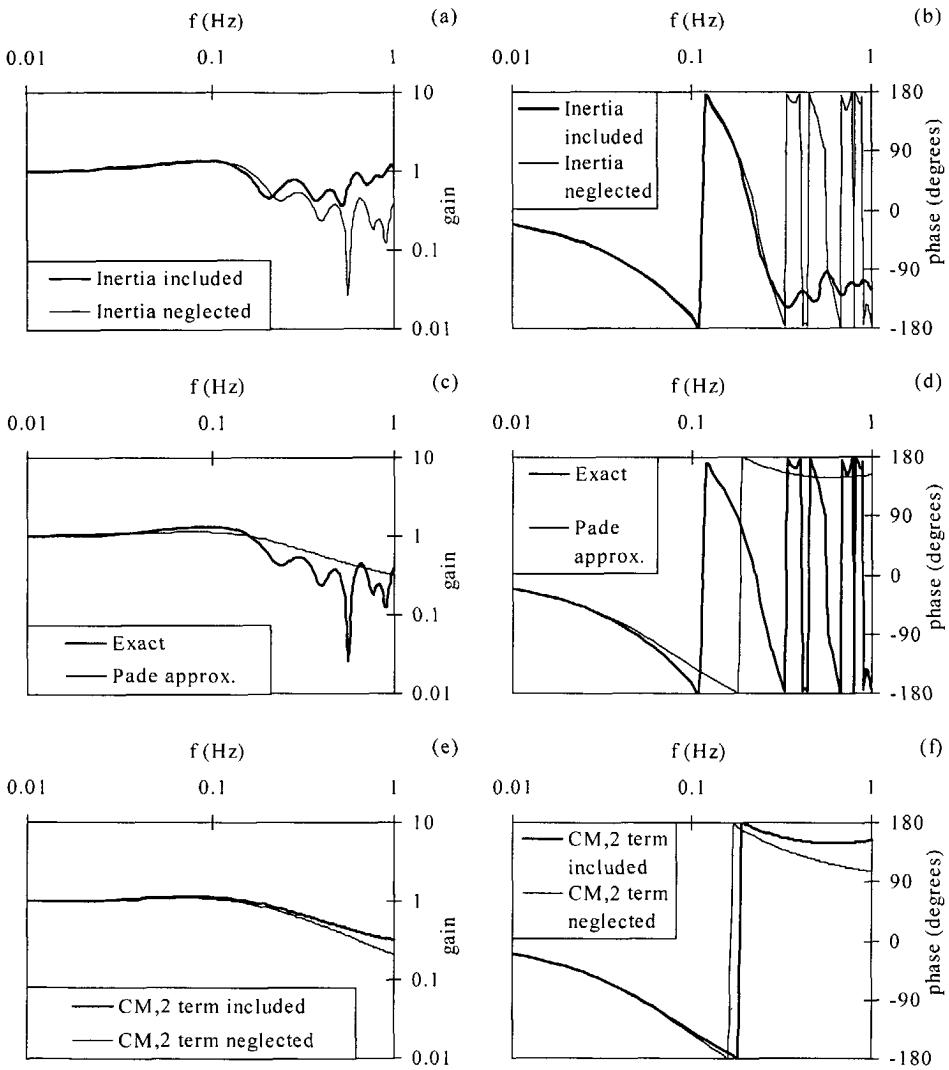


Figure 6-9. Effect of modeling assumptions on the Bode diagrams of the boiling boundary transfer function $\delta Z_{bb}^*/\delta M_{C,i}^*$, for case 3 in Table 6-1 ($Z_{bb}^*=1.58$). The impact of neglecting the inertial pressure losses on the boiling boundary dynamics is investigated in Figs. 6-9a and 6-9b. Inertia is neglected in Figs. 6-9c through 6-9e. The influence of the applied Padé approximation is shown in Figs. 6-9c and 6-9d. Setting the $C_{M,2}$ -term equal to zero in the final boiling boundary equation (5-26) has a small effect, as Figs. 6-9d and 6-9e demonstrate.

boundary transfer function $\delta Z_{bb}^*/\delta M_{C,i}^*$ is shown in Figs. 6-9a and 6-9b, respectively. The inertial pressure drop is proportional to the time derivative of the mass flux density. The magnitude of this pressure drop term, and its impact on the saturation enthalpy at the boiling boundary, therefore increases linearly as a function of the oscillation frequency in the

frequency domain. Figure 6-9a indeed shows that the relative importance of this pressure drop term is small at low frequencies (<0.2 Hz), but increases at higher frequencies. Because we are mainly interested here in the dynamic behavior at low frequencies (≈ 0.1 Hz), the neglect of inertia in the boiling boundary model is a reasonable assumption. Notice that the gain of the boiling boundary transfer function increases and decreases at higher frequencies due to interference phenomena in the one-phase region. This effect has been encountered and explained before in our boiling boundary model without flashing.⁵

The effect of the applied Padé approximation [of the exponential term in the boiling boundary transfer function, see Eq. (5-24)] is investigated in Figs. 6-9c and 6-9d. Good agreement is found for frequencies ≤ 0.1 Hz. Larger discrepancies are visible for higher frequencies, caused by the low-order approximant used here. Applying a higher-order Padé approximation improves the results,⁵ but leads to a more complex (higher-order) ODE when we transform the boiling boundary transfer function back to the time domain.

Finally, we proposed in Chapter 5 to neglect the $d^2 M_{C,i}^*(t^*)/dt^{*2}$ -term in the boiling boundary equation (5-26), by setting its coefficient, labeled as $C_{M,2}$, equal to zero. This neglect has a small impact on the results, as Figs. 6-9e and 6-9f show. A second-order time derivative term is proportional to the square of the oscillation frequency in the frequency domain, and is therefore important only at relatively high frequencies (>0.3 Hz).

6.3.1.2. Energy Conservation Equation

The effect of modeling assumptions in the nodal energy equation (5-6) is considered in this section. As an example, the step response of the normalized (core-inlet) mass flux density $M_{C,i}^*$ is shown in Fig. 6-10 for five different model variants (labeled as a through e). These variants differ in the degree of simplification in Eqs. (5-6) and (5-26). Table 6-2 summarizes which terms in these equations are neglected. For instance, in model variant c the $dL_1^*(t^*)/dt^*$ -term in Eq. (5-6) is neglected, whereas the $d\langle h_f^*(t^*) \rangle_1/dt^*$ -term is included in the calculations. The $d^2 Z_{bb}^*(t^*)/dt^{*2}$ - and $d^2 M_{C,i}^*(t^*)/dt^{*2}$ -terms in Eq. (5-26) are also neglected in variant c.

The equilibrium position of the boiling boundary is located close to the riser inlet ($Z_{bb}^* = 1.05$; $N_{flash} = 1.91$). Therefore, the coefficient $C_{Z,2}$ of the $d^2 Z_{bb}^*/dt^{*2}$ -term in the boiling boundary ODE (5-26) is relatively small. Note that $C_{Z,2}$ vanishes for in-core boiling [see Appendix D]. Neglecting this term, Eq. (5-26) reduces to a first-order differential equation, because $C_{M,2}$ is set equal to zero as well (see Section 6.3.1.1). Step response a in Fig. 6-10 is calculated in this case.

Starting from variant a, the effect of successive simplifications in Eq. (5-6) is considered in cases b through d. The effect of the $d\langle h_f^*(t^*) \rangle_1/dt^*$ -term is illustrated by the difference between case a ($d\langle h_f^*(t^*) \rangle_1/dt^* \neq 0$) and case b ($d\langle h_f^*(t^*) \rangle_1/dt^* = 0$). The $dL_1^*(t^*)/dt^*$ -term is

neglected in case c, but the $d\langle h_f^*(t^*) \rangle_1 / dt^*$ -term is included. Model variant b provides a better approximation (compared to case a) than variant c, indicating the importance of including the $dL_1^*(t^*)/dt^*$ -term in Eq. (5-6). Both the $d\langle h_f^*(t^*) \rangle_1 / dt^*$ - and $dL_1^*(t^*)/dt^*$ -terms are neglected in case d. The oscillatory time evolution of $M_{C,i}^*$ almost completely disappears after these simplifications in Eq. (5-6), indicating that this model variant gives a poor prediction of dynamic stability.

Table 6-2. Model Variants Investigated in Section 6.3.1.2

Model Variant	Nodal Energy Equation (5-6)		Boiling Boundary Equation (5-26)	
	$dL_1^*(t^*)/dt^*$ -term	$d\langle h_f^*(t^*) \rangle_1 / dt^*$ -term	$d^2 Z_{bb}^* / dt^{*2}$ -term	$d^2 M_{C,i}^* / dt^{*2}$ -term
a	Included	Included	Neglected	Neglected
b	Included	Neglected	Neglected	Neglected
c	Neglected	Included	Neglected	Neglected
d	Neglected	Neglected	Neglected	Neglected
e	Included	Neglected	Included	Neglected

As remarked before, model variant a is accurate only when $C_{Z,2}=0$, i.e. when $Z_{bb}^* \downarrow 1$. Therefore, we include the effect of the $d^2 Z_{bb}^* / dt^{*2}$ -term in Eq. (5-26) in the final calculational model (variant e). We were forced, however, to neglect the $d\langle h_f^*(t^*) \rangle_1 / dt^*$ -term in the energy equation, in order to find solutions with the numerical ODE solver applied here. Future research should consider the application of more advanced numerical algorithms, able to solve Eqs. (5-6) and (5-26) directly without simplifications.

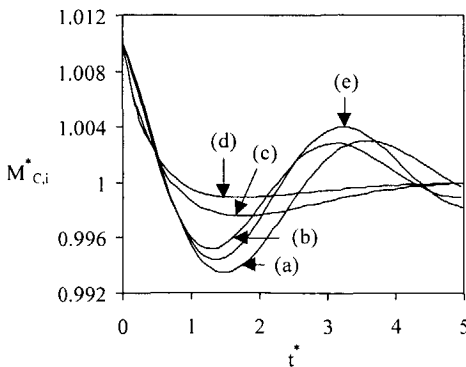


Figure 6-10. Effect of modeling assumptions in the boiling boundary equation (5-26) and energy equation (5-6) on the dynamic response of the (core inlet) mass flux density $M_{C,i}^*$ ($Z_{bb}^*=1.05$, $N_{flash}=1.91$). In cases a through d the $C_{Z,2}$ -term in the model for the boiling dynamics is neglected. The complete energy equation is solved in case a. In case b the $d\langle h_f^*(t^*) \rangle_1 / dt^*$ -term is neglected, whereas in case c the $dL_1^*(t^*)/dt^*$ -term is set equal to zero (see Table 6-2). Both the $d\langle h_f^*(t^*) \rangle_1 / dt^*$ - and $dL_1^*(t^*)/dt^*$ -terms are neglected in case d. The dynamic response with $C_{Z,2} \neq 0$ and $d\langle h_f^*(t^*) \rangle_1 / dt^* = 0$ is shown in case e. This is the final calculational model.

6.3.2. Stability Analysis

Neglecting the effect of flashing and employing the homogeneous two-phase flow model, we proved in Ref. 4 that the influence of the operating conditions on the thermohydraulic stability of a natural circulation BWR is determined by only two dimensionless numbers, i.e. N_{Zu} and N_{sub} . This theoretical observation was then used in Chapter 3 to generate pressure-invariant stability boundaries in the Zuber-subcooling stability plane. An example of such a dimensionless stability map is shown in Fig. 6-11a. A natural circulation system without nuclear feedback, and without the influence of flashing ($N_{flash}=0$), is considered here. At the core exit, the coolant is one phase (1ϕ) in the half plane left of the diagonal ($N_{Zu} < N_{sub}$) and two phase (2ϕ) right of the diagonal.

Unstable density-wave oscillations of the Type-I occur in a narrow region right of the boundary between one- and two-phase flow. These Type-I oscillations occur when the flow quality at the core exit is small (i.e. when $Z_{bb}^* = N_{sub}/N_{Zu} \rightarrow 1$). Under these circumstances, the two-phase flow dynamics is mainly governed by the significant gravitational pressure drop over the riser section. The effect of the frictional pressure drop on the momentum balance is relatively small, because the coolant is almost entirely single phase in the core section. We demonstrated in Chapter 3 that the importance of the Type-I feedback mechanism increases at

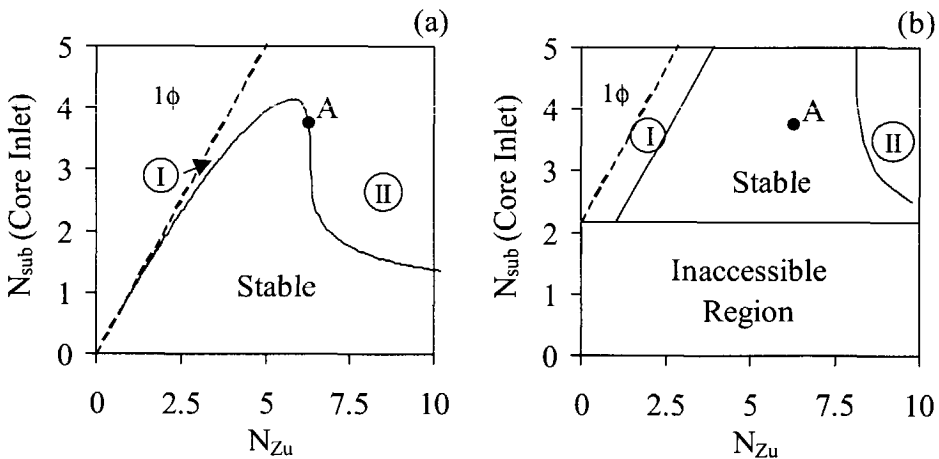


Figure 6-11. (a) Dimensionless stability map for a thermohydraulic natural circulation system, when flashing is neglected ($N_{flash}=0$). The coolant is one phase (1ϕ) in the half plane left of the diagonal ($N_{Zu} < N_{sub}$). Unstable oscillations of the Type-I occur in a narrow region right of this diagonal. The Type-II unstable region is located at higher values of N_{Zu} . (b) Stability map for $N_{flash}=2.17$ ($P_{Re}=4.85$ bar). The region with N_{sub} (core inlet) $< N_{flash}$ is inaccessible during operation, because N_{sub} (core inlet) increases proportional to N_{flash} [see Eq. (6-1)]. Single-phase flow now occurs if $N_{Zu} < N_{sub}$ (core inlet) $- N_{flash}$. The size of the Type-I unstable region expands, compared to Fig. 6-11a, due to unstable void flashing in the riser. Flashing has a stabilizing effect on the Type-II oscillations in this dimensionless plane. The dynamics in point A is investigated in detail in Fig. 6-12.

lower pressure and power levels. Therefore, we expect that the Type-I instability mechanism is dominant under typical reactor startup conditions (for instance cases 1 through 4 in Table 6-1).

The Type-II instability region is located at larger values of N_{Zu} , i.e. when the void fraction in the core is relatively high. The Type-II oscillations are caused by a significant delay of the core outlet flow (and the two-phase frictional pressure drop) with respect to perturbations of the inlet flow. Because ex-core boiling is dominant under low power and pressure conditions (see Section 6.2.2), the Type-II instability mechanism is not expected to be very important during the reactor startup.

We remarked in Chapter 3 that Type-I oscillations have a much lower resonance frequency (≈ 0.1 Hz) than Type-II oscillations (≈ 1 Hz), because the former type of oscillations occurs under low quality conditions, when the flow velocity (especially in the riser section) is low. Therefore we focused in Section 6.3.1 on the performance of our dynamic model in the low frequency range (≤ 0.1 Hz), which will be of primary interest during low power and pressure (reactor startup) conditions.

The incorporation of the flashing effect in our BWR stability model, see Chapter 5, resulted in an additional dimensionless number, N_{flash} , quantifying the effect of void flashing. The SB in the Zuber-subcooling map therefore depends on the pressure level if we include the flashing effect. As an example, the SB for a pressure of 4.85 bar ($N_{flash}=2.17$) is shown in Fig. 6-11b. The region with $N_{sub_{c,i}} < N_{flash}$ is now inaccessible during operation, because $N_{sub_{c,i}}$ has an minimum value of N_{flash} [see Eq. (6-1)]. The boundary between the one- and two-phase regions also shifts in the Zuber-subcooling plane, and is now located at $N_{Zu} = N_{sub_{c,i}} - N_{flash}$ [see the discussion following Eq. (5-16) in Chapter 5]. The region in the stability plane where two-phase flow exists is thus extended in Fig. 6-11b to lower values of N_{Zu} , compared to Fig. 6-11a. When $N_{sub_{c,i}} - N_{flash} < N_{Zu} < N_{sub_{c,i}}$, the heating process alone is not strong enough to induce boiling in the core and riser sections. The boiling point is therefore reached in this region due to the *combined* effect of heating and flashing. Reducing the Zuber number from $N_{sub_{c,i}}$ to $N_{sub_{c,i}} - N_{flash}$, the effect of heating diminishes and void flashing out of the reactor core becomes dominant. Close to the one-phase boundary in Fig. 6-11b single-phase convection becomes more important. Inada et al.⁶ reported that flow instabilities do not occur when the heating power is too low to generate voids in the riser section and the convection is driven by single-phase density differences.

The region in Fig. 6-11b where ex-core boiling occurs ($1 < Z_{bb}^* < 1 + L_R^*$) coincides with the Type-I instability region. This means that, according to our model, void flashing in the riser is an unstable phenomenon at the low-pressure conditions simulated in Fig. 6-11b. At a higher pressure (i.e. smaller value of N_{flash}), stable void flashing out of the core is also possible, especially when the boiling boundary is located close to the riser inlet. The transition from stable to unstable void flashing in the riser (as a function of the operating conditions) is

studied in detail in Section 6.3.3. Our observations agree well with the theoretical results reported by Inada and Ohkawa.³ They predicted diverging oscillations when boiling starts in the riser ($Z_{bb}^* > 1$), whereas boiling in the heated reactor core ($Z_{bb}^* < 1$) stabilizes the flow.

The effect of flashing on the dynamic stability for $Z_{bb}^* < 1$ is investigated in detail in Fig. 6-12. Figure 6-12a shows the step response of $M_{C,i}^*$ in point A in Fig. 6-11 ($N_{Zu}=6.28$, $N_{sub}=3.75$). Point A is located on the Type-II SB for $N_{flash}=0$, but is located in the stable region for $N_{flash}=2.17$, as the dynamic responses in Fig. 6-12a confirm. To explain the stabilizing effect of flashing on the oscillations in point A, we need to consider the influence of this phenomenon on the dynamics of the boiling boundary. Assume, for instance, that the (core-inlet) mass flux density increases. The specific energy of the coolant will then decrease, and therefore the boiling boundary will shift upwards. An increase of the mass flux density, however, also causes a larger frictional pressure drop over the one-phase region. The saturation temperature will therefore decrease in the subcooled region, and the boiling

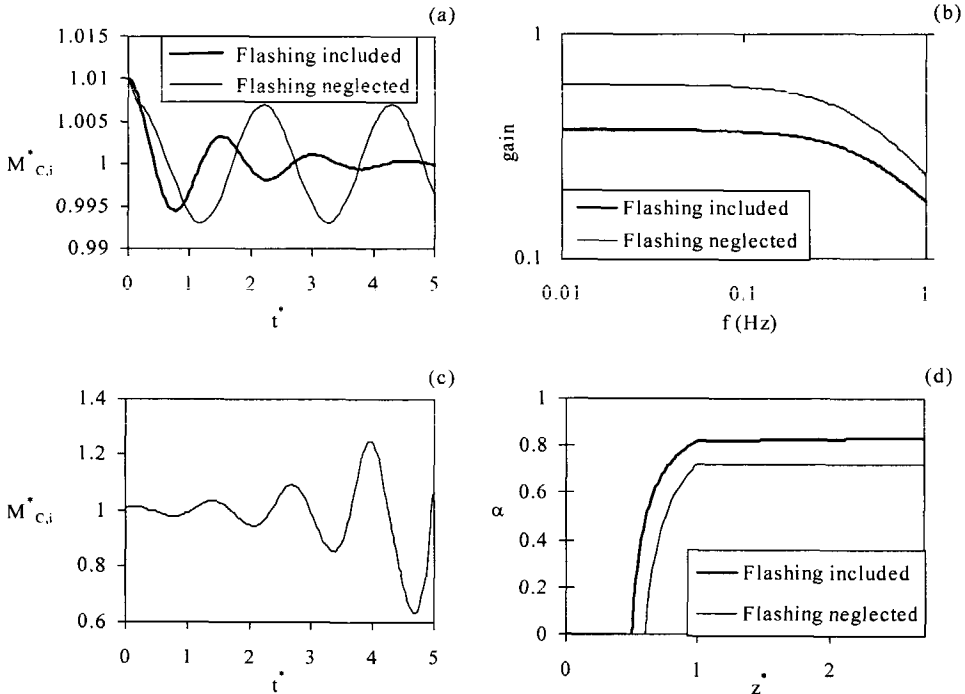


Figure 6-12. (a) Step responses in point A in Fig. 6-11 ($N_{Zu}=6.28$, $N_{sub}=3.75$) for $N_{flash}=0$ and 2.17, respectively. (b) The damped oscillation in Fig. 6-12a is caused by the reduced gain of the boiling boundary transfer function $\delta Z_{bb}^*/\delta M_{C,i}^*$ under low-pressure conditions. (c) The effect of the pressure level on the boiling boundary dynamics is neglected here, resulting in an undamped oscillation. (d) The instability in Fig. 6-12c can be explained by the higher void fraction in the core due to the flashing effect.

boundary moves downwards. So, due to a changing saturation temperature, perturbations of the boiling boundary are partly canceled. Figure 6-12b confirms this qualitative argument: The gain of the boiling boundary transfer function $\delta Z_{bb}^*/\delta M_{c,i}^*$ decreases at lower pressures, when the pressure-driven fluctuations of the saturation temperature become more important.

Previous theoretical⁵ and experimental⁷ studies have demonstrated that smaller oscillations of the boiling boundary result in a more stable two-phase flow system. Consider, for instance, the stable region below the Type-II SB in Fig. 6-11a, which is located at high power/low subcooling conditions. Under these (rather extreme) circumstances, the coolant starts to boil close to the core inlet, i.e. the length of the boiling region is almost equal to the height of the core. Fluctuations in the length of the boiling region (for instance caused by flow oscillations) will therefore be relatively small under these circumstances. Keeping the Zuber number constant and increasing the subcooling number in Fig. 6-11a, the single-phase region in the core appears. The length of the two-phase region will then become more sensitive to oscillations of the boiling boundary. This effectively causes an amplification of the oscillations in the two-phase frictional pressure drop, and the Type-II stability decreases. The boiling boundary oscillations finally destabilize the two-phase flow as N_{sub} is increased to its value on the Type-II SB.

Exploring the dynamics in point A further, we now neglect the influence of a changing saturation temperature on the boiling boundary dynamics. The resulting step response is shown in Fig. 6-12c. Keeping the saturation temperature constant in the one-phase region, the amplitude of the oscillations of the boiling boundary becomes larger, which has a strong destabilizing effect. Figure 6-12d explains why this simplified system is less stable than the original model without flashing, considered in Fig. 6-12a. The flashing effect causes a higher void fraction in the core. Hence, the two-phase frictional pressure drop over this section becomes larger, and the Type-II stability decreases.

The location of the SBs and the boundary between one- and two-phase flow is independent of the system pressure in Fig. 6-11a (where flashing is neglected). However, if we account for the effect of flashing, see Fig. 6-11b, not only the SBs change, but also the location of the boundary between one- and two-phase flow. Furthermore, an inaccessible region emerges in Fig. 6-11b, which was not present in Fig. 6-11a. We remove this inaccessible region from the stability plane in Fig. 6-13, by using the subcooling number relative to the *riser exit* as the ordinate. By definition, $N_{sub}(\text{riser exit}) = N_{sub}(\text{core inlet}) - N_{flash}$, see Eq. (C-1), so Fig. 6-11b is simply translated N_{flash} units downwards in Fig. 6-13. This coordinate transformation also cancels the shift of the boundary between one- and two-phase flow. Figure 6-13 is therefore a more convenient stability plane than Fig. 6-11b: The SBs change as a function of N_{flash} , but the size of the two-phase flow region remains constant.

At a fixed value of $N_{sub_{R,e}}$ in Fig. 6-13, $N_{sub_{c,i}} (= N_{sub_{R,e}} + N_{flash})$ increases proportional to N_{flash} . The single-phase region in the core will therefore be relatively long for large values of

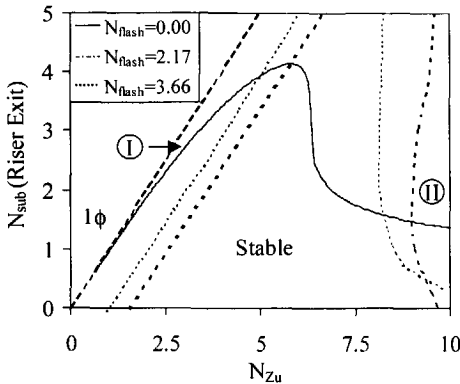


Figure 6-13. Stability map for different values of the flashing number ($N_{flash}=0, 2.17$ and 3.66 , respectively). The ordinate in this figure is the subcooling number with respect to the riser exit [$N_{sub}(\text{riser exit})=N_{sub}(\text{core inlet}) - N_{flash}$]. The boundary between the one and two-phase regions is now independent of N_{flash} , and the inaccessible region in Fig. 6-11b disappears as well. Hence, the strong effect of flashing on the size of the Type-I and Type-II instability regions can be judged more conveniently in this dimensionless plane. Note that the size of the Type-I instability region increases as a function of N_{flash} .

N_{flash} , even when $N_{sub_{R,e}}$ is small. We argued before that the existence of a significant subcooled region has a strong destabilizing effect. Figure 6-13 indeed shows that the ‘island of stability’ below the Type-II SB disappears for large values of N_{flash} .

The size of the Type-I instability region expands in Fig. 6-13 as the flashing effect becomes more important, i.e. in the low-pressure regime. Section 6.3.3 investigates the impact of a pressure decrease on stability when the reactor is operated near the Type-I SB. Furthermore, the influence of the power level and the feedwater temperature on Type-I stability is considered in Section 6.3.3.

6.3.3. Influence of the Operating Conditions

The influence of the power level and the feedwater temperature on the dimensionless stability coordinates is shown in Fig. 6-14. The ordinate in Fig. 6-14 is calculated by rewriting Eq. (6-1):

$$N_{sub_{R,e}} = N_{sub_{C,i}} - N_{flash} = \chi_{R,e} \frac{h_{f_{R,e}} - h_{fw}}{h_{fg,C,i}} (N_p^{-1} - 1). \tag{6-3}$$

Case 4 in Table 6-1 ($P_{th}=5.5$ MW, $P_{R,e}=20.3$ bar) is the reference operating point in Fig. 6-14. The feedwater temperature for case 4 is not available. Therefore, we first investigate the influence of changing this temperature, keeping the power and pressure level fixed at the reference values. The resulting trajectory in Fig. 6-14 shows that, as expected, the subcooling increases if we supply colder feedwater, and vice versa. The supply of relatively cold feedwater will also reduce the void fraction in the core and riser sections. Consequently, the natural circulation flow rate will become smaller. Because the Zuber number is inversely proportional to the flow rate, this number will increase slightly as the feedwater temperature decreases. This trend is indeed visible in Fig. 6-14. The impact of changing the feedwater

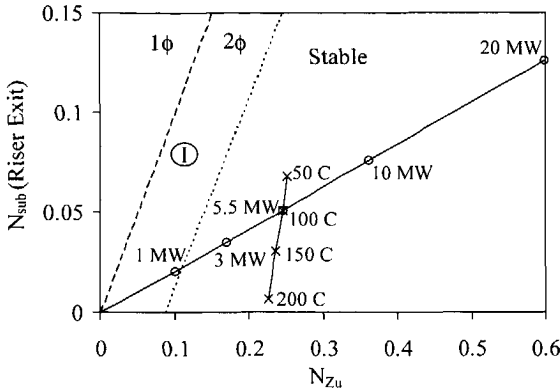


Figure 6-14. Influence of the power level and feedwater temperature on the Type-I stability characteristics, at a (fixed) system pressure of 20.3 bar ($N_{flash}=0.2$, cf. case 4 in Table 6-1). The dotted line separates the two-phase region in unstable and stable areas. Decreasing the power level clearly has a destabilizing effect: The trajectory crosses the SB at $P_{th} \approx 1.4$ MW. The influence of the feedwater temperature on the operating conditions is small, due to the relatively small feedwater flow rate at low power and pressure conditions.

temperature on Type-I stability appears to be small. Figure 6-14 shows that the margin to the Type-I SB only decreases slightly if we reduce the feedwater temperature.

Keeping the feedwater at a fixed temperature of 100 °C, we next investigate the influence of the power level on the stability coordinates. Increasing the reactor power (i.e. increasing the Zuber number), the riser exit quality increases, resulting in a larger subcooling number [see Eq. (6-3)]. This has a strong stabilizing effect: Figure 6-14 shows that the margin to the Type-I SB increases at higher power levels. Reducing the power has the opposite, destabilizing, effect. The Type-I SB is crossed in Fig. 6-14 for $P_{th} \approx 1.4$ MW. Notice that the model without flashing predicts that the Type-I SB crosses the origin of the Zuber-subcooling plane (see Fig. 6-11a). This implies that the SB is *not* crossed if we reduce the power level in this case. We can therefore conclude that without flashing no Type-I instabilities occur.

The influence of the reactor power on the decay ratio and the oscillation frequency in the vicinity of the Type-I SB is investigated in detail in Fig. 6-15a ($P_{R,e}=20.3$ bar, $T_{fw}=100$ °C). The DR is defined as the ratio of two successive maxima of the flow oscillations caused by an external perturbation, so the DR is larger than unity in the Type-I instability zone in Fig. 6-14. Notice the rapid increase of the DR as the power level is decreased from 2 to 1 MW. The oscillations are critically damped for $P_{th}=2$ MW ($DR=0$), but quickly diverge if the power level is reduced to 1 MW ($DR=2.4$). The oscillation frequency is rather low in the neighborhood of the Type-I SB (≈ 0.1 Hz), but increases for higher power levels (when the flow velocity increases). Figure 6-15b shows the DR and oscillation frequency as a function of the boiling boundary position. The Type-I SB is crossed ($DR=1$) if $Z_{bb}^* = 1.34$. Stable void flashing in the riser occurs for $1 < Z_{bb}^* < 1.34$. At lower pressures (larger N_{flash}), stable void flashing out of the core does not exist, and the DR is larger than unity for $Z_{bb}^* > 1$.

Finally, the influence of the pressure level on the Type-I stability characteristics is studied (again for $P_{R,e}=20.3$ bar and $T_{fw}=100$ °C). The Type-I SBs for three different system pressures (20.3, 4.85 and 3.5 bar) are shown in Fig. 6-16. The 20.3 bar SB ($N_{flash}=0.2$) has been

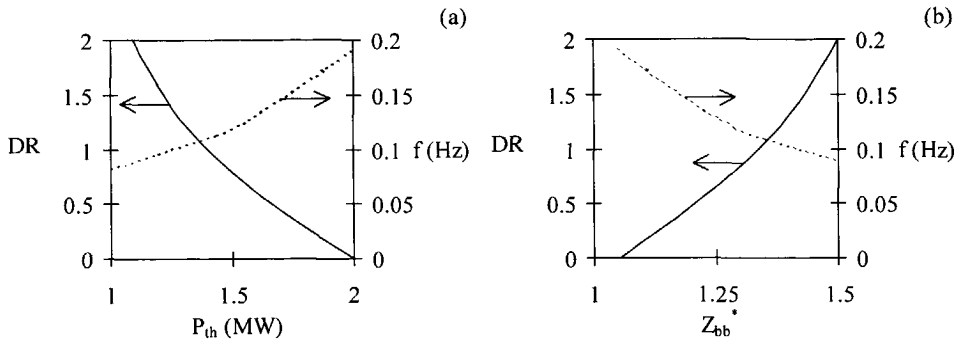


Figure 6-15. (a) Influence of the power level on the decay ratio and the oscillation frequency ($P_{R,c}=20.3$ bar and $T_{f,w}=100$ °C, see Fig. 6-14). Notice the rapid increase of the DR as the power level is decreased from 2 to 1 MW. The oscillation frequency is rather low (~ 0.1 Hz), but increases for higher power levels. (b) Impact of the boiling boundary position Z_{bb}^* on the dynamic characteristics. The DR increases strongly as Z_{bb}^* becomes larger than one, i.e. when the coolant only boils in the riser. A shorter boiling length also corresponds to a lower oscillation frequency.

presented before in Fig. 6-14. The SBs at 4.85 and 3.5 bar ($N_{flash}=2.17$ and 3.66, respectively) are taken from Fig. 6-13. Decreasing the pressure (while keeping the power and feedwater temperature constant) has two effects in the stability plane: The Type-I instability region expands [because N_{flash} increases at lower pressures, see Fig. 6-13], and the dimensionless coordinates of the operating point change.

The trajectory of the operating point as a function of the pressure level is shown in Fig. 6-16. The Zuber number increases at lower pressures, due to a decreasing vapor to liquid density ratio N_p . Because both the Zuber number and the flashing number become larger (i.e. both heating and void flashing become more effective), the riser exit quality increases at lower pressures. Therefore the increase of N_{Zu} is accompanied in Fig. 6-16 by an increase of $N_{sub,R,c}$, see Eq. (6-3). At a pressure of 20.3 bar, the operating point is located on the stable

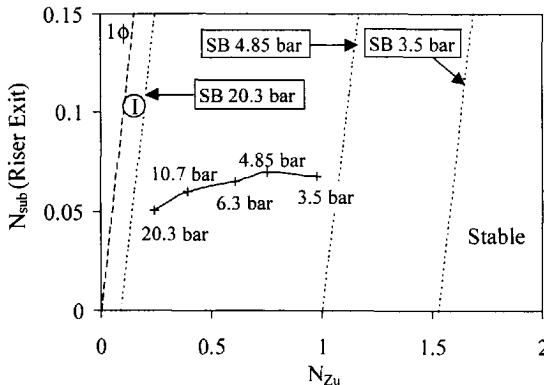


Figure 6-16. Influence of the system pressure on the Type-I stability characteristics ($P_{th}=5.5$ MW and $T_{f,w}=100$ °C). At a pressure of 20.3 bar, the operating point is located on the stable side of the (20.3 bar) SB. Decreasing the pressure to 4.85 or 3.5 bar, the operating point shifts to the right in the stability map. The region with unstable Type-I oscillations also expands strongly, however, and therefore the system becomes unstable.

side of the (20.3 bar) SB in Fig. 6-16. At a reduced pressure of 4.85 bar, however, the operating point has become unstable, due to the rapid expansion of the Type-I instability region. Decreasing the pressure from 4.85 to 3.5 bar, the margin to the Type-I SB increases further. This confirms the recent concern about the stability of natural circulation BWRs in the low power and pressure domain.

6.4. CONCLUSIONS

A comprehensive parametric study, focusing on the statics and dynamics of natural circulation BWRs under low-pressure conditions, is presented. The theoretical model described in Chapter 5 was employed here. We compared this model successfully with alternative models.

The effect of the operating conditions on the void production in the natural circulation loop has been determined. At a low pressure, the subcooling of the fluid entering the core increases rapidly, due to the axial variation of the saturation temperature in the natural circulation loop. This suppresses the occurrence of boiling at low heating powers. Ex-core boiling, due to void flashing in the riser, is therefore expected to be dominant during the reactor startup phase. This implies that nuclear feedback effects are of minor interest under these conditions.

Various assumptions in the dynamic model, suggested in Chapter 5, have been assessed systematically. The simplified model used in this parametric study captures the main physical phenomena under low-pressure conditions and is therefore a valuable analytical tool. A comparison of our analytical model with predictions of detailed thermohydraulic codes is an interesting topic for future research.

A parametric study of low-pressure BWR dynamics has been performed in the Zuber-subcooling number stability plane. We argued that the strong effect of void flashing on the size of the Type-I and Type-II instability regions can be judged most conveniently if we define the subcooling number with respect to the riser exit in the Zuber-subcooling stability plane. The Type-I instability region expands strongly in this plane if the pressure level is reduced, due to the occurrence of unstable void flashing in the riser. The influence of variations in the saturation temperature on the boiling boundary dynamics, very important when boiling in the reactor core occurs, is investigated in detail.

Finally, we studied the impact of changing the operating conditions on the Type-I stability characteristics in the Zuber-subcooling plane. Reactor stability decreases when, operating near the Type-I SB, the reactor power is reduced. Reducing the pressure level also has a strong destabilizing effect. These results confirm the recent concern about the stability of natural circulation BWRs in the low power and pressure domain.

REFERENCES

1. D.D.B. van Bragt and T.H.J.J. van der Hagen, "Stability of Natural Circulation Boiling Water Reactors. Part II - Parametric Study of Coupled Neutronic-Thermohydraulic Stability," *Nucl. Technol.*, **121**, 52 (1998); also published as Chapter 3 of this thesis.
2. D.D.B. van Bragt, Rizwan-uddin, and T.H.J.J. van der Hagen, "Nonlinear Analysis of a Natural Circulation Boiling Water Reactor," To appear in *Nuclear Science and Engineering* (Jan. 1999); also published as Chapter 4 of this thesis.
3. F. Inada and T. Ohkawa, "Thermo-Hydraulic Instability of Natural Circulation BWRs (Explanation on Instability Mechanisms at Start-Up by Homogeneous and Thermo-Dynamic Equilibrium Model Considering Flashing Effect)," *Proc. Int. Conference on New Trends in Nuclear System Thermohydraulics*, May 30 - June 2, 1994, Pisa, Italy, p. 187 (1994).
4. D.D.B. van Bragt and T.H.J.J. van der Hagen, "Stability of Natural Circulation Boiling Water Reactors. Part I - Description Stability Model and Theoretical Analysis in Terms of Dimensionless Groups," *Nucl. Technol.*, **121**, 40 (1998); also published as Chapter 2 of this thesis.
5. D.D.B. van Bragt, "A Theoretical Model for Coupled Neutronic-Thermohydraulic Out-of-Phase Oscillations in Boiling Water Reactors," IRI-131-95-015, Interfaculty Reactor Institute, Delft University of Technology (1995).
6. F. Inada, M. Furuya, and A. Yasuo, "Thermo-Hydraulic Instability of Boiling Natural Circulation Loop Induced by Flashing (Analytical Consideration)," *Proc. 8th Int. Mtg. Nuclear Reactor Thermal-Hydraulics (NURETH-8)*, Kyoto, Japan, September 30-October 4, 1997, p. 1769 (1997).
7. P. Saha, M. Ishii, and N. Zuber, "An Experimental Investigation of the Thermally Induced Flow Oscillations in Two-Phase Systems," *J. of Heat Transfer*, **98**, 616 (1976).

Chapter 7

Validation of the Theoretical Models^{a,b)}

Abstract - The theoretical BWR stability models, developed within the framework of this thesis, are benchmarked against experimental data. The predictions of the thermohydraulics module are successfully compared with a set of detailed void-fraction measurements in the DESIRE facility, and with Type-II oscillations that have been reported in two-phase flow literature. The dynamic model for a natural circulation cooled BWR, outlined in Chapter 2, is used to simulate stability measurements in the Dutch Dodewaard BWR. Experimentally observed trends in the high power (Type-II) domain are explained successfully with this analytical model. The nonlinear reactor model, analyzed in Chapter 4, was also validated successfully against measured nonlinear power oscillations. The oscillations encountered in the low power and pressure (Type-I) domain, during the startup of the Dodewaard reactor, are simulated with the low-pressure BWR model that has been developed in Chapter 5. Evaluation of the experiments shows that void flashing in the riser is important in the low-pressure regime, in agreement with the parametric results presented in Chapter 6. Further numerical and experimental work on this topic is recommended.

^{a)}Sections 7.2, 7.3, 7.4.2 and 7.4.3 of this chapter have been published (in a modified form) as: D.D.B. van Bragt and T.H.J.J. van der Hagen, "Experimental Validation of a Low-Dimensional Physical Model for Coupled Neutronic-Thermohydraulic Power Oscillations in Boiling Water Reactors," *Proc. 5th Int. Conf. Nuclear Engineering (ICONE-5)*, Nice, France, May 26-30, 1997, ICONE5-2138 (on CD-rom), American Society of Mechanical Engineers, New York, NY (1997).

^{b)}Section 7.4.4 is part of a contribution submitted to Nuclear Science and Engineering (see Chapter 4).

7.1. INTRODUCTION

The theoretical models, developed within the framework of this thesis, are validated in this chapter. The analytical model describing the stability of BWRs under high-pressure conditions, outlined in Chapters 2 through 4, is compared with experimental data in Sections 7.2 through 7.4. The thermohydraulics module is first benchmarked in Section 7.2 against a set of steady-state void fraction measurements in the DESIRE (Delft Simulated Reactor) facility of the Interfaculty Reactor Institute. Type-II oscillations reported in two-phase flow literature are analyzed in Section 7.3. The complete BWR model, incorporating nuclear feedback effects, is validated in Section 7.4 using a series of well-prepared and well-documented experiments in the natural circulation Dodewaard reactor. During one measurement in the Dodewaard reactor (at the end of cycle 26), a large-amplitude oscillation of the reactor power was encountered. This instability is evaluated using modern bifurcation theory and direct model simulations. Section 7.5 focuses on BWR dynamics in the low-pressure range. The analytical model, developed and analyzed in Chapters 5 and 6, is used to explain the physical processes observed during the startup of the Dodewaard BWR. Our model calculations are compared with high-fidelity TRACG calculations (for the cycle 23 startup).¹ Conclusions and suggestions for future research are provided in Section 7.6.

7.2. THE DESIRE FACILITY

The DESIRE facility of the Interfaculty Reactor Institute is a natural circulation loop including a scaled model of one assembly of the Dodewaard BWR (consisting of 6×6 simulated fuel rods), with Freon-12 as a working fluid.² Operational experience with this facility is described in detail by Kok.³ Kok adopted the thermohydraulic module of our analytical BWR model⁴ to DESIRE by changing the appropriate dimensions and parameters (e.g. the friction factors) of the model. He also equipped the DESIRE facility with an artificial void reactivity feedback loop, to investigate *nuclear-coupled* instabilities.

The impact of the (artificial) void reactivity coefficient and fuel time constant on stability was consequently explored in model simulations and experiments. Kok's theoretical and experimental results are consistent with the parametric study presented in Chapter 3.⁵ For instance, increasing the magnitude of the void coefficient in the DESIRE feedback loop has a destabilizing effect (cf. Section 3.3.1). Increasing the value of the fuel time constant, another key parameter determining coupled neutronic-thermohydraulic stability, has a stabilizing effect in the DESIRE facility (cf. Section 3.3.3). A direct evaluation of the measurements in the Zuber-subcooling stability plane proved to be difficult, because, at present, only a very limited region of the operating plane can be studied with the DESIRE facility.

As an example of the analytical and experimental research on DESIRE, we here present

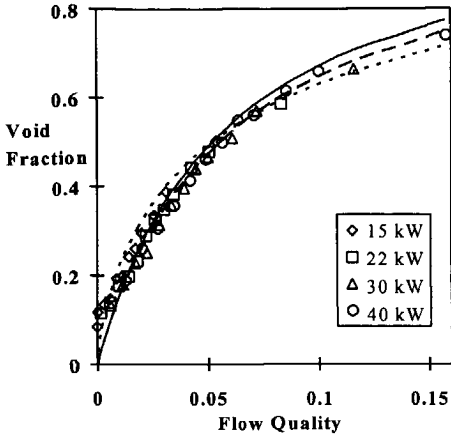


Figure 7-1. DESIRE facility void fraction measurements at different axial positions and power levels compared with the void fraction-flow quality relation used in our model: with $C_0=1$ (solid line), $C_0=1.04$ (dashed line) and C_0 calculated with Dix' relation [Eq. (7-1)] (dotted line). In the last case C_0 increases from 0 to 1.08 as the flow quality increases from 0 to 0.17.

used three different values of the void distribution parameter C_0 in the calculations: $C_0=1$ (no integral slip), a fitted value of $C_0=1.04$ (independent of the flow regime), and a flow regime dependent calculation of C_0 using the relation of Dix:⁶

$$C_0 = \beta \left[1 + \left(\frac{1}{\beta} - 1 \right)^b \right], \text{ with } \beta = \frac{1}{1 + \frac{1 - \chi}{\chi} \frac{\rho_g}{\rho_l}} \text{ and } b = \left(\frac{\rho_g}{\rho_l} \right)^{0.1}. \tag{7-1}$$

Good agreement between measurements and calculations is found in Fig. 7-1. The underestimation of the void fraction for low flow qualities is due to the occurrence of subcooled boiling. This non-equilibrium phenomenon is not taken into account in our model. The influence of the nonuniform void fraction distribution over the channel cross-section is visible for higher values of the void fraction. A void distribution parameter of $C_0=1.04$ correlates the measured data well. The Dix relation for C_0 in Eq. (7-1) is dependent on the flow regime, and correctly describes the measurements for small and large values of the void fraction.

7.3. THERMOHYDRAULIC STABILITY BENCHMARK

The thermohydraulic part of our dynamic model is benchmarked against the experimental data set of Saha et al.⁷ Saha et al. conducted their experiments with a forced-convection

void-fraction measurements in the heated section of this facility at different axial positions and several power levels. The void fraction was measured with gamma transmission tomography. The mass flux density was kept constant during the measurements with a flow control valve. The results of the measurements are depicted in Fig. 7-1. The thermohydraulic model proposed in Chapter 2 employs the homogeneous flow model, i.e. void slip is neglected. Here, we also investigate the influence of the integral void slip that originates from the cross-sectional averaging of a nonuniform void profile in the channel (see Appendix B). Therefore we used three different values of the void distribution parameter C_0 in the calculations: $C_0=1$ (no integral slip), a

Freon-113 loop. They investigated the effect of the operational conditions and the inlet and outlet flow restrictions on the high power Type-II stability boundary. The influence of the system pressure on thermohydraulic stability was investigated for a pressure of 12.1 bar (set 1), 13.8 bar (set 2), and 10.3 bar (set 3). The influence of the system pressure on the experimentally determined stability boundary is eliminated to a large extent, as can be seen in Fig. 7-2, by converting the actual operating conditions to the dimensionless Zuber number N_{Zu} and subcooling number N_{sub} . It should be noted, that the flow velocity was kept at approximately the same value (~ 1 m/s) in sets 1 through 3. Changes in the Froude number [which is proportional to the square of the flow velocity, see Eq. (2-25)] are therefore small during these experiments, and not expected to affect the location of the stability boundary in Fig. 7-2.

Fig. 7-2 demonstrates that our model correctly predicts the measured trends in the dimensionless plane. Compared with the exact solutions of the differential two-phase flow equations (obtained without simplifying spatial assumptions in the one- and two-phase regions, and with $C_0=1$), the quantitative agreement with the measurements is even better in the region of low subcooling and high Zuber numbers. This apparent paradox can be explained as follows. The equilibrium model overestimates the destabilizing fluctuations of the boiling boundary in the low subcooling and high Zuber number region, because subcooled

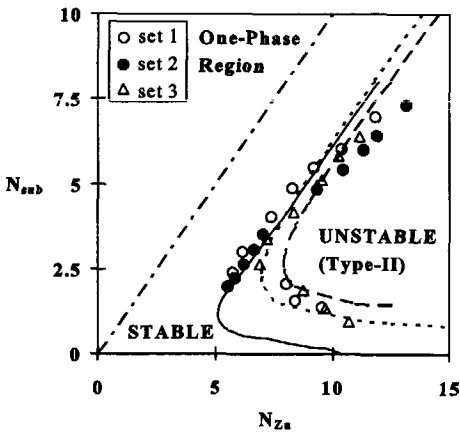


Figure 7-2. Comparison of the stability boundaries calculated with our model [dotted line ($C_0=1$), and dashed line ($C_0=1.07$)] with experimentally determined points on the threshold of instability (sets 1-3 of Ref. 7) and the exact solutions of the differential two-phase flow equations (solid line). The operating conditions are represented with dimensionless Zuber-subcooling coordinates, which absorb the influence of pressure on thermohydraulic stability.

boiling is neglected. Subcooled boiling effectively reduces the volume of the one-phase fluid in the channel, and therefore diminishes the oscillations of the boiling boundary, resulting in a more stable system than predicted by the exact solutions of the equilibrium model. Our low-dimensional model was derived using spatial assumptions regarding the one-phase enthalpy and two-phase quality. Karve et al.⁸ have demonstrated that these approximations lead to a *nonconservative* prediction of thermohydraulic stability. This explains the good agreement with the experimental data: the simplifying assumptions used in our model partly compensate for the neglect of subcooled boiling. The exact solutions of the differential model solutions are, however, more accurate for higher values of the

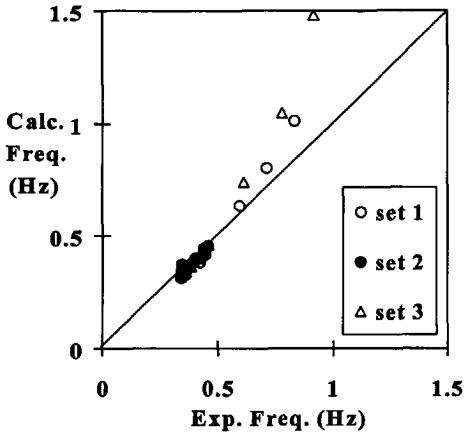


Figure 7-3. Experimental versus calculated resonance frequencies for data sets 1-3 of Ref. 7. The oscillations with a relatively low frequency are located on the high subcooling branch in Fig. 7-2. The points on the low subcooling branch in Fig. 7-2 have a significantly higher resonance frequency.

operating points. At lower values of the subcooling number, the length of the single-phase region decreases. The void fraction therefore increases rapidly. Hence, the velocity of the two-phase mixture increases, and the oscillation frequency becomes higher. Fig. 7-3 shows that our model overestimates the experimentally measured resonance frequency at very low subcooling numbers.

This result is rather surprising, because our model neglects the influence of subcooled boiling. This phenomenon causes a rapid increase of the void fraction (and the velocity of the two-phase mixture) in the lower part of the core. Hence, the present model, that does not account for subcooled boiling, is expected to *underestimate* the measured oscillation frequency. Since this is not the case in Fig. 7-2, we suggest, as an interesting topic for future research, to evaluate the impact of the spatial assumptions in the model on the predicted oscillation period.

7.4. DODEWAARD HIGH-POWER (TYPE-II) EXPERIMENTS

7.4.1. Introduction

From February 1992 (cycle 23) through January 1996 (cycle 26), a team of specialists from several Dutch institutes (GKN, KEMA and IRI) has performed a large number of measurements in the natural circulation cooled Dodewaard BWR. The aim of these unique

subcooling number. The discrepancy with the experimental data for the high subcooling branch can be explained partly by the influence of a nonuniform void distribution over the channel flow area. A value of $C_0=1.07$, calculated with Eq. (7-1), already leads to a better prediction of the experimental stability boundary for high values of the subcooling number, in agreement with results of Rizwan-uddin and Dorning.⁹

The measured resonance frequencies for sets 1-3 are compared with our model (with $C_0=1.0$) in Fig. 7-3. The agreement between model and experiment is excellent for points located on the highly subcooled branch in Fig. 7-2. The oscillation frequency is relatively low for these

experiments was to create a comprehensive and well-documented database of the statics and dynamics of a natural circulation cooled BWR, for a wide range of operating conditions. A summary and evaluation of the experimental data is presented in Ref. 10. The measurements at relatively high power levels, i.e. when the Type-II feedback mechanism is dominant, are compared with the predictions of our stability model for natural circulation BWRs in this section.

The influence of the operating conditions, like the power and pressure level, on the natural circulation flow rate in the Dodewaard BWR is investigated first in Section 7.4.2. Results of our analytical model are also compared in that section with predictions of the high-fidelity RAMONA BWR code.¹¹ A model simulation of the Dodewaard Type-II stability experiments is next provided in Section 7.4.3. Data set II from Chapter 3 is used as the input data for the analytical model in Sections 7.4.2 and 7.4.3. The nonlinear dynamics governing an unstable reactor oscillation, which was encountered at the end of the cycle 26 measurements, is analyzed in detail in Section 7.4.4. A fine-tuned friction and void reactivity model is used in that section, to simulate the experimental conditions as accurately as possible with our theoretical model. Experiments performed during the reactor startup phase, at very low power and pressure levels, are evaluated in Section 7.4.5.

7.4.2. Dodewaard Natural Circulation Flow Predictions

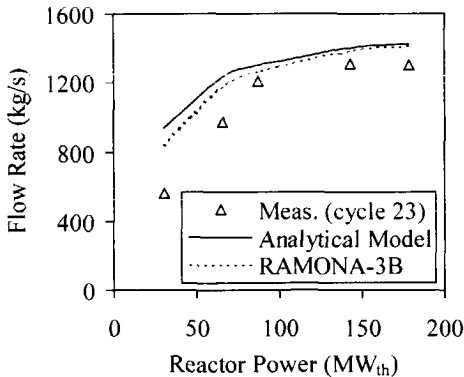


Figure 7-4. Measured and calculated natural circulation flow rates for the Dodewaard BWR as a function of the thermal reactor power. The measurements were performed during cycle 23, at the (nominal) pressure of 75.5 bar. The experimental results are compared with our analytical model and RAMONA-3B calculations. Note that both models systematically overestimate the flow rate at low power levels. The agreement between model and experiment improves, however, at higher power levels.

Experimental values of the Dodewaard natural circulation flow rate as a function of the thermal reactor power are compared with the predictions of our model in Fig. 7-4. The model calculations were performed with an axially peaked power profile (with a peaking factor f_p equal to 1.4). The measurements in Fig. 7-4 were carried out during cycle 23, at the nominal reactor pressure of 75.5 bar.¹⁰ The flow rate was determined indirectly during these experiments. By correlating the noise signals of a down-stream and an up-stream thermocouple, the transit time of the coolant between both thermocouples was measured. This transit time can be linked with the flow rate if accurate information about the (nonuniform) flow field in the

downcomer is available. Stekelenburg performed numerical fluid flow calculations to establish a calibration curve between the measured transit time and the flow rate.¹² The total error in the calculated flow rate was estimated to be rather small ($\pm 5\%$) for flow rates between 579 kg/s and 1477 kg/s. It should be noted, however, that this calibration curve is based on theoretical models instead of experiments. Hence, it remains rather difficult to provide a good estimation of the experimental uncertainty in the flow rate. During one experiment in Fig. 7-4 a rather small flow rate (560 kg/s) was measured, at the lower end of the calibration curve. Relatively large experimental errors are to be expected in this case.

Figure 7-4 shows that the flow rate increases rapidly if the power is increased at an initially low power level. At higher power levels, pressure losses due to friction become important and limit a further increase of the flow rate. The model predictions agree quite well with the experimental data for high flow rates. However, an overestimation of the flow rate is visible at low power levels. To check whether this is due to model limitations, accurate 3D-calculations were performed using the RAMONA-3B code.¹¹ Carry under is incorporated in RAMONA. Figure 7-4 shows that this high-fidelity model has similar problems predicting the measured flow rate at a low reactor power. The RAMONA results agree very well, however, with the flow rate predictions of our analytical model, especially at higher power levels.

The measured flow rate at the end of cycle 26 is shown in Fig. 7-5. During these

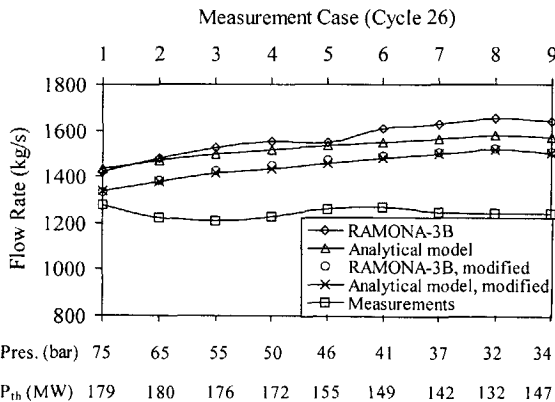


Figure 7-5. Measured and calculated flow rates for the Dodewaard BWR (cycle 26, Jan. '96). The RAMONA-3B code and the analytical model both overestimate the flow rate for all measured cases. The agreement between the two alternative models improves when some modifications are made in the codes. Bypass flow, carry under, and local slip are neglected in the modified RAMONA model. The adjusted analytical model, on the other hand, employs a bottom-peaked power profile, C_0 is set equal to 1.11, and the two-phase friction model in the RAMONA code is adopted.

experiments, the power and pressure level were decreased simultaneously from the nominal operating conditions (case 1: $P_{th}=179$ MW and $P=75.2$ bar) to the final measurement at a reduced pressure and relatively high reactor power (case 9: $P_{th}=147$ MW and $P=34.4$ bar).¹⁰ The impact of such a strong pressure reduction on reactor stability is discussed in detail in Sections 7.4.3 and 7.4.4.

Figure 7-5 shows that the measured flow rate remains almost constant when we change the power and pressure level simultaneously. At high powers and pressures (e.g. case 1), changing the power has only a

small effect on the flow rate, see Fig. 7-4. The effect of a pressure reduction on the flow rate will be small as well at high pressures, because the fluid properties (densities, enthalpies) are only weakly dependent on the pressure level under these circumstances. At lower pressures, however, the void production will increase due to a smaller vapor to liquid density ratio. Because the power level decreases as well at lower pressures during these experiments, the void fraction increase will, however, be limited. The net effect on the recirculation flow is therefore small, as Fig. 7-5 confirms.

Our analytical model and the RAMONA code both overestimate the measured flow rate for all cases shown in Fig. 7-5. This systematic deviation, encountered before in Fig. 7-4, is probably caused by an underestimation of the frictional pressure losses in the calculational models. A fine-tuned friction model, yielding the correct flow rate for measurement case 9, is therefore applied in Section 7.4.4.

The agreement between the predictions of our analytical model and the RAMONA code further improves when some modifications are made in both codes. Our analytical model neglects carry under and bypass flow (i.e. leakage flow paths in the fuel assemblies). Hence, these phenomena were neglected as well in a modified RAMONA model. Bypass flow is normally specified in RAMONA as a (user-defined) fraction of the total core flow rate. Comparative RAMONA calculations, with and without bypass channel, show that the effect of the bypass flow on the flow rate in the *heated* channels is very small. Accounting for bypass flow thus directly increases the total core flow, whereas the flow through the heated coolant channels remains essentially constant. Figure 7-5 shows that the calculated flow rate decreases significantly in the modified RAMONA model. This means that the (negative) effect of carry under on the flow rate is smaller than the (positive) contribution of the bypass flow to the total natural circulation flow rate. We also adjusted our analytical model, to simulate the thermohydraulic model in the RAMONA code as accurately as possible. For example, we used the same value of the void distribution parameter in our analytical model as in the RAMONA code ($C_0=1.11$). Local slip, not modeled in the analytical model, was neglected in the RAMONA code by setting the local drift velocity of the vapor equal to zero. Furthermore, we incorporated RAMONA's model for the two-phase friction multiplier¹¹ (Becker's correlation) in our model. Finally, the axial power profile, calculated with the RAMONA code, was approximated in our analytical model with a bottom-peaked power profile. Figure 7-5 shows that the agreement between both modified models is excellent (the relative difference between the models is less than 1% for all cases in Fig. 7-5), and demonstrates that the results of our analytical model are consistent with the predictions of this stripped RAMONA model.

7.4.3. Dodewaard Type-II Stability Tests

The model prediction of the dependence of the reactor decay ratio (DR) on the operating conditions is compared with the experimental data in Fig. 7-6. The error in the experimentally determined decay ratio is approximately 4% ($\pm 2\sigma$ error).¹³ The calculation of the contours

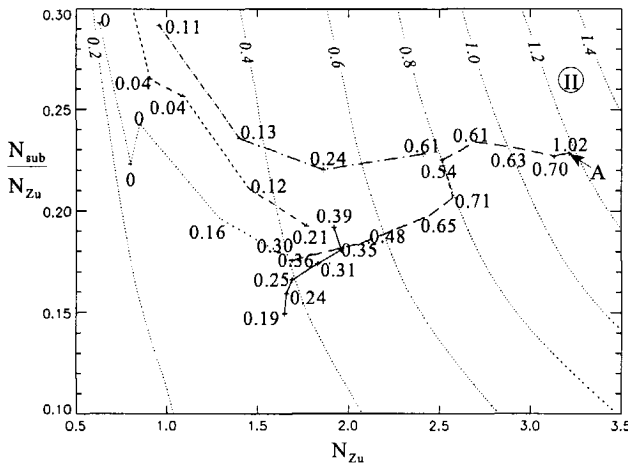


Figure 7-6. Measured and calculated decay ratios for different Dodewaard stability tests: (a) cycle 23, Sep. '92 (solid line), (b) cycle 23, Jan. '93 (dotted line), (c) cycle 24, Jan. '94 (dashed line), (d) cycle 25, Jan. '95 (dash dot), and (e) cycle 26, Jan. '96 (long dashes). The unstable case at the end of cycle 26 is denoted with an "A". Unstable Type-II oscillations are predicted in region II, where the decay ratio is larger than unity.

with equal decay ratio in Fig. 7-6 is performed with an axially peaked power profile (with a peaking factor of 1.4), to improve the accuracy of the predictions. The calculations were performed with the developed frequency-domain code, which is free from numerical

problems and provides exact solutions for the two-phase flow dynamics in the riser.⁴

The strong influence of the system pressure and the thermal power on reactor stability, predicted in Section 3.3.6, is confirmed by the experimental data in Fig. 7-6. During cycle 23, in September 1992, the pressure was reduced from 75.5 bar (DR=0.19) to 60 bar (DR=0.39). The thermal power level was approximately 165-172 MW during this session. At the end of the same cycle, in January 1993, the power decreased from 179 MW (DR=0.30) to 30 MW (DR=0), keeping the pressure at its nominal value (cf. Fig. 7-4). At the end

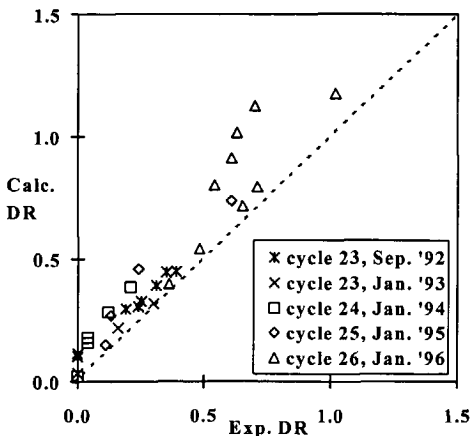


Figure 7-7. Measured versus calculated decay ratios for the Dodewaard BWR.

of cycle 24, in January 1994, the same shutdown procedure was followed, but under reduced pressure conditions of 60 bar. At a pressure of 60 bar, the DR decreased from 0.21 (148 MW) to 0 (20 MW). At the end of cycle 25, in January 1995, the pressure was reduced to 45 bar

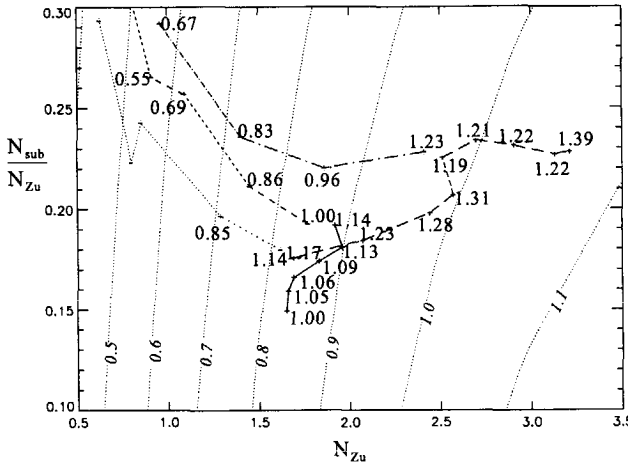


Figure 7-8. Measured and calculated resonance frequencies (Hz) for different Dodewaard stability tests: (a) cycle 23, Sep. '92 (solid line), (b) cycle 23, Jan. '93 (dotted line), (c) cycle 24, Jan. '94 (dashed line), (d) cycle 25, Jan. '95 (dash dot), and (e) cycle 26, Jan. '96 (long dashes).

during the shutdown before the reactor power was diminished from 154 MW (DR=0.61) to 51 MW (DR=0.11). The shutdown measurement session of January 1996 (cf. Fig. 7-5) ended in an unstable reactor oscillation (with a DR of 1.02) at a pressure as low as 34 bar (this case is denoted by an "A" in Fig. 7-6). At 80% full power (f.p.) initially, the reactor scrambled automatically at an oscillation amplitude of 200% f.p. This case is described in more detail in

Ref. 10 and Section 7.4.4. A comparison of the measured DR versus the calculated DR in Fig. 7-7 shows that the theoretical model predicts the trends quite well. However, the calculated DR is systematically too high (especially for several conditions during the cycle 26 experiments), indicating that further tuning or refining of the theoretical model is desirable. Hence, a fine-tuned void reactivity and friction model is applied in the next section.

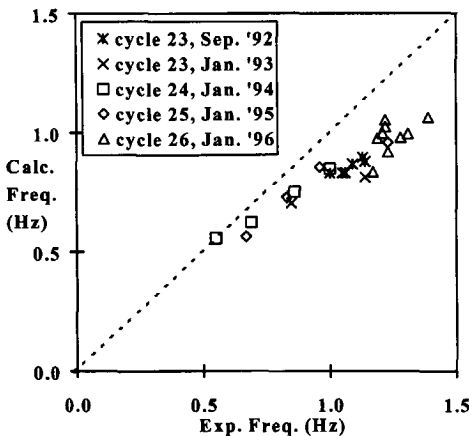


Figure 7-9. Measured and calculated resonance frequencies for the Dodewaard BWR.

The measured operating points and the calculated contours of equal resonance frequency are depicted in the stability plane in Fig. 7-8. Notice that reducing the power

and increasing the pressure both has a frequency lowering effect (and vice versa). Typical trajectories in the stability plane, as a function of the operating conditions, have been presented before in Fig. 3-12. Again, the measured trends in the resonance frequency are predicted successfully by the model. Figure 7-9 shows that the quantitative agreement is not entirely satisfying: the calculated resonance frequency is systematically too low.

No experiments have been performed to date that investigate the influence of the feedwater inlet temperature on reactor stability. Experimental work on this topic, for instance in the DESIRE facility, is strongly recommended, since our model predicts a strong dependence of reactor stability on this independent variable (see Fig. 3-12).

7.4.4. Nonlinear Analysis of the Dodewaard Cycle 26 Instability

The experimentally observed Type-II instability, at the end of the cycle 26 measurements, is analyzed in more detail in this section. We use the experimental data shown in Fig. 7-10 to validate the nonlinear (Hopf-bifurcation) model analyzed in Chapter 4. Figure 7-10a presents

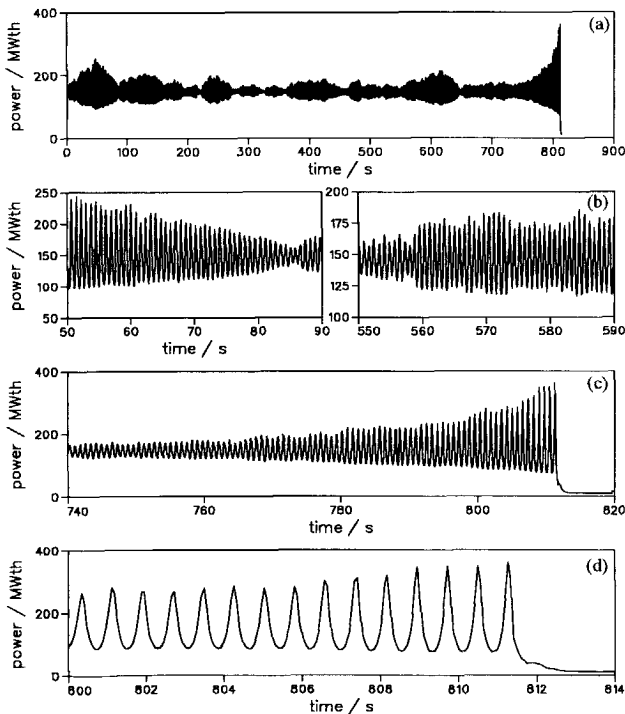


Figure 7-10. Time trace of the measured thermal reactor power of the Dodewaard reactor at the end of cycle 26 (taken from Ref. 10). Figure 7-10a shows the last 800 seconds of the signal, the other graphs present enlargements of certain time intervals.

the measured time trace of the thermal reactor power. The amplitude of the power oscillations increases and decreases several times during the experiment, before it diverges to the high-flux scram level. Details of the time trace are visible in Figs. 7-10b through 7-10d. The diverging oscillation after $t=740$ s is probably induced by the manual control of the feedwater flow during the experiment. The nonlinear character of the growing oscillations is clearly visible in Fig. 7-10d.

The operating point of interest is located in the Type-II unstable region, so the influence of the gravitational pressure drop over the riser is

relatively small, and therefore only one riser node was used in the nonlinear calculations. The core inlet and outlet friction coefficients and the void reactivity model were adjusted to simulate the experiment in Fig. 7-10 as accurately as possible. The friction coefficients, listed in Table 7-1, were fine-tuned to match the measured flow rate at the given operating conditions. The void reactivity coefficients in the neutronics model were also adjusted to simulate the diverging oscillation of the reactor power in Fig. 7-10d. Applying the void reactivity coefficients listed in Table 7-2, the model prediction of the decay ratio is equal to 1.02, identical to the experimentally observed decay ratio in Fig. 7-10d.

Table 7-1. Frictional Numbers
Applied in Section 7.4.4

Λ_C	1.03
Λ_R	0.10
$k_{C,i}$	9.41
$k_{C,e}$	3.49
$k_{R,e}$	1.00
$k_{D,i}$	1.00

Table 7-2. Void Reactivity Coefficients
Applied in Section 7.4.4

$\Gamma_{a,1}$	-0.017
$\Gamma_{a,2}$	-0.288

The bifurcation curves in the Type-II instability region for this Dodewaard reactor model

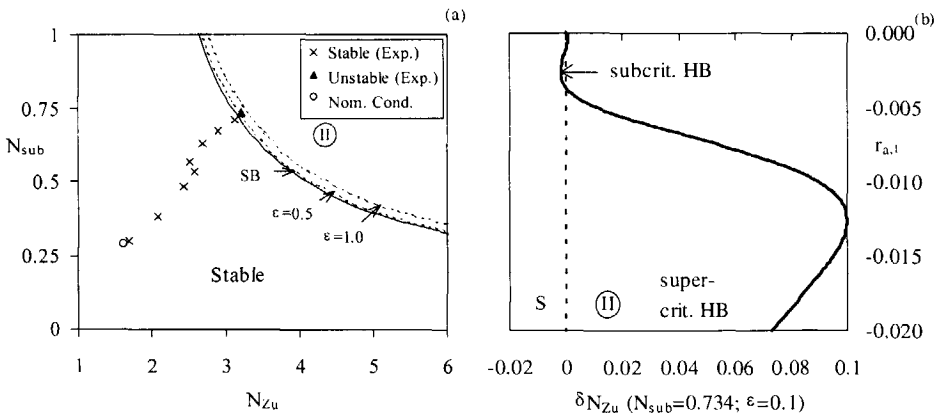


Figure 7-11. (a) Bifurcation diagram in the Type-II instability region for the natural circulation Dodewaard reactor. A supercritical Hopf bifurcation occurs when the stability boundary is crossed. Two contours of equal amplitude of the relative reactor power N^* are shown. The stable and the unstable cases during the cycle 26 experiments are also plotted. (b) Influence of the void reactivity feedback on the bifurcation mode, for a subcooling number equal to the value for the unstable experimental case ($N_{sub} \approx 0.734$). The Hopf bifurcation is strongly supercritical for the values of the void reactivity coefficients used in Fig. 7-11a (see Table 7-2).

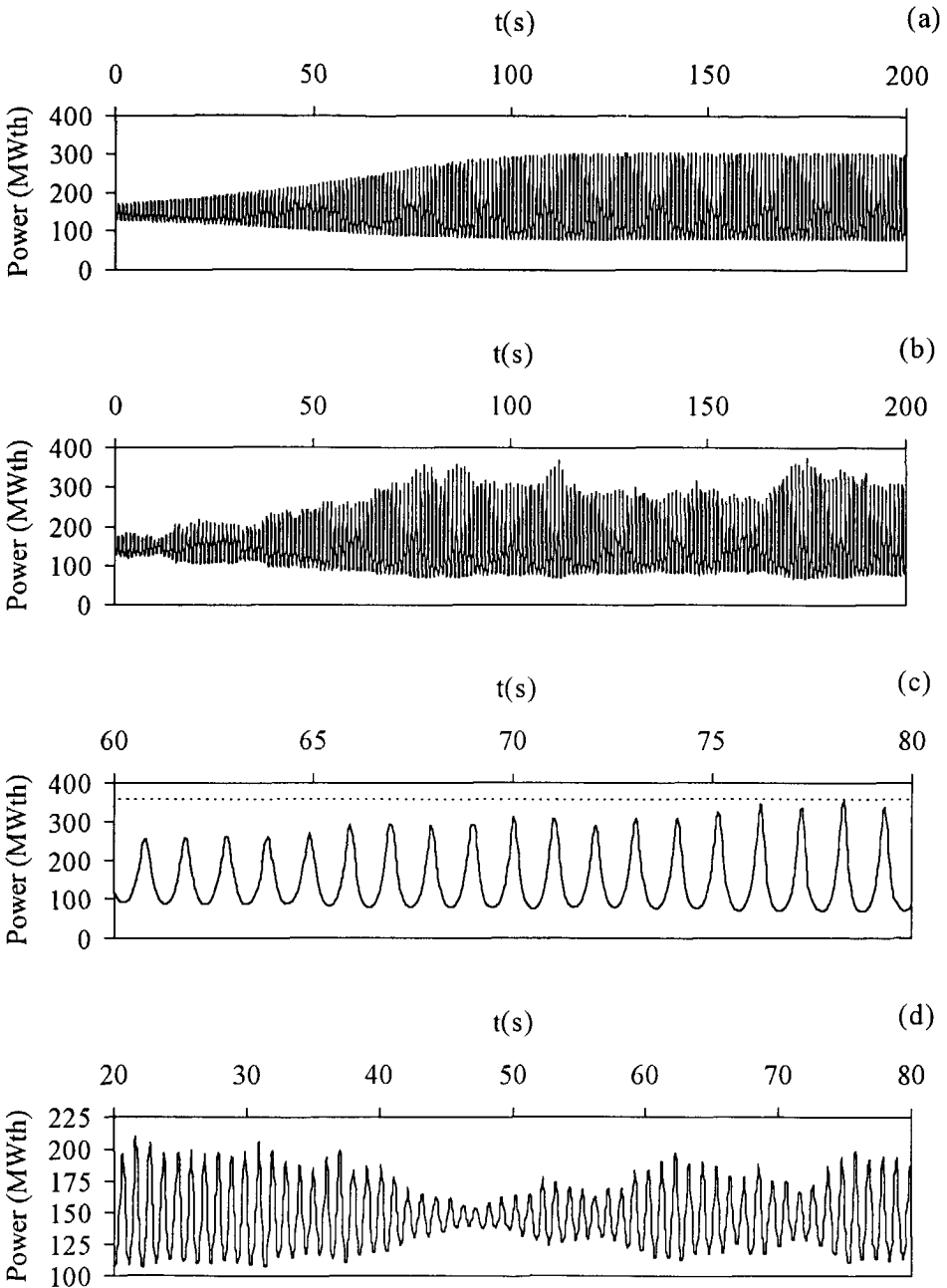


Figure 7-12. Nonlinear model simulations of the unstable case in Fig. 7-10. (a) The development of a stable nonlinear oscillation at the unstable experimental conditions ($DR=1.02$; $\sigma_{noise}=0$). (b) The influence of stochastic fluctuations in the thermohydraulic subsystem on the reactor power ($DR=1.02$; $\sigma_{noise}=0.02$). (c) Enlargement of Fig. 7-12b. The reactor scram level (indicated with the horizontal dotted line) is reached at $t=78$ s. (d) Simulation of the time trace in Fig. 7-10b ($DR=0.98$; $\sigma_{noise}=0.02$).

are presented in Fig. 7-11. The model predicts the occurrence of a supercritical Hopf bifurcation when the Type-II stability boundary in the Zuber-subcooling plane is crossed (see Fig. 7-11a). The power oscillations thus evolve to *stable* nonlinear oscillations (limit cycles) in the linearly *unstable* region. Two contours of equal amplitude of the normalized reactor power N^* are shown in the unstable Type-II region. Also shown are the experimental points at which the reactor was operated. Notice that all measured stable cases during the cycle 26 measurements are indeed located on the stable side of the stability boundary. Figure 7-10b illustrates the strong influence of the void reactivity feedback on the reactor bifurcation mode. The subcooling number in the calculations of Fig. 7-11b is equal to the value for the unstable experimental case ($N_{sub} = 0.734$). The void reactivity coefficient $r_{a,2}$ is changed proportional to $r_{a,1}$ in Fig. 7-11b: $r_{a,2} = r_{a,1} \times 0.228/0.017$. This implies that the reactor without nuclear feedback is simulated in Fig. 7-11b by setting $r_{a,1}$ equal to zero, whereas the nominal values for the reactivity coefficients (see Table 7-2) are obtained for $r_{a,1} = -0.017$. Figure 11b shows that the Hopf bifurcation is strongly supercritical for the nominal values of the void reactivity coefficients, as Fig. 7-11a confirms. The region in the $N_{zu} - r_{a,1}$ space where subcritical bifurcations exist is rather small, and located at much smaller values of $r_{a,1}$ and $r_{a,2}$.

The BifDD bifurcation code predicts a limit-cycle oscillation amplitude of 105 MWth under the measured unstable conditions. This result agrees well with the time-domain oscillation amplitude of 112 MWth in Fig. 7-12a. Apart from the deterministic time trace presented in Fig. 7-12a, the influence of noise on reactor dynamics is also simulated with the model, by adding a Gaussian white noise source (with $\sigma_{noise} = 0.02$) to the right hand side of the (normalized) core exit quality ODE [Eq. (B-9)]. This noise source is included in the thermohydraulic subsystem to model the influence of stochastic fluctuations in the void production on the reactor power. Notice that the strength of the noise source is a 'free' input parameter in our model. However, simulations with other noise levels lead to similar results.

The time evolution of the reactor power, under the influence of noise, is depicted in Fig. 7-12b. An enlargement shown in Fig. 7-12c strikingly resembles the measured time trace in Fig. 7-10d. Because of the stochastic excitations, the reactor scram level (indicated with the horizontal dotted line) is reached in Fig. 7-12c, whereas the oscillations without noise in Fig. 7-12a actually saturate at a lower amplitude. The power oscillations before the final diverging oscillation ($0 < t < 740$ s in Fig. 7-10a) can also be simulated with our stochastic model, by reducing the decay ratio from 1.02 to 0.98 (compare Fig. 7-12d with Fig. 7-10b).

7.5. DODEWAARD STARTUP (TYPE-I) EXPERIMENTS

7.5.1. Natural Circulation Flow Predictions

The measured operating conditions during the Dodewaard startup for cycles 24-26 are

summarized in Table 7-3. Table 6-1 contains the measurement results of the cycle 23 experiments.

Table 7-3. Operating Conditions During the Startup of the Dodewaard BWR (Cycles 24-26)
(Cycle 23 Startup Data are Summarized in Table 6-1)

Case	$P_{R,e}$ (bar)	P_{th} (MW)	ϕ (kg/s)	h_{fw} (J/kg)	T_{sub} (K)	N_{Zu}	$N_{subc,i}$	N_{flash}	$N_{Zu} - N_{subc,i} + N_{flash}$
Cycle 24									
1	2.3	4.3	4.66E2	3.35E5	7.3	2.6	8.8	7.1	1.0
2	3.8	2.0	6.16E2	3.35E5	7.0	0.6	5.7	3.2	-1.9
3	5.1	1.4	7.46E2	4.01E5	3.5	0.3	2.2	2.0	0.05
4	7.6	3.4	8.25E2	3.38E5	2.5	0.4	1.2	1.0	0.3
5	10.1	3.3	7.55E2	3.64E5	2.2	0.4	0.8	0.6	0.2
Cycle 25									
1	2.0	4.5	3.96E2	N.A.	9.0	3.6	12.0	8.7	0.2
2	2.0	4.5	3.72E2	N.A.	8.2	3.8	11.0	8.7	1.5
3	3.5	4.5	8.71E2	3.12E5	3.7	1.0	3.2	3.7	1.5
4	3.4	2.7	4.69E2	3.13E5	3.1	1.2	2.7	3.6	2.1
5	4.9	3.0	5.98E2	3.26E5	2.7	0.8	1.8	2.2	1.1
6	4.8	3.1	3.95E5	3.21E5	2.8	1.2	1.9	2.0	1.3
Cycle 26									
1	3.1	6.6	4.92E2	3.97E5	6.4	3.0	6.2	4.6	1.4
2	3.1	6.5	4.93E2	3.25E5	6.5	3.0	6.3	4.6	1.2
3	3.1	6.5	5.75E2	0.91E5	6.7	2.5	6.5	4.6	0.6
4	4.2	6.7	5.86E2	3.10E5	5.5	2.0	4.1	2.7	0.6
5	4.2	6.7	4.88E2	3.54E5	5.9	2.4	4.4	2.7	0.7
6	4.2	6.7	4.81E2	3.62E5	6.0	2.4	4.5	2.7	0.6

The measured natural circulation flow rates are compared with the predictions of our

analytical model in Fig. 7-13. The 'error bars' in Fig. 7-13 reflect the influence of the experimental uncertainties on the calculated flow rate. Most measurement equipment is calibrated under nominal conditions and not fine-tuned for the reactor startup range. The measurement accuracy is therefore not optimal. Furthermore, stating an accurate heat balance of the reactor vessel is difficult under low-power conditions, because phenomena like control rod cooling become important. Control rod cooling, for instance, dissipates ~4 MW under nominal conditions. Uncertainties of ± 0.5 K in the subcooling,¹ and ± 1 MW in the thermal power¹⁴ are accounted for in the calculations in Fig. 7-13. The experimental error in the pressure level is neglected here, but can be important as well, especially in the low pressure range. For instance, if we decrease the pressure with 1 bar (from 5.1 to 4.1 bar) for case 3 of cycle 24, the calculated flow rate increases from 430 kg/s to 730 kg/s, close to the measured flow rate of 746 kg/s. Figure 7-13 shows that the error bars are relatively large in the low power and pressure range. At higher pressures, for instance for cases 6 through 9 of cycle 23,

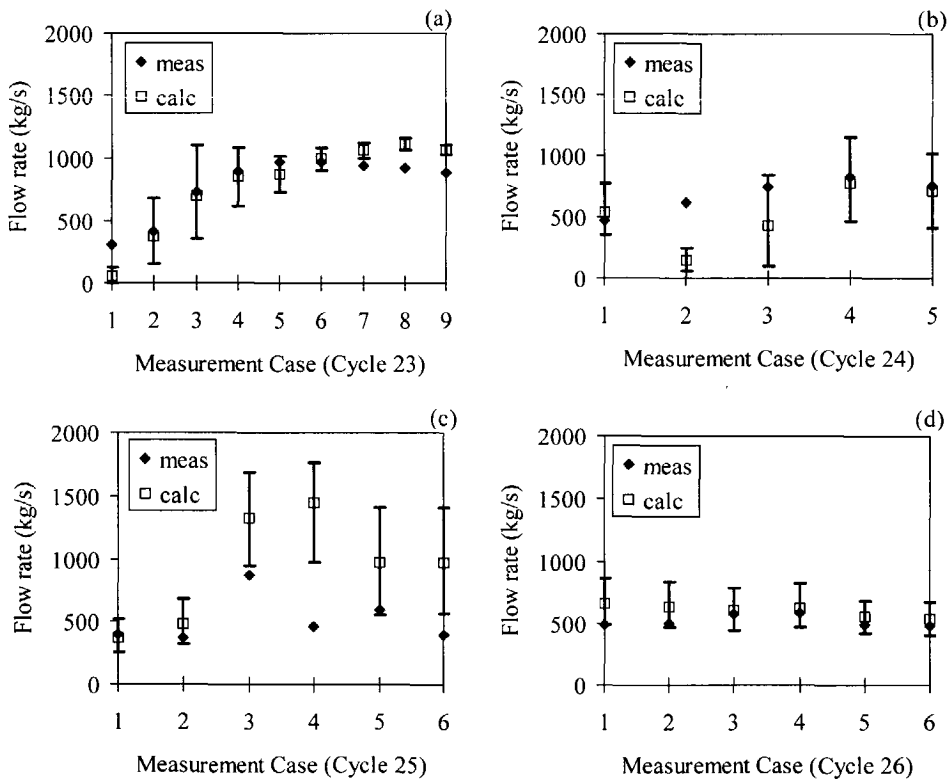


Figure 7-13. Measured vs. calculated flow rates during the startup phase of the Dodewaard BWR (cycles 23-26). The 'error bars' reflect the impact of the uncertainties in the measured subcooling (± 0.5 K) and thermal reactor power (± 1 MW) on the calculated flow rates.

the experimental inaccuracies become less important. The impact of the operating conditions on the void production and natural convection has been discussed in detail in Section 6.2.2.

We now discuss the experimental data and model results for each cycle in more detail. The agreement of the model predictions with the cycle 23 experiments is satisfactory for cases 2 through 6. The measured flow rate for case 1 is significantly larger, however, than the calculated flow rate. TRACG simulations by Wouters et al. of the cycle 23 startup¹ indicate that subcooled boiling starts at the exit of the hot channels at the low power and pressure conditions of case 1. The voids are consequently collapsed at the entrance of the riser section, due to mixing with the subcooled water from the bypass. The influence of local power peaking and subcooled boiling is not included in our theoretical models, and the steam production at the core exit is therefore underestimated. Furthermore, single-phase convection of the fluid, very important in the low-power regime, is neglected in the model calculations.

The calculated flow rates for cases 7 through 9 in Fig. 7-13a are systematically too high, compared to the measurements. This overestimation of the flow rate is possibly caused by an underestimation of the friction losses in the calculations, see Section 6.4.2. As an example, we repeated the calculation for case 9 with the fine-tuned friction model in Table 7-1. The model then yields a natural circulation flow rate of 890 kg/s (instead of 1060 kg/s), much closer to the measured value of 882 kg/s. We will not perform all flow calculations with the fine-tuned friction coefficients listed in Table 7-1, however, because this friction model depends on measured flow data (which hinders a 'fair' comparison between model and experiment).

Figure 7-13b shows that the agreement between the model predictions and the cycle 24 experiments is good for all cases except case 2. Going from case 1 to case 2, the pressure level increases and the power level decreases, while the subcooling remains almost constant (see Table 7-3). Because the void production diminishes as the pressure increases and the power decreases (see Section 6.2.2), one would expect a smaller flow rate for case 1 than for case 2. This is not the case, however, see Table 7-3, possibly due to the large uncertainties in the experimental conditions.

A systematic overestimation of the flow rate is visible for cases 3 through 6 of cycle 25 in Fig. 7-13c. This discrepancy could be caused by the phenomenon of carry under [the presence of voids in the (upper part) of the downcomer]. Due to carry under the pressure drop over the downcomer decreases, and the intensity of void flashing in the riser becomes smaller. The flow rate will therefore diminish, especially under low power and pressure conditions when the void production due to flashing is significant. The flow rate also becomes smaller because the density difference between core/riser and downcomer decreases when voids are dragged into the downcomer section. We already mentioned in Section 6.2.2 that the criterion $N_{\text{sub},c,i} \geq N_{\text{flash}}$ is not satisfied for all cases during cycle 25. Table 7-3 indeed shows that $N_{\text{sub},c,i}$ is smaller than N_{flash} for cases 3 through 6. The flashing number is calculated in Table 7-3 by

assuming that the coolant is single phase in the downcomer. This assumption is obviously violated when voids are dragged into this section. The gravitational pressure gain in the downcomer then becomes smaller and N_{flash} is overestimated in our model. Carry under also increases the frictional pressure losses in the downcomer, yielding an additional decrease of N_{flash} . Furthermore, the subcooling at the core inlet becomes smaller due to carry under. These three effects possibly explain why $N_{sub_{C,i}} < N_{flash}$ for cases 3 through 6 of cycle 25.

Our model correctly predicts the flow rate for all measurement cases during the cycle 26 startup. Table 7-3 shows that the experimental conditions are almost equal for cases 1-3 and cases 4-6. This measurement series therefore provides a good indication of the experimental accuracy.

7.5.2. Dodewaard Type-I Stability Tests

All measured operating conditions during the startup of the Dodewaard BWR are mapped into the dimensionless Zuber-subcooling stability plane in Fig. 7-14. The diagonal in Fig. 7-14 separates the cases with one- and two-phase flow. Two measured cases (case 1 of cycle 23 and case 2 of cycle 24) are located above the diagonal. These two cases are not considered further in the stability analysis. The convection in this region is presumably driven by single-phase density differences or subcooled boiling at the outlet of the hot channels (see the discussion in Section 7.5.1). Research on single-phase convection suggests that the natural convection is stable under these conditions,¹⁵ in agreement with the experimental results.

Below the diagonal, i.e. in the boiling region, the operating points are clustered in three different parts of the dimensionless map. In the early startup phase, at very low power levels, the flow rate will be small. The Zuber number (inversely proportional to the flow rate) will therefore be relatively large, yielding a group of points to the far right in Fig. 7-14. At higher power levels the flow rate rapidly increases and the Zuber number becomes smaller. Many

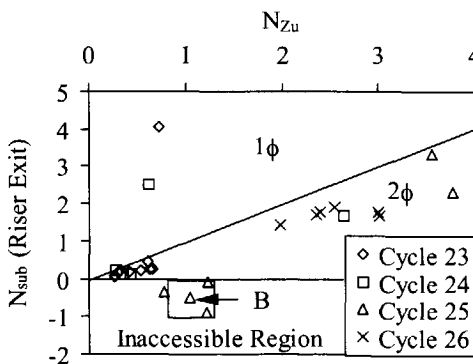


Figure 7-14. Mapping of the startup conditions of the Dodewaard BWR into the dimensionless Zuber-subcooling stability plane. The diagonal separates the regions with one-phase (1φ) and two-phase (2φ) flow. Our model predicts the occurrence of boiling for most startup conditions. Note that four measurements during the cycle 25 startup have a *negative* subcooling with respect to the riser exit, possibly due to the influence of carry under. A self-sustained flow oscillation was measured in point B. The influence of the experimental uncertainties in the operating conditions on the position of point B is indicated by the box surrounding this point.

operating points are therefore located close to the origin in Fig. 7-14. Finally, four cases (cases 3-6 of cycle 25) have a negative subcooling (with respect to the riser exit), possibly due to the influence of carry under (see Section 7.5.1). A significant decrease of Type-I stability was encountered during these experiments. Low-frequency fluctuations (≤ 0.1 Hz) of the reactor power, with a modest amplitude of only a few percent, were measured.¹⁶ The stability characteristics during the cycle 25 experiments are summarized in Table 7-4.

Table 7-4. Stability Characteristics
Dodewaard Cycle 25 Experiments

Case	DR	f (Hz)
1	0	N.A.
2	0.5	0.05
3 ("B" in Fig. 7-14)	1.0	0.07
4	0.4	0.1
5	0	N.A.
6	0.36	0.05

A self-sustained oscillation (i.e. with a DR equal to unity) was encountered at measurement case 3. This case is labeled with a "B" in Fig. 7-14. The influence of the experimental uncertainties in the operating conditions on the location of point B is indicated by the box surrounding this point in Fig. 7-14. An evaluation of the stability characteristics of cases 3-6 in Table 7-4 is not possible with our present BWR model, because we did not consider the influence of carry under. Future analysis of these experiments, with an extended model incorporating carry under, is strongly recommended.

We found in Chapter 6 that the location of the stability boundary in the dimensionless Zuber-subcooling plane is strongly dependent on the system pressure during the reactor startup. A direct evaluation of stability is therefore not possible in Fig. 7-14, because the operating points mapped in this plane were measured over a wide range of pressure levels [from 2.0 bar (cases 1 and 2 of cycle 25) to 69.7 bar (case 9 of cycle 23)]. Notice that the stability analysis in the high power and pressure range, where the stability characteristics are almost invariant in the dimensionless plane, was performed directly for all measured operating points in Fig. 7-6.

The operating points located below the diagonal and above the horizontal axis have been evaluated with the present model, see Table 7-5.

Table 7-5. Calculated Margin to the Type-I Stability Boundary for the Dodewaard BWR (Cycles 23-26)^{c)}

Cycle	Case	$N_{Zu}(\text{Exp.}) - N_{Zu,c}(\text{Calc.})$	$\sigma N_{Zu}(\text{Exp.})$	$Z_{bb}^*(\text{Exp.})$	$Z_{bb,c}^*(\text{Calc.})$
23	2	-0.55	0.48	2.46	>1
23	3	-0.07	0.11	1.60	1.20
23	4	0.06	0.05	0.85	1.16
23	5	0.07	0.03	0.80	1.06
23	6	0.18	0.02	0.58	1.04
23	7	0.29	0.02	0.47	1.02
23	8	0.40	0.01	0.41	1.02
23	9	0.37	0.01	0.42	>1
24	1	-1.63	0.61	2.17	>1
24	3	-0.86	0.20	2.64	>1
24	4	-0.22	0.13	1.78	1.02
24	5	-0.11	0.11	1.68	1.10
25	1	-2.82	0.79	2.62	>1
25	2	-1.58	0.84	1.98	>1
26	1	-0.42	0.46	1.47	>1
26	2	-0.54	0.46	1.61	>1
26	3	-1.14	0.39	2.22	>1
26	4	-0.60	0.30	2.00	>1
26	5	-0.50	0.35	1.84	>1
26	6	-0.54	0.36	1.92	>1

No major oscillations were measured for the cases listed in Table 7-5, case 2 of cycle 25 (see Table 7-4) excepted. A weak resonance was however encountered in the normalized auto-power spectral density (NAPSD) of the neutron power noise for cases 1-5 during

^{c)}The experimental position of the boiling boundary, $Z_{bb}^*(\text{Exp.})$, was estimated in Table 7-5 with the theoretical model, on the basis of the measured operating conditions.

cycle 24.¹⁷ This resonance peak was located at a low frequency (below 0.2 Hz), and became more pronounced at lower pressures. This suggests that this resonance is caused by small-amplitude flow oscillations, probably induced by void flashing.

The third column of Table 7-5 lists the *calculated* margin to the Type-I stability boundary (located at $N_{Zu,c}$). Only the Zuber number is changed in the calculations, the subcooling number is kept constant at the experimental value. Because all cases listed in Table 7-5 are stable, the *experimental* margin to the Type-I stability boundary is always positive. Our model thus provides a conservative estimation of stability. Notice, however, that the experimental uncertainties are relatively large, especially in the low-pressure regime where our model predicts the occurrence of unstable Type-I oscillations. The fourth column lists the (substantial) experimental uncertainty in the Zuber number, due to the experimental uncertainty in the thermal power. The experimental uncertainty in the subcooling number is also significant, see the box surrounding point B in Fig. 7-14.

The results for cases 2 and 3 of cycle 23 can be compared with the TRACG calculations reported by Wouters et al.¹ During the measurements of case 1, the operators did not change the reactor conditions. As a result, power was lost to the vessel internals, the vessel wall and the drywell. The occurrence of subcooled boiling at the outlet of the hot channel, see Section 7.5.1, therefore stopped due to the decrease in temperature. Going from case 1 to case 2, the reactor power level was increased, and boiling again occurred at the exit of the hot channel. These voids collapse in the riser, and form hot slugs with a temperature slightly below the saturation temperature. The boiling boundary in the riser therefore moves downwards, and the coolant starts to flash at the riser exit. The TRACG code predicts the development of self-sustained Type-I oscillations under these circumstances (the initially diverging oscillations rapidly converge to stable nonlinear oscillations with a modest amplitude, cf. Ref. 18). At higher power and pressure levels, no longer all voids generated in the hot channels are collapsed at the riser inlet, and boiling occurs in the entire riser section. This effectively reduces the fluctuations of the driving head, and the flow stabilizes.

The results of our elementary model agree qualitatively well with the TRACG simulation of the early startup phase of cycle 23. Boiling starts at the end of the riser when the conditions of case 2 are simulated, see the fifth column in Table 7-5. Under these low pressure conditions (~6 bar), void flashing out of the heated reactor core is unstable according to our model (the flow becomes unstable in our transient model if the boiling boundary is located above the critical value listed in the last column of Table 7-5). Increasing the power and pressure level further, the boiling boundary moves downwards, and the Type-I oscillations disappear when the coolant starts to boil in the reactor core (for instance for case 4).

The startup measurements during cycles 24-26 focused on the early startup phase (pressures below 10 bar), to investigate the phenomenon of void flashing in the riser in more detail. Our model indicates that the operating conditions were chosen correctly during these

measurements, because the coolant was indeed flashing in the riser for all measured cases listed in Table 7-5 (cycles 24-26). Evaluation of these experiments with advanced thermohydraulic codes (like TRACG or MONA¹⁹) is strongly recommended. A simultaneous effort should focus on the performance of state-of-the-art experiments in the low power and pressure domain. An overview of the experimental facilities investigating the dynamics of BWRs at startup conditions has been given in Section 5.2. A new facility is currently under construction at Delft University of Technology. This setup, CIRCUS (Circulation at Startup), consists of four independently heated channels and four unheated bypass channels. The flow channels are connected with a riser section, steam dome and downcomer loop. High-fidelity void fraction and flow velocity measurements will be performed using gamma-transmission and Laser Doppler Anemometry (LDA) equipment.

7.6. CONCLUSIONS

The theoretical BWR stability models, developed within the framework of this thesis, are benchmarked against experimental data in this chapter. The thermohydraulics module is applied to a set of detailed void fraction measurements in the DESIRE facility at the Interfaculty Reactor Institute. Good agreement was found, especially when the nonuniformity of the void fraction over the channel cross-section is taken into account. Thermohydraulic instabilities that have been reported in two-phase flow literature were also correctly predicted, over a wide range of operating conditions.

Stability tests in the Dutch natural circulation Dodewaard BWR were simulated with the coupled neutronic-thermohydraulic reactor model. Under high power (Type-II) conditions, the model explains the experimentally observed trends. The nonlinear model was validated against nonlinear power oscillations measured at the end of the cycle 26 measurements. The stochastic nature of the measured time trace was reproduced successfully with the nonlinear time-domain model, by introducing a noise source in the thermohydraulic subsystem.

The encountered oscillations at the startup of the Dodewaard reactor are caused by the Type-I feedback mechanism, according to our model. An evaluation of the experiments shows that void flashing in the riser becomes important under low-pressure startup conditions. Further evaluation of the available reactor data, for instance using advanced thermohydraulic codes, is strongly recommended. A complementary effort should focus on performing high-fidelity measurements in test facilities, to provide accurate data on the stability of two-phase flow under low-pressure conditions.

REFERENCES

1. J.A.A. Wouters, J.B. Morales, and H.T. Kim, "TRACG Simulation of the February 1992 Startup of the

- Dodewaard Natural Circulation BWR," *Proc. 4th Int. Conf. Nuclear Engineering (ICONE-4)*, New Orleans, Louisiana, March 10-14, 1996, Vol. 3, p. 149, American Nuclear Society (1996).
2. T.H.J.J. van der Hagen, H. van Dam, and H.V. Kok, "The Delft DESIRE Facility for Studies on (Natural Circulation) BWR Primary System Statics and Dynamics," *Proc. ENS Class 1 Topical Meeting on Research Facilities for the Future of Nuclear Energy*, Brussels, Belgium, June 4-6, 1996, p. 365 (1996).
 3. H.V. Kok, "Experiments on a Natural Circulation Loop - From Void Fraction to Coupled Nuclear Thermal-Hydraulic Dynamics," PhD Thesis, Delft University of Technology, Delft, The Netherlands (1998).
 4. D.D.B. van Bragt and T.H.J.J. van der Hagen, "Stability of Natural Circulation Boiling Water Reactors: Part I - Description Stability Model and Theoretical Analysis in Terms of Dimensionless Groups," *Nucl. Technol.*, **121**, 40 (1998); also published as Chapter 2 of this thesis.
 5. D.D.B. van Bragt and T.H.J.J. van der Hagen, "Stability of Natural Circulation Boiling Water Reactors: Part II - Parametric Study of Coupled Neutronic-Thermohydraulic Stability," *Nucl. Technol.*, **121**, 52 (1998); also published as Chapter 3 of this thesis.
 6. G.E. Dix, "Vapor Void Fractions for Forced Convection with Subcooled Boiling at Low Flow Rates," NEDO-10491, General Electric Company (1971).
 7. P. Saha, M. Ishii, and N. Zuber, "An Experimental Investigation of the Thermally Induced Flow Oscillations in Two-Phase Systems," *J. of Heat Transfer*, **98**, 616 (1976).
 8. A.A. Karve, Rizwan-uddin, and J.J. Dorning, "On Spatial Approximations for Liquid Enthalpy and Two-Phase Quality During Density-Wave Oscillations," *Trans. Am. Nucl. Soc.*, **71**, 533 (1994).
 9. Rizwan-uddin and J.J. Dorning, "Some Nonlinear Dynamics of a Heated Channel," *Nucl. Eng. Des.*, **93**, 1 (1986).
 10. T.H.J.J. van der Hagen, D.D.B. van Bragt, F.J. van der Kaa, D. Killian, W.H.M. Nissen, A.J.C. Stekelenburg, and J.A.A. Wouters, "Exploring the Dodewaard Type-I and Type-II Stability; From Start-Up to Shut-Down, From Stable to Unstable," *Ann. Nucl. Energy*, **24**, 659 (1997).
 11. W. Wulff, H.S. Cheng, D.J. Diamond, and M. Khatibrahbar, "A Description and Assessment of RAMONA-3B Mod. 0 Cycle 4: A Computer Code with Three-Dimensional Neutron Kinetics for BWR-System Transients," BNL-NUREG-51748 (1984).
 12. A.J.C. Stekelenburg, "Statics and Dynamics of a Natural Circulation Boiling Water Reactor," PhD Thesis, Delft University of Technology, Delft, The Netherlands (1994).
 13. T.H.J.J. van der Hagen, F.J. van der Kaa, D. Killian, W.H.M. Nissen, and A.J.C. Stekelenburg, "Shutdown of the Dodewaard Natural Circulation Boiling Water Reactor at the End of Cycle 26," GKN-Report 96-023/FY/R, Gemeenschappelijke Kernenergiecentrale Nederland (1996).
 14. T.H.J.J. van der Hagen, Interfaculty Reactor Institute, Delft University of Technology, Personal Communication (Feb. 1997).
 15. F. Inada, M. Furuya, and A. Yasuo, "Thermo-Hydraulic Instability of Boiling Natural Circulation Loop Induced by Flashing (Analytical Consideration)," *Proc. 8th Int. Mtg. Nuclear Reactor Thermal-Hydraulics (NURETH-8)*, Kyoto, Japan, September 30-October 4, 1997, p. 1769 (1997).
 16. T.H.J.J. van der Hagen, A.J.C. Stekelenburg, S. Kaart, and J.C. Schouten, "Investigations on Start-Up Flow Oscillations in Natural Circulation BWRs," *Proc. National Heat Transfer Conf.*, Houston, Texas, August 3-6, 1996, Vol. 9, 188, American Nuclear Society (1996).
 17. T.H.J.J. van der Hagen, F.J. van der Kaa, D. Killian, W.H.M. Nissen, and A.J.C. Stekelenburg, "Startup of the Dodewaard Natural Circulation Boiling Water Reactor: Measurements at Low Pressures in Cycle 24," GKN-Report 96-033/FY/R, Gemeenschappelijke Kernenergiecentrale Nederland (1996).
 18. J.G.M. Andersen and L.A. Klebanov, "TRACG Analyses of Flashing Instability During Start-Up," *Proc. 3rd Int. Conf. Nuclear Engineering (ICONE-3)*, Kyoto, Japan, April 23-27, 1995 (1995).

-
19. G. Grandi, "RAMONA-4 Development Project: Product Test Report MONA Model," TN-16/41.15.26, ScandPower (1997).

Chapter 8

Conclusions and Recommendations

Dynamics of BWRs was studied successfully with low-dimensional analytical models. The analytical approach was followed to increase insight into the main physical processes determining BWR stability. Many aspects of modern stability analysis were considered in this thesis, e.g. coupled neutronics-thermohydraulics, natural circulation core cooling, space-dependent oscillations, Type-I and Type-II density-wave oscillations, low-pressure stability and nonlinear dynamics. Progress made in each of these fields will be reviewed briefly in this final chapter. Recommendations for further theoretical and experimental work are made as well.

The main conclusion from this thesis is that the developed BWR models appear to have the right 'ingredients' to qualify as successful analytical models. They consist, for instance, of only a few interconnecting building blocks (neutron point-kinetics, first-order fuel dynamics and thermohydraulics), are flexible, and easy to use in fast parametric studies. Moreover, the models predict the measured trends in BWRs and experimental setups very well, indicating that the most important processes determining BWR stability are accounted for in sufficient detail.

Transformation of the model equations to a nondimensional basis, as described in Chapters 2 and 5, proves to be an extremely powerful method to identify the main (dimensionless) numbers determining stability. For a natural circulation BWR, all necessary information about the operating conditions is, for instance, incorporated in only three dimensionless numbers: the Zuber number N_{Zu} (also known as the 'phase change' number), the subcooling number N_{sub} , and the flashing number N_{flash} .

Moreover, at high pressures (>20 bar) N_{flash} becomes negligibly small. Hence, the location of the stability boundary in the N_{Zu} - N_{sub} map is almost completely pressure invariant in the high-pressure domain. Therefore, using this dimensionless stability map, instead of the traditional power-flow map, is strongly recommended in the stability analysis of (natural circulation) BWRs.

Two major types of BWR instabilities have been studied in this thesis (see Chapters 3 and

6). Experimentally observed instabilities in forced-convection BWRs are all of the *Type-II*. This type of instability has a thermohydraulic origin – phase lags between the one- and two-phase friction in the reactor core – and is amplified strongly by the neutronics feedback. It occurs typically at high-power and low-flow conditions, i.e. when N_{Zu} is large. Experimental work on this instability type in the DESIRE setup, which features an artificial void reactivity feedback loop, is currently progressing.

In natural circulation BWRs, the significant gravitational pressure drop over the riser section (installed to enhance the natural circulation flow rate) causes an additional type of reactor instabilities. These *Type-I* instabilities become especially important during low-power and low-pressure (reactor startup) conditions. Under these circumstances, the influence of pressure variations on the saturation enthalpy becomes significant. This effect is therefore incorporated in a low-pressure BWR model, developed in Chapter 5.

A parametric study with this analytical model, reported in Chapter 6, shows that ex-core boiling due to void flashing in the unheated riser section is dominant during the startup of a natural circulation BWR. Nuclear feedback effects are small under these conditions.

Stability characteristics change dramatically at lower pressures. The Type-I instability region in the N_{Zu} - N_{sub} plane expands, for instance, strongly if the reactor pressure is reduced, due to the occurrence of unstable (flashing-induced) Type-I oscillations. Our stability model, however, appears to be rather conservative (i.e. stability is underestimated) in the low-pressure regime, as an evaluation of stability data from the natural circulation Dodewaard reactor shows. A comparison with detailed TRACG simulations indicates that this might be due to model limitations (for instance the neglect of subcooled boiling and local power peaking). Incorporating these effects in the analytical models is possible, but at the expense of an increasing model complexity. Experimental work on low-pressure BWR dynamics will be performed in the CIRCUS facility, which is currently under construction.

Space-dependent oscillations have been evaluated in Chapter 3. The most important subcritical mode in BWRs is the first-azimuthal or ‘out-of-phase’ mode. This spatial mode can be excited in large-radius reactors, where the subcriticality of the out-of-phase mode becomes small (in an absolute sense). Local power monitoring is therefore recommended in large BWRs.

The high-pressure BWR model was also analyzed in the nonlinear domain with a numerical Hopf-bifurcation code (see Chapter 4). This nonlinear model was validated in Chapter 7 against nonlinear power oscillations measured in the Dodewaard reactor. The stochastic nature of the measured time trace was reproduced successfully with the nonlinear time-domain model, by introducing a noise source in the thermohydraulic subsystem.

A comprehensive parametric study clarified the impact of various design and operating parameters on the nature of bifurcation (subcritical vs. supercritical; stable periodic oscillations vs. growing amplitude oscillations). More theoretical work is, however, still

needed to assess the influence of modeling assumptions (especially in the thermohydraulics model) on the bifurcation characteristics.

Both supercritical (unstable steady-state but stable oscillations) and subcritical (stable steady-state but unstable oscillations) bifurcations were encountered, depending on the operating conditions and the strength of the nuclear feedback. The practical importance of the existence of subcritical bifurcations is significant, because they can in principle result in diverging and undamped power oscillations in the linearly stable region, especially if the reactor is operated in the vicinity of the stability boundary. A cascade of period-doubling pitchfork bifurcations, 'deep' in the unstable region, was also encountered. The oscillation amplitude of the reactor power becomes very large when the period-doubling sequence starts. The practical relevance of period-doubling bifurcations is therefore limited, because a reactor scram system should prevent their occurrence.

Appendices

APPENDIX A: OUT-OF-PHASE NEUTRON KINETICS

A.1. Modal Point-Kinetic Equations

The space-dependent neutron kinetics equation is the starting point to derive a suitable equation for higher harmonic oscillations of the neutron flux density¹:

$$\begin{aligned} \frac{1}{v} \frac{\partial \Phi(\vec{r}, t)}{\partial t} &= -M(\vec{r}, t) \Phi(\vec{r}, t) + (1 - \beta) F(\vec{r}, t) \Phi(\vec{r}, t) + \lambda C(\vec{r}, t), \\ \text{and } \frac{\partial C(\vec{r}, t)}{\partial t} &= \beta F(\vec{r}, t) \Phi(\vec{r}, t) - \lambda C(\vec{r}, t), \end{aligned} \quad (\text{A-1})$$

where $\Phi(\vec{r}, t)$ is the space (\vec{r}) - and time (t) - dependent neutron flux density. Only one (effective) energy - and one delayed neutron group have been taken into account in Eq. (A-1), to simplify the analysis. However, an extension to more energy- and delayed-neutron groups is possible.² The destruction operator $M(\vec{r}, t)$ and production operator $F(\vec{r}, t)$ in Eq. (A-1) are time-dependent due to void- and Doppler feedback effects (burnup can be neglected due to the different time scale). These operators consist of steady and oscillatory components, respectively:

$$M(\vec{r}, t) = M(\vec{r}) + \delta M(\vec{r}, t) \quad \text{and} \quad F(\vec{r}, t) = F(\vec{r}) + \delta F(\vec{r}, t). \quad (\text{A-2})$$

We now expand the neutron flux density $\Phi(\vec{r}, t)$ and precursor concentration $C(\vec{r}, t)$ in an infinite number of flux density modes:

$$\begin{aligned} \Phi(\vec{r}, t) &= N_0 \phi(\vec{r}) + \sum_{k=0}^{\infty} n_k(t) \phi_k(\vec{r}), \\ \text{and } C(\vec{r}, t) &= \frac{C_0 \phi(\vec{r})}{v} + \sum_{k=0}^{\infty} \frac{c_k(t) \phi_k(\vec{r})}{v}, \end{aligned} \quad (\text{A-3})$$

where $n_k(t)$ and $c_k(t)$ are time-dependent expansion coefficients (amplitudes) of the different flux density modes ϕ_k . N_0 and C_0 are steady-state amplitudes. The right hand side of Eq. (A-3) is divided by the neutron velocity v , to ensure that the dimension of the precursor concentration is m^{-3} . In equilibrium state, Eqs. (A-1) and (A-3) yield $C_0 = v(\beta/\lambda)FN_0$.

The lower-order spatial harmonics can be approximated with the static λ -modes¹:

$$M\phi_k(\vec{r}) = \frac{1}{\lambda_k} F\phi_k(\vec{r}) \text{ and } \langle \phi_m^\dagger, F\phi_k \rangle = 0 \text{ (} m \neq k\text{),} \quad (\text{A-4})$$

where λ_k is the eigenvalue of the k -th harmonic mode and ϕ_m^\dagger is the solution of the adjoint equation. Substituting Eqs. (A-2) and (A-3) into Eq. (A-1) and rearranging using Eq. (A-4) leads to an expression that can be multiplied by ϕ_m^\dagger ($m \neq 0$) and integrated over the reactor core to yield the modal point kinetics equations:

$$\begin{aligned} \frac{dn_m(t)}{dt} &= \frac{\rho_m^S - \beta}{\Lambda_m} n_m(t) + \lambda c_m(t) + \frac{\rho_{m0}^F(t)}{\Lambda_m} N_0 + \sum_{n=0}^{\infty} \frac{\rho_{mn}^F(t)}{\Lambda_m} n_n(t), \\ \frac{dc_m(t)}{dt} &= \frac{\beta}{\Lambda_m} n_m(t) - \lambda c_m(t), \end{aligned}$$

$$\text{where } \rho_m^S \equiv 1 - \frac{1}{\lambda_m},$$

$$\rho_{mn}^F(t) \equiv \frac{\langle \phi_m^\dagger, (\delta F - \delta M)(\vec{r}, t) \phi_n \rangle}{\langle \phi_m^\dagger, F\phi_m \rangle},$$

$$\text{and } \Lambda_m \equiv \frac{\langle \phi_m^\dagger, \frac{\phi_m}{v} \rangle}{\langle \phi_m^\dagger, F\phi_m \rangle},$$

(A-5)

where m is the order of the harmonic mode ($m=1,2,\dots$), ρ_m^S is the subcriticality of the m -th mode, and ρ_{mn}^F is the excitation reactivity of the m -th mode due to a net change in the n -th mode reaction rate. Equation (A-5) shows that the kinetics of the m -th mode is driven by both a linear feedback term, and an infinite summation of nonlinear terms (coupling the m -th mode with all other harmonics). The nonlinear terms are omitted in the frequency-domain calculations of Chapter 3. The (orthogonal) spatial modes are then decoupled.

A.2. λ -Modes in a (Homogeneous) Cylindrical Reactor Core

To get an impression of the different λ -modes in a reactor, we consider, as an example, a bare homogeneous cylindrical reactor core with (extrapolated) radius \tilde{R} and (extrapolated) height \tilde{L}_C . In a cylindrical coordinate system, the appropriate form of the one-group diffusion equation is³:

$$\frac{1}{r} \frac{\partial}{\partial r} r \frac{\partial \phi}{\partial r} + \frac{1}{r^2} \frac{\partial^2 \phi}{\partial \theta^2} + \frac{\partial^2 \phi}{\partial z^2} + B^2 \phi = 0, \quad (\text{A-6})$$

where B^2 is the (geometric) buckling. Equation (A-6) is a homogeneous partial differential equation (the 'Helmholtz' equation), and can be solved analytically using separation of

variables:

$$\phi(r, \theta, z) = R(r)T(\theta)Z(z). \quad (\text{A-7})$$

Substituting Eq. (A-7) in Eq. (A-6) and dividing by ϕ yields:

$$\frac{1}{R(r)} \frac{\partial^2 R(r)}{\partial r^2} + \frac{1}{rR(r)} \frac{\partial R(r)}{\partial r} + \frac{1}{r^2 T(\theta)} \frac{\partial^2 T(\theta)}{\partial \theta^2} + \frac{1}{Z(z)} \frac{\partial^2 Z(z)}{\partial z^2} + B^2 = 0. \quad (\text{A-8})$$

Introducing a separation constant τ^2 , we can solve the axial component of Eq. (A-8):

$$\frac{1}{Z(z)} \frac{\partial^2 Z(z)}{\partial z^2} = -\tau^2. \quad (\text{A-9})$$

The eigenfunctions and eigenvalues of this equation are well known. Applying the axial boundary conditions $Z(z=0) = Z(z=\tilde{L}_C) = 0$ we find:

$$Z_i(r) \sim \sin(\tau_i z), \quad \tau_i^2 = \left(\frac{(i+1)\pi}{\tilde{L}_C} \right)^2, \quad i=0, 1, 2, \dots \quad (\text{A-10})$$

Substituting Eq. (A-9) in Eq. (A-8) and multiplying by r^2 then leads to:

$$\frac{r^2}{R(r)} \frac{\partial^2 R(r)}{\partial r^2} + \frac{r}{R(r)} \frac{\partial R(r)}{\partial r} + \frac{1}{T(\theta)} \frac{\partial^2 T(\theta)}{\partial \theta^2} + \alpha^2 r^2 = 0, \quad (\text{A-11})$$

where we introduced $\alpha^2 = B^2 - \tau^2$. Now we can solve the azimuthal component, introducing a separation constant k^2 :

$$\frac{1}{T(\theta)} \frac{\partial^2 T(\theta)}{\partial \theta^2} = -k^2. \quad (\text{A-12})$$

The azimuthal solutions have to be periodic, i.e. $T(\theta + 2\pi) = T(\theta)$. Applying this constraint we find:

$$T_k(\theta) \sim C_1 \sin(k\theta) + C_2 \cos(k\theta), \quad k=0, 1, 2, \dots \quad (\text{A-13})$$

Substituting Eq. (A-12) in Eq. (A-11) and multiplying by $R(r)$ leads to the equation for the radial solutions $R(r)$:

$$r^2 \frac{\partial^2 R(r)}{\partial r^2} + r \frac{\partial R(r)}{\partial r} + (\alpha^2 r^2 - k^2) R(r) = 0. \quad (\text{A-14})$$

With the appropriate boundary condition $R(r=\tilde{R}) = 0$ we can solve Eq. (A-14). For each value of k , the general solution of the radial part of Eq. (A-14) can be written as a linear combination of k -th order Bessel functions of the first kind $J_k(\alpha r)$ and $J_{-k}(\alpha r)$ and k -th order Bessel

functions of the second kind $Y_k(\alpha r)$ ^{a)}:

$$R(r) = C_3 Y_k(\alpha r) + C_4 J_k(\alpha r) + C_5 J_{-k}(\alpha r). \quad (\text{A-15})$$

It is important to realize that $J_k(\alpha r)$ and $J_{-k}(\alpha r)$ are linearly dependent when k is an integer, so we can set C_5 equal to zero. Furthermore, because $Y_k(\alpha r) \rightarrow -\infty$ as $r \rightarrow 0$, we also set C_3 equal to zero. Applying our boundary condition at $r = \tilde{R}$, we find:

$$R_{k,j}(r) \sim J_k(\alpha_{k,j} r), \quad \alpha_{k,j}^2 = \left(\frac{v_{k,j+1}}{\tilde{R}} \right)^2, \quad j = 0, 1, 2, \dots, \quad (\text{A-16})$$

where $v_{k,j+1}$ is the $(j+1)$ -th zero of J_k .

Substituting Eqs. (A-10), (A-13) and (A-16) in Eq. (A-7) yields:

$$\begin{aligned} \phi_{i,j,k} &= J_k \left(v_{k,j+1} \frac{r}{\tilde{R}} \right) \sin \left[(i+1) \pi \frac{z}{\tilde{L}_C} \right] [C_1 \sin(k\theta) + C_2 \cos(k\theta)], \quad i, j, k = 0, 1, 2, \dots, \\ \text{and } B_{i,j,k}^2 &= \left(\frac{v_{k,j+1}}{\tilde{R}} \right)^2 + \left(\frac{(i+1)\pi}{\tilde{L}_C} \right)^2. \end{aligned} \quad (\text{A-17})$$

The indices i , j and k denote the i -th harmonic axial -, the j -th harmonic radial -, and the k -th harmonic azimuthal mode, respectively. It is convenient to label each harmonic mode with a triple index (i,j,k) .

A.3. Importance of the Out-of-Phase Mode

We can relate the geometric buckling of the modes in Eq. (A-17) with their subcriticality using a simple one-group diffusion theory relationship:

$$B_m^2 = - \frac{\nabla^2 \phi_m(r)}{\phi_m(r)} = \frac{\nu \Sigma_f (1 - \rho_m^S) - \Sigma_a}{D}. \quad (\text{A-18})$$

where Σ_a is the macroscopic absorption cross section, ν the (average) number of neutrons released per fission, Σ_f the macroscopic fission cross section, and D the diffusion constant.

Clearly, mode $(0,0,0)$ has the smallest geometric buckling and is thus the least subcritical (in an absolute sense). This mode is traditionally called the fundamental mode. In a critical reactor, the subcriticality of this mode is zero. Rearranging Eq. (A-18) then enables us to calculate the subcriticality of the higher harmonic modes:

^{a)}To be precise, (complex) Bessel functions of the third kind (Hankel functions) are also solutions of Eq. (A-14). However, because we search real solutions, we do not need to consider these functions. A detailed description of Bessel and Hankel functions is provided in Ref. 4.

$$\rho_m^S = \frac{D}{v\Sigma_f} \Delta B_m^2, \tag{A-19}$$

where ΔB_m^2 is the buckling difference between the fundamental mode and the higher harmonic mode m . Which higher harmonic mode has the least negative ρ_m^S depends on the actual core geometry. In general, a large radius to height ratio favors the first azimuthal mode (0,0,1) over the first axial mode (1,0,0) [see Eq. (A-17)]. By substituting typical BWR values⁵ for \bar{R} (2.286 m) and \tilde{L}_C (3.708 m), the buckling difference between the fundamental and first azimuthal mode is equal to -1.703 m^{-2} . On the other hand, the buckling difference between the fundamental and first axial mode is equal to -2.153 m^{-2} . Therefore, the first azimuthal mode is the first subcritical mode. The first azimuthal mode is also called the out-of-phase mode (see Fig. 1-7). Equation (A-17) shows that the azimuthal harmonic modes are in fact degenerate eigenfunctions, because the eigenvalue of these modes is not dependent on rotations around the z -axis. Therefore, a linearly independent azimuthal mode (rotated over $\pi/2$ - radians in case of the out-of-phase mode in Fig. 1-7) is also a solution of Eq. (A-6).

We can explicitly calculate the subcriticality of the out-of-phase mode when we combine Eqs. (A-17) and (A-19):

$$\rho_1^S = \rho_{(0,0,1)}^S = \frac{D}{v\Sigma_f} \frac{1}{\bar{R}^2} [v_{0,1}^2 - v_{1,1}^2]. \tag{A-20}$$

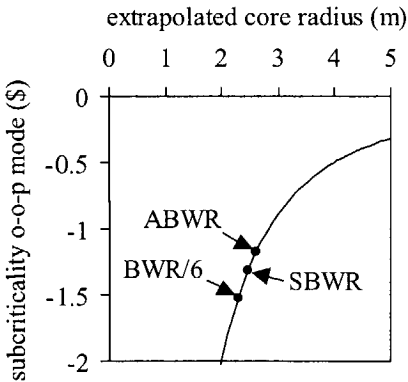


Figure A-1. Subcriticality of the out-of-phase (o-o-p) mode as a function of the core radius [calculated with Eq. (A-20)]. Typical (homogenized) BWR data have been used (see Ref. 6). The subcriticality of the o-o-p mode for a BWR/6, ABWR and the (abandoned) SBWR concept are shown as well.

This simple expression reveals that the subcriticality of the out-of-phase mode is inversely proportional with the square of the core-radius and inversely proportional to the macroscopic fission cross-section. The subcriticality of the out-of-phase mode as a function of the core radius is shown in Fig. A-1. We use $D=1.0 \times 10^{-2} \text{ m}$ and $v\Sigma_f = 2.0 \text{ m}^{-1}$ in this figure. We furthermore assumed that $\beta=0.0056$, to express the subcriticality in Fig. A-1 in \$ (data from Ref. 6). Notice the rapid decrease of the subcriticality (in an absolute sense) as the core radius increases.

It is important to emphasize that the dependence of subcriticality on control rod patterns, burnup, the presence of burnable poisons, etc., is not incorporated in this simple

(homogeneous) reactor model. Furthermore, three-dimensional harmonics code calculations⁵

show that the buckling difference between the fundamental mode and the first harmonic mode, as calculated with Eq. (A-17), could be an overestimation, indicating that a small subcriticality (in absolute sense) of the first harmonic mode is possible. New BWR designs like the ABWR have a larger core radius than the currently operational BWR/6 (to reduce the power density), which leads to an even smaller damping of out-of-phase oscillations in the neutronic subsystem, see Fig. A-1.

One important question remains to be answered here: How can a *subcritical* mode be sustained? In the linear approximation, the only remaining reactivity feedback term in Eq. (A-5) is ρ_{10}^F (we denote the out-of-phase mode as mode $m=1$). The (time- and space-dependent) oscillation operator $(\delta F - \delta M)(\vec{r}, t)$ is mainly determined by thermohydraulic state-variables as the void fraction and fuel temperature. During out-of-phase oscillations, this operator therefore has a spatial distribution similar to the $m=1$ mode:

$$(\delta F - \delta M)(r, z, \theta, t) \sim J_1 \left(v_{1,1} \frac{r}{\tilde{R}} \right) \sin \left(\frac{\pi z}{\tilde{L}_C} \right) \sin(\theta) \sin(\omega t). \quad (\text{A-21})$$

The excitation reactivity ρ_{10}^F of the out-of-phase mode now becomes:

$$\rho_{10}^F \sim \langle \phi_1^\dagger, (\delta F - \delta M)(r, z, \theta, t) \phi_0 \rangle$$

$$\sim \int_{r=0}^{\tilde{R}} J_1^2 \left(v_{1,1} \frac{r}{\tilde{R}} \right) J_0 \left(v_{0,1} \frac{r}{\tilde{R}} \right) 2\pi r dr \int_{z=0}^{\tilde{L}_C} \sin^2 \left(\frac{\pi z}{\tilde{L}_C} \right) dz \int_{\theta=0}^{2\pi} \sin^2(\theta) d\theta \sin(\omega t). \quad (\text{A-22})$$

The terms under the integral-signs are all non-negative in the domain of integration, and therefore the excitation reactivity of the out-of-phase mode is non-zero [and proportional to $\sin(\omega t)$].

REFERENCES

1. K. Hashimoto, "Linear Modal Analysis of Out-of-Phase Instability in Boiling Water Reactor Cores," *Ann. Nucl. Energy*, **20**, 789 (1993).
2. K. Hashimoto, A. Hotta, and T. Takeda, "Neutronic Model for Modal Multichannel Analysis of Out-of-Phase Instability in Boiling Water Reactor Cores," *Ann. Nucl. Energy*, **24**, 99 (1997).
3. J.J. Duderstadt and L.J. Hamilton, *Nuclear Reactor Analysis*, John Wiley & Sons, New York (1976).
4. M. Abramowitz and I.A. Stegun, *Handbook of Mathematical Functions*, Dover Publications, New York (1965).
5. Y. Takeuchi, Y. Takigawa, and H. Uematsu, "A Study on Boiling Water Reactor Regional Instability from the Viewpoint of Higher Harmonics," *Nucl. Technol.*, **106**, 300 (1994).
6. J. March-Leuba and E.D. Blakeman, "A Mechanism for Out-of-Phase Power Instabilities in Boiling Water Reactors," *Nucl. Sci. Eng.*, **107**, 173 (1991).

APPENDIX B: EQUATIONS OF THE HIGH-PRESSURE BWR MODEL

The dimensionless model equations for the high-pressure BWR model have been derived systematically in Chapter 2. This model is extended in this appendix, by including the effect of nonuniform (but symmetrical) axial power distributions in the equations. Furthermore, we account for the influence of nonuniform void distributions over the channel cross-section. This effect is incorporated in the void distribution parameter C_0 .¹ Finally, the original *mixed* system of algebraic relations and ODEs, see Chapter 2, is rewritten as a system consisting of ODEs only.

B.1. Neutron Kinetics

$$\frac{dN^*(t^*)}{dt^*} = \frac{\rho}{\Lambda^*} N^*(t^*) + \frac{\beta}{\Lambda^*} [C^*(t^*) - N^*(t^*)], \tag{B-1}$$

$$\frac{dC^*(t^*)}{dt^*} = \lambda^* [N^*(t^*) - C^*(t^*)], \tag{B-2}$$

cf. Eqs. (2-1) and (2-2). The different components of the reactivity term in Eq. (B-1) are described in detail in Eq. (2-3). The dimensionless variables and parameters in Eqs. (B-1) and (B-2) are defined as follows:

$$N^*(t^*) \equiv \frac{N(t^*)}{N}, \quad C^*(t^*) \equiv \frac{C(t^*)}{C}, \quad \Lambda^* \equiv \frac{\Lambda M_{C,i}}{L_C \rho_f}, \quad \lambda^* \equiv \frac{\lambda L_C \rho_f}{M_{C,i}}. \tag{B-3}$$

B.2. Fuel Dynamics

$$\frac{d\langle q''(t^*) \rangle_C^*}{dt^*} = \frac{1}{\tau_f^*} [\langle q'(t^*) \rangle_C^* - \langle q''(t^*) \rangle_C^*],$$

with $\tau_f^* \equiv \frac{\tau_f M_{C,i}}{L_C \rho_f}$, $\langle q'(t^*) \rangle_C^* \equiv \frac{\langle q'(t^*) \rangle_C}{\langle q' \rangle_C}$, and $\langle q''(t^*) \rangle_C^* \equiv \frac{\langle q''(t^*) \rangle_C}{\langle q'' \rangle_C}$, (B-4)

cf. Eq. (2-4). Because $\langle q'(t^*) \rangle_C^* = N^*(t^*)$, Eqs. (B-4) and (B-1) are directly coupled.

We assume that $q'(z^*, t^*)$ and $q''(z^*, t^*)$ can be written as the product of a time-dependent and a space-dependent term. We furthermore assume that the axial profile of the linear power production is approximately a sine-profile superimposed on a space-independent term^{2,3}:

$$q'(z^*, t^*) = \langle q'(t^*) \rangle_c AP(f_p, z^*),$$

$$\text{with } AP(f_p, z^*) \equiv \frac{1}{1 - \frac{2}{\pi}} \left[\left(1 - \frac{2f_p}{\pi} \right) + (f_p - 1) \sin(\pi z^*) \right], \quad (\text{B-5})$$

where we introduced the (normalized) function $AP(f_p, z^*)$ that depends on the (normalized) axial position z^* and the axial peaking factor f_p .

B.3. Boiling Boundary Dynamics

$$\frac{dZ_{bb}^*(t^*)}{dt^*} = \frac{1}{P_d} \left(M_{C,e}^*(t^*) \left[1 + J_{2,C}^*(t^*) \right] - \left[1 - Z_{bb}^*(t^*) \right] \langle q''(t^*) \rangle_{2\phi}^* N_{Zu} - Z_{bb}^*(t^*) \langle q''(t^*) \rangle_{1\phi}^* \frac{N_{Zu}}{N_{sub}} \right), \quad (\text{B-6})$$

cf. Eqs. (2-29) and (2-33). The factor P_d characterizes the influence of the axial peaking factor on the dynamic behavior of the boiling boundary. Applying the symmetrical power profile in Eq. (B-5), this factor becomes³:

$$P_d \equiv \frac{1 + 2\gamma Z_{bb}^*}{\left(1 + \gamma Z_{bb}^* \right)^2} \left(\frac{1}{2} + \frac{1}{3} \gamma Z_{bb}^* \right), \quad \text{with } \gamma \equiv \frac{\pi}{2} \frac{f_p - 1}{1 - \frac{2f_p}{\pi}}. \quad (\text{B-7})$$

The $J_{2,C}^*$ function in Eq. (B-6) is defined as in Eq. (2-30):

$$J_{2,C}^*(t^*) \equiv \chi_{C,e}^*(t^*) (N_{Zu} - N_{sub}). \quad (\text{B-8})$$

B.4. Core Void Dynamics

$$\frac{d\chi_{C,e}^*(t^*)}{dt^*} = \frac{\left[1 - Z_{bb}^*(t^*) \right] N_{Zu} \langle q''(t^*) \rangle_{2\phi}^* - J_{2,C}^*(t^*) M_{C,e}^*(t^*) + \frac{1}{C_0} \left\{ \frac{J_{2,C}^*(t^*) - \ln \left[J_{2,C}^*(t^*) + 1 \right]}{J_{2,C}^*(t^*)} \right\} \frac{dZ_{bb}^*(t^*)}{dt^*}}{\frac{1}{C_0} (N_{Zu} - N_{sub}) \left\{ \left[1 - Z_{bb}^*(t^*) \right] \left\{ \frac{J_{2,C}^*(t^*) + 1}{J_{2,C}^*(t^*)} \ln \left[\frac{J_{2,C}^*(t^*) + 1}{J_{2,C}^*(t^*)} \right] - J_{2,C}^*(t^*) \right\} \right\}}, \quad (\text{B-9})$$

cf. Eqs. (2-30) through (2-33).

B.5. Void Dynamics for the n-th Riser Node

$$\frac{d\chi_{R,n}^*(t^*)}{dt^*} = \left[2 \times \frac{J_{2,R,n}^*(t^*) - J_{2,R,n-1}^*(t^*)}{1 + J_{2,R,n-1}^*(t^*)} - 1 \right] \frac{d\chi_{R,n-1}^*(t^*)}{dt^*} + 2C_0 \times \frac{N_R}{L_R^*} \frac{[J_{2,R,n-1}^*(t^*) - J_{2,R,n}^*(t^*)] [1 + J_{2,R,n-1}^*(t^*)] [1 + J_{2,C}^*(t^*)]}{(N_{Zu} - N_{sub}) [1 + J_{2,R,n}^*(t^*)]} \frac{M_{C,e}^*(t^*)}{A_R^*}, \tag{B-10}$$

cf. Eqs. (2-34) through (2-39). The $J_{2,R,n}^*$ function in Eq. (B-10) is defined as in Eq. (2-35):

$$J_{2,R,n}^*(t^*) \equiv \chi_{R,n}^*(t^*) (N_{Zu} - N_{sub}). \tag{B-11}$$

Variables labeled with a subscript ‘n-1’ in Eq. (B.10) are evaluated at the ‘inlet’ of the n-th riser node. The subscript ‘n’ denotes the n-th node ‘outlet’. The $J_{2,R,0}^*$ function, appearing in the equation for the first riser node (n=1), is equal to $J_{2,C}^*$.

B.6. Mass Flux Density Dynamics

All pressure drop terms accounted for in the model are summarized systematically in Table 2-1. Using Eqs. (B-1) through (B-11), and manipulating, a (complicated) ODE for $M_{C,e}^*$ was generated with the Mathematica package. For brevity, this expression is not reported here.

REFERENCES

1. N.E. Todreas and M.S. Kazimi, *Nuclear Systems I - Thermal Hydraulic Fundamentals*, Hemisphere Publishing Corporation, New York (1990).
2. A.J.C. Stekelenburg, “Statics and Dynamics of a Natural Circulation Cooled Boiling Water Reactor,” PhD Thesis, Delft University of Technology, Delft, The Netherlands (1994).
3. D.D.B. van Bragt, “A Theoretical Model for Coupled Neutronic-Thermohydraulic Out-of-Phase Oscillations in Boiling Water Reactors,” IRI-131-95-015, Interfaculty Reactor Institute, Delft University of Technology (1995).

APPENDIX C: DIMENSIONLESS NUMBERS AND VARIABLES IN THE LOW-PRESSURE BWR MODEL

The dimensionless numbers and variables in the high-pressure BWR model have been presented before in Eqs. (2-25) through (2-28) and Eqs. (B-3) and (B-4). The definition of the pressure-dependent numbers and variables needs to be refined in the low-pressure BWR model. In this model, see Chapter 5, the vapor and liquid densities (ρ_l and ρ_g) and the evaporation enthalpy (h_{fg}) are assumed to be constant in the flow loop. These properties are evaluated at the core inlet in Eq. (C-1). However, alternative definitions, for instance with respect to the local pressure at the riser exit, are also possible. Because the pressure dependence of the saturation enthalpy is accounted for in the low-pressure model, the dimensionless subcooling of the fluid with respect to the riser exit, $N_{sub_{r,e}}$, will differ from the core-inlet subcooling $N_{sub_{c,i}}$. The difference between $N_{sub_{c,i}}$ and $N_{sub_{r,e}}$ is equal to the flashing number N_{flash} . This number is assumed to be zero in the high-pressure model developed in Chapter 2 and Appendix B (i.e. $N_{sub_{r,e}} = N_{sub_{c,i}}$).

$$\begin{aligned}
 N_{Zu} &\equiv \frac{L_C q / c}{A_C M_{C,i} h_{fg_{C,i}}} \frac{\rho_{f_{C,i}}^{-\rho_{g_{C,i}}}}{\rho_{g_{C,i}}}, \quad N_{Fr} \equiv \frac{(M_{C,i} / \rho_{f_{C,i}})^2}{g_C L_C}, \quad N_\rho \equiv \frac{\rho_{g_{C,i}}}{\rho_{f_{C,i}}}, \\
 N_{sub_{c,i}} &\equiv \frac{h_{f_{C,i}} - h_{l_{C,i}}}{h_{fg_{C,i}}} \frac{\rho_{f_{C,i}}^{-\rho_{g_{C,i}}}}{\rho_{g_{C,i}}}, \quad N_{sub_{r,e}} \equiv \frac{h_{f_{r,e}} - h_{l_{C,i}}}{h_{fg_{C,i}}} \frac{\rho_{f_{C,i}}^{-\rho_{g_{C,i}}}}{\rho_{g_{C,i}}}, \\
 N_{flash} &\equiv N_{sub_{c,i}} - N_{sub_{r,e}} = \frac{h_{f_{C,i}} - h_{f_{r,e}}}{h_{fg_{C,i}}} \frac{\rho_{f_{C,i}}^{-\rho_{g_{C,i}}}}{\rho_{g_{C,i}}}, \\
 t^* &\equiv \frac{t M_{C,i}}{L_C \rho_{f_{C,i}}}, \quad s^* \equiv \frac{s L_C \rho_{f_{C,i}}}{M_{C,i}}, \\
 h^*(t^*) &\equiv \frac{h(t^*) - h_{f_{C,i}}}{h_{f_{r,e}} - h_{f_{C,i}}}, \quad P^*(t^*) \equiv \frac{P(t^*)}{M_{C,i}^2 / \rho_{f_{C,i}}}, \\
 \Lambda^* &\equiv \frac{\Lambda M_{C,i}}{L_C \rho_{f_{C,i}}}, \quad \lambda^* \equiv \frac{\lambda L_C \rho_{f_{C,i}}}{M_{C,i}}.
 \end{aligned}
 \tag{C-1}$$

APPENDIX D: COEFFICIENTS OF EQ. (5-26)

The coefficients of the ordinary differential equation (5-26) for the boiling boundary are listed in this appendix. The partial derivatives of the saturation enthalpy, see Eq. (5-20), are used to simplify the expressions for these coefficients:

$$\begin{aligned}
 C_{Z,0} &= (1 - b_R) N_{Zu} + N_{flash} \frac{\partial \delta h_f^*(Z_{bb}^*, s^*)}{\partial \delta Z_{bb}^*(s^*)}, \\
 C_{Z,1} &= C_{Z,0} \frac{1}{2} (\tau_{1\phi,C}^* + \tau_{1\phi,R}^*) \\
 C_{Z,2} &= C_{Z,0} \frac{1}{4} \tau_{1\phi,C}^* \tau_{1\phi,R}^*, \\
 C_{Q,0} &= -N_{Zu} \tau_{1\phi,C}^*, \\
 C_{Q,1} &= N_{Zu} \frac{1}{2} \tau_{1\phi,C}^* \tau_{1\phi,R}^*, \\
 C_{M,0} &= N_{Zu} \tau_{1\phi,C}^* - N_{flash} \frac{\partial \delta h_f^*(Z_{bb}^*, s^*)}{\partial \delta M_{C,i}^*(s^*)}, \\
 C_{M,1} &= \frac{1}{2} (\tau_{1\phi,C}^* + \tau_{1\phi,R}^*) (C_{M,0} - N_{Zu} \tau_{1\phi,C}^*) - N_{Zu} \frac{1}{2} \tau_{1\phi,C}^* \tau_{1\phi,R}^*, \\
 C_{M,2} &= \frac{1}{4} \tau_{1\phi,C}^* \tau_{1\phi,R}^* (C_{M,0} - N_{Zu} \tau_{1\phi,C}^*). \tag{D-1}
 \end{aligned}$$

The last coefficient, $C_{M,2}$, is set equal to zero in the calculational model.

Nomenclature

I. LIST OF MOST IMPORTANT SYMBOLS

A	= cross-sectional flow area (m^2) relative atomic weight
AP(z)	= axial power profile
B^2	= geometric buckling (m^{-2})
b_R	= $b_R = 0$ if boiling occurs in the core; $b_R = 1$ if boiling only occurs in the riser
C	= precursor concentration (m^{-3})
C_0	= void distribution parameter steady-state amplitude in Eq. (A-3) ($m^{-2} \cdot s^{-1}$)
c_k	= expansion coefficient (amplitude) in Eq. (A-3) ($m^{-2} \cdot s^{-1}$)
D	= hydraulic diameter (m) diffusion constant (m)
F	= production operator (m^{-1})
f	= frequency (s^{-1}) Darcy-Weisbach friction factor
f_p	= axial peaking factor
G_a	= thermohydraulic transfer function
G_F	= fuel heat transfer function
G_R	= zero-power reactor transfer function
G_T	= closed-loop reactor transfer function
$G_{y,x}$	= transfer function from x to y
G_1	= auxiliary thermohydraulic transfer function [see Eq. (2-18)]
g_c	= gravitational acceleration (m/s^2)
h	= enthalpy (J/kg)
I_{eff}	= effective resonance integral (m^2)
J_k	= k-th order Bessel function of the first kind
J_1, J_2, J_3	= auxiliary dimensionless functions (see Chapter 2 and Appendix B)
k	= local pressure drop coefficient separation constant
k_{eff}	= effective multiplication factor

k_f	= heat transfer coefficient ($J/s \cdot m^2 \cdot K$)
L	= length (m)
(L/A)	= equivalent inertia length of the downcomer (m^{-1})
M	= mass flux density ($kg/m^2 \cdot s$) destruction (or "migration") operator (m^{-1})
N	= neutron number density (m^{-3})
N_C	= total number of nodes in the core
N_R	= total number of nodes in the riser
N_0	= steady-state amplitude of the neutron flux density ($m^{-2} \cdot s^{-1}$)
n_k	= k-th expansion coefficient (amplitude) of the neutron flux density ($m^{-2} \cdot s^{-1}$)
P	= pressure ($kg/m \cdot s^2$)
P_d	= auxiliary function [see Eq. (B.7)]
P_{th}	= thermal reactor power (J/s)
p	= resonance escape probability
q'	= linear power produced in the fuel ($J/s \cdot m$)
q''	= heat flux density from fuel to coolant ($J/s \cdot m^2$)
R	= core radius (m)
$R(r)$	= radial component of $\phi(r, \theta, z)$
r	= radial coordinate (m)
\bar{r}	= spatial coordinate (m)
r_a	= void reactivity coefficient
$r_{a,1}, r_{a,2}$	= void reactivity coefficients
\tilde{r}_a	= adjusted void reactivity coefficient
r_D	= Doppler reactivity coefficient (K^{-1})
\tilde{r}_D	= adjusted Doppler reactivity coefficient
s	= Laplace variable (s^{-1})
T	= temperature (K) oscillation period (s)
T_f	= fuel temperature (K)
T_{sub}	= fluid subcooling (K)
$T(\theta)$	= azimuthal component of $\phi(r, \theta, z)$
t	= time (s)
V	= volume (m^3)
v	= neutron velocity (m/s)
\vec{v}_1	= eigenvector of the linearized system
\vec{x}	= state vector
Y_k	= k-th order Bessel function of the second kind
Z_{bb}	= boiling boundary position (m)

- $Z(z)$ = axial component of $\phi(r,\theta,z)$
 z = axial position (relative to the core inlet) (m)

Greek

- α = void fraction
 β = delayed neutron fraction
characteristic coefficient
 β_2 = expansion coefficient
 $\delta(z)$ = Dirac's delta function
 ϵ = oscillation amplitude
 θ = azimuthal angle (rad)
 Λ = generation time (s)
frictional number
 λ = bifurcation parameter
precursor decay constant (s^{-1})
 λ_k = eigenvalue k-th harmonic mode
 μ = bifurcation parameter
 μ_2 = expansion coefficient
 ν = average number of neutrons released per fission
 ν_{kj} = j-th zero of J_k
 ξ = mean lethargy gain per collision
heated perimeter (m)
 ρ = density (kg/m^3)
reactivity
 ρ_{mn}^F = excitation reactivity m-th mode, due to a change in the n-th mode reaction rate
 ρ_m^S = subcriticality m-th harmonic mode
 Σ_a = macroscopic absorption cross-section (m^{-1})
 Σ_f = macroscopic fission cross-section (m^{-1})
 σ = microscopic cross section (m^2)
standard deviation
 σ_{noise} = noise source strength
 τ = time constant (s)
transit time (s)
separation constant
 τ_2 = expansion coefficient
 τ_f = fuel time constant (s)

Φ	= neutron flux density ($\text{m}^{-2}\cdot\text{s}^{-1}$)
ϕ	= flow rate (kg/s) flux density shape
ϕ^2	= two-phase friction multiplier
χ	= quality
ω	= angular frequency (rad/s)

Subscripts

a	= void
C	= core
c	= critical
D	= downcomer Doppler
e	= exit
ext	= external
f	= saturated liquid
fg	= difference between vapor and (saturated) liquid properties
fuel	= property of the fuel
fw	= feedwater
g	= vapor
i	= inlet
l	= liquid
m	= moderator
R	= riser
res	= resonance
s	= scattering
sat	= saturated
t	= total
0	= base
1	= out-of-phase mode
1 ϕ	= one phase
2 ϕ	= two phase

Superscripts

*	= normalized
---	--------------

† = adjoint

Operators

Δ = difference
(steady-state) riser node height, see Eq. (5-4)

δ = fluctuating part
deviation from the critical value

\sim = extrapolated

$\langle \rangle$ = average

$\langle \rangle$ = integration over reactor core

Dimensionless numbers

N_{Fr} = Froude number

N_{flash} = flashing number

N_{sub} = subcooling number

N_{Zu} = Zuber number

N_p = density ratio number

II. LIST OF ABBREVIATIONS

ABWR = advanced boiling water reactor

BWR = boiling water reactor

CIRCUS = Circulation at Startup

CRIEPI = Central Research Institute of Electric Power Industry

CWI = "Centrum voor Wiskunde en Informatica"
(National Research Institute for Mathematics and Computer Science)

DESIRE = Delft Simulated Reactor

DR = decay ratio

ESBWR = European simplified boiling water reactor

f.p. = full power

GE = General Electric

GKN = "Gemeenschappelijke Kernenergiecentrale Nederland N.V."

HB = Hopf bifurcation

HEM = homogeneous equilibrium mixture model

HRTL = heating reactor test loop

INET = Institute of Nuclear Energy and Technology

IRI	= Interfaculty Reactor Institute
i-p	= in-phase mode
KEMA	= "N.V. tot Keuring van Electrotechnische Materialen"
LDA	= Laser Doppler Anemometry
N.A.	= not available
NAPSD	= normalized auto-power spectral density
NEA	= Nuclear Energy Agency
NRC	= U.S. Nuclear Regulatory Commission
NWO	= "Nederlandse Organisatie voor Wetenschappelijk Onderzoek" (Netherlands Organization for Scientific Research)
ODE	= ordinary differential equation
OECD	= Organisation for Economic Co-operation and Development
o-o-p	= out-of-phase mode
PINK	= "Programma ter Instandhouding van Nucleaire Kompetentie"
S	= stable
SB	= stability boundary
SBWR	= simplified boiling water reactor

Summary (in Dutch)

De dynamica van kokendwaterreactoren (BWRs) is bestudeerd met vereenvoudigde analytische modellen. We richten ons op de dynamische instabiliteiten die worden veroorzaakt door de nucleaire en thermohydraulische processen in het reactorvat van een BWR. Onze analytische modellen vergroten het fysisch inzicht in de complexe processen die de stabiliteit van een BWR bepalen. Ze zijn ook zeer geschikt voor het uitvoeren van snelle (lineaire en niet-lineaire) parameterstudies (in tegenstelling tot grootschalige BWR-codes, die vaak uiterst tijdrovend zijn). Een breed scala van stabiliteitsproblemen wordt onderzocht: gekoppelde neutronica-thermohydraulica, niet-lineaire dynamica, plaatsafhankelijke oscillaties, natuurlijke-circulatie BWRs en dynamica bij lage drukken.

Eerst wordt een theoretisch model voor de hogedrukstabiliteit van natuurlijke-circulatie BWRs besproken. Dit thermonucleaire model bestaat uit benaderende modellen voor de neutronenkinetiek, splijstofdynamica en thermohydraulica. Deze systemen zijn met elkaar gekoppeld door de invloed van stoomvorming en het nucleaire Doppler-effect op het reactorvermogen. De vergelijkingen in het model zijn getransformeerd naar dimensieloze coördinaten om de expliciete drukafhankelijkheid in de modelvergelijkingen te elimineren.

Dit analytische model voorspelt dat twee instabiliteitstypen met name van belang zijn voor BWRs. BWRs zonder schoorsteen (bv. BWRs die worden gekoeld door middel van geforceerde convectie) zijn gevoelig voor zogenaamde *Type-II* instabiliteiten. Dit instabiliteitstype wordt veroorzaakt door fase draaiingen tussen de eenfasige en tweefasige frictiedrukvalen in de reactor kern. Deze stromingsinstabiliteit wordt in belangrijke mate versterkt door de nucleaire terugkoppelingsprocessen. *Type-II* instabiliteiten zijn vooral van belang wanneer het reactorvermogen hoog is en het koeldebiet gering. Natuurlijke-circulatie BWRs zijn tevens gevoelig voor zogenaamde *Type-I* instabiliteiten. *Type-I* instabiliteiten worden veroorzaakt door de gravitatie-drukval over de schoorsteen van een natuurlijke-circulatie BWR. Instabiliteiten van het *Type-I* treden op bij een gering reactorvermogen en een lage druk (bv. bij het opstarten van de reactor). De invloed van plaatsafhankelijke 'uit-fase' oscillaties op de *Type-I* en *Type-II* stabiliteit is onderzocht.

Het analytische model is geanalyseerd in het niet-lineaire domein met behulp van een Hopf-bifurcatieprogramma en numerieke tijddomeinsimulaties. De twee belangrijkste bifurcatietypen in BWRs, de superkritieke en de subkritieke Hopf-bifurcatie, zijn bestudeerd in uiteenlopende systemen (zuiver thermohydraulische systemen versus reactoren, geforceerde koeling versus

natuurlijke circulatie). De bifurcatiekarakteristieken zijn gevoelig voor de sterkte van de nucleaire terugkoppeling, de bedrijfscondities en de toegepaste nodalisatie in het model. Het tijddomeinmodel voorspelt verder dat 'diep' in het Type-II instabiliteitsgebied een opeenvolging van periodeverdubbende bifurcaties optreedt (na de eerste superkritieke Hopf-bifurcatie).

Vervolgens is een model ontwikkeld dat de dynamica van natuurlijke-circulatie BWRs bij een lage druk beschrijft. Dit model beschouwt de invloed van (axiale) drukverschillen in het koelmiddelcircuit op de verzadigingsenthalpie van de koelvloeistof. Bij een lage reactordruk is de verzadigingsenthalpie in sterke mate drukafhankelijk. De afnemende hydrostatische druk in de stroomrichting (wanneer het koelmiddel omhoog stroomt door de kern en schoorsteen) veroorzaakt in dit geval een sterke afname van de verzadigingsenthalpie. Dit kan mogelijk zelfs leiden tot een plotselinge stoomvorming. Een parameterstudie laat zien dat, tijdens het opstarten van een natuurlijk-circulatie BWR, voornamelijk stoomvorming in de schoorsteen plaatsvindt (en niet in de verhitte reactor kern). De invloed van nucleaire terugkoppel-effecten is, naar verwachting, in dit geval klein. Bij lage drukken neemt de gevoeligheid voor Type-I instabiliteiten sterk toe, omdat het stoomvormingsproces in de schoorsteen bij lage drukken een instabiel verschijnsel is. Dit bevestigt de recente zorg over de stabiliteit van natuurlijke-circulatie BWRs gedurende de opstartfase.

De ontwikkelde analytische modellen zijn met succes gevalideerd aan de hand van meetgegevens uit een natuurlijke-circulatie BWR (de Nederlandse Dodewaard-reactor) en experimentele opstellingen. Experimenteel waargenomen tendensen in het hoogvermogen (Type-II) gebied worden correct voorspeld. Het niet-lineaire reactormodel is gevalideerd aan de hand van grote vermogensoscillaties, gemeten in de Dodewaard-reactor. Oscillaties die in deze reactor gemeten zijn bij lage vermogens en drukken (het Type-I gebied) zijn gesimuleerd met het lage-druk BWR-model. Een evaluatie van deze experimenten toont aan dat stoomvorming in de schoorsteen inderdaad van belang is bij lage reactordrukken, in overeenstemming met de theoretische voorspellingen.

Summary (in Japanese)

内容梗概

沸騰水型軽水炉(BWR)の動特性を一次元解析モデルを用いて解析した。本研究は BWR 炉内の核および熱水力現象により生じる動的不安定現象を対象とし、導出した解析モデルにより BWR の安定性を左右する複雑な過程を物理的に考察した。長い計算時間が要求される大規模な BWR 炉心解析コードと比較すると、このモデルはパラメーターサーベイを短時間で行うことが出来る。核熱結合、非線形動特性、逆位相振動、自然循環 BWR、並びに低圧時の動特性など、広範囲に亘る安定性の問題を解明した。

第一に、自然循環 BWR に対する核熱結合振動の理論モデルを記述した。モデルは中性子動特性、燃料棒熱伝導、および熱水力挙動を簡略化したモデルから構成される。それぞれの要素はボイドおよびドブラー反応度によって結合されている。モデルの陽的な圧力依存性を減少させるために、モデル式を無次元化した。

二つの主要な BWR 不安定現象を解析モデルにより予測した。ライザー部分のない BWR(強制循環炉など)は、いわゆるタイプ II 不安定に陥りやすい。この不安定現象は熱水力挙動(炉心内の单相と二相の摩擦損失の差)支配であり、核フィードバックにより不安定は増大される。この不安定現象は、典型的には高出力低流量状態で生じる。これは無次元 Zuber 数が大きい場合に相当する。他方、自然循環冷却型 BWR はタイプ I 不安定に陥りやすい。タイプ I 不安定現象は、自然循環 BWR のライザー部分の水頭損失変動により引き起こされる。この現象は低出力かつ低圧の場合(原子炉起動時)に特に重要になる。またタイプ I とタイプ II 不安定の逆位相振動についても、詳しく調べた。

解析モデルを Hopf 分岐解析コードと時間領域の数値解析に適用した。超臨界および未臨界 Hopf 分岐という主に二種類の分岐現象が BWR では見られる。それらを、熱水力のみと核熱結合を考慮した原子炉とで比較、並びに強制循環炉と自然循環炉とで比較した。分岐特性は核フィードバック、運転状態、およびモデルの分割近似法に大きく影響されることを示した。時間領域モデルでは、最初の超臨界 Hopf 分岐後に三分岐型の周期倍分岐過程をタイプ II 不安定領域の「奥深く」で発見した。

次に、低圧状態における自然循環 BWR の動特性モデルを開発した。このモデルでは、(循環ループ内の軸方向の)圧力変化が冷却材の飽和エンタルピーに及ぼす影響を考慮している。炉心圧力が低い場合には飽和エンタルピーは圧力に強く依存する。冷却材は炉心からライザー部に向かって上昇し、流れに沿って静圧が減少することにより急速に飽和エンタルピーが減少する。これによりフラッシングが起こる可能性がある。パラメーターサーベイにより、自然循環 BWR の起動時には、非加熱ライザーでフラッシングすることによる炉外沸騰が顕著になることを示した。この状態ではボイド反応度の影響は小さいと考えられる。低圧ではライザー内で不安定要因であるフラッシングが生じるために、タイプ I 不安定現象の発生領域は圧力の減少に伴い急激に拡大する。これは自然循環 BWR の起動時安定性に関する最近の指摘と一致している。

導出した解析モデルを、自然循環冷却型 BWR(オランダの Dodewaard 炉)と実験設備で得られた実験データを基に検証した。高出力で実験的に得られた傾向(タイプ II)を、解析においても正しく再現した。非線形モデルについては Dodewaard BWR で観測された振幅の大きい出力変動データを用いて検証した。原子炉起動時の低圧かつ低出力(タイプ I)領域で生じた不安定現象を低圧 BWR モデルで解析した。これらの起動手法の評価により、理論予測と同じく、低圧ではライザー内でのフラッシングが重要であることを示した。

List of Publications

I. REFEREED JOURNAL PUBLICATIONS

E. Tiesinga, B.J. Verhaar, H.T.C. Stoof, and D.D.B. van Bragt, "Spin-Exchange Frequency-Shift in a Cesium Atomic Fountain," *Phys. Rev. A*, **45**, 2671 (1992).

T.H.J.J. van der Hagen, D.D.B. van Bragt, F.J. van der Kaa, D. Killian, W.H.M. Nissen, A.J.C. Stekelenburg, and J.A.A. Wouters, "Exploring the Dodewaard Type-I and Type-II Stability; From Start-Up to Shut-Down, From Stable to Unstable," *Ann. Nucl. Energy*, **24**, 659 (1997).

D.D.B. van Bragt, Rizwan-uddin, and T.H.J.J. van der Hagen, "Nonlinear Analysis of a Natural Circulation Boiling Water Reactor," To appear in *Nuclear Science and Engineering* (January 1999).

D.D.B. van Bragt and T.H.J.J. van der Hagen, "Stability of Natural Circulation Boiling Water Reactors: Part I - Description Stability Model and Theoretical Analysis in Terms of Dimensionless Groups," *Nucl. Technol.*, **121**, 40 (1998).

D.D.B. van Bragt and T.H.J.J. van der Hagen, "Stability of Natural Circulation Boiling Water Reactors: Part II - Parametric Study of Coupled Neutronic-Thermohydraulic Stability," *Nucl. Technol.*, **121**, 52 (1998).

II. CONFERENCE PROCEEDINGS

D.D.B. van Bragt and T.H.J.J. van der Hagen, "Reduced-Order Linear Analysis of BWR Stability," *Proc. 9th Topical Mtg. on Problems of Nuclear Reactor Safety*, Moscow, MEPhI, h/c "Volga", September 4-8, 1995, Vol. 1, p. 180 (1995).

D.D.B. van Bragt and T.H.J.J. van der Hagen, "A Six-Dimensional Model for Coupled Neutronic-Thermohydraulic Out-of-Phase Oscillations in Boiling Water Reactors," *Proc. National Heat Transfer Conf.*, Houston, Texas, August 3-6, 1996, Vol. 9, p. 179, American Nuclear Society (1996).

D.D.B. van Bragt and T.H.J.J. van der Hagen, "Analytical Modelling of Coupled Neutronic-Thermohydraulic Stability of Boiling Water Reactors," *Proc. Jahrestagung Kerntechnik '97*, Aachen, Germany, May 13-15, 1997, p. 3 (1997).

D.D.B. van Bragt and T.H.J.J. van der Hagen, "Experimental Validation of a Low-Dimensional Physical Model for Coupled Neutronic-Thermohydraulic Power Oscillations in Boiling Water Reactors," *Proc. 5th Int. Conf. Nuclear Engineering (ICONE-5)*, Nice, France, May 26-30, 1997, ICONE5-2138 (on CD-ROM), American Society of Mechanical Engineers, New York, NY (1997).

T.H.J.J. van der Hagen, A.J.C. Stekelenburg, and D.D.B. van Bragt, "Reactor Experiments on Type-I and Type-II BWR Stability," *Proc. 8th Int. Topical Mtg. on Nuclear Reactor Thermal-Hydraulics (NURETH-8)*, Kyoto, Japan, September 30-October 4, 1997, Vol. 1, p. 397 (1997).

T.H.J.J. van der Hagen, D.D.B. van Bragt, H.V. Kok, H. van Dam, and B.T. Adams, "Dynamics of Innovative BWRs," *Proc. 9th Int. Conf. on Emerging Nuclear Systems (ICENES '98)*, Tel-Aviv, Israel, June 28-July 2, 1998, p. 601 (1998).

D.D.B. van Bragt, Rizwan-uddin, and T.H.J.J. van der Hagen, "Effect of Void Distribution Parameter and Axial Power Profile on BWR Bifurcation Characteristics," To appear in *Proc. Int. Conf. on the Physics of Nucl. Science and Technol.*, Long Island, NY, October 5-8, 1998.

III. PUBLISHED REPORTS

D.D.B. van Bragt, "A Theoretical Model for Coupled Neutronic-Thermohydraulic Out-of-Phase Oscillations in Boiling Water Reactors," IRI-131-95-015, Interfaculty Reactor Institute, Delft University of Technology (1995).

D.D.B. van Bragt, "A Theoretical and Numerical Study of the Stability of a Natural Circulation Boiling Water Reactor," IRI-131-96-006, Interfaculty Reactor Institute, Delft University of Technology (1996).

D.D.B. van Bragt, "Hopf-Bifurcation Analysis of a Natural Circulation Boiling Water Reactor Model - Results for the Thermohydraulic Subsystem," IRI-131-97-010, Interfaculty Reactor Institute, Delft University of Technology (1997).

A.J.P. Rancuret and D.D.B. van Bragt, "Analytical Modelling of a 51 M Type U-Tube Steam Generator on the Basis of a Model for BWR Dynamics," IRI-131-98-004, Interfaculty Reactor Institute, Delft University of Technology (1998).

Acknowledgments

‘I forget my opinions constantly,
but refuse to learn them by heart’

—Bertold Brecht

Thanks, many thanks to everyone involved in and contributing to this Ph.D. thesis. In particular, I want to mention,

- Prof. Van Dam for offering an excellent educational program in reactor physics, a strong basis for my research work.
- Tim van der Hagen for his enthusiastic support, vision, flexibility and ever good humour. This thesis certainly became to a large extent what it is now due to his keen ‘fathership’.
- My collaborators in the stability field at IRI, especially Arnoud Rancuret, Robert Zboray, Haico Kok, Annalisa Manera, and Masahiro Furuya for using my models and further improving them.
- Shyam Khorana, of General Electric, who organized a very interesting visit to the GE offices in March 1996. His continuing interest in my work is also appreciated.
- Prof. Rizwan-uddin, who soon became my ‘second adviser’ after I visited the University of Illinois at Urbana-Champaign in the summer of 1997. He is the driving force behind the work on nonlinear dynamics, as reported in Chapter 4 and various publications. I especially want to thank him for making my stay at his university a very pleasant one.
- Dr. Inada, who helped to organize my trip to the Central Research Institute of Electric Power Industry (CRIEPI) in the summer of 1998 and assisted me in a truly excellent way in Japan.
- Mr. Swakhoven, Mark de Jonge, and my father, for designing and formatting the cover.
- My colleges from the Reactor Physics Department at IRI, my close friends, and my family for supporting me along the whole way. Thanks to you all, I’ll look back to four years of hard work, stimulating discussions, far journeys and all the rest...

Curriculum Vitae

David Dominique Bernard van Bragt

Date of birth: May 3, 1969

Place of birth: Roermond (The Netherlands)

- 1981-1987 Gymnasium β ('Bisschoppelijk College Broekhin' Roermond)
- 1987-1991 MS, Applied Physics (Eindhoven University of Technology)
Graduated June 26, 1991
Graduate subject: Determination of the accuracy of atomic clocks
- 1991-1993 MA, Philosophy (University of Amsterdam)
Graduated August 27, 1993
Graduate subject: Philosophy of language - metaphors
- 1994-1998 Ph.D. student at the Department of Reactor Physics (Interfaculty Reactor
Institute, Delft University of Technology)
Ph.D. subject: Analytical modeling of boiling water reactor dynamics
- Participant Frédéric Joliot Summer School at Cadarache, France
 (August 22-30, 1995)
- Visit to the General Electric company at San Jose, USA (March 24-31, 1996)
- Stay at the University of Illinois at Urbana-Champaign, USA
 (April-July, 1997)
- Participant course on management of large-scale research
 (February-April, 1998)
- Stay at the Central Research Institute of Electric Power Industry (CRIEPI),
 Tokyo, Japan (May-July, 1998)
- 1998-2000 Postdoc at the National Research Institute for Mathematics and Computer
Science in the Netherlands (CWI)

